



UNIVERSIDAD NACIONAL AUTÓNOMA DE MÉXICO

Programa de Maestría y Doctorado en Ingeniería  
Ingeniería Civil - Estructuras

---

# Numerical studies on the evaluation of the wind-induced dynamic response of wind turbine support structures

---

TESIS  
que para optar por el grado de:  
DOCTOR EN INGENIERÍA

*Presenta:*  
**Jesús Osvaldo MARTÍN DEL CAMPO Preciado**

*Tutor:*  
Dr. Adrián POZOS ESTRADA



Ciudad de México  
Septiembre de 2022



Universidad Nacional  
Autónoma de México

Dirección General de Bibliotecas de la UNAM

**Biblioteca Central**



**UNAM – Dirección General de Bibliotecas**  
**Tesis Digitales**  
**Restricciones de uso**

**DERECHOS RESERVADOS ©**  
**PROHIBIDA SU REPRODUCCIÓN TOTAL O PARCIAL**

Todo el material contenido en esta tesis esta protegido por la Ley Federal del Derecho de Autor (LFDA) de los Estados Unidos Mexicanos (México).

El uso de imágenes, fragmentos de videos, y demás material que sea objeto de protección de los derechos de autor, será exclusivamente para fines educativos e informativos y deberá citar la fuente donde la obtuvo mencionando el autor o autores. Cualquier uso distinto como el lucro, reproducción, edición o modificación, será perseguido y sancionado por el respectivo titular de los Derechos de Autor.

**JURADO ASIGNADO:**

Presidente: Dr. Luis Esteva Maraboto  
Secretario: Dr. Roberto Gómez Martínez  
1<sup>er</sup> Vocal: Dr. Adrián Pozos Estrada  
2<sup>do</sup> Vocal: Dr. Alberto López López  
3<sup>er</sup> Vocal: Dr. Han-Ping Hong

Lugar donde se realizó la tesis:

INSTITUTO DE INGENIERÍA, UNAM.

**TUTOR DE LA TESIS:**



---

Adrián Pozos Estrada

[This page intentionally left blank]



*“Truth is ever to be found in simplicity,  
and not in the multiplicity and confusion of things.”*

Isaac Newton

[This page intentionally left blank]

# Abstract

The tendency evinced in the design of contemporaneous wind turbines towards elements of greater size and flexibility has favored the employment of numerical models for their analysis and optimization. Notwithstanding the constant technological advancements that allow more detailed numerical analysis at a lower computational cost, the adequate assessment of structural performance and reliability levels for these machines demands large sample sizes, which can make the analysis prohibitive even nowadays.

This dissertation seeks to contribute to the proposal and development of methodologies that allow the performance of numerical analysis of the structural response of wind turbines at a lower computing cost without the implication of a significant loss of accuracy from the results. Emphasis is made on two particular cases relevant to the structural response of wind turbine towers: extreme wind loads due to tropical cyclones and fatigue damage due to normal turbine operation. The first two chapters of the document present a brief context on the growth of relevance of wind energy worldwide, along with aspects in which structural engineering is pertinent for that growth. Also, the second chapter presents a series of basic concepts of relevance for understanding the studies developed in the dissertation. The following chapters present the cases of study where the evaluation of the structural response of several wind turbines takes place: one of the turbines is off-employed as a reference for studies on the subject, and the other three were defined from statistics of actual turbines installed in Mexico. For the structural response evaluation, the performed analyses account for aeroelastic effects due to the interaction of the wind flow with the structure. A methodology developed to include fluid-structure interaction effects in elemental finite-element models is applied. Also, the enhancement in structural performance employing passive damping systems is explored, and it is evaluated in terms of structural reliability and risk estimation. The last of the studies presented in the document corresponds to a methodology for the simplified structural analysis and fatigue damage estimation on operating wind turbines. The said methodology is based on concepts of stochastic non-Gaussian stationary process simulation. The conclusions of all the above-listed studies, as well as some appendices, are presented at the end of the document.

**Key words:** Wind energy, wind turbines, wind engineering, tropical cyclones, structural reliability, passive damping systems, non-Gaussian stochastic processes, fatigue analysis.

[This page intentionally left blank]

# Resumen

La tendencia en el diseño de turbinas eólicas contemporáneas hacia elementos de mayor tamaño y flexibilidad ha propiciado el empleo de modelos numéricos para su análisis y optimización. Los constantes avances tecnológicos permiten análisis numéricos más detallados a un menor costo de cómputo, no obstante, la determinación adecuada de los niveles de desempeño y confiabilidad estructurales de estas máquinas demanda muestras de gran tamaño, lo cual puede llegar a hacer que los análisis de estas estructuras resulten prohibitivos aún hoy en día.

La presente disertación busca contribuir en la propuesta y desarrollo de metodologías que permitan llevar a cabo análisis numéricos de la respuesta estructural de turbinas eólicas a un bajo costo de cómputo, sin que ello implique una mengua significativa en la precisión de los resultados. Se hace énfasis en dos casos particulares de relevancia para la respuesta estructural de torres de turbinas eólicas: cargas de vientos extremos debido a ciclones tropicales y daño por fatiga debido a la operación normal de la turbina. Los primeros dos capítulos del documento presentan un breve contexto del aumento en la relevancia de la energía eólica en el mundo, así como aspectos de ello donde se ve implicada la ingeniería estructural. Además, en el segundo capítulo se presenta una serie de conceptos básicos relevantes para el entendimiento de los estudios que se desarrollan en la tesis. Los siguientes capítulos presentan los casos de estudio donde se evalúa la respuesta estructural de las torres de varios aerogeneradores: una de ellas es empleada comúnmente como referencia para estudios en la materia, y las otras tres fueron definidas con base en estadísticas de las turbinas eólicas instaladas en la República Mexicana. Los análisis realizados para la evaluación de la respuesta estructural contemplan los efectos aeroelásticos debidos a la interacción del flujo de viento sobre la estructura. Para ello, se desarrolló e implementó una metodología que permite incluir la interacción fluido-estructura en modelos básicos de elemento finito. También se explora la mejora del desempeño estructural mediante el empleo de sistemas de amortiguamiento pasivo, la cual es evaluada en términos de confiabilidad estructural y estimación de riesgo. El último de los estudios presentados corresponde a una metodología para simplificar la estimación de la respuesta estructural y el daño por fatiga en turbinas eólicas operantes. Dicha metodología se basa en conceptos para la simulación de procesos estocásticos estacionarios no-Gaussianos. Las conclusiones de los trabajos realizados, así como varios apéndices con comentarios y deducciones relacionados al contenido de la tesis, se presentan al final del documento.

**Palabras clave:** Energía eólica, turbinas eólicas, ingeniería de viento, ciclones tropicales, confiabilidad estructural, sistemas de amortiguamiento pasivo, procesos estocásticos no-Gaussianos, análisis de fatiga.

[This page intentionally left blank]

# Acknowledgements

The financial support from the National Council for Science and Technology (**CONACyT**) of Mexico, as well as from the **Institute of Engineering** of the National Autonomous University of Mexico (UNAM), is gratefully acknowledged.

I want to express my appreciation and gratitude to my advisor, Dr. **Adrián Pozos Estrada**. The time he spent listening to my dubieties about the dissertation always gave rise to guidance and excellent references to improve my work. I am thankful to him for being always responsive and supportive when such concerns appeared.

I thank the members of my doctoral committee: Professors **Luis Esteva Maraboto** and **Roberto Gómez Martínez** of the Institute of Engineering of UNAM, Professor **Alberto López López** of the National Institute of Electricity and Clean Energies (INEEL), and Professor **Han-Ping Hong** of the University of Western Ontario. I have been honored to be evaluated by such an eminent committee, their participation was a great motivation for me to exert myself.

A big thank-you to my companions of the **Wind Engineering Group** at the Institute of Engineering of UNAM, those breaks for a *chocolatín* at the wind tunnel lab were always refreshing.

I am ever grateful to my parents, **Carmen** and **Jesús**, for all their love and support. Undoubtedly, they have been the most solid pedestal on which I've founded anything I've accomplished. Thanks also to my sisters, **Astrid** and **Carmen**, for cheering on me and for being supportive of each other; thank you also for taking me to a new place with tasty food every time I visited you. A *two-pesos* thank-you (they'll get the joke) to my lifetime friends (almost-family) from Arandas, cheers to all of you! And of course, I am thankful to **Alhelí**, who has been more than support and inspiration during this journey.

This dissertation is a milestone for me, both personally and professionally. I betted on the UNAM for the pursuit of my Master's degree, and subsequent PhD: this is the culmination of that (more-than) six-year pilgrimage that involved leaving behind my job, city, and amenities, as well as distancing spatially from my family and friends (although I always kept them in my thoughts). Such valuable persons have represented more than motivation and encouragement during these strenuous years, made more arduous during the pandemic. These lines are insufficient to pour all my gratitude toward them, may they be at least a memento of the support such persons represented for me.

[This page intentionally left blank]



# List of Figures

1.1	Levelised costs of electricity generation . . . . .	2
1.2	Global wind energy capacity distribution . . . . .	3
1.3	Wind Farms installed in Mexico (2019) . . . . .	4
1.4	<i>La Bufa</i> wind farm (Zacatecas, Mexico) . . . . .	5
2.1	Schematic of the global atmospheric circulation . . . . .	16
2.2	Mean speed distribution in the PBL . . . . .	17
2.3	PSDFs of $u(t)$ estimated from wind tunnel measurements . . . . .	19
2.4	Structure of a tropical cyclone . . . . .	21
2.5	Schematic of a HAWT . . . . .	23
2.6	One-dimensional actuator disc concept . . . . .	25
2.7	Aerodynamic blade section and velocity and force vectors . . . . .	26
2.8	Rotationally sampled correlation function for different blades and radial coordinates: (a) for the same blade and same radii, (b) for the same blade and different radii, and (c) for different blades and different radii . . . . .	28
2.9	Normalized thrust spectra for a three-blade rotor . . . . .	30
3.1	Comparison between tropical cyclone turbulence field and conventional values (Left: normalized turbulence spectra, Right: coherence values) . . . . .	42
3.2	Simulated tropical cyclone parameters and mean speed profiles for the two selected sites	44
3.3	Turbulence spectra from the wind field simulations, for a height $z = 150$ m . . . . .	44
3.4	Aerodynamic coefficients for the airfoils that define the blade of the reference wind turbine . . . . .	47
3.5	Finite element model for the 5-MW reference wind turbine . . . . .	49
3.6	Finite element model for the 5-MW reference wind turbine including added damping and rigidity elements . . . . .	51
3.7	Spectral comparison between aeroelastic (AE) and non-aeroelastic (STR) time-history tower displacements . . . . .	52
3.8	Spectral comparison between aeroelastic (AE) and non-aeroelastic (STR) time-history tower-base moments . . . . .	52
3.9	Normal-distribution probability plot of displacements from aeroelastic (AE) and non- aeroelastic (STR) analyses . . . . .	53
3.10	Measured linear correlation coefficients from aeroelastic (AE) and non-aeroelastic (STR) analyses . . . . .	54
3.11	Skewness and kurtosis from structural responses . . . . .	55
3.12	Kurtosis values from structural responses . . . . .	56
3.13	Evaluation of goodness of response amplitude distributions . . . . .	57
3.14	Peak factors computed from the structural response . . . . .	58
3.15	Probability distribution of tower stress maxima for the Category I analyses . . . . .	60
3.16	Probability distribution of tower stress maxima for the Category III analyses . . . . .	60
4.1	Wind turbines in Mexico (2019) . . . . .	66
4.2	Structural summary of the hypothetical and reference wind turbines . . . . .	69

4.3	Section moduli of the hypothetical and reference wind turbines . . . . .	70
4.4	TCBL flow-field simulations for the 1 MW wind turbine: (a) Mean velocity profile, (b) Height of maximum wind, (c) Radius of maximum wind . . . . .	71
4.5	Aerodynamic coefficients of the assumed blades . . . . .	72
4.6	Along-wind displacement at the top of the tower: (a) for the 1MW turbine, (b) for the 2.5MW turbine, (c) for the 3.3MW turbine . . . . .	73
4.7	Summary from goodness-of-the-fit tests performed on the response maxima (from the top row to the bottom row: for DS1, DS2, and DS3) . . . . .	75
4.8	Fragility functions for the analyzed wind turbines under cyclone-induced action . . . . .	77
5.1	Modeling of a structure with a TMD . . . . .	82
5.2	Modeling of a TMD for finite element analysis . . . . .	85
5.3	Results from harmonic analyses of the structures with a TMD: (a) for the 1MW turbine, (b) for the 2.5MW turbine, and (c) for the 3.3MW turbine . . . . .	89
5.4	Displacement histories for the three turbines with and without TMD: (a) for the 1MW turbine, (b) for the 2.5MW turbine, and (c) for the 3.3MW turbine . . . . .	90
5.5	Spectral densities of tower-top displacement for $\bar{U}(10) = 50$ m/s. From top to bottom: for the 1, 2.5, and 3.3 MW wind turbines . . . . .	92
5.6	Fittings for the median of the demand parameters for the undamped and optimal cases. From left to right: for the 1, 2.5, and 3.3 MW wind turbines . . . . .	95
5.7	Fittings for the natural logarithm of the estimated median for the optimal cases, and observations . . . . .	96
5.8	Probability plots of raw residuals of Equation 5.18 . . . . .	97
5.9	Comparison of fragility values for the studied wind turbines . . . . .	98
5.10	Fragility enhancement achieved with a TMD on the structures: (a) for the 1 MW wind turbine, (b) for the 2.5 MW wind turbine, and (c) for the 3.3 MW wind turbine . . . . .	99
5.11	Annual exceedance rate for a site in Oaxaca, according to Jaimes et al. <sup>10</sup> . . . . .	101
6.1	Wind loading chain . . . . .	108
6.2	Non-Gaussian aerodynamic load signal: (a) Thrust force signal, (b) Amplitude histogram, (c) Q-Q plot of force amplitudes . . . . .	114
6.3	Direct translation of a stochastic process . . . . .	115
6.4	Degrees of freedom for the representation of a HAWT support structure . . . . .	116
6.5	Rotor speed and pitch angle criteria of the 5MW reference wind turbine <sup>34</sup> . . . . .	122
6.6	Standard errors measured for mean thrust force and mean tower displacement for $\bar{U}_{hub}$ of 10 and 15 m/s, and $I_u$ of 10 and 20% . . . . .	123
6.7	Statistical moments of aerodynamic forces on the operating rotor . . . . .	124
6.8	Measured correlation between the load histories in different DOFs for the seed sample . . . . .	125
6.9	Moment-based simulated rotor thrust forces for application on the simplified model . . . . .	126
6.10	Moment-based simulated rotor in-plane forces for application on the simplified model . . . . .	127
6.11	Non-parametrically transformed simulated rotor thrust forces for application on the simplified model . . . . .	128
6.12	Non-parametrically transformed simulated rotor in-plane forces for application on the simplified model . . . . .	129
6.13	Moduli of the frequency-response functions in the four DOFs involved in the simplified structural model . . . . .	130
6.14	Damping estimates in each DOF from the samples used as seed . . . . .	132
6.15	Kernel density estimations of damping values for the four DOFs needed for the simplified structural model . . . . .	133
6.16	Response histories and their respective spectral densities for the four DOFs accounted for in the simplified evaluation . . . . .	134
6.17	Maxima and minima of tower top displacement from simplified analyses . . . . .	136
6.18	Probability plots and $p$ -values from a two-sample Kolmogorov-Smirnov test from the control sample and replicated data . . . . .	137

---

6.19	Values of skewness $\alpha_3$ and kurtosis $\alpha_4$ measured from the seed sample, and application regions for the moment-based translations models . . . . .	138
6.20	Kernel density estimations of the resultant displacement amplitude . . . . .	139
6.21	Normal probability plots of resultant response maxima, and $p$ -values from a two-sample Kolmogorov-Smirnov test . . . . .	140
6.22	Signals of stress derivatives, as well as their spectral and statistical characteristics . . . .	142
6.23	Signals of stress amplitudes, as well as their spectral and statistical characteristics . . . .	143
6.24	Rainflow histograms for stress histories at the base of the tower: (a) from a full-model signal, and (b) from a replicated signal . . . . .	144
6.25	Kernel density estimations of range and mean of stress cycles: (a) from the full-model signal, (b) from the replicated signal, and (c) a normalized comparison of both . . . . .	145
6.26	Stress signal from the seed sample and replicated signals (a), normalized histogram from the original stress signal and kernel density estimations from the replicas (b), and PSDFs from the original signal and its replicas (c) . . . . .	147
6.27	Fatigue damage summary from originals and replicas of stress histories at the tower base	148
B.1	Fluid-induced forces on a structural element and responses . . . . .	161
B.2	Structural response of a 3-DOF system . . . . .	165

[This page intentionally left blank]

# List of Tables

1.1	Turbine classification according to IEC 61400-1 . . . . .	8
2.1	Saffir-Simpson hurricane scale . . . . .	21
3.1	Pressure differences deduced for the Saffir-Simpson classification of tropical cyclones, and their distribution parameters . . . . .	40
3.2	Mean wind speed and turbulence parameters for flow-field simulations . . . . .	43
3.3	General properties of the NREL 5-MW Baseline HAWT . . . . .	46
3.4	Distribution of the aerodynamic properties of the blade for the 5-MW reference wind turbine . . . . .	46
3.5	Blade dynamic properties computed from the APDL model . . . . .	48
3.6	Dynamic properties of the 5-MW reference wind turbine . . . . .	49
3.7	Evaluation of adequacy ( $p$ -values) of various distributions for the response maxima on the tower . . . . .	59
3.8	Probability of failure for the two sites and performance levels evaluated . . . . .	61
4.1	Summary of blade properties for the three wind turbines . . . . .	68
4.2	Summary of hub and nacelle properties for the three wind turbines . . . . .	68
4.3	Overall dimensions of the modeled wind turbine towers . . . . .	68
4.4	Dynamic properties of the modeled wind turbine towers . . . . .	69
4.5	Damage states defined for the fragility analyses . . . . .	75
4.6	Parameters for the fragility functions . . . . .	76
5.1	Modal properties of the modeled wind turbine towers . . . . .	87
5.2	Parameters for harmonic analyses and TMDs . . . . .	88
5.3	Average response reduction achieved with the TMDs . . . . .	91
5.4	Model estimators for the median structural response and uncertainties . . . . .	95
5.5	Annual probability of structural failure due to tropical cyclones . . . . .	101
6.1	Parameters of the 5MW reference wind turbine <sup>34</sup> for the simplified analyses . . . . .	121
6.2	Summary of fatigue damage from the analyses performed in FAST and the replicated signals . . . . .	147

[This page intentionally left blank]

# List of Abbreviations

## Institutions

<b>CFE</b>	Federal Electricity Commission (acronym in Spanish)
<b>IEA</b>	International Energy Agency
<b>IEC</b>	International Electrotechnical Commission
<b>NEA</b>	Nuclear Energy Agency
<b>NREL</b>	National Renewable Energy Laboratory
<b>WWEA</b>	World Wind Energy Association

## Technologies and technical terms

<b>ABL</b>	Atmospheric Boundary Layer
<b>APDL</b>	ANSYS Parametric Design Language
<b>ARMA</b>	Auto-Regressive Moving-Average (model)
<b>ASL</b>	Atmospheric Surface Layer
<b>BEM</b>	Blade Element Momentum
<b>CCGT</b>	Combined Cycle Gas Turbine
<b>CCUS</b>	Carbon Capture, Use (and) Storage
<b>CDF</b>	Cumulative Distribution Function
<b>CHP</b>	Combined Heat (and) Power
<b>CSP</b>	Concentrated Solar Power
<b>DOF</b>	Degree Of Freedom
<b>DS</b>	Damage State
<b>FEA</b>	Finite Element Analysis
<b>FEM</b>	Finite Element Model/Modelling
<b>FRF</b>	Frequency-Response Function
<b>FSI</b>	Fluid-Structure Interaction
<b>HAWT</b>	Horizontal Axis Wind Turbine
<b>LCOE</b>	Levelised Cost Of Energy
<b>LES</b>	Large Eddy Simulation
<b>LTO</b>	Long-Term Operation
<b>PBL</b>	Planetary Boundary Layer
<b>PDF</b>	Probability Density Function
<b>PSDF</b>	Power Spectral Density Function
<b>PV</b>	Photo-Voltaic
<b>RMS</b>	Root-Mean-Square
<b>TCBL</b>	Tropical Cyclone Boundary Layer
<b>TD</b>	Tropical Depression
<b>TLCD</b>	Tuned Liquid Column Damper
<b>TMD</b>	Tuned Mass Damper
<b>TS</b>	Tropical Storm

[This page intentionally left blank]



# Physical Constants

Gravitational Acceleration	$g$	$= 9.80665 \text{ m/s}^2$
Von Kármán constant	$\kappa$	$\approx 0.4$
Rotational Speed of the Earth	$\omega$	$= 7.292115 \times 10^{-5} \text{ rad/s}$

[This page intentionally left blank]

# List of Symbols

## Roman

$a, a'$	Axial and tangential induction factors	[-]
$a, b, c$	Moment-based (Hermitian) translation-model coefficients	[-]
$a_i, b$	Model parameters for estimation of median response	Various
$a_\delta, b_\delta, c_\delta$	Parameters in Snaiki and Wu's model for the height of maximum wind	Various
$A, I, S$	Cross-section area, moment of inertia, and elastic section modulus	$m^2, m^4, m^3$
$A_K, B_K, C_K$	Constants in the Kaimal turbulence spectrum	[-]
$A_c, B_c$	Parameters in the exponential coherence function	[-]
$a_*$	Parameter on Vickery et al.'s hurricane model	[-]
$b$	Holland's scale parameter of pressure gradient	[-]
$b_i, \varphi$	Moment-based (non-Hermitian) translation-model coefficients	[-]
$B, R$	Background and resonant components of response	[-]
$c$	Chord length	m
$C$	Scale parameter for the Weibull probability distribution	Various
<b>C, K, M</b>	Damping, stiffness, and mass matrices	Various
$c_d, k_d, m_d$	Damping, stiffness, and mass of tuned damper	Various
$C_D, C_L, C_M$	Aerodynamic force coefficients (drag, lift and moment)	[-]
$C_P, C_T$	Power and thrust coefficients of a turbine rotor	[-]
$c_s, k_s, m_s$	Damping, stiffness, and mass of single DOF system	Various
<b>d</b>	Structural response vector	Various
$D, L$	Drag, and lift forces	N
$D$	Fatigue damage	[-]
$D_c$	Tower section outer diameter	m
$d_j$	Structural displacement in the $j$ -direction	m
$DP$	Demand parameter	Various
$E$	Elastic modulus	Pa
<b>f</b>	Force vector	Various
$f_c$	Coriolis parameter	rad/s
$f_X, F_X$	Probability distribution and cumulative distribution functions	Various, [-]
$\hat{F}_j(x)$	Empirical cumulative distribution function	[-]
$F_{cr}$	Critical stress of tower section	Pa
$F_i(IM)$	Fragility function for an $i$ -th damage state	[-]
$F_{RR}$	Gust-response factor (CFE standard)	[-]
$F_y$	Yield stress of steel	Pa
$g$	Gravitational acceleration	$m/s^2$
$g(\cdot)$	Limit state function, translation function	Various, [-]
$H$	Hub height	m
$He_n(\cdot)$	$n$ -th Hermite polynomial	[-]
$h_n$	$n$ -th Hermite moment	[-]

$\tilde{h}_i$	Hermite series coefficient	[-]
$H^*$	Boundary layer height estimate in Vickery et al.'s hurricane wind profile model	m
$H(i\omega)$	Frequency-response function	Various
$He(\cdot)$	Hermite polynomial	[-]
$I$	Inertial stability	$s^{-1}$
$I_j$	Second area moment around the $j$ -axis	$m^4$
$IM$	Intensity measure	Various
$I_{ref}$	Reference turbulence intensity (IEC standard)	[-]
$I_u$	Turbulence intensity in the along-wind direction	[-]
$k$	Shape parameter for the Weibull probability distribution	[-]
$k_p$	Peak factor	[-]
$k(\cdot)$	Kernel density estimation	Various
$K_m(\cdot)$	Bessel function of second kind and $m$ -th order	[-]
$K_r, m$	Material constants defining the S-N curve	$MPa^m, [-]$
$L_u, L_v, L_w$	Integral length scale of turbulence measured in the along-wind direction for the $u, v$ , and $w$ wind velocity components	m
$m(\cdot)$	Lumped mass of a structural element	kg
$M$	Torque or moment	$N \cdot m$
$M_j$	Moment around the $j$ -axis	$N \cdot m$
$M_n, M_p, M_y$	Nominal, plastic, and yielding moment of a structural section	$N \cdot m$
$n$	Temporal frequency	Hz
$n^*$	Exponent on Vickery et al.'s hurricane wind profile model	[-]
$N$	Number of load cycles	[-]
$p, p_{cs}$	Atmospheric pressure, central surface pressure	hPa
$p_s$	Surface pressure	hPa
$P$	Power output, probability	W, [-]
$P_{af}$	Mean annual frequency of structural failure	[-]
$P_f$	Probability of failure	[-]
$P_u$	Acting axial force on the tower	N
$\mathbf{q}$	Structural response vector in modal coordinates	[-]
$r$	Radius of curvature for an isobar, or radial coordinate at a rotor blade	km, m
$r_{v_m}$	Radius of maximum wind during a tropical cyclone	km
$R$	Rotor radius, structural capacity	m, Various
$Ro_s$	Modified Rossby number	[-]
$s$	Distance between two points in space	m
$S$	Actions on a structural system, in-plane forces on a rotor	Various, N
$S_T$	Thrust force power spectrum	$N^2/Hz$
$S_u, S_v, S_w$	Single-sided power spectrum of the turbulence in the $x, y$ , and $z$ directions	$m^2 \cdot s^{-2}/Hz$
$S_u^o$	Rotationally-sampled along-wind turbulence spectrum	$m^2 \cdot s^{-2}/Hz$
$S_\zeta, S_\xi$	Single-sided spectral density of stress amplitudes and stress derivatives	$Pa^2/Hz, Pa^2/s$
$t$	Time	s
$t_c$	Thickness of tower section	m
$T$	Thrust force, or length of a signal	N, s
$T_r$	Return period	years
$u, v, w$	Time-varying components of wind velocity in the $x, y$ , and $z$ directions	m/s
$u_*$	Friction velocity	m/s
$U$	Longitudinal component of wind velocity	m/s
$U_3, U_{600}$	3-s, and 10-min averaged mean wind speed	m/s
$v_g$	Gradient wind speed	m/s

$v_m$	Maximum wind speed	m/s
$V_r, v_r$	Resultant velocity	m/s
$V_{ref}$	Reference velocity (IEC standard)	m/s
$x, y, z$	Cartesian coordinates	m
$X, Y, Z$	Random variables	Various
$z$	Vertical coordinate, or non-Gaussian random variable	m, Various
$z_g$	Gradient wind height	m
$z_{geo}$	Height of geostrophic balance	m
$z_h$	Zero-plane displacement height	m
$z_{ref}, z_s$	Reference height	m
$z_0$	Roughness length	m

## Greek

$\alpha$	Power-law exponent, angle of attack	[-], °
$\alpha_n$	$n$ -th statistical moment	Various
$\beta$	Pitch angle	°
$\gamma$	Euler's constant	[-]
$\Gamma(\cdot)$	Gamma function	[-]
$\delta$	Height of maximum wind in Snaiki and Wu's cyclone wind profile model	m
$\Delta F$	Fragility enhancement	[-]
$\Delta p_s$	Central pressure deficit	hPa
$\Delta \zeta$	Stress range	Pa
$\epsilon$	Normalized error	[-]
$\epsilon$	Error-terms vector	Various
$\zeta, \eta$	Structural displacement	m
$\eta_0, \eta_1$	Constants for the Snaiki and Wu's cyclone wind profile model	[-]
$\theta$	Structural rotation	rad
$\vartheta, \varphi$	Phase angles of harmonic force and harmonic response	rad
$\kappa$	Von Kármán constant	[-]
$\kappa_s, \kappa_p$	Structural curvature, plastic curvature	m <sup>-1</sup>
$\kappa_u$	Correlation function of wind turbulence in the $x$ -direction	m <sup>2</sup> /s <sup>2</sup>
$\kappa_w$	Scaling factor in Winterstein's translation model	[-]
$\lambda(IM)$	Annual exceedance rate	year <sup>-1</sup>
$\Lambda_1$	Turbulence scale parameter (IEC standard)	m
$\mu, \sigma$	Lognormal distribution parameters	[-]
$\mu_d, \varphi_d, \xi_d$	Mass, frequency and damping ratio of a tuned damper	[-]
$\nu$	Rate of up-crossings	Hz
$\xi_{opt}$	Optimum damping ratio of a tuned damper	[-]
$\xi_j$	Damping ratio estimated for the $j$ -th mode	[-]
$\xi_w(\cdot)$	Function for the moment-based transformation	[-]
$\rho$	Density of air	kg/m <sup>3</sup>
$\varrho$	Reliability index	[-]
$\sigma_u, \sigma_v, \sigma_w$	Standard deviations of wind velocity in the $x, y,$ and $z$ directions	m/s
$\sigma_b, \sigma_{\ln(r_{vm})}$	Standard deviations of models for Holland's $b$ parameter and $\ln(r_{vm})$	[-]
$\sigma_{\ln DP}$	Standard deviation of the natural logarithm of a demand parameter	[-]
$\sigma_T$	Thrust force standard deviation	N

$\zeta$	Stress amplitude	Pa
$\phi$	Latitude angle	°
$\varphi, \vartheta$	Phase angles	rad
$\varphi_{\text{opt}}$	Optimum tuning frequency ratio of a tuned damper	[-]
$\Phi(\cdot)$	Standard-normal cumulative distribution function	[-]
$\Phi$	Modal matrix	[-]
$\psi$	Angle of wind incidence	°
$\psi_t(z)$	Shape function of the support structure	[-]
$\omega$	Rotational speed of the Earth, or angular frequency	rad/s
$\omega_d, \omega_s$	Natural angular frequency of a damper, and of a single DOF system	rad/s
$\omega_j$	Natural angular frequency of the wind turbine support structure in the $j$ -direction	rad/s
$\Omega$	Rotational speed of the rotor	rpm

## Sub- and Superscripts

-	Time average
$\dot{\quad}$	First time derivative
$\ddot{\quad}$	Second time derivative
$\circ$	Denotes a rotationally-sampled function
$\hat{\quad}$	Used to denote the maximum and minimum values of a variable
$\hat{\quad}$	Denotes estimation of a quantity
$0, 1$	Used to denote mean and quasi-steady quantities
$a$	Denotes an aerodynamic matrix or vector
$d$	Indicates a damper-related quantity
$f$	Denotes a flow-induced force
$K$	Denotes a parameter relative to the Kaimal turbulence model
$s$	Denotes a structural matrix or quantity
$vK$	Denotes a parameter relative to the von Kármán turbulence model
$x, y, z$	Indicate a vector component in the $x$ -, $y$ -, or $z$ -direction

# Contents

<b>Abstract</b>	<b>vii</b>
<b>Resumen</b>	<b>ix</b>
<b>Acknowledgements</b>	<b>xi</b>
<b>1 Introduction</b>	<b>1</b>
1.1 The growth of wind energy . . . . .	1
1.1.1 Wind energy in Mexico . . . . .	4
1.2 Challenges for structural engineering in modern wind energy . . . . .	5
1.2.1 Numerical models for wind turbine structures . . . . .	7
1.3 Wind turbine standards . . . . .	8
1.4 Objectives and scope of the dissertation . . . . .	8
1.5 Outline of the dissertation . . . . .	9
1.6 Co-authorship statement . . . . .	10
<b>2 Fundamentals</b>	<b>15</b>
2.1 Basic concepts of wind engineering . . . . .	15
2.1.1 Wind characteristics in the ABL . . . . .	17
2.1.2 The tropical cyclone boundary layer . . . . .	20
2.2 Basic concepts of wind turbine aerodynamics . . . . .	23
2.2.1 Aerodynamic forces on operating rotors . . . . .	25
2.2.2 Wind turbulence on operating rotors . . . . .	27
2.2.3 Thrust force on operating rotors . . . . .	29
<b>3 Structural response of wind turbines under cyclone-induced loads</b>	<b>35</b>
3.1 Wind turbine response from cyclone-induced loads . . . . .	35
3.2 Wind field simulation . . . . .	37
3.2.1 The Tropical Cyclone Boundary Layer . . . . .	37
3.2.2 Turbulence in the TCBL . . . . .	40
3.2.3 Simulations . . . . .	42
3.3 Model description . . . . .	45
3.3.1 Description of the turbine . . . . .	45
3.3.2 Structural model . . . . .	46
3.3.3 Aeroelastic modeling . . . . .	49
3.4 Results . . . . .	51
3.4.1 Exploration of the results . . . . .	51
3.4.2 Peak factor . . . . .	54
3.4.3 Reliability evaluation . . . . .	58
3.5 Conclusions . . . . .	61

---

<b>4</b>	<b>Fragility evaluation of typical wind-turbine structures under cyclone-induced loads</b>	<b>65</b>
4.1	Wind farms in Mexico	65
4.2	Definition of hypothetical wind turbine structures	66
4.2.1	Definition of blades and nacelle	67
4.2.2	Definition of the tower	68
4.3	Wind loads	70
4.3.1	Wind field simulation	70
4.3.2	Aerodynamic loads	71
4.4	Results and fragility analyses	72
4.4.1	Response histories	73
4.4.2	Damage states	73
4.4.3	Fragility functions	75
4.5	Conclusions	76
<b>5</b>	<b>Reliability enhancement of wind turbine structures with passive damping devices</b>	<b>81</b>
5.1	Introduction	81
5.1.1	Passive devices and wind turbines	83
5.2	Passive damping devices	85
5.2.1	Description of numerical models	85
5.2.2	Modal parameters of the main structure	86
5.2.3	Harmonic analyses	87
5.3	Results	89
5.3.1	Spectral comparisons	91
5.4	Fragility analysis	92
5.4.1	Characterization of structural response maxima	93
5.4.2	Development of fragility functions	97
5.5	Reliability enhancement	98
5.5.1	Quantification of reliability enhancement	99
5.5.2	Risk enhancement	100
5.6	Conclusions	101
<b>6</b>	<b>Simplified evaluation of the structural response of wind turbines</b>	<b>107</b>
6.1	Introduction	107
6.1.1	Summary of the simplified methodology	109
6.2	Simulation of non-Gaussian stochastic processes	111
6.2.1	Translation models for non-Gaussian processes	111
6.2.2	Direct process translation	113
6.3	Simplified wind turbine support-structure model	116
6.3.1	Four-DOF model	116
6.4	Simplified method for simulation of stress signals	119
6.5	Numerical example	121
6.5.1	Description of the turbine	121
6.5.2	Equivalent structural model	122
6.5.3	Simulation of response signals	137
6.6	Conclusions	148
<b>7</b>	<b>Concluding remarks</b>	<b>153</b>
7.1	Structural response of wind turbine support structures under tropical cyclones	154
7.2	Fragility evaluation of representative wind turbines under cyclone hazard	155
7.3	Reliability enhancement of wind turbine support structures by passive damping devices	156
7.4	Simplified structural analyses for reliability evaluation	157
<b>A</b>	<b>Commentaries on Chapter 3 with possible applications to standards and practice</b>	<b>159</b>
A.1	Commentaries about the mean-speed profile	159
A.2	Commentaries about the peak factor	160



<b>B</b>	<b>Quasi-steady aeroelastic terms</b>	<b>161</b>
B.1	Fluid damping and rigidity matrices . . . . .	161
B.1.1	Equation of motion . . . . .	162
B.2	Implementation in FEA . . . . .	164
<b>C</b>	<b>Derived publications</b>	<b>167</b>

[This page intentionally left blank]

# Chapter 1

## Introduction

It can be said that the history of human civilization is the history of technological advances, and thus — in a sense — of wind harvesting. The wind resource has been an important contributor to the development of cultures. Civilizations like the Egyptians, Phoenicians, or Romans may not have used windmills nearly 3,000 years ago,<sup>1</sup> but the wind certainly played a role in their consolidation as Mediterranean powers, being an essential resource to carry their naval excursions for trading or warfare purposes. Subsequent utilization of wind technology in human activities has been present until our time. Windmills, for example, were built all over Europe and Asia to aid in agriculture, and windpumps also became common in the Americas to be used for extracting water from the subsoil. Nowadays, modern wind turbines are machines technologically much more complex and evolved than the windmills that inspired Miguel de Cervantes Saavedra for his famous passage in *Don Quixote*, but the physical concept of their operation remains. Today, in the 21st century, the environmental obligations of our time lead us once more to avail of this renewable resource. Thus, we must use the understanding we have gained over the years about the wind resource and related phenomena for its harvesting, all within the boundaries of sustainability and reliability.

This section presents a summary of the expansion of wind energy as a mainstream energy source in the last decades, and some of the challenges that demand the proper involvement of structural engineering for its successful and continuous development. It is intended to serve as a brief and general contextualization for the topics covered in the dissertation. Although the concepts from the work performed in this thesis are of application to any site in the world, particular emphasis is made on the hazard context of Mexico. The objectives of the thesis, and how it is organized in this document, are also described.

### 1.1 The growth of wind energy

The estimated growth of the global population is expected to increase the energy demand by more than 52% by the year 2050, compared to the average demand estimated in 2017.<sup>2</sup> Also, the necessity of reducing greenhouse gas emissions in the atmosphere, as a measure to mitigate global warming, has become one of the major concerns in policy making for many countries in the last decades. These premises have motivated large investments toward the development of renewable energy technology for the sake of a more climate-resilient and efficient energy generation.<sup>3</sup> Wind energy has become an attractive resource to contribute to these objectives because the estimated available wind power of the planet is more than enough to supply several times the total current global energy demand.<sup>4</sup> Thus, the investment in technological development for wind energy production has led to turbines of greater efficiency and lower costs of generation.

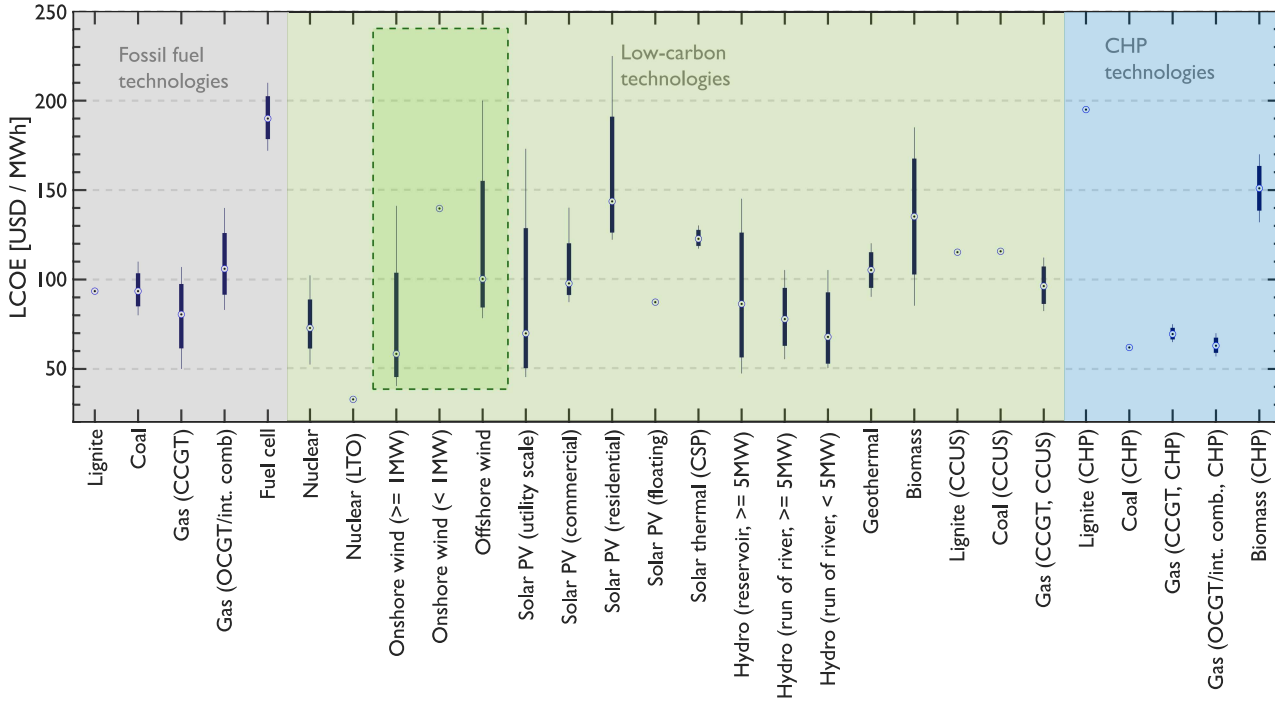


Figure 1.1: Levelised costs of electricity generation

The levelised cost of energy (LCOE) is a measure of the average cost of energy generation for infrastructure and technologies over its lifetime. According to the 5-year report of the International Energy Agency (IEA) and the Nuclear Energy Agency (NEA), wind energy generation, as well as other low-carbon energy sources, have become cost competitive, and the costs of generating energy from these sources are expected to diminish in the future.<sup>5</sup> Figure 1.1 depicts the estimated costs of energy production for different technologies according to said reference<sup>5</sup> (the wind-resource technologies are marked within green dashed lines). From Figure 1.1 it can be seen that, although the cost of wind-energy generation has great variability — since wind energy potential is site-dependent —, its median cost of production from inland infrastructure is below other mainstream sources, including all fossil fuel technologies. Offshore wind energy cost is still above some of the other sources, but its prices are expected to decrease in a short-term period.

The diminishing costs of wind energy production are also reflected in the increase of the overall installed capacity worldwide. According to the World Wind Energy Association (WWEA), in nearly two decades the total installed capacity by wind resources (onshore and offshore) has increased from 24 GW estimated in 2001, to 651 GW estimated in 2019.<sup>6</sup> Although the increase in installed capacity has not been uniform for every region, it has been present in the five continents. How the wind energy capacity is distributed globally (by 2021) is depicted in Figure 1.2,<sup>6</sup> which considers both onshore and offshore infrastructure for wind energy generation.

Wind energy has been an attractive option to produce electricity for industrialized countries with low hydrocarbon production. That is insofar as it allows them energy independence from fossil fuels of volatile prices and, in some cases, from politically unstable regions.<sup>7</sup> It is also seen as a resource for economical development, along with other renewable energy sources. For example, Ortega-Izquierdo and del Río have presented an analysis of the social-economic and environmental benefits of wind energy in several European countries.<sup>8</sup> They determined that wind energy deployment in Europe represented a reduction of 828.3 million tons of carbon dioxide (MtCO<sub>2</sub>) between 2008 and 2016. They translated this quantity to savings of 27,462 million euros.<sup>8</sup> From the social-economic point of view, according to their analyses, wind energy represented 2.54 million jobs within the foremen-

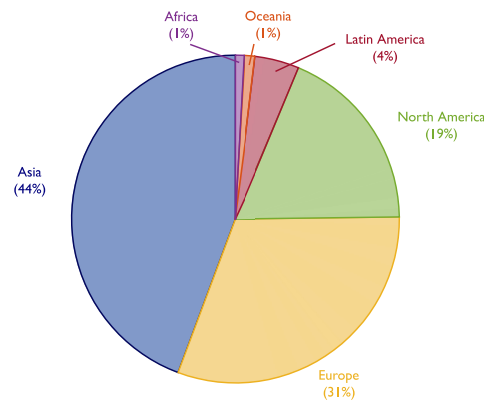


Figure 1.2: Global wind energy capacity distribution

tioned time interval. Of this number, 2.2 million corresponded to onshore infrastructure, and 0.34 million to offshore sources. For onshore wind, 56% of the jobs came from manufacturing stages, 17% from installation, and 27% from operation and maintenance; whereas for offshore, these fractions are, respectively, 72%, 22%, and 6%.<sup>8</sup> Among other social-economic benefits of wind energy is the land lease paid to landowners, since wind-farm operators pay these during the operation of the wind power plant.

The diversification of energy generation by means of renewable energy sources leads to the decentralization of the energy supply, which is another of the incentives for their deployment. That is, the diverse regional energy potential leads to spatially dispersed infrastructure of smaller scale, which also allows some regions of greater energy potential to become energy exporters.<sup>9</sup> For example, this has been taken as an opportunity for economically less-favored regions in Germany with high wind potential, where some of these regions have the aim of producing 300% of their energy share from wind sources to export energy to regions of lesser potential.<sup>9</sup>

These examples of developed countries illustrate why wind energy has gained attention in the last decades. Nonetheless, in the case of some developing countries, wind energy is still in very early stages of deployment. The climate finance gap in many of these countries is still significant, and it accentuates the need for government policies that promote renewable energy investment.<sup>10,11</sup> According to social-economic analyses, as stated already previously, renewables are seen to constitute opportunities to diminish poverty and unemployment, as well as to sustainably develop low-income economies.<sup>11</sup> According to research that encompasses data from 1990 to 2014 from 27 countries in Central and Eastern Europe, Central Asia, and the Caucasus, economic growth and unemployment diminution have been some of the driving reasons promoting the deployment of renewable energy in the aforementioned regions.<sup>12</sup>

The implementation of wind energy plants (or wind farms) in some developing countries is not straightforward, prompting the need for foreign investment for its development. Studies have determined that, among the diverse factors that intervene in the decisions for foreign investment in wind energy projects, renewable-energy support policies have the greater effect in encouraging investors to support these projects in developing countries.<sup>13</sup> Although the technological development of the target region is not a driving factor for its wind energy growth,<sup>12</sup> the technical nature of wind farm projects requires a certain level of regional development to reflect a noticeable beneficial impact on a local economy level. Vasconcellos and Couto analyzed the social-economic impacts of wind energy projects in the North-Eastern region of Brazil, one of the least developed regions in that country, but with the greatest wind potential.<sup>14</sup> Their results show that direct effects, i.e., the flow of products, services, and industries needed to implement wind-energy projects, represent 10 jobs/MW in the studied region, while the total effect was estimated at 31.9 jobs/MW.

The deployment of wind energy projects in developing countries is not only of economical motives but also of environmental nature. The importance of reducing the emissions from developing countries appears crucial: CO<sub>2</sub> emissions from them are expected to grow faster, since they encompass some of the most dynamic economies.<sup>15</sup> The survey of 71 developing countries, which are part of the Paris agreement from 2015, indicates that these countries represent 60% of the total global greenhouse gas emissions. Among these countries, China and India alone represented in 2012 25% and 10% of the emissions, respectively.<sup>15</sup> According to this survey, Azerbaijan, Argentina, Belarus, Chile, Mexico, and Moldova were the countries with the most ambitious targets for control of greenhouse gas emissions; and these countries could achieve their collective emission goals by mitigating their emissions from electricity generation alone. These countries represented collectively 1,428 MtCO<sub>2</sub> in 2012, and they must limit their collective emissions to 1,579 MtCO<sub>2</sub> by 2030 to achieve their less ambitious emission target. A total of \$41 billion USD was invested in renewable energy projects within these countries from 2007 to 2016, from which the investment in Chile and Mexico alone were \$15 billion USD and \$19 billion USD, respectively.<sup>15</sup>

### 1.1.1 Wind energy in Mexico

Mexico was one of the developing countries with a more ambitious greenhouse gas emission control target according to the Climatescope survey from 2017.<sup>15</sup> Also, the renewable energy investment nearly four-folded from 2016 to the third quarter of 2017.<sup>15</sup> This impulse in renewable energy investment placed Mexico among the ten countries members of the IEA with greater wind-energy capacity growth in 2017.<sup>16</sup> Nonetheless, the country still has a large gap between its CO<sub>2</sub> emission objectives and the current power generation status.

Nowadays, the greatest share of energy in Mexico comes from fossil fuels, natural gas, and coal. These sources account for 69% of the total capacity of the country, and ~80% of the energy production.<sup>17,18</sup> Of the low-carbon energy generated in Mexico by 2019, renewables represented between 8% and 10%, according to diverse sources.<sup>17,18</sup> As for wind-source renewables, the wind potential of Mexico from inland sources was estimated beyond 70 GW in 2010,<sup>19</sup> which has motivated the exploitation of wind energy in the country during the last decade.

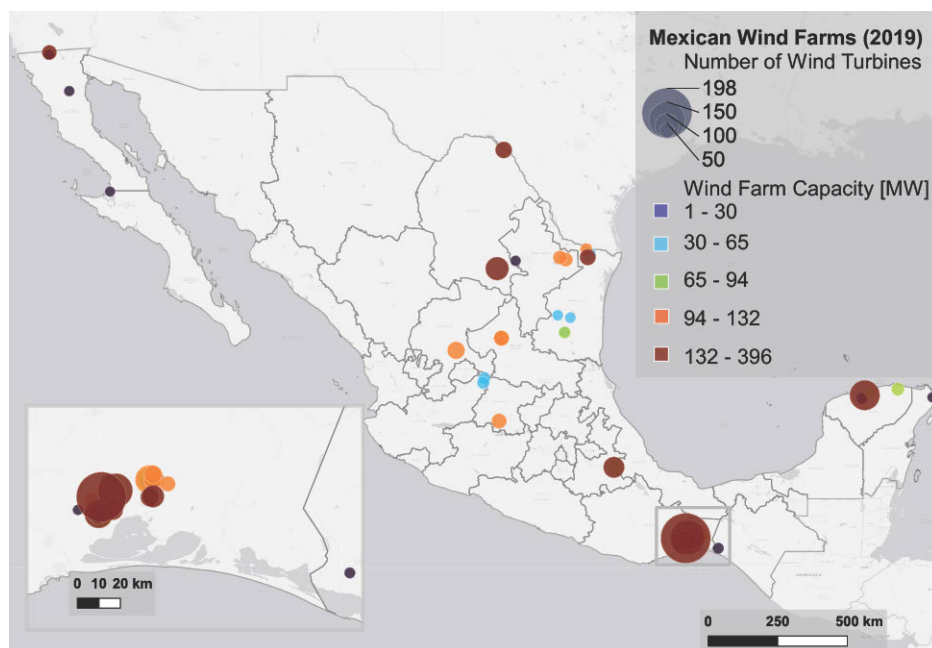


Figure 1.3: Wind Farms installed in Mexico (2019)



Wind energy in Mexico has followed a more-or-less steady tendency of growth, having an average yearly increase of installed capacity of 0.6 GW from 2010 to 2020,<sup>20</sup> going from 0.5 GW installed in 2010 to a total installed capacity by onshore wind energy sources of  $\sim 6$  GW by the beginning of the year 2020.<sup>17,20</sup> This capacity is currently (by the end of 2021) generated by 68 wind farms across the country,<sup>20</sup> the ones installed until 2019 are displayed in Figure 1.3, classified with respect to the capacity of each of the wind power plants.<sup>21</sup>

According to the information presented by Jaimes et al.,<sup>21</sup> the average capacity of the installed wind turbines in Mexico is  $\sim 2.1$  MW, whereas the average height of them is  $\sim 80$  m (e.g., Figure 1.4). Moreover, the following facts are notorious from Figure 1.3: (i) The major part of the installed wind capacity comes from the southwestern state of Oaxaca (nearly 45% of the total capacity by 2020), which depicts a high concentration of wind farms in a sole small region. (ii) A considerable number of wind farms are also located in the region near the Gulf of Mexico and the Caribbean sea (state of Tamaulipas and the Yucatan peninsula), nearly a third part of the wind farms are located in that region.<sup>20</sup> These facts imply that there is still a great part of the Mexican territory that will demand proper characterization and refinement of environmental hazards for the development of wind projects. Also, that a considerable fraction of the wind farms currently installed in Mexico is located in sites prone to hurricane hazards or strong earthquakes, scenarios that require further characterization of environmental actions on the wind turbine structures than those covered by conventional wind energy standards.



Figure 1.4: *La Bufa* wind farm (Zacatecas, Mexico)

## 1.2 Challenges for structural engineering in modern wind energy

As the global tendencies in energy demand lead to more wind-energy infrastructure wind turbines continue to grow in size and efficiency. This implies that wind turbine components are becoming more flexible in order to achieve more power extraction from the wind flow. The growth of energy demand is also leading wind turbines to sites where hazards from extreme environmental events are of greater concern for their deployment. Moreover, as many wind farms from early years start to

reach their projected service life, the necessity to avail of existing wind farm infrastructure surges as a capital task in order to achieve resilient and low-cost energy generation. These scenarios lead to challenges for science and engineering that have not been faced by wind energy before.

According to a comprehensive review presented by several remarkable researchers,<sup>2</sup> the major challenges faced by modern wind energy include a wide area for multidisciplinary studies. These challenges are summarized as: (i) the need for a better understanding of the physics of the wind flow of large-scale weather effects, i.e., modeling adequately the link between mesoscale and the microscale wind flow; (ii) proper aero- and structural- dynamic analyses, and proper modeling of the interaction of wind turbine dynamics with complex flow patterns; and (iii) the integration of wind farms to future electric infrastructure.

The changes in turbulence conditions in the atmospheric boundary layer (ABL) due to wind turbine operation add relevance to the first point mentioned. As turbulence represents the wind speed variation at short time intervals and, due to the operation of wind turbines, the rate of oscillations in the flow within a wind farm is increased in the wake of an operating wind turbine.<sup>22,23</sup> These changes in turbulence affect not only individual turbines but also entire wind power plants adjacent to other upwind-located operating plants, as well as the micro-climate at the site.<sup>2</sup> Structurally, the increment in wind-speed oscillations affects the number of load cycles to which a wind turbine structure is subjected, therefore increasing the fatigue damage that it must endure over its service life. Recent research has studied the influence of uncertainty in the environmental actions affecting the structural performance of wind turbines and how to characterize it properly.<sup>24</sup> These studies include in their considerations the effects of wake-induced turbulence, but there is still work of research to be done.

The power output of any horizontal axis wind turbine is proportional to the square of its rotor diameter.<sup>25</sup> That is, if the size of a wind turbine rotor is increased three times, its power output will be nine times the original output. Thus, as wind turbines become larger for the sake of more efficient systems, and improved power output per unit of land area, their components grow in size, flexibility, and slenderness. These increments in size of structural components, like wind turbine blades and towers, demand different methods of analysis,<sup>26,27</sup> and fabrication.<sup>28,29</sup> The task of structural engineering is to determine the proper criteria for the analyses to define the actions on these structures. Due to its economy and growing computational affordability, the greater part of the research conducted on wind turbine structural analysis is performed from numerical models (e.g., as reported for seismic evaluation of wind turbine structural response studies<sup>30</sup>) whereas experimental and on-site studies, although not uncommon, constitute information reported less frequently.

The structural design conditions established in the majority of current wind turbine standards are based on the hazard context of Europe and North America.<sup>31</sup> Nonetheless, as reported in Section 1.1, the greater part of the globally deployed wind-energy infrastructure is located in Asia. From that region, China alone represents 90% of the installed capacity.<sup>6</sup> The ambitious wind-energy goals from that country have added momentum to the deployment of offshore wind power plants.<sup>32</sup> In other regions of the world, similar scenarios are also being seen, and the wind energy deployment aims to offshore infrastructure.<sup>33</sup> This wind-energy expansion to new zones with high wind potential has moved the hazard-research attention to studies on the influence of extreme environmental events (like tropical cyclones) on wind energy infrastructure. According to an elaborate review of wind turbine failure cases presented by Ma et al.,<sup>34</sup> approximately 40% of the reviewed wind turbine structure collapses occurred during a tropical cyclone. Thus, the study of the structural response of wind turbines under tropical cyclones is highlighted, either from onshore<sup>21,35</sup> or offshore infrastructure.<sup>32,33</sup> For that purpose, an important consideration is the description of the wind field during a tropical cyclone. The definition of models that describe the wind field in tropical cyclones is currently being performed either from numerical studies<sup>36,37</sup> or determined from field-measurement databases.<sup>38</sup> Both approaches are justified by the differences observed between the flow field from the tropical cyclones and the conventional neutral ABL assumptions.



As summarized by Ortegon et al.,<sup>39</sup> any technology has four phases of market development: growth, maturity, declination, and obsolescence. Contemporaneous wind energy is still in the growth phase. Nevertheless, the average operational lifetime of a wind turbine is  $\sim 20$  years.<sup>40</sup> This implies that many of the wind energy projects erected around the beginning of the century are about to reach the end of their service life, and many others are beyond it. Once wind-power plant infrastructure has reached that point, common trajectories for the wind farms are: repowering, or decommissioning.<sup>39</sup> The former implies reconditioning or replacing the wind turbines within a wind farm to continue its operation with up-to-date units, whereas the latter implies the complete removal of infrastructure and re-vegetation of the site.<sup>39</sup>

Repowering of outdated wind farms becomes a lucrative and feasible alternative because the value of restored facilities is often greater than the value of any recovered material. The lifetime extension of a wind farm can vary from 5 to 15 years beyond its original lifetime, depending on diverse involved factors and the history of each wind turbine.<sup>40</sup> Fatigue damage on structural and mechanical elements of the wind turbines is thus of major concern for lifetime extension. In this sense, the structural health monitoring systems become indispensable to avail of the existing wind turbine structures,<sup>40,41</sup> posing new challenges for structural engineering. Real structural response measurements are a key element for a reliable estimation of the structural performance and capacity availability of wind turbine structures.<sup>42</sup> This information can be combined with numerical analyses to estimate reliably, not only the physical stage of the elements involved in the wind turbine repowering, but also the expected damage at the end of the extended service life. Nevertheless, dealing with uncertainties in fatigue estimation analysis of wind turbines is a task far from facile.

The non-linearity induced by the operation of the wind turbine, and inconstant environmental conditions, introduce a great number of variables and sources of uncertainty in the analyses. To overcome these problems, the tendencies in reliability analysis aim to avail of computational power to estimate the fatigue damage on wind turbines. This is done by means of surrogate models built from artificial neural networks<sup>43</sup> or Gaussian interpolation,<sup>44-46</sup> which are trained from massive sets of numerical analyses performed on aero-servo-hydro-elastic software for wind turbine applications. Although these techniques are gaining popularity for newborn projects, no evidence of their application to the extension of wind-farm service life has been found in the literature survey conducted by the author at the time this dissertation was written. Further, despite the practicality allowed by modern computational tools, there is still room for studies focused on the development of techniques to improve the computational economy of these analyses, and the definition of their uncertainties.

### 1.2.1 Numerical models for wind turbine structures

Numerical analysis of wind turbine components has been a key part in the development of wind energy. The greater portion of the studies concerning wind turbine engineering has been performed from numerical models, either related to flow field<sup>47,48</sup> or structural analyses.<sup>30,49,50</sup> As mentioned before, large-scale tests of wind-turbine structural components constitute research less frequently reported, although not uncommon. Perhaps wind turbine blades are the most common full-size tested structural elements,<sup>51</sup> however, in many cases, they are also studied from numerical analyses. This is due to the fact that, as in many areas of engineering, experimental tests are more expensive than numerical studies. Also, the oft-growing size of wind turbine components demands experimental facilities that are non-ubiquitous.<sup>51</sup> The difficulties and expenses that imply experimental tests have motivated numerical simulation, not only in wind energy but also in many other areas of research, including structural engineering.

Advances in numerical studies have been possible due to the growth of computational capacities. Nevertheless, intricate numerical models might still not be commonly adopted by practitioners in many cases, due to the time and computational power demanded by the technicalities of the analyses. A great part of the full wind-turbine model studies is performed on aero-servo-hydro-elastic software designed for the specific purpose of horizontal axis wind turbine analysis, like HAWC2,<sup>52</sup>

or FAST.<sup>53</sup> These codes have enabled important advances for wind energy and wind turbine studies, and have become a referent to validate many studies on the subject. The purpose-specific modules that complement these codes cover with practical flexibility a wide variety of cases common for wind turbine design and analysis. Nonetheless, for studies out of the quotidian cases, a fair degree of programming skills is needed to mold the capabilities of these analysis tools into the needs of the problem.

### 1.3 Wind turbine standards

The main referents for wind turbine component design and load specification are the standards published by the International Electrotechnical Commission (IEC). In its standard IEC 61400-1,<sup>54</sup> the basic design requirements to ensure the integrity of wind turbines of different sizes are established, including security factors for structural and mechanical design, environmental actions, as well as other requirements. Other standards commonly referred are the ones published by the formerly technical supervisory organizations Germanischer Lloyd, and Det Norske Veritas (nowadays both merged into DNV). The documents once published by the aforementioned organizations<sup>55,56</sup> cover the same classification criteria presented in the IEC 61400, where the wind turbines are classified into 4 types in accordance to the wind intensity they must endure, and three categories that depend on the level of turbulence assumed for its design. This classification is summarized in Table 1.1.

**Table 1.1:** Turbine classification according to IEC 61400-1

Turbine class	I	II	III	S
$V_{ref}$ (m/s)	50	42.5	37.5	Values
Category A $I_{ref}$		0.16		specified
Category B $I_{ref}$		0.14		by
Category C $I_{ref}$		0.12		designer

In Table 1.1,  $V_{ref}$  stands for the reference wind velocity, which represents the 10-minute averaged wind speed at hub height, whereas  $I_{ref}$  represents the reference turbulence intensity (i.e., the ratio between the wind speed variation and the mean wind speed). The reference velocity is assumed to be concordant to a return period of 50 years for the extreme wind model as defined by the IEC 61400-1. The normal wind model is defined as 80% of the aforementioned value. According to the IEC 61400-1, these turbine classifications are meant to cover neither offshore wind turbines nor tropical cyclone wind speeds. For the latter, the turbine must be classified as 'S', and the wind intensity values must be specified by the designer in the project information.<sup>54</sup>

Within the context of Mexican structural specifications for wind turbines, the handbook of civil works published by the Federal Electricity Commission (CFE, for its acronym in Spanish) in its latest edition for wind actions already defines some criteria for the characterization of aerodynamic effects on wind turbine structures. These criteria are meant for extreme wind events alone, and the handbook defines expressions for the dynamic analysis of wind turbine support structures, the specifications of which are similar to those established for the analysis of chimneys and lattice towers.<sup>57</sup> The wind intensity defined for the analysis and design of wind turbines assumes a return period of 200 years, for these structures are classified as structures of high importance according to the aforementioned reference.

### 1.4 Objectives and scope of the dissertation

In view of the foregoing contextualization, this work is focused on contributing to the development of computationally-economical numerical models for the analysis of wind turbine support structures. This implies developing a simplification of analytic methods when pertinent, avoiding excessive loss

of accuracy. These methods rely on well-defined analytic bases and justified models that represent adequately the flow characteristics of the phenomena under analysis, as well as the dynamic response of the structure.

For this purpose, the work is centered on two operating conditions of wind turbines that can be related to the design situations defined in the IEC 61400-1 as: power production with the normal turbulence model, and parked without yaw misalignment with the extreme wind model. The studied structures are land-based wind turbines. The cases covered in the analyses are centered on fatigue evaluation of the wind turbine support structure, the study of its structural response under extreme wind events, and the evaluation and enhancement of its structural performance and reliability. The tools employed for the numerical analyses are mainly the commercial finite element software ANSYS, and the wind-turbine-specific code FAST, developed by the National Renewable Energy Laboratory (NREL). Other computations were performed on the matrix-based language MATLAB. The structural analyses performed assume linear-elastic properties, although for the definition of performance thresholds of the evaluated structures some models that accounted for material non-linearities were developed.

To synthesize, the objectives of the work are summarized as follows:

- (i) Develop wind field simulations representing the tropical-cyclone boundary layer conditions.
- (ii) Study the aeroelastic response of a benchmark wind turbine under tropical cyclone action by means of finite element modeling.
- (iii) Define the finite element models, for structural performance evaluation, of three generic land-based wind turbines representative of the ones installed in Mexico.
- (iv) Estimate the probability of structural failure of the generic turbines under extreme wind events.
- (v) Define passive damping devices for the generic turbines and evaluate their structural response under extreme events.
- (vi) Estimate the enhanced probability of structural failure under extreme wind events achieved with the use of passive damping devices.
- (vii) Develop a simplified model to evaluate the aeroelastic response of wind turbines in operation.
- (viii) Develop a simplified method for fatigue analysis of wind turbine structural components.

## 1.5 Outline of the dissertation

The studies presented in this document are centered on the numerical evaluation of the structural response of land-based wind turbines. The dissertation is focused on fatigue and extreme response evaluation, thus, some of the subjects covered in each chapter may differ from their antecedent or following ones. Therefore, each part is intended to be quasi-independent, and a list of references is included at the end of each of them.

As already presented, **Chapter 1** provides a general context of the motives behind the expansion of wind energy in the last decades. The role of structural and wind engineering in this fact has also been summarized in this chapter.

**Chapter 2** presents a definition of basic concepts concerning wind engineering and wind turbine aerodynamics. It attempts to provide fundamental knowledge on these subjects for the unversed reader. Although it is assumed some degree of knowledge of certain areas of study, the reader is referred to other sources whenever a detailed concept definition is of no addition to the present dissertation.

**Chapter 3** presents a study on the evaluation of the aeroelastic response of a benchmark wind turbine under cyclonic winds. The turbulence characteristics of the wind field used for the analyses, as well as the mean velocity profile, are intended to represent the expected conditions of real tropical cyclones.

In **Chapter 4** three generic wind turbines are defined, based on statistical models defined from real wind turbines. The dimensions and characteristics of the generic wind turbines seek to represent those installed and to-be installed in Mexico. A fragility analysis is performed on the support structure of each of the generic turbines, assuming extreme wind action on them.

**Chapter 5** explores the enhancement in the probability of structural failure reached with the use of passive damping devices on wind turbines. The passive damping systems are defined as tuned mass dampers (TMDs), for which the optimal parameters that define the dampers are first estimated from harmonic analyses. Models that describe the median expected peak response of the structure are defined from the damping and structural parameters.

In **Chapter 6** a simplified model for the evaluation of the aeroelastic response of wind turbine support structures is presented. Also, a simple method for fatigue damage estimation is established, based on stochastic simulation of stress signals. The simplifications assume that the support structure is governed by the first bending modes in the fore-aft and side-to-side directions. A discussion on the distribution of response amplitudes is presented, as well as some commentaries on the influence of aerodynamic damping.

**Chapter 7** outlines some of the contributions from the described studies. It also highlights the implications of many of the assumptions that had to be made in the analyses, as well as presents some suggestions for improvements that can be implemented in future studies.

**Appendix A** discusses some observations that can be taken into account in practice for improved analyses of wind turbines, as well as comments for its consideration in future versions of Mexican standards. **Appendix B** displays some analytic aerodynamic derivations and their implementation in a finite element code in the ANSYS Parametric Design Language (APDL). **Appendix C** presents a list of the publications derived from this dissertation and related studies.

## 1.6 Co-authorship statement

This dissertation includes information from manuscripts that have been published or are to be sent for possible publication in refereed journals. Results presented in Chapter 3 are to be sent for peer revision in co-authorship of J. O. Martín del Campo with Dr. Adrián Pozos Estrada. Chapter 4 includes results and data from an article published in co-authorship between doctors M. A. Jaimes, D. A. García Soto, and A. Pozos Estrada with J. O. Martín del Campo. Chapter 5 includes results from an article published in co-authorship between J. O. Martín del Campo with doctors Adrián Pozos Estrada and Óscar Pozos Estrada. Information from Chapter 6 has been published in a peer-reviewed journal in co-authorship of J. O. Martín del Campo with Dr. Adrián Pozos Estrada.

## References

1. Hau, E. *Wind Turbines: Fundamentals, technologies, application, economics* 2nd ed. (Springer, Berlin, Germany, 2006).
2. Veers, P. *et al.* Grand challenges in the science of wind energy. *Science* **366**, eaau2027 (2019). doi: 10.1126/science.aau2027.

3. IRENA. *Future of wind: Deployment, investment, technology, grid integration and socio-economic aspects (A global energy transformation paper)* tech. rep. (International Renewable Energy Agency, Abu Dhabi, 2019).
4. Tong, W. *Wind Power Generation and Wind Turbine Design* (WIT Press, Southampton, UK, 2010).
5. IEA. *Projected costs of generating electricity* <https://www.iea.org/reports/projected-costs-of-generating-electricity-2020>.
6. WWEA. *Global Wind Power Statistics* <https://library.wwindea.org/global-statistics/>. (accessed: 19.07.2021).
7. EWEA. *The economics of wind energy* tech. rep. (EWEA, 2009).
8. Ortega-Izquierdo, M. & del Rio, P. An analysis of the socioeconomic and environmental benefits of wind energy deployment in Europe. *Renewable Energy* **160**, 1067–1080. ISSN: 0960-1481 (2020). doi: 10.1016/j.renene.2020.06.133.
9. Jenniches, S. Assessing the regional economic impacts of renewable energy sources – A literature review. *Renewable and Sustainable Energy Reviews* **93**, 35–51. ISSN: 1364-0321 (2018). doi: 10.1016/j.rser.2018.05.008.
10. Agbemabiese, L., Nyangon, J., Lee, J.-S. & Byrne, J. Enhancing climate finance readiness: A review of selected investment frameworks as tools of multilevel governance. *University of Delaware, Center for Energy & Environmental Policy, Working Paper Series* (2018). doi: 10.2139/ssrn.3082542.
11. Ragoša, G. & Warren, P. Unpacking the determinants of cross-border private investment in renewable energy in developing countries. *Journal of Cleaner Production* **235**, 854–865 (2019). doi: 10.1016/j.jclepro.2019.06.166.
12. Przychodzen, W. & Przychodzen, J. Determinants of renewable energy production in transition economies: A panel data approach. *Energy* **191**, 116583 (2020). doi: 10.1016/j.energy.2019.116583.
13. Keeley, A. R. & Ikeda, Y. Determinants of foreign direct investment in wind energy in developing countries. *Journal of Cleaner Production* **161**, 1451–1458 (2017). doi: 10.1016/j.jclepro.2017.05.106.
14. Vasconcellos, H. & Couto, L. C. Estimation of socioeconomic impacts of wind power projects in Brazil's Northeast region using Interregional Input-Output Analysis. *Renewable and Sustainable Energy Reviews* **149**, 111376 (2021). doi: 10.1016/j.rser.2021.111376.
15. Climatescope. *Clean energy and the Paris promises* <http://global-climatescope.org/en/insights/climate-policy/>. (accessed: 10.08.2021).
16. IEA-Wind. *IEA Wind Technology Collaboration Programme 2017 Annual Report* tech. rep. (International Energy Agency, 2017). <https://iea-wind.org/iea-publications/#ut-portfolio-details-wrap-101>.
17. Climatescope. *Climatescope 2020* <https://global-climatescope.org/results/mx#power-market>. (accessed: 11.08.2021).
18. SENER. *Balance Nacional de Energía 2021* <https://www.gob.mx/sener/es/articulos/balance-nacional-de-energia-2019-265005?idiom=es>. (in Spanish).
19. INEEL. *Project "Wind Atlas for Mexico (AEM)"* <https://aems.ineel.mx/aemdata/About.aspx>. (accessed: 12.08.2021).
20. AMDEE. *El viento en números* <https://amdee.org/el-viento-en-numeros.html>. (accessed: 10.08.2021).
21. Jaimes, M. A., García-Soto, A. D., Martín del Campo, J. O. & Pozos-Estrada, A. Probabilistic risk assessment on wind turbine towers subjected to cyclone-induced wind loads. *Wind Energy* **23**, 528–546 (2020). doi: 10.1002/we.2436.
22. Frandsen, S. *Turbulence and turbulence-generated structural loading in wind turbine clusters* English. PhD thesis (Technical University of Denmark, 2007). ISBN: 87-550-3458-6. Risø-R-1188(EN).

23. Porté-Agel, F., Bastankhah, M. & Shamsoddin, S. Wind-turbine and wind-farm flows: a review. *Boundary-Layer Meteorology* **174**, 1–59 (2020). doi: 10.1007/s10546-019-00473-0.
24. Toft, H. S., Svenningsen, L., Sørensen, J. D., Moser, W. & Thøgersen, M. L. Uncertainty in wind climate parameters and their influence on wind turbine fatigue loads. *Renewable Energy* **90**, 352–361 (2016). doi: 10.1016/j.renene.2016.01.010.
25. Burton, T., Jenkins, N., Sharpe, D. & Bossanyi, E. *Wind Energy Handbook* 2nd ed. ISBN: 978-0-470-69975-1 (John Wiley and Sons, Ltd., Chichester, UK, 2011).
26. Rosemeier, M., Berring, P. & Branner, K. Non-linear ultimate strength and stability limit state analysis of a wind turbine blade. *Wind Energy* **19**, 825–846 (2016). doi: 10.1002/we.1868.
27. Sayed, M., Lutz, T., Krämer, E., Shayegan, S. & Wüchner, R. Aeroelastic analysis of 10 MW wind turbine using CFD–CSD explicit FSI-coupling approach. *Journal of Fluids and Structures* **87**, 354–377 (2019). doi: 10.1016/j.jfluidstructs.2019.03.023.
28. Jay, A. *et al.* Spirally welded steel wind towers: Buckling experiments, analyses, and research needs. *Journal of Constructional Steel Research* **125**, 218–226 (2016). doi: 10.1016/j.jcsr.2016.06.022.
29. Mahmoud, A. *et al.* Modeling the flexural collapse of thin-walled spirally welded tapered tubes. *Journal of Structural Engineering* **144**, 04017201 (2018). doi: 10.1061/(ASCE)ST.1943-541X.0001950.
30. Katsanos, E. I., Thöns, S. & Georgakis, C. T. Wind turbines and seismic hazard: a state-of-the-art review. *Wind Energy* **19**, 2113–2133 (2016). doi: 10.1002/we.1968.
31. Clausen, N.-E. *et al.* *Wind farms in regions exposed to tropical cyclones in European Wind Energy Conference* **15** (2007), 61400–3.
32. Hong, L. & Möller, B. An economic assessment of tropical cyclone risk on offshore wind farms. *Renewable Energy* **44**, 180–192 (2012). doi: 10.1016/j.renene.2012.01.010.
33. Hallowell, S. T. *et al.* Hurricane risk assessment of offshore wind turbines. *Renewable Energy* **125**, 234–249 (2018). doi: 10.1016/j.renene.2018.02.090.
34. Ma, Y., Martinez-Vazquez, P. & Baniotopoulos, C. Wind turbine tower collapse cases: a historical overview. *Proceedings of the Institution of Civil Engineers – Structures and Buildings* **172**, 547–555 (2019). doi: 10.1680/jstbu.17.00167.
35. Amirinia, G. & Jung, S. Along-wind buffeting responses of wind turbines subjected to hurricanes considering unsteady aerodynamics of the tower. *Engineering Structures* **138**, 337–350 (2017). doi: 10.1016/j.engstruct.2017.02.023.
36. Worsnop, R. P., Bryan, G. H., Lundquist, J. K. & Zhang, J. A. Using large-eddy simulations to define spectral and coherence characteristics of the hurricane boundary layer for wind-energy applications. *Boundary-Layer Meteorology* **165**, 55–86 (2017). doi: 10.1007/s10546-017-0266-x.
37. Ma, T. & Sun, C. Large eddy simulation of hurricane boundary layer turbulence and its application for power transmission system. *Journal of Wind Engineering and Industrial Aerodynamics* **210**, 104520 (2021). doi: 10.1016/j.jweia.2021.104520.
38. Snaiki, R. & Wu, T. A semi-empirical model for mean wind velocity profile of landfalling hurricane boundary layers. *Journal of Wind Engineering and Industrial Aerodynamics* **180**, 249–261 (2018). doi: 10.1016/j.jweia.2018.08.004.
39. Ortegon, K., Nies, L. F. & Sutherland, J. W. Preparing for end of service life of wind turbines. *Journal of Cleaner Production* **39**, 191–199 (2013). doi: 10.1016/j.jclepro.2012.08.022.
40. Rubert, T., McMillan, D. & Niewczas, P. A decision support tool to assist with lifetime extension of wind turbines. *Renewable Energy* **120**, 423–433 (2018). doi: 10.1016/j.renene.2017.12.064.

41. Beganovic, N. & Söffker, D. Structural health management utilization for lifetime prognosis and advanced control strategy deployment of wind turbines: An overview and outlook concerning actual methods, tools, and obtained results. *Renewable and Sustainable Energy Reviews* **64**, 68–83 (2016). doi: 10.1016/j.rser.2016.05.083.
42. Loraux, C. & Brühwiler, E. *The use of long term monitoring data for the extension of the service duration of existing wind turbine support structures* in *Journal of Physics: Conference Series* **753** (2016), 072023. doi: 10.1088/1742-6596/753/7/072023.
43. Li, X. & Zhang, W. Long-term fatigue damage assessment for a floating offshore wind turbine under realistic environmental conditions. *Renewable Energy* **159**, 570–584 (2020). doi: 10.1016/j.renene.2020.06.043.
44. Morató, A., Sriramula, S. & Krishnan, N. Kriging models for aero-elastic simulations and reliability analysis of offshore wind turbine support structures. *Ships and Offshore Structures* **14**, 545–558 (2019). doi: 10.1080/17445302.2018.1522738.
45. Slot, R. M., Sørensen, J. D., Sudret, B., Sørensen, L. & Thøgersen, M. L. Surrogate model uncertainty in wind turbine reliability assessment. *Renewable Energy* **151**, 1150–1162 (2020). doi: 10.1016/j.renene.2019.11.101.
46. Wilkie, D. & Galasso, C. Gaussian process regression for fatigue reliability analysis of offshore wind turbines. *Structural Safety* **88**, 102020 (2021). doi: 10.1016/j.strusafe.2020.102020.
47. Miller, A., Chang, B., Issa, R. & Chen, G. Review of computer-aided numerical simulation in wind energy. *Renewable and Sustainable Energy Reviews* **25**, 122–134 (2013). doi: 10.1016/j.rser.2013.03.059.
48. O'Brien, J., Young, T., O'Mahoney, D. & Griffin, P. Horizontal axis wind turbine research: A review of commercial CFD, FE codes and experimental practices. *Progress in Aerospace Sciences* **92**, 1–24 (2017). doi: 10.1016/j.paerosci.2017.05.001.
49. Rahman, M., Ong, Z. C., Chong, W. T., Julai, S. & Khoo, S. Y. Performance enhancement of wind turbine systems with vibration control: A review. *Renewable and Sustainable Energy Reviews* **51**, 43–54 (2015). doi: 10.1016/j.rser.2015.05.078.
50. Zuo, H., Bi, K. & Hao, H. A state-of-the-art review on the vibration mitigation of wind turbines. *Renewable and Sustainable Energy Reviews* **121**, 109710 (2020). doi: 10.1016/j.rser.2020.109710.
51. Zhou, H. F. *et al.* A review of full-scale structural testing of wind turbine blades. *Renewable and Sustainable Energy Reviews* **33**, 177–187 (2014). doi: 10.1016/j.rser.2014.01.087.
52. Larsen, T. & Hansen, A. *How 2 HAWC2, the user's manual* English. Denmark. *Forskningscenter Risoe. Risoe-R 1597(ver. 3-1)(EN)*. ISBN: 978-87-550-3583-6 (Risø National Laboratory, 2007).
53. Jonkman, J. M. & Buhl Jr., M. L. *FAST User's Guide* National Renewable Energy Laboratory (Golden, Colorado, 2005). NREL/EL-500-29798.
54. IEC. *Wind turbines – Part 1: Design requirements* 3rd ed. International Electrotechnical Commission (Geneva, Switzerland, 2005).
55. GL. *Guideline for the Certification of Wind Turbines* Germanischer Lloyd (Hamburg, Germany, July 2010).
56. DNV-GL. *DNVGL-ST-0437: Loads and site conditions for wind turbines* DNV GL (Nov. 2016).
57. INEEL & CFE. *Manual de Obras Civiles, Diseño por Viento* tech. rep. (Instituto Nacional de Electricidad y Energías Limpias, México, July 2020). (In Spanish).

[This page intentionally left blank]



## Chapter 2

# Fundamentals

The masses of air moving in the atmosphere have been one of the phenomena that have captured the curiosity of mankind for centuries. The wind has been represented in ancient cultures as nature deities, some times benevolent and gentle, and others of rather a dreadful temper. For example, the *Anemoi*, the wind deities in ancient Greek mythology, were named based on the cardinal direction where they came from, and were associated with different weathers and seasons. Other cultures, like the Mayans, named the god of wind and storms *Hun-rakan*, who was represented as a one-legged serpent-like being (perhaps trying to explain and represent meteorological phenomena like water-spouts). *Fujin*, the wind god in Shintoism, is represented by a demon-like deity, and typhoons are regarded as his making. The embodiment of wind as a deity can be owed to the fact that, despite its destructive potential, mankind also often has been served by it for its benefit.

This section describes some of the fundamental concepts and mathematical expressions that are commonly used in the characterization of wind actions on structures and, particularly, in wind turbines. It is not intended as an exhaustive revision on the subject, and the reader is rather directed to other references whenever a wider description of the subject might be pertinent.

### 2.1 Basic concepts of wind engineering

Wind can be described as the masses of air moving with respect to the surface of the Earth.<sup>1</sup> The movement is originated due to the solar radiation heating with non-uniform intensity the surface of the planet, as it hits with its maximum intensity over the Equator and the Tropics. This causes the air in these warm zones to be lighter, which creates buoyancy forces and differences in pressure that produce movement of the surrounding air in the atmosphere. The colder air that flows from the northern and southern poles towards the Tropics is moved to the west due to the Coriolis force, which is a product of the rotation of the Earth. Near the poles, the Coriolis force is stronger, and the atmospheric circulation is modified. This movement creates complex circulation systems of large scale (comparable to the radius of the Earth),<sup>2</sup> known as the *Hadley*, *Ferrel*, and *Polar* cells (Figure 2.1). These systems comprehend the whole thickness of the lower part of the atmosphere, known as the *troposphere*.

The troposphere is the part of the atmosphere where it makes contact with the surface of the Earth and contains about 80% of the total mass of the atmosphere.<sup>2</sup> It is distinguished by a monotonic reduction of pressure and temperature with altitude, and it extends to altitudes between 8 and 15 km above sea level. Also, half of its mass is estimated to be concentrated up to an altitude of  $\sim 5,500$  m.<sup>2</sup> The interaction between the wind flow and the surface of the Earth occurs at the lower part of the troposphere, which is called the planetary boundary layer (PBL). The height of the PBL can be understood as the elevation where the aforementioned Coriolis force is in equilibrium with the spatial pressure differences, or pressure gradient. Due to this equilibrium, at this height it is commonly said that the wind flow has reached *geostrophic balance*.<sup>1</sup> The equilibrium between the Coriolis force,

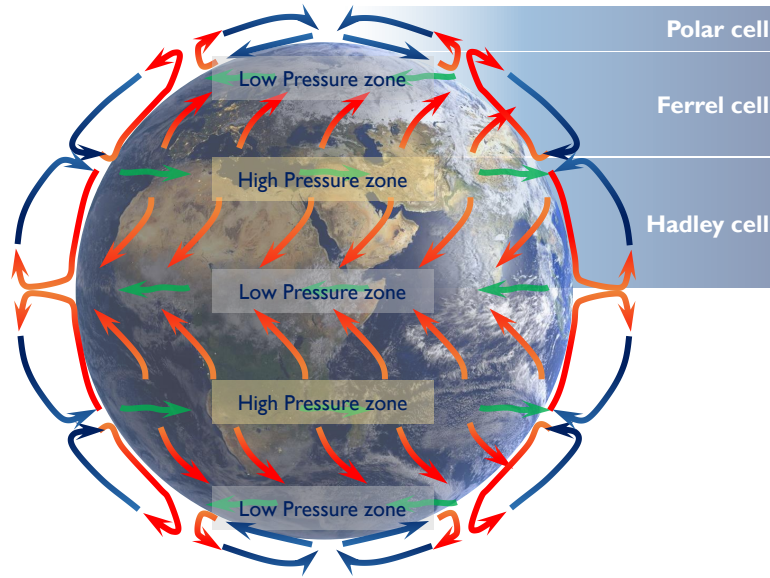


Figure 2.1: Schematic of the global atmospheric circulation

pressure gradient, and centrifugal forces (product of isobar curvature) per unit mass can be expressed from the following equation:

$$\frac{v_g^2}{r} \pm |f_c|v_g \mp \frac{1}{\rho} \left| \frac{\partial p}{\partial r} \right| = 0 \quad (2.1)$$

where  $\partial p / \partial r$  represents the pressure gradient. The wind speed, represented as  $v_g$ , is known as *gradient wind*. The symbol  $f_c$  represents the Coriolis parameter, defined as  $2\omega \sin \phi$ , where  $\omega$  is the angular speed of rotation of the Earth, and  $\phi$  is the latitude angle. The involvement of the latitude angle implies that  $f_c$  is negative for sites in the Southern hemisphere. In Equation 2.1,  $\rho$  represents the air density, whereas  $r$  denotes the radius of curvature of the isobar under analysis. Note that the first term in the equation can be neglected for large isobar-curvature radii, which case gives the expression for the *geostrophic wind* approximation.<sup>3</sup> Lastly, the ‘plus’ and ‘minus’ signs for the second and third terms on the left of the equality, respectively, correspond to trajectories around low-pressure centers (i.e., cyclonic movement). Opposite signs are correspondent to movement around high-pressure centers.

Bellow the height of geostrophic balance, the effects of friction between the surface of the Earth and the wind flow start to gain importance. They become notorious under an altitude known as *gradient height*,<sup>3</sup> and denoted  $z_g$ . From this elevation downwards the wind speed is mainly governed by the effects of friction forces, and the mean wind speed starts to decrease the closer it is measured from the ground. This portion of the atmosphere is defined in wind engineering as the atmospheric boundary layer (ABL). The depth of the ABL may vary from hundreds of meters to a few kilometers,<sup>3</sup> depending on various parameters — like wind speed, the roughness of terrain, and latitude, among others. Nevertheless, wind engineering standards commonly define it solely from terrain-surface parameters. Figure 2.2 presents a schematic that summarizes how these layers are distributed, based on the one used by relevant wind tunnel testing references.<sup>4</sup> In the figure, the geostrophic level is represented as  $z_{geo}$ , and the abbreviation ASL stands for ‘atmospheric surface layer’. Further description of these parameters can be found in the literature.<sup>1-5</sup>

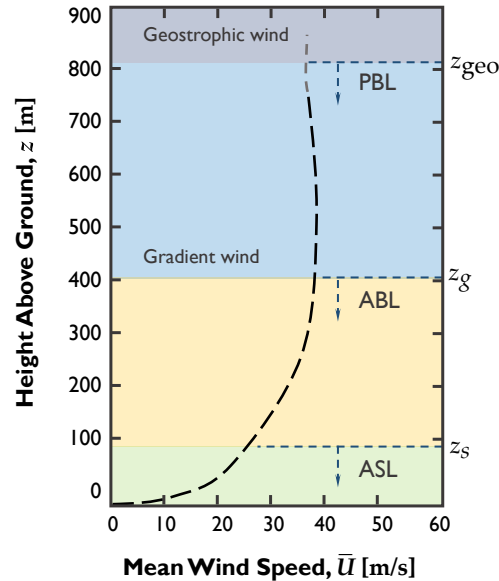


Figure 2.2: Mean speed distribution in the PBL

### 2.1.1 Wind characteristics in the ABL

The main assumption in many wind engineering standards is that the flow is horizontally homogeneous and takes place over flat terrain.<sup>6</sup> That is, the physical quantities of the flow depend only on elevation and time. Also, the stationarity of the flow and the neutral stability of the ABL are other practical simplifications for many wind engineering problems. These imply that the statistical properties that describe the flow have no time dependency and that the moving masses of air experience no buoyancy forces, since they are assumed to hold the same density as their surrounding environment. Virtually all the wind engineering standards for civil applications adopt these criteria for general cases.

Wind velocity is thus separated into three orthogonal components, each one parallel to the main axes of a three-dimensional Cartesian coordinate system. Conveniently, the main contribution of the wind velocity vector (namely in the 'longitudinal direction'),  $U$ , is assumed to be parallel to the  $x$ -axis. The components in the transverse and vertical directions, namely  $V$ , and  $W$ , respectively, are assumed to be parallel to the  $y$ - and  $z$ -axes. A common representation of the three velocity components follows an Eulerian criterion, i.e., it attempts to describe the evolution of quantities that characterize the flow as a function of time.<sup>7,8</sup> As in many flows of interest, these three components will be affected by turbulence. The random nature of turbulence has prompted a statistical perspective on it for physics and engineering problems. In wind engineering, as in various areas of fluid dynamics,<sup>7,9</sup> each velocity component is separated into a time-averaged part (quasi-static part), and a time-varying part of stochastic nature (turbulent part), when the assumption of a stationary phenomenon is applicable. Thus, the longitudinal component of wind velocity is often expressed as  $U = \bar{U} + u(t)$ , where  $\bar{U}$  is the mean or time-averaged component, and  $u(t)$  is the stochastic part of the wind velocity vector in the  $x$ -direction. It is commonly the case that the time-averaged terms of the transverse and vertical components are assumed to be negligible, given the horizontal homogeneity premise,<sup>6</sup> thus these components are simply expressed from their time-varying components as  $v(t)$ , and  $w(t)$ , respectively.

The mean wind speed variation with height is often described from the *log-law profile*, which states that the mean wind speed in the longitudinal direction, over flat terrain, increases with height as a function of the friction velocity  $u_*$  and the roughness length  $z_0$ , as expresses Equation 2.2. The friction velocity is a function of the shear stress at the surface, whereas the roughness length is defined as

the height where the mean speed is zero.<sup>4</sup> In Equation 2.2,  $\kappa$  represents the von Kármán constant ( $\approx 0.4$ ), and  $z_h$  is the ‘zero-plane displacement’, which is the vertical coordinate where the wind speed reaches zero due to large obstacles. Another common expression to describe the mean wind speed variation with height is the *power-law profile* (Equation 2.3), which states that the mean wind speed can be scaled from a value of wind speed at a reference height,  $\bar{U}(z_{ref})$ , for any  $z$  coordinate given an exponent  $\alpha$ . The values taken by this exponent are conventionally defined as a function of the roughness classification of the surface.

$$\bar{U}(z) = \frac{u_*}{\kappa} \ln \left( \frac{z - z_h}{z_0} \right) \quad (2.2)$$

$$\bar{U}(z) = \bar{U}(z_{ref}) \left( \frac{z}{z_{ref}} \right)^\alpha \quad (2.3)$$

In both cases, the variation of wind speed with height is governed by the roughness of the terrain. Both expressions give wind speed profiles within the ABL similar to the one presented in Figure 2.2, and are accepted by many wind engineering standards. References in the literature can be found where the involved parameters are defined in greater detail.<sup>1,3,4,6</sup> In the case of the power-law profile (Equation 2.3), it is the expression suggested by the wind turbine standard IEC 61400-1.<sup>10</sup> The value of  $z_{ref}$  is defined as the hub height of the turbine, whereas  $\alpha$  is defined as 0.2 for the normal turbulence model and 0.11 for the extreme wind model, according to the aforementioned standard.

The magnitude of  $\bar{U}$  at a given height is not ‘unvarying’ *per se* in the sense that different time windows where the averaging is performed will give different values of speed. Many standards define the maximum mean wind speed as a 3-s gust average, sustained winds during cyclones are conventionally measured from 1-min intervals, and 10-min average wind speeds are commonly used for analyses related to the dynamic response of structures. These differences in the computed values are caused by the turbulent fluctuations in the flow,<sup>3</sup> represented by the time-varying part of the wind speed.

Turbulence can be understood as a superposition of eddies of various sizes in the flow, where the ones of larger size are the ones containing the greater portion of the turbulent kinetic energy.<sup>6</sup> The eddies of smaller size are the ones dissipating through viscous motion the energy transferred to them from the larger eddies.<sup>9</sup> The previous statements follow what is known as *Kolmogorov’s first hypothesis*. Further, a *second hypothesis* states that, for large Reynolds numbers, there is a range of sizes of eddies for which the energy transfer is independent of viscosity,<sup>3,9</sup> known as the *inertial sub-range*. An ingenious manner to visualize the energetic contribution and evolution of the scales of the eddies is from spectral representation (presented in the frequency domain in this dissertation). The spectral representation of turbulence is taken as the power spectral density function (PSDF) of the stochastic component of the flow velocity. The inertial sub-range part of the energy transfer is characterized by a negative slope at mid-high frequencies represented by a -5/3 exponent. It is often taken as a referent to validate any turbulence model or measurement. Several expressions proposing PSDFs that describe the distribution of turbulent kinetic energy along frequency can be found in the literature.<sup>3,4</sup> Two widely accepted models that describe this phenomenon in wind engineering are the ones proposed by von Kármán,<sup>11</sup> and Kaimal.<sup>12</sup> Equations 2.4 and 2.5 present their respective expressions for the longitudinal turbulent component of velocity  $u(t)$ :

$$\frac{nS_u(z, n)}{\sigma_u^2} = \frac{4nL_{u,vK}/\bar{U}}{\left[1 + 70.8 (nL_{u,vK}/\bar{U})^2\right]^{5/6}} \quad (2.4)$$

$$\frac{nS_u(z, n)}{\sigma_u^2} = \frac{4nL_{u,K}/\bar{U}}{\left[1 + 6nL_{u,K}/\bar{U}\right]^{5/3}} \quad (2.5)$$

In Equations 2.4 and 2.5,  $n$  represents the temporal frequency in Hz, and  $S_u(z, n)$  the single-sided PSDF of the turbulent component  $u(t)$ . Two parameters that have had no mention so far in the text appear in these equations: (i)  $\sigma_u$ , which is the standard deviation of  $u(t)$ , and (ii)  $L_{u,i}$ , which is known as the ‘integral length scale of turbulence’ (the sub-index  $i$  represents the sub-indexes  $vK$  or  $K$ , which refer to either the von Kármán or the Kaimal spectra, respectively). The integral length scale of turbulence (abbreviated as *length scale* in the rest of the dissertation) can be understood as the average size of the larger eddies, further discussion on this parameter can be found in the literature.<sup>3</sup> A visualization of Equations 2.4 and 2.5 fitted to ABL wind-tunnel simulation measurements, along with a schematic of the hypotheses of Kolmogorov, is displayed in Figure 2.3.

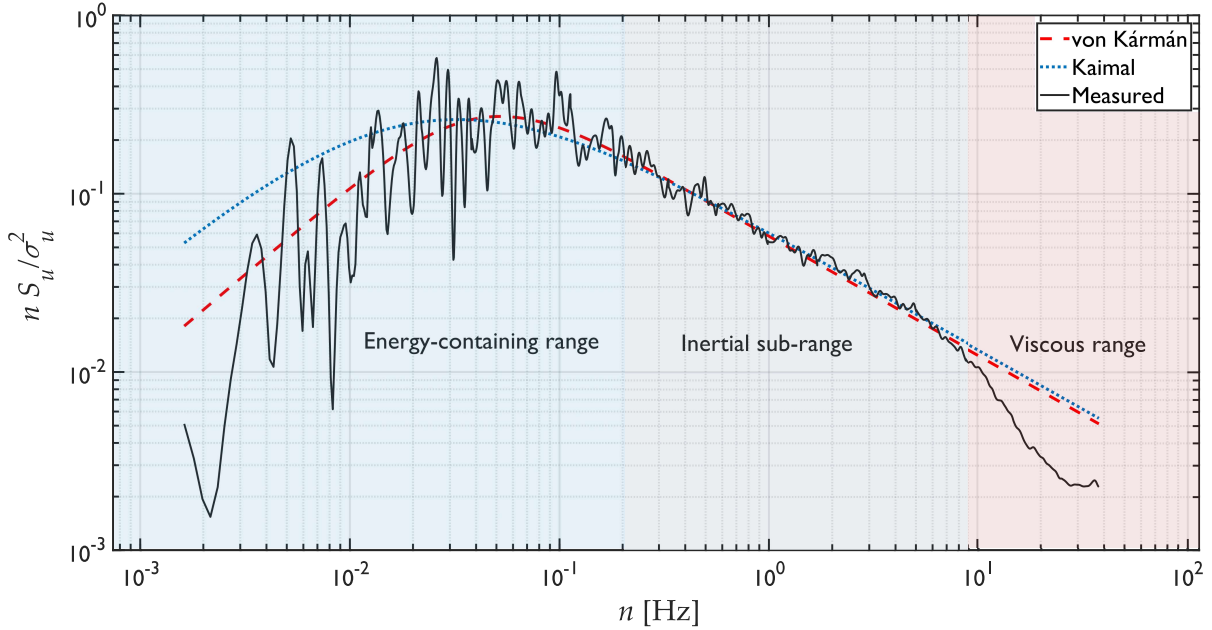


Figure 2.3: PSDFs of  $u(t)$  estimated from wind tunnel measurements

It can be seen from Figure 2.3 that Equations 2.4 and 2.5 show the same asymptotic limit, implying that there exists a linear relation between their respective length scales.<sup>13</sup> As mentioned before, both expressions are widely adopted in wind engineering, and some adaptations based on their functional form have been proposed in the literature to overcome some observed deficiencies from measurements.<sup>14,15</sup> In the case of the von Kármán spectra, they are widely used for consistency with analytic expressions for correlations, and for experimental studies.<sup>13</sup> Whereas the Kaimal spectra are given in the wind turbine standards provided by the IEC for turbulent load estimation,<sup>10</sup> defining the length scales in the  $x$ -,  $y$ -, and  $z$ -directions, respectively, as  $8.1\Lambda_1$ ,  $2.7\Lambda_1$ , and  $0.66\Lambda_1$ . The length scale parameter  $\Lambda_1$  is defined as  $0.7z$  for hub heights lower than 60 m, and 42 m for greater hub heights. The standard deviations for the  $u$ ,  $v$ , and  $w$  components are defined, respectively, as  $\sigma_u$ ,  $0.8\sigma_u$ , and  $0.5\sigma_u$  in the IEC standard.

The wind characteristics described so far follow the assumption of geostrophic balance, as mentioned earlier in this section. It implies that the Coriolis forces are in balance with the pressure forces, and neglect any centrifugal force due to the curvature of isobars. Under this assumption, as summarized in Figure 2.2, the wind profile tends to a maximum nearly-constant profile once it reaches the gradient, and subsequent geostrophic, levels. This assumption is valid for the effects of winds produced by large-scale atmospheric phenomena. However, in other common phenomena of smaller scale, as in the flow around strong low-pressure centers, some important considerations need to be addressed, especially for structures of great heights.

## 2.1.2 The tropical cyclone boundary layer

The phenomena known as *tropical cyclones* are complex low-pressure rotating systems that take place in the atmosphere. They are formed over the oceans of warm waters where the temperature surpasses 26 °C, usually in latitudes between 5° and 20°, i.e, over the Tropics. At the genesis stage of a cyclone, it begins as a *tropical disturbance* when thunderstorms last for 24 hours, or more, over the ocean. Once a circulation system is formed, the disturbance scales to a *tropical depression*. If the sustained wind during the tropical depression increases in intensity, it scales to a *tropical storm*, and it is said that the cyclone has reached its mature stage.<sup>16</sup> At their mature stage, tropical cyclones consist of strong rotational circulation and well-organized clouds around the low-pressure center.<sup>17</sup> In this stage, they can reach radial dimensions that usually cover from a few to several hundreds of kilometers (but can be larger than a thousand<sup>18</sup>), and develop wind speeds that can be devastating to anything on its path. The damage potential of a tropical cyclone does not come from wind intensity alone, because they are accompanied by heavy precipitation which translates into floods and landslides, once they make landfall.

A tropical cyclone is one of the most interesting phenomena that occur in the atmosphere. Perhaps the following description of its structure makes no justice to such a fascinating phenomenon, but it is made for the sake of a better contextualization, following the schematic displayed in Figure 2.4:

- (i) The wind flowing at low heights starts to do it spirally in a cyclonic movement towards the center of low pressure, increasing its velocity. At the outer radii of the cyclone, the incoming air converges and convection of cumulus starts. As the air is taken closer and closer to the center of the storm by the strong pressure defect, its radial velocity rapidly increases. Radial and tangential velocities are not the only quantities to increase at smaller radii, but also the low-level moisture and precipitation.<sup>17</sup>
- (ii) At a distance that can vary from tens up to a hundred kilometers, the incoming air suddenly turns upwards in an intense convection ring around the center of the storm. This is known as the *eye-wall*, the highest wind speeds, as well as the heaviest rainfall, occur at this radius. Within the eye-wall radius, wind speed and rainfall rapidly decrease. At the center, known as the *eye* of the storm, calm and often descending winds are flowing. This is one of the principal characteristics of tropical cyclones. The eye of the cyclone constitutes a convergence zone where the radial and tangential components of wind velocity collapse. Locally, the centrifugal force also collapses, and the pressure rises. This implies a relative calm in the eye, with respect to the intense wind at the eye wall.<sup>2,17</sup>
- (iii) The air flowing spirally upwards in the eye-wall is restricted by the stable air at the stratosphere, turning the flow outwards and away from the storm center.

Figure 2.4 also depicts typical plots of the variation of  $v_g$  along the storm radius, it also displays the pressure variation at surface level. The gradient wind can be described along the radius of the storm by means of Equation 2.1, which, as mentioned before, implies clock-wise rotation for cyclones in the Southern hemisphere. Further details on the subject can be found in excellent references in the literature.<sup>2,16,17</sup>

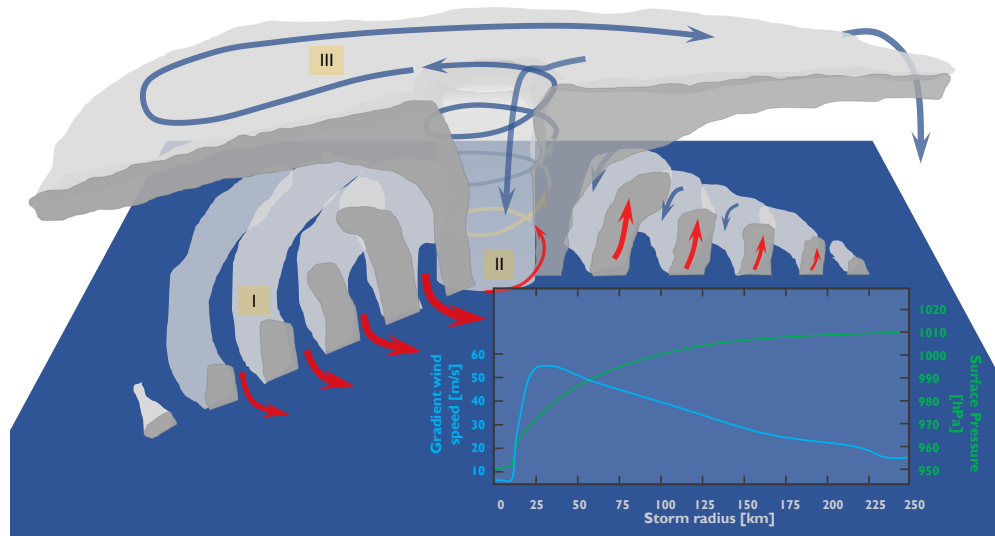


Figure 2.4: Structure of a tropical cyclone

Tropical cyclones are called *hurricanes* in the Atlantic Ocean and Eastern Pacific, and *typhoons* in the Western Pacific. Aside from their names, the atmospheric mechanisms behind their origins are the same. A categorization of these phenomena is conventionally made from the Saffir-Simpson scale. It classifies the cyclone by strength, according to diverse observed intensities that characterize the phenomenon. Table 2.1 displays the classification of tropical cyclones according to the aforementioned scale, where  $p_{cs}$  denotes the pressure at the center of the storm measured at surface level.

Table 2.1: Saffir-Simpson hurricane scale

Category	Central pressure $p_{cs,min}$ [hPa]	Maximum Sustained Wind Speed (Over Water) <sup>a</sup> [m/s]	Maximum Gust Speed (Over Water) <sup>a</sup> [m/s]	Maximum Gust Speed (Over Land, $z_0 = 0.03 \text{ m}$ ) <sup>a</sup> [m/s]
TD <sup>c,d</sup>	1007	< 17.0	< 21.0	< 18.6
TS <sup>c,d</sup>	< 1000	17.0 - 33.0	21.0 - 40.6	18.6 - 36.8
I <sup>b</sup>	$\geq 980$	33.1 - 42.0	40.6 - 51.9	36.8 - 48.1
II <sup>b</sup>	979 - 965	42.0 - 49.6	51.9 - 61.7	48.1 - 58.1
III <sup>b</sup>	964 - 945	49.6 - 58.1	61.7 - 72.7	58.1 - 69.7
IV <sup>b</sup>	944 - 920	58.1 - 69.3	72.7 - 87.3	69.7 - 85.5
V <sup>b</sup>	< 920	> 69.3	> 87.3	> 85.5

<sup>a</sup>The sustained wind speed considers an averaging time of 1 minute, whereas the gust speed considers an averaging time of 3 s.

<sup>b</sup>Values for Hurricanes as presented in HAZUS.<sup>19</sup>

<sup>c</sup>Values for Tropical Depression (TD) and Tropical Storm (TS) as presented by Kantha.<sup>20</sup>

<sup>d</sup>The Gust factors for TD and TS assume values of 1.23 and 1.09 for over-water and over-land gusts, respectively.<sup>21</sup>

The documentation of cyclonic events has evinced the presence of what is known as *supergradient* winds near the eye-wall of hurricanes.<sup>22–24</sup> This phenomenon is one of the characteristics of the tropical cyclone boundary layer (TCBL), which becomes of major interest for the analysis and design of high-rise structures. The TCBL differs from the neutral *synoptic* and *extra-tropical* ABL in various aspects, particularly in the aforementioned supergradient winds, which imply that the tangential velocity during the tropical cyclone can surpass the gradient wind speed below  $z_g$  (cf. Figure 2.2). Analytic studies have been performed on the physics behind this complex feature.<sup>25–27</sup> Moreover, empirical models have been developed and adopted for the estimation of the mean-wind profile within the TCBL. For example, Vickery et al.<sup>24</sup> proposed a model that estimates the mean velocity profile in the TCBL based on an analysis of dropsonde data that encompassed six years of tropical cyclone

data, mostly from the Atlantic Ocean and the Gulf of Mexico. The developed model is an adaptation of Equation 2.2, where the mean-wind velocity depends on the height of the maximum wind speed during the storm, and is defined as:

$$\bar{U}(z) = \frac{u_*}{\kappa} \left[ \ln \left( \frac{z}{z_0} \right) - a_* \left( \frac{z}{H^*} \right)^{n^*} \right] \quad (2.6)$$

where  $a_*$  and  $n^*$  are constant parameters of the model, taken as 0.4 and 2.0, respectively, for all values of  $r$  and  $H^*$ . The latter is the estimate of the boundary layer height, defined for over-sea radii near and outside the *radius of maximum winds*,  $r_{v_m}$ , respectively as:

$$H^* = 343.7 + \frac{0.26}{I} \quad (2.7a)$$

$$H^* = 186.6 + \frac{12.66}{\sqrt{I}} \quad (2.7b)$$

where the variable  $I$  is the inertial stability of the atmosphere during the cyclone, which can be understood as a measure of the balance between the centrifugal and pressure-gradient forces. A more insightful discussion on  $I$  can be found in the literature.<sup>5,28</sup> The inertial stability can be expressed in terms of  $v_g$ ,  $r$ , and  $f_c$  as:

$$I = \sqrt{\left( f_c + \frac{2v_g}{r} \right) \left( f_c + \frac{v_g}{r} + \frac{\partial v_g}{\partial r} \right)} \quad (2.8)$$

Another semi-empirical approach to define an expression that describes the mean-velocity profile during hurricanes has been proposed by Snaiki and Wu.<sup>29</sup> Analogously to the expression proposed by Vickery et al.,<sup>24</sup> the proposed models are adaptations of the conventional mean-velocity log- and power-law equations. These models were adjusted to fit measured data from the Weather Surveillance Doppler Radar for land-falling hurricanes over the Atlantic and the Gulf of Mexico, and GPS dropsondes for hurricanes over these regions and the Caribbean. The data encompass a time window from 1995 and 1996 until 2012, respectively. Equation 2.9 presents the log-law expression suggested by Snaiki and Wu<sup>29</sup>:

$$\bar{U}(z) = \frac{u_*}{\kappa} \left[ \ln \left( \frac{z}{z_0} \right) + \eta_0 \sin \left( \frac{z}{\delta} \right) \exp \left( -\frac{z}{\delta} \right) \right] \quad (2.9)$$

where  $\eta_0$  is a parameter defined as 9.026, and  $\delta$  is the height of maximum wind, defined from a regression model proposed by the aforementioned authors.<sup>29</sup>

The intricate nature of turbulence is knotted even further by the complex fluid-dynamics mechanisms involved in the TCBL. Attempts to describe the relationships among its different turbulence components have been published in the literature.<sup>30</sup> Yet, a well-defined consensus on the characteristics of turbulence for tropical cyclones has not been reached.<sup>31</sup> Supporting the efforts to improve the understanding of the matter, numerical studies have focused on the replication of the flow field during tropical cyclones.<sup>32-34</sup> These models used the estimated PSDF of turbulence from measured data to validate their simulations, where a -5/3 doubly-logarithmic slope at the inertial sub-range is identified. This feature is not uncommon in the measurements of tropical cyclone wind speed,<sup>35-37</sup> despite the existent dissensus on the subject. Some approaches from observations have suggested that there is a significantly higher contribution from low frequencies, compared to the non-hurricane spectra (cf. Equation 2.5), and have presented their own models.<sup>35</sup> Diverse publications have concluded that Equation 2.4 represents adequately the distribution of turbulent kinetic energy,<sup>36</sup> whereas others have proposed corrections to Equation 2.5 to represent greater contribution from higher frequencies to the spectral amplitude.<sup>33</sup> These considerations encourage further studies on the turbulence characteristics of the TCBL and its effects on high and flexible structures.



## 2.2 Basic concepts of wind turbine aerodynamics

A wind turbine is a machine designed to transform the kinetic energy from the wind flow into mechanical energy, and subsequently into electrical energy via a generator. The kinetic energy is extracted from the stream due to the lift forces generated on the *blades* of the turbine. These are the “wing-like” elements rotating around the axis of a shaft connected to a gearbox and a generator. If these elements are configured to rotate around a horizontal shaft, the turbine is called a horizontal axis wind turbine (HAWT). Nowadays, virtually all the energy generated worldwide from wind resources is extracted from HAWTs. Modern HAWTs are technologically advanced machines equipped with a number of sensors, actuators, and hardware necessary to optimize the operation of the whole turbine in varying wind conditions. Among the functions of this equipment are included the turbine orientation (*yaw angle*), the blade orientation (*pitch angle*), or even its start-ups and shut-downs, among other operations.<sup>13</sup> An ideal wind turbine rotor should always be perpendicular to the wind stream,<sup>38</sup> nevertheless, it is given a small *tilt angle*, and the blades are given a *precone angle* to avoid the impact between the blades and the tower for *upwind* HAWTs (i.e., turbines that operate with the tower located downwind from the rotor). Figure 2.5 gives a general depiction of some of the basic components of a HAWT, as well as some of their motions and orientations.

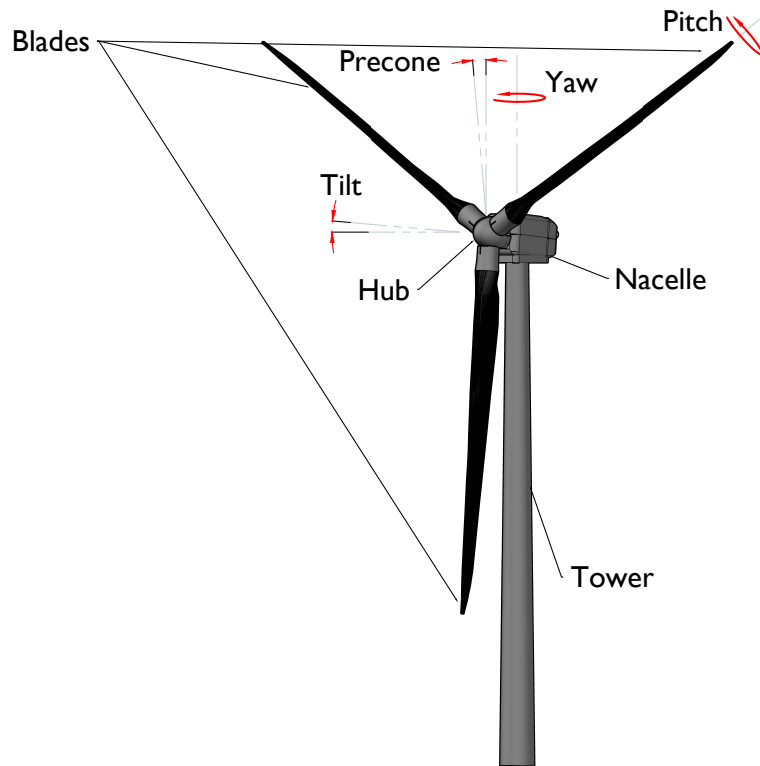


Figure 2.5: Schematic of a HAWT

Two important dimensions that can describe a HAWT are the *hub height*, and the rotor diameter. The former is important due to the increment in wind speed with height, as described in Subsection 2.1.1, which aids in increasing the power extracted by the turbine; the latter is as important because the power output is directly proportional to the area swept by the rotor. These facts are justified by the expression that estimates the power output of a HAWT:

$$P = \frac{1}{2} \rho C_P U^3 A \quad (2.10)$$

where  $C_P$  is the power coefficient, and  $A$  is the area swept by the wind turbine blades, i.e.,  $\pi R^2/4$  (where  $R$  is the maximum radius of the rotor).  $C_P$  has a physical maximum limit, known as Betz (or Lanchester-Betz) limit, which is 0.593.<sup>13,38</sup> This limit can be demonstrated from mass conservation and momentum balance since the extracted kinetic energy from the stream must produce a reduction in wind velocity. Within this context, if the rotor of the turbine is visualized as a permeable drag device on a stream tube (where the control volume is defined by the mass of air affected by the rotor), the upstream section of the ‘tube’ would have a smaller section, whereas the downstream section would have to be larger, due to mass conservation of the flow. The force responsible for the change in momentum of the flow is the result of the pressure drop necessary for the conservation of energy, according to Bernoulli’s equation. That is, for an incompressible horizontal flow, it can be stated that:

$$\begin{aligned}\frac{1}{2}\rho U_{\text{upwind}}^2 + p_{\text{upwind}} &= \frac{1}{2}\rho U_{\text{rotor}}^2 + p_{\text{rotor}}^+ \\ \frac{1}{2}\rho U_{\text{rotor}}^2 + p_{\text{rotor}}^- &= \frac{1}{2}\rho U_{\text{downwind}}^2 + p_{\text{downwind}}\end{aligned}\quad (2.11)$$

In view of this, assuming that the pressure far downstream of the rotor eventually balances, the following relation results:

$$p_{\text{rotor}}^+ - p_{\text{rotor}}^- = \frac{1}{2}\rho \left( U_{\text{upwind}}^2 - U_{\text{downwind}}^2 \right) \quad (2.12)$$

Further, if a factor named  $a$  is defined as the fraction of the stream-velocity reduction at the rotor, i.e.,  $a = 1 - U_{\text{rotor}}/U_{\text{upwind}}$  (known as *axial induction factor*), it can be stated that:

$$\frac{1}{2}\rho \left( U_{\text{upwind}}^2 - U_{\text{downwind}}^2 \right) A = \rho(1-a)A \left( U_{\text{upwind}} - U_{\text{downwind}} \right) U_{\text{upwind}} \quad (2.13)$$

Thus, the *thrust force*  $T$  on the disc representing the rotor can be found as  $T = (p_{\text{rotor}}^+ - p_{\text{rotor}}^-)A$ , whereas the power extracted is  $P = TU_{\text{rotor}}$ . Therefore:

$$P = 2\rho A U_{\text{upwind}}^3 a (1-a)^2 \quad (2.14)$$

where taking into account Equation 2.10 implies that:

$$C_P = 4a(1-a)^2 \quad (2.15)$$

By solving  $\frac{dC_P}{da} = 0$  the value of the Lanchester-Betz limit can be found. Moreover, the *thrust coefficient* of the rotor,  $C_T$ , can also be defined from the axial induction factor  $a$  from:

$$C_T = 4a(1-a) \quad (2.16)$$

This approach is known as the ‘actuator disc’ concept, or one-dimensional momentum theory, Figure 2.6 displays these variables for the sake of a clearer description. Further, the maximum power coefficient is achieved at a value of  $a = 1/3$ .

Notwithstanding, following the criteria already presented would imply that, for an increasing value of  $a$ , the downwind flow eventually would ‘reverse’ for values of  $a$  greater than  $\sim 0.4$ . Nonetheless, observations from experiments have shown that, when the difference between  $U_{\text{upwind}}$  and  $U_{\text{downwind}}$  becomes too large, momentum is transported from the outer flow field into the wake. Empirical expressions have been proposed to overcome this limitation. Moreover, it can be observed that the deductions presented so far in this section have neglected the effects of the rotation of the equivalent rotor on the flow field. The angular momentum product of the rotation of the disc can also be considered in the deductions, resulting in a *tangential induction factor*,  $a'$ . For brevity, further formulae

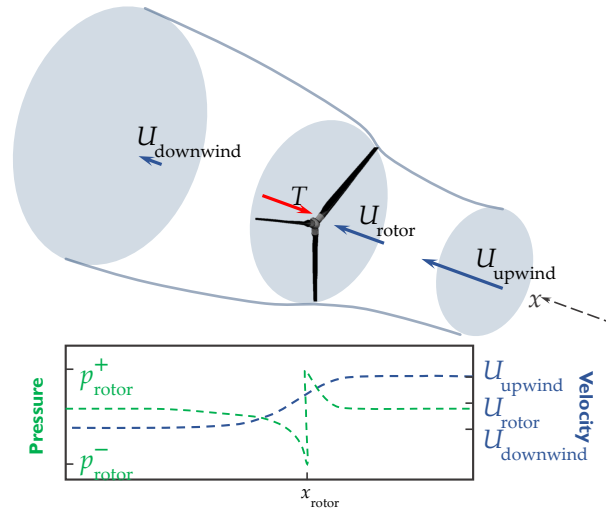


Figure 2.6: One-dimensional actuator disc concept

on the subject are not included, but the reader is encouraged to examine consummate references in the literature that dissert with wider detail these fundamental concepts of wind energy,<sup>13,38,39</sup> and its applications.<sup>40</sup>

Another consideration necessary for the aerodynamic analysis of wind turbine rotors, not regarded so far in what has been summarized here, is that the thrust force on the rotor is not uniformly distributed. One possibility to overcome this limitation is dividing the equivalent disc into annular sections of width  $dr$ . Nevertheless, the geometrical characteristics of the blades still have to be considered for a detailed computation of the forces on the rotor. Some basic aspects of such criteria will be presented in the following.

### 2.2.1 Aerodynamic forces on operating rotors

The change in axial and angular momentum in the stream of air that passes through the rotor is the product of the aerodynamic forces on the blades of the turbine. The most commonly-used method to compute these forces is the blade element momentum (BEM) theory, due to its computational affordability and satisfactory predictions.<sup>41</sup> The main assumptions of the BEM theory can be summarized as: (i) each analyzed element is independent of the adjacent elements, (ii) the induced velocity generated by the rotation of the blades is known, (iii) the two-dimensional aerodynamic force coefficients of each blade profile are known for a sufficient range of *angles of attack* and Reynolds numbers, and (iv) the velocity component in the span-wise direction of the blade is ignored.

Figure 2.7 shows a cross-section of a blade at a radius  $r$  (in this context,  $r$  represents the radial coordinate of a blade element, rather than the isobar radius), where the velocity and force vectors acting on the blade are defined. The variable  $\Omega$  stands for the rotational speed of the rotor, whereas  $U_{rel}$  represents the resultant velocity vector, which reaches the blade with an angle  $\psi$  with respect to the rotor plane. The angle  $\beta$  is the total pitch angle of the blade, i.e., the sum of the default twist of the blade and the gyration imposed by the control systems of the turbine. The angle of attack  $\alpha$  is measured from the chord line of the section, which has a chord of length  $c$  and width  $dr$ . Note that the precone and tilt angles of the rotor have been neglected in the schematic for a clearer illustration of the concepts.

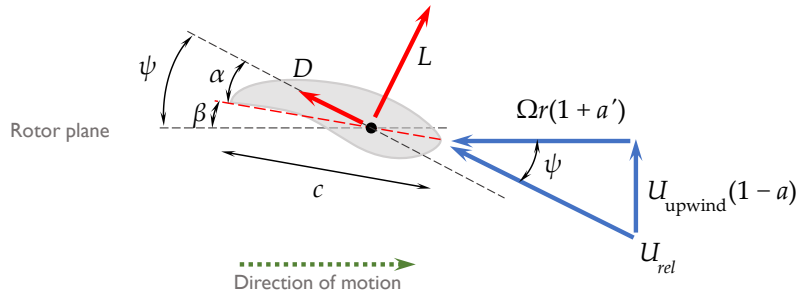


Figure 2.7: Aerodynamic blade section and velocity and force vectors

The angle of attack of the wind velocity on the blade can be estimated as  $\alpha = \psi - \beta$ , where the incidence angle can be estimated from:

$$\psi = \arctan \left[ \frac{U_{\text{upwind}}(1-a)}{\Omega r(1+a')} \right] \quad (2.17)$$

If the aerodynamic force coefficients of the blade section are known, the lift ( $L$ ) and drag ( $D$ ) forces on the blade element can be determined from:

$$L = \frac{1}{2} \rho U_{\text{rel}}^2 c(r) C_L(\alpha) dr \quad (2.18)$$

$$D = \frac{1}{2} \rho U_{\text{rel}}^2 c(r) C_D(\alpha) dr \quad (2.19)$$

Further, the thrust force on the individual blade element, as well as the related torque moment, can respectively be computed once the incidence angle  $\psi$  is defined:

$$dT = L \cos(\psi) + D \sin(\psi) \quad (2.20)$$

$$dM = r [L \sin(\psi) + D \cos(\psi)] \quad (2.21)$$

The total thrust force on the whole rotor is computed from the integration of Equation 2.20 from 0 to  $R$ , accounting for the respective value of  $c$  at every radial position, and for each of the blades that compose the rotor of the turbine. This is analogous to the rotor torque, but using Equation 2.21.

The values of  $a$ ,  $a'$ , and  $\psi$ , are computed iteratively from estimations until their values converge to a defined tolerance. Moreover, as mentioned earlier in this section, when the values of  $a$  surpass  $1/3$ , the BEM theory is no longer valid. Empirical corrections for  $a$  have been proposed in the literature. The most popular implies multiplying  $a$  for a factor equal to  $0.25(5 - 3a)$  for values of  $a$  greater than  $0.3$ .<sup>41</sup> Details on the implementation of an algorithm for the estimation of  $a$  and  $a'$  can be found clearly described in the literature,<sup>38</sup> as well as the corrections for these factors on highly axially-loaded rotors.

Revisiting Figure 2.7 another consideration becomes pertinent: if the value of  $a$  is high-enough, the lift force becomes nearly normal to the rotor plane. This implies that the resultant force contributes little to the torque, which is translated to less extracted power. This effect is more notable at the outer radii of the blade, where the tangential velocity of the blade dominates the vectorial composition of  $U_{\text{rel}}$ . Some empirical solutions have been proposed to overcome this problem in the computation of

the forces on the blade.<sup>13</sup> The most popular approach is the one developed by Prandtl, which states a correction factor that goes from 1 at the root of the blade to 0 at the tip. Further, a similar torque-loss situation occurs at the root of the blade. Thus, the values of the induction factors must be corrected to account for these losses. For brevity, the expressions for tip and root corrections are not presented, but they can be found in references on the subject.<sup>13,38</sup> Lastly, in reality, the pitch angle of the blades, or the rotor speed, varies during the operation of the turbine. This implies that there will exist a time delay in the aerodynamic loads on the rotor which can represent an amplification of the loads for a time-lapse proportional to the rotor dimensions and the wind speed. This effect is known as ‘dynamic inflow’, or ‘dynamic wake’, and is disregarded in the current section. Nevertheless, information on the subject can be consulted in the literature.<sup>38</sup>

The rotation of the blades plays an important role not only in the magnitudes of the forces experienced by the blade itself but also in how the turbulent kinetic energy is distributed by the eddies passing the rotor. The following subsection presents some expressions that allow estimating the distribution of turbulent kinetic energy accounting for the effects of blade rotation.

### 2.2.2 Wind turbulence on operating rotors

As described in Section 2.1.1, the wind speed flowing on a flat surface varies mainly with height, and it is also represented by the addition of a quasi-static component and a time-varying component. It was also defined that turbulence is the superposition of eddies of different sizes and that the largest eddies are the ones containing the greater portion of turbulent kinetic energy. A rotating blade of a HAWT sweeps several times any passing eddy in a relatively short time interval, thus, the wind forces on the blade crossing this region several times experience a distortion of the energy spectrum of turbulence (compared to the one of a non-moving reference point). This distortion in the energy of the time-varying component of wind is significant. Neglecting this effect might lead to important misestimations of the stochastic forces on wind turbines, and consequently, any result of fatigue or structural response analyses disregarding this effect would be unavailing.

Paraphrasing what has been stated in the previous paragraph: if the dimensions of a turbine rotor are comparable to the largest eddies, i.e.,  $L_u \gg R$ , the rotor will periodically sample the same eddy structure until it has completely passed the rotor plane. This will produce peaks in the PSDF of turbulence, or in the correlation function (if it is measured from the time-domain), at multiples of the passing frequency or multiples of the period of rotation, respectively. This phenomenon is known as ‘gust slicing’, and has been observed from measurements since the late 1970s and early 1980s, although incipient theoretical statements of it have been reported from earlier decades.<sup>42,43</sup> Furthermore, there is a direct relationship between the along-wind fluctuation of wind speed and the stochastic forces produced by it. Therefore, the concentrated energy at certain frequencies affects considerably the loads on the blades and the whole wind turbine structure.

The function describing the distribution of turbulent energy in the frequency, as ‘seen’ from the rotating blade, is called the *rotationally-sampled* spectrum. The rotationally-sampled PSDF of along-wind turbulence,  $S_u^o$ , can be estimated numerically by sampling turbulent velocity signals from a wind-field simulation at radially distributed points. A more formal estimation of it is usually computed from the Fourier transform of the rotationally-sampled correlation function  $\kappa_u^o$ . Kristensen and Frandsen presented a deduction of  $\kappa_u^o$  from the von Kármán turbulence spectrum (Equation 2.4), assuming that the turbulence is stationary, homogeneous, and isotropic.<sup>44</sup> Another clear and complete description of the deduction of  $\kappa_u^o$  from the von Kármán turbulence model is also presented by Burton et al.,<sup>13</sup> following their notation,  $\kappa_u^o$  is expressed as:

$$\kappa_u^o(r_1, r_2, \tau) = \frac{2\sigma_u^2}{\Gamma\left(\frac{1}{3}\right)} \left(\frac{s/2}{1.34L_{u,vK}}\right)^{\frac{1}{3}} \left[ K_{1/3}\left(\frac{s}{1.34L_{u,vK}}\right) - \frac{s}{2(1.34L_{u,vK})} K_{2/3}\left(\frac{s}{1.34L_{u,vK}}\right) \left(\frac{r_1^2 + r_2^2 - 2r_1r_2 \cos(\Omega\tau)}{s^2}\right) \right] \quad (2.22)$$

where  $\Gamma(\cdot)$  is the gamma function, and  $K_{1/3}$  and  $K_{2/3}$  are modified Bessel functions of second kind and orders 1/3 and 2/3, respectively, evaluated at  $s/1.34L_{u,vK}$ . The time lag is represented by  $\tau$ . The variable  $s$  represents the distance between an incoming air particle at a horizontal distance  $\overline{U}\tau$  upwind of the rotor, and two points within the rotor plane separated by a distance  $\sqrt{r_1^2 + r_2^2 - 2r_1r_2 \cos \Omega\tau}$  between them. It must be noted that Equation 2.22 accounts for the cross-correlation between the turbulence measured at radial coordinates  $r_1$  and  $r_2$ , and it can also account for cross-correlation among points at different blades if the angle between them is included in the cosine function involved. Figure 2.8 displays an example of  $\kappa_u^o$  computed for a three-blade rotor with  $R = 63$  m, a passing frequency  $\Omega = 12.1$  rpm (i.e., 0.2017 Hz), and a length scale of 146 m, for different radial positions at two consecutive blades.

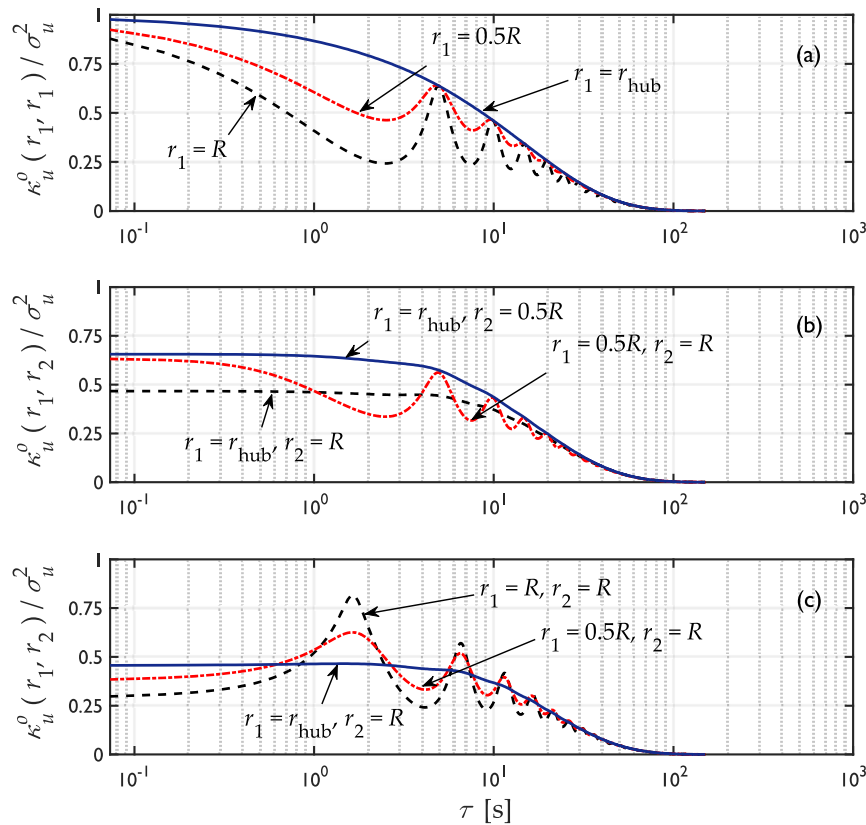


**Figure 2.8:** Rotationally sampled correlation function for different blades and radial coordinates: (a) for the same blade and same radii, (b) for the same blade and different radii, and (c) for different blades and different radii

From Figure 2.8(a) it must be noted that the peaks in the correlation function appear each 4.96 s, i.e., at the passing period of the blade. This is notorious also in Figure 2.8(b) for the radial positions closer to  $R$ . In both cases, the closer the points are located to the center of the rotor, the lesser sensitivity to the rotation effects is found in the correlation function, and it resembles the correlation function

of a static point. Moreover, in Figure 2.8(c) the peaks are shifted to the left two-thirds of the passing period. This is justified in the fact that, once the first blade has crossed a point in space, the second blade will pass by the same point (if the radial position is the same) after a third of the time that the first blade takes to complete a rotation cycle.

All these periodical effects in the turbulence give particularities to the stochastic part of the forces on the rotor that need to be properly addressed. Blade forces computed from the BEM theory need to be rotationally-sampled to account for the aforementioned periodicity, and corroboration should always be provided in any structural analysis that attempts to regard it. The periodicity of the rotating blades is not represented by the turbulence models commonly used in wind engineering without any modification, or rotational sampling algorithm. Further, the inclusion of the correlated periodical forces of the whole rotor will produce similar spectra that have to be accounted for in the estimation of their effects on the support structure of a HAWT, as will be presented in the following.

### 2.2.3 Thrust force on operating rotors

It was briefly explained in Section 2.2 that the thrust force on a rotor is directly related to the power extracted by the HAWT, making it the action that governs the analysis of the turbine structure in operation. Subsequently, it was detailed in Subsection 2.2.1 that the thrust force depends highly on the operation and aerodynamic conditions of the rotor, and also on the wind velocity; therefore, it becomes highly influenced by turbulence in short time intervals. Due to the stochastic nature of turbulence, the thrust force will also show variations at short time intervals that can also be described from a spectral approach. Further, the turbulence spectra used for the derivation of the thrust spectrum must account for the effects of the gust-slicing phenomenon.

Regarding Equations 2.18–2.20, the thrust force on a blade element can be rewritten as:

$$dT = \frac{c\rho}{2} U_{rel}^2 [C_L \cos(\psi) + C_D \sin(\psi)] dr \quad (2.23)$$

If the thrust force on the element, likewise the wind speed, is expressed by a quasi-static and a time-varying component — say,  $dT_0$  and  $dT_1$ , respectively — it appears logical to assume that the time-varying component is dependent on the turbulence. Thus,  $dT$  can be linearly expressed as  $dT = dT_0 + dT_1 \approx dT_0 + u\partial(dT)/\partial u$ . Moreover, for large rotors operating at a near-optimal level,  $\Omega r \gg U_{upwind}$  for the greater part of the blade. Therefore, assuming that the incidence angle is small, its rate of change with respect to the turbulence can be simplified to  $\frac{d\psi}{du} \cong \frac{1}{\Omega r}$ .<sup>13</sup> This simplification also assumes that the turbulent eddy structures are transported horizontally and remain unaffected by the induction factors of the rotor. Further, the rate of change of  $U_{rel}$  with respect  $u$  is small for the greater part of the blade, thus it can be disregarded and, consequently,  $dT_1$  can be expressed as:

$$dT_1 \cong u \frac{\rho\Omega}{2} rc \left[ \frac{\partial C_L}{\partial \psi} + C_D \right] dr \quad (2.24)$$

Hence, the total standard deviation of the force normal to the rotor plane for a single blade is stated as:

$$\sigma_T = \frac{\rho\Omega}{2} \int_0^R \left[ \frac{\partial C_L}{\partial \psi} + C_D \right] \sigma_u cr dr \quad (2.25)$$

From Equation 2.25 two observations are pertinent: (i) since  $\frac{\partial C_L}{\partial \psi} = \frac{\partial \alpha}{\partial \psi} \frac{dC_L}{d\alpha}$ , for a constant rotor speed, and if the pitch angle of the blade  $\beta$  is not varying during the analysis,  $\frac{\partial C_L}{\partial \psi} = \frac{dC_L}{d\alpha}$ , since  $\alpha = \psi - \beta$ . And (ii), the values of  $\sigma_u$  can be estimated radially from the Fourier transform of Equation 2.22. Thereupon, the variance of the thrust force on the whole rotor (repeating the symbol  $\sigma_T$ ) can be stated as:

$$\sigma_T^2 = \left(\frac{\Omega\rho}{2}\right)^2 \int_0^R \int_0^R \left[ \int_0^\infty S_u^o(r_1, r_2, n) dn \right] \left[ \frac{dC_L(r_1)}{d\alpha} + C_D(r_1) \right] \left[ \frac{dC_L(r_2)}{d\alpha} + C_D(r_2) \right] c(r_1)c(r_2)r_1r_2 dr_1 dr_2 \quad (2.26)$$

The distribution of Equation 2.26 in the frequency, i.e., the thrust spectrum, is given fundamentally by the term within the first rectangular brackets, which is the rotationally-sampled turbulence PSDF. It is thus observed that, for the whole rotor, the thrust PSDF can be expressed as:

$$S_T(n) = \left(\frac{\rho\Omega}{2}\right)^2 \oint \oint S_{uJ,K}^o(r_1, r_2, n) \frac{dC_L(r_1)}{d\alpha} \frac{dC_L(r_2)}{d\alpha} c(r_1)c(r_2)r_1r_2 dr_1 dr_2 \quad (2.27)$$

where  $S_{uJ,K}^o(r_1, r_2, n)$  represents the rotationally-sampled turbulence spectrum in the along-wind direction, for radial coordinates  $r_1$ , and  $r_2$ , at blades  $J$ , and  $K$ , respectively. The contour integral symbols are the notation used by Burton et al.<sup>13</sup> to represent that the integration accounts for all blades and radial coordinates for the whole rotor. Moreover, the aerodynamic derivatives of the lift coefficient are assumed constant in the aforementioned reference, which implies that those terms would be placed outside the integrals. Further, the contribution of the drag coefficients to the thrust force has been neglected, since the values of  $C_D \sim 0$  for small angles of attack.

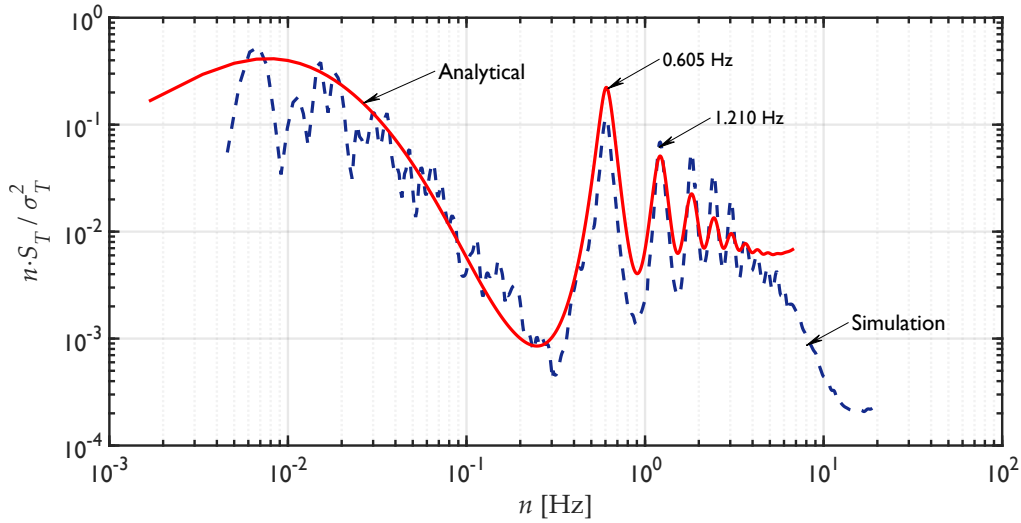


Figure 2.9: Normalized thrust spectra for a three-blade rotor

Figure 2.9 shows an example of the normalized PSDF of thrust force on the same three-bladed rotor presented before in Subsection 2.2.2, assuming the same operating conditions. A comparison with the spectrum estimated from numerical simulations on HAWT-specialized software is also included. The peaks displayed in the PSDF are due to the contribution of the rotationally sampled turbulence spectra. Notwithstanding, it must be noted that, despite the fact that the passing frequency of the blades is 0.2017 Hz, the peaks are located at three times that value and its harmonics. This is justified in the number of blades that form the rotor, since a gust contributing to the loads on the rotor would be ‘sampled’ three times with every rotation cycle.

The distortion in the thrust-force spectra produced by the rotation of the blades is not negligible, and it depends completely on the aerodynamic configuration of the blades and the operation state of the turbine. Thus, it is inconstant for every value of wind speed that makes incidence on the rotor, and accounting for these operation changes implies knowledge of parametric values imposed by the



generator-torque and blade-pitch control systems of the turbine. Furthermore, as discussed latterly in this dissertation, the spectral and statistical features of the forces acting on the wind turbine structure become of great importance when estimating fatigue damage during HAWT operation.

## References

1. Holmes, J. D. *Wind Loading of Structures* 3rd ed. (CRC Press, Boca Ratón, FL, 2015).
2. Moreau, R. *Air and Water: Trade Winds, Hurricanes, Gulf Stream, Tsunamis and Other Striking Phenomena* (Springer, Cham, Switzerland, 2017).
3. Simiu, E. & Yeo, D. *Wind Effects on Structures* 4th ed. (John Wiley & Sons, Chichester, UK, 2019).
4. Cermak, J. E., Davenport, A. G., Durgin, F. H., et al. *Wind Tunnel Studies of Buildings and Structures* (ed Isyumov, N.) *ASCE Manuals and Reports on Engineering Practice* **67** (ASCE, Reston, USA, 1999).
5. Holton, J. R. *An Introduction to Dynamic Meteorology* 4th ed. (eds Dmowska, R., Holton, J. R. & Rossby, H. T.) (Elsevier, San Diego, USA, 2004).
6. Kaimal, J. C. & J., F. J. *Atmospheric Boundary Layer Flows: Their Structure and Measurement* (Oxford University Press, New York, USA, 1994).
7. Lesieur, M. *Turbulence in Fluids* 4th ed. (ed Moreau, R.) (Springer, Dordrecht, Netherlands, 2008).
8. Tampieri, F. *Turbulence and Dispersion in the Planetary Boundary Layer* (Springer, Switzerland, 2017).
9. Wilcox, D. C. *Turbulence Modeling for CFD* 3rd ed. (DCW Industries, La Cañada, USA, 2006).
10. IEC. *Wind turbines – Part 1: Design requirements* 3rd ed. International Electrotechnical Commission (Geneva, Switzerland, 2005).
11. Von Kármán, T. Progress in the statistical theory of turbulence. *Proceedings of the National Academy of Sciences of the United States of America* **34**, 530–539 (1948).
12. Kaimal, J. C., Wyngaard, J. C., Izumi, Y. & Coté, O. R. Spectral characteristics of surface-layer turbulence. *Quarterly Journal of the Royal Meteorological Society* **98**, 563–589 (1972).
13. Burton, T., Jenkins, N., Sharpe, D. & Bossanyi, E. *Wind Energy Handbook* 2nd ed. ISBN: 978-0-470-69975-1 (John Wiley and Sons, Ltd., Chichester, UK, 2011).
14. Højstrup, J., Larsen, S. E. & Madsen, P. H. *Power Spectra of Horizontal Wind Components in the Neutral Atmospheric Surface Layer* in *Proc. 9th Symp. on Turbulence and Diffusion* (eds Jensen, N. O., Kristensen, L. & E., L. S.) (American Meteorological Society, Roskilde, Denmark, Apr. 1990), 305–308.
15. Harris, R. I. Some further thoughts on the spectrum of gustiness in strong winds. *Journal of Wind Engineering and Industrial Aerodynamics* **33**, 461–477. ISSN: 0167-6105 (1990). doi: 10.1016/0167-6105(90)90001-S.
16. Fitzpatrick, P. J. in (ed Wang, Y.) chap. Tropical Cyclones (CRC Press, Boca Ratón, USA, 2014). doi: 10.1081/E-ENRA-120047660.
17. Anthes, R. A. *Tropical Cyclones: Their Evolution, Structure and Effects Meteorological Monographs* **41** (American Meteorological Society, Boston, USA, 1982).
18. Dunnavan, G. M. & Diercks, J. W. An Analysis of Super Typhoon Tip (October 1979). *Monthly Weather Review* **108**, 1915–1923 (1980). doi: 10.1175/1520-0493(1980)108<1915:AAOSTT>2.0.CO;2.
19. FEMA. *Hazus Hurricane Model Technical Manual* Federal Emergency Management Agency (Mar. 2021).
20. Kantha, L. Time to replace the Saffir-Simpson hurricane scale? *Eos, Transactions American Geophysical Union* **87**, 3–6 (2006). doi: 10.1029/2006EO010003.

21. Simiu, E., Vickery, P. & Kareem, A. Relation between Saffir–Simpson Hurricane Scale Wind Speeds and Peak 3-s Gust Speeds over Open Terrain. *Journal of Structural Engineering* **133**, 1043–1045 (2007). doi: 10.1061/(ASCE)0733-9445(2007)133:7(1043).
22. Kepert, J. D. Observed boundary layer wind structure and balance in the hurricane core. Part I: Hurricane Georges. *Journal of the atmospheric sciences* **63**, 2169–2193 (2006). doi: 10.1175/JAS3745.1.
23. Kepert, J. D. Observed boundary layer wind structure and balance in the hurricane core. Part II: Hurricane Mitch. *Journal of the atmospheric sciences* **63**, 2194–2211 (2006). doi: 10.1175/JAS3746.1.
24. Vickery, P. J., Wadhera, D., Powell, M. D. & Chen, Y. A hurricane boundary layer and wind field model for use in engineering applications. *Journal of Applied Meteorology and Climatology* **48**, 381–405 (2009). doi: 10.1175/2008JAMC1841.1.
25. Kepert, J. The dynamics of boundary layer jets within the tropical cyclone core. Part I: Linear theory. *Journal of the Atmospheric Sciences* **58**, 2469–2484 (2001). doi: 10.1175/1520-0469(2001)058<2469:TDOBLJ>2.0.CO;2.
26. Kepert, J. & Wang, Y. The dynamics of boundary layer jets within the tropical cyclone core. Part II: Nonlinear enhancement. *Journal of the atmospheric sciences* **58**, 2485–2501 (2001). doi: 10.1175/1520-0469(2001)058<2485:TDOBLJ>2.0.CO;2.
27. Vogl, S. *Tropical Cyclone Boundary-Layer Models* PhD thesis (Ludwig-Maximilians-Universität München, Regensburg, Germany, May 2009). doi: 10.5282/edoc.10274.
28. Thompson, C. F. *Inertial Instability and Tropical Cyclogenesis* PhD thesis (University of Manchester, 2019).
29. Snaiki, R. & Wu, T. A semi-empirical model for mean wind velocity profile of landfalling hurricane boundary layers. *Journal of Wind Engineering and Industrial Aerodynamics* **180**, 249–261 (2018). doi: 10.1016/j.jweia.2018.08.004.
30. Li, L. *et al.* Turbulence spectra for boundary-layer winds in tropical cyclones: a conceptual framework and field measurements at coastlines. *Boundary-Layer Meteorology* **154**, 243–263 (2015). doi: 10.1007/s10546-014-9974-7.
31. Li, L., Kareem, A., Xiao, Y., Song, L. & Zhou, C. A comparative study of field measurements of the turbulence characteristics of typhoon and hurricane winds. *Journal of Wind Engineering and Industrial Aerodynamics* **140**, 49–66 (2015). doi: 10.1016/j.jweia.2014.12.008.
32. Bryan, G. H., Worsnop, R. P., Lundquist, J. K. & Zhang, J. A. A simple method for simulating wind profiles in the boundary layer of tropical cyclones. *Boundary-Layer Meteorology* **162**, 475–502 (2017). doi: 10.1007/s10546-016-0207-0.
33. Worsnop, R. P., Bryan, G. H., Lundquist, J. K. & Zhang, J. A. Using large-eddy simulations to define spectral and coherence characteristics of the hurricane boundary layer for wind-energy applications. *Boundary-Layer Meteorology* **165**, 55–86 (2017). doi: 10.1007/s10546-017-0266-x.
34. Ma, T. & Sun, C. Large eddy simulation of hurricane boundary layer turbulence and its application for power transmission system. *Journal of Wind Engineering and Industrial Aerodynamics* **210**, 104520 (2021). doi: 10.1016/j.jweia.2021.104520.
35. Yu, B., Chowdhury, A. G. & Masters, F. J. Hurricane wind power spectra, cospectra, and integral length scales. *Boundary-Layer Meteorology* **129**, 411–430 (2008). doi: 10.1007/s10546-008-9316-8.
36. Huang, P., Xie, W. & Gu, M. A comparative study of the wind characteristics of three typhoons based on stationary and nonstationary models. *Natural Hazards* **101**, 785–815 (2020). doi: 10.1007/s11069-020-03894-0.
37. Zhao, Z., Chan, P., Wu, N., Zhang, J. A. & Hon, K. Aircraft observations of turbulence characteristics in the tropical cyclone boundary layer. *Boundary-Layer Meteorology* **174**, 493–511 (2020). doi: 10.1007/s10546-019-00487-8.
38. Hansen, M. O. L. *Aerodynamics of Wind Turbines* 3rd ed. (Routledge, Abingdon, UK, 2015).

39. Hau, E. *Wind Turbines: Fundamentals, technologies, application, economics* 2nd ed. (Springer, Berlin, Germany, 2006).
40. Mikkelsen, R. F. *Actuator Disc Methods Applied to Wind Turbines* PhD thesis (Technical University of Denmark, Jan. 2004).
41. Hansen, M. O. L., Sørensen, J. N., Voutsinas, S., Sørensen, N. & Madsen, H. A. State of the art in wind turbine aerodynamics and aeroelasticity. *Progress in Aerospace Sciences* **42**, 285–330 (2006). doi: 10.1016/j.paerosci.2006.10.002.
42. Connell, J. R. *Turbulence Spectrum Observed by a Fast-Rotating Wind Turbine Blade* tech. rep. PNL-3426 (Pacific Northwest Laboratory, Richland, USA, June 1980).
43. Connell, J. R. The spectrum of wind speed fluctuations encountered by a rotating blade of a wind energy conversion system. *Solar Energy* **29**, 363–375 (1982). doi: 10.1016/0038-092X(82)90072-X.
44. Kristensen, L. & Frandsen, S. Model for power spectra of the blade of a wind turbine measured from the moving frame of reference. *Journal of Wind Engineering and Industrial Aerodynamics* **10**, 249–262 (1982). doi: 10.1016/0167-6105(82)90067-8.

[This page intentionally left blank]

## Chapter 3

# Structural response of wind turbines under cyclone-induced loads

The climatological classification commonly used in wind engineering for strong winds can be listed in three kinds of systems: (i) synoptic wind, i.e., wind flow product of atmospheric mechanisms of great scale, dominated by geostrophic wind, where the pressure forces in the atmosphere are balanced by with the Coriolis force; (ii) cyclonic tropical systems, which are the product of atmospheric phenomena of smaller scale than the synoptic winds, e.g., tropical cyclones, where the forces product of isobar curvature gain importance; and (iii) non-synoptic winds, which include a variety of atmospheric phenomena of even smaller scale, difficult to forecast, but capable of producing large wind intensities, e.g., tornadoes, thunderstorms, and downbursts, among others.<sup>1</sup>

This section presents an analysis concerning the second kind of wind phenomena listed: tropical cyclones, and their effects on wind turbine support structures. The wind field simulation described in this section is concordant with studies and measurements on the tropical cyclone phenomena. Moreover, two sites within Mexico are selected to perform the comparatives, where the wind hazard is considerably different, but nonexempt of the occurrence of tropical cyclones. The probability of failure on a benchmark wind turbine is also evaluated, as well as some dynamic-response factors for the support structure.

### 3.1 Wind turbine response from cyclone-induced loads

According to the 2017 Climate Science Special Report, extreme storms, like tropical cyclones, may increase in intensity due to rising sea temperatures. Notwithstanding, a poleward migration in the location of their peak intensities has been observed.<sup>2</sup> The former statement is concordant to theoretical and numerical analyses, for example, numerical simulations of landfalling tropical cyclones in the Yucatan Peninsula, which have indicated an increase in the frequency of intense events.<sup>3</sup> This implies that cyclonic events once considered 'rare' are becoming rather 'typical', thus, the response of vulnerable structures to such events needs to be assessed adequately and efficiently.

Current specifications for wind turbines provide no criteria for their design under tropical cyclones. The standard IEC 61400-1<sup>4</sup> states that turbines exposed to such conditions should be classified as 'Special', and the design values should be specified by the designer. Moreover, the growth of off- and onshore wind energy in cyclone-prone areas motivates the research on the topic, further encouraged by the catastrophic effects of cyclone-induced loads on wind turbine support structures.

A review of wind-turbine collapse cases presented by Ma et al.<sup>5</sup> stated that, among the extreme events evaluated in the review, typhoons represented the vast majority of collapses. Further, 'post mortem' analyses of collapse cases of wind turbines subjected to Category-IV winds have evinced that the

rotor plays an important role in the loads that act on the wind turbine support structure during the storm. Also, these analyses suggest that the fully-parked state of the turbine represents its most critical load condition during these kinds of events,<sup>6</sup> compared to other conditions such as idling-rotor position.

Diverse studies in the literature have focused on analyzing the structural response of — mainly offshore — wind turbines under tropical cyclones. Amirinia and Jung presented in two publications the analysis of the structural response of onshore, and offshore, wind turbines.<sup>7,8</sup> Their studies consisted of a comparison between the effects of the turbulence spectra proposed by Kaimal et al.,<sup>9</sup> Li et al.,<sup>10</sup> and Yu et al.<sup>11</sup> on the structural response of the turbine. According to the results from the work of Amirinia and Jung, the differences between the structural response computed from the different spectra showed values up to 6% for the support structure, and greater differences were found for the blade responses. Moreover, they stated that the recommendations for wind turbine support structures from the IEC standards resulted conservative for some cases, and underestimated the structure capacity for others. This statement was based on the comparison of the fittings performed for different probability distributions on the evaluated response maxima.

Hallowell et al.<sup>12</sup> developed a risk assessment for offshore wind turbines from fragility analyses that considered the action of wind and wave, using the compression stresses in the tower and monopile support structures as demand parameters. The risk assessment considered wind farm locations along the Atlantic coast of the United States. Their analyses assumed idling rotor conditions, and two possible yaw orientations: (i) with the rotor facing directly to the wind, and (ii) with a yaw error of 35°. The structural response was evaluated in FAST,<sup>13</sup> from the Kaimal turbulence spectrum for wind actions,<sup>9</sup> and the JONSWAP spectrum for wave actions.<sup>14</sup>

Due to the intricate nature of turbulence, further complicated during tropical cyclones,<sup>15,16</sup> the wind field is an important issue to attend when analyzing the dynamic structural response of any wind-sensitive system. To overcome the empirical limitations of common turbulence-spectra models, the use of computational fluid dynamics becomes a feasible option when sufficient computer power is an available resource. For example, the development of large eddy simulations (LES) has been used to study the turbulence characteristics of tropical cyclone flow fields.<sup>17-19</sup> In that context, Kapoor et al.<sup>20</sup> performed the structural analysis of a benchmark reference 10-MW offshore wind turbine, where a Category-V hurricane wind field was simulated by means of an LES. The turbulent field characteristics at different storm radii were loaded to the turbulence simulator TurbSim,<sup>21</sup> and the structural response of the turbine was computed in FAST.<sup>13</sup> From the analyses performed by Kapoor et al.,<sup>20</sup> gust factors greater than 1.7 were found, as well as extremely large values of structural responses, like blade deflections and bending moments.

Notwithstanding the relevance and novelties achieved from the studies summarized above, some limitations are still found: (i) Only wind turbine models analyzed from LES account for a complete tropical cyclone wind field. However, LES can be computationally expensive and can be made even more expensive when the phenomenon under analysis (e.g., tropical cyclones) demands large control volumes as well as small time steps and grid refinement. (ii) Most of the structural analyses found in the literature accounting for extreme-event analysis of wind turbines are performed in FAST, which is a tool meant for elastic analyses only. Non-linear analyses that account for fluid-structure interaction (FSI) can gain valuable information on the structural behavior of wind turbines. The more complete approach would be developing integrated computational fluid dynamics and finite element analysis (FEA) models. Nevertheless, these can also be computationally expensive. Therefore, a first step to overcome this limitation is the development of a methodology to achieve computationally economical structural analyses accounting for FSI, thus the non-linear structural response of wind turbines can be further investigated subsequently. (iii) In the literature survey performed, few recent studies were found concerning the structural analysis of tropical cyclone actions on onshore wind turbines. This is justified by the fact that offshore wind energy is expected to expand largely in the next decades.

However, the onshore wind potential in tropical regions is still large, and still with lower costs of generation compared to offshore wind energy.<sup>22</sup> Thus, the structural behavior of onshore wind turbine structures also needs to be addressed properly to continue the exploitation of wind potential.

## 3.2 Wind field simulation

Two sites prone to the occurrence of tropical cyclones have been selected for the evaluation of the structural response of a reference horizontal axis wind turbine (HAWT) in this case study. The first one corresponds to a site in the Mexican state of Oaxaca, which holds the greater part of the installed HAWTs in that country, and is exposed to cyclones from the Pacific basin. The second site is assumed in the Yucatan Peninsula, which is a site of great wind potential, both for onshore and offshore wind energy, and is exposed to cyclonic events from the Atlantic basin. Notwithstanding that both sites are prone to the occurrence of tropical cyclones, the wind hazard is dissimilar between them. The Pacific basin displays a greater yearly occurrence of tropical cyclones, and the landfalling storms generated in that basin impact more frequently in northern states of the western Mexican coasts; whereas the Atlantic basin shows less cyclogenesis, but it is prone to events of greater intensity.<sup>3,23</sup> The relevance of the site selection, as will be explained ahead, lies in the fact that the mean speed profile from tropical cyclones depends on the latitude of the site.

Several wind field simulations are performed. For that purpose, the determination of tropical-cyclone parameters is accomplished by means of Monte Carlo simulations. Empirical models to determine such parameters are used when these are available, and the marginal probability distribution function (PDF) of other storm parameters is assumed based on studies and observations. Moreover, the turbulence spectra and coherence function are derived from studies of the tropical cyclone wind field. The following subsections detail the necessary deductions, assumptions, and their implications.

### 3.2.1 The Tropical Cyclone Boundary Layer

The supergradient wind is one of the features of the tropical cyclone boundary layer (TCBL). This feature is capable of displaying differences of magnitude that can be important for tall structures, compared to the wind speed profile from the geostrophic wind approximation. Snaiki and Wu presented a semi-empirical model for the mean speed profile in the TCBL, based on the data from the Weather Surveillance Radar-1988 Doppler network and from GPS dropsondes.<sup>24</sup> A mathematical expression for the logarithmic mean wind speed profile, as well as for the power-law expression, was proposed in their work. For this case study, the latter will be used. According to Snaiki and Wu,<sup>24</sup> the expression of the power-law mean wind speed profile during a tropical cyclone is given by:

$$\bar{U}(z) = \bar{U}(10) \left[ \left( \frac{z}{10} \right)^\alpha + \eta_1 \sin \left( \frac{z}{\delta} \right) \exp \left( -\frac{z}{\delta} \right) \right] \quad (3.1)$$

where  $\bar{U}$  is the mean wind speed in the longitudinal direction, as a function of height  $z$ .  $\bar{U}(10)$  represents the mean speed at  $z = 10$  m, and  $\alpha$  is the exponent that defines the variation of mean wind speed with height. In Equation 3.1,  $\delta$  is the height of maximum wind speed  $v_m$ , and  $\eta_1$  is a constant determined by the condition  $\partial \bar{U} / \partial z|_{z=\delta} = 0$ , presented by Snaiki and Wu as<sup>24</sup>:

$$\eta_1 = \frac{(\delta/10)^\alpha \alpha e}{\sin(1) - \cos(1)} \quad (3.2)$$

The height of maximum winds  $\delta$  can be estimated from the model proposed in the same reference<sup>24</sup>:

$$\ln(\delta) = a_\delta \ln(I) + b_\delta \ln(Ro_s) + c_\delta \quad (3.3)$$

where  $a_\delta, b_\delta, c_\delta$  are constants equal to -0.2452, -0.05, and 5.6149, respectively (these values are the ones

suggested for the data from radar observations, for data from the dropsondes the values are -0.487, -0.05, and 4.0221, respectively<sup>24</sup>). In Equation 3.3,  $Ro_s$  and  $I$  are, respectively, the modified surface Rossby number and the inertial stability, defined as:

$$Ro_s = \frac{v_g}{Iz_0} \quad (3.4)$$

$$I = \sqrt{\left(f_c + \frac{2v_g}{r}\right) \left(f_c + \frac{v_g}{r} + \frac{\partial v_g}{\partial r}\right)} \quad (3.5)$$

Recalling variables that appear in Equations 3.4 and 3.5,  $f_c$  is the Coriolis parameter,  $r$  is the radial position with respect to the center of the storm,  $z_0$  is the surface roughness, and  $v_g$  is the gradient wind, which can be expressed for cyclonic movement from Equation 2.1 as:

$$v_g = -\frac{|f_c|r}{2} + \sqrt{\frac{(f_c r)^2}{4} + \frac{r}{\rho} \left| \frac{\partial p_s}{\partial r} \right|} \quad (3.6)$$

where  $p_s$  is the surface pressure, and  $\rho$  is the air density. The derivative of Equation 3.6 with respect to the storm radius can be expressed as:

$$\frac{\partial v_g}{\partial r} = -\frac{|f_c|}{2} + \frac{\frac{f_c^2 r}{4} + \frac{1}{2\rho} \left| \frac{\partial p_s}{\partial r} \right| + \frac{r}{2\rho} \frac{d}{dr} \left| \frac{\partial p_s}{\partial r} \right|}{\sqrt{\frac{(f_c r)^2}{4} + \frac{r}{\rho} \left| \frac{\partial p_s}{\partial r} \right|}} \quad (3.7)$$

From Equations 3.6 and 3.7, the need for an expression that describes the surface pressure  $p_s$  as a function of the storm radius becomes evident. Thus, the widely employed model proposed and revised by Holland et al.<sup>25</sup> can be adopted, which states the following form:

$$p_s = p_{cs} + \Delta p_s \exp \left[ - \left( \frac{r_{v_m}}{r} \right)^b \right] \quad (3.8)$$

where  $\Delta p_s$  is the pressure difference between the outermost closed isobar and the storm center, i.e., the *central pressure deficit*. The exponent  $b$  is a scaling parameter that defines the pressure gradient near the radius of maximum wind  $r_{v_m}$ . Regarding Equation 3.8,  $\partial p_s / \partial r$  and  $d|\partial p_s / \partial r| / dr$  are expressed as:

$$\frac{\partial p_s}{\partial r} = \frac{\Delta p_s b}{r} \left( \frac{r_{v_m}}{r} \right)^b \exp \left[ - \left( \frac{r_{v_m}}{r} \right)^b \right] \quad (3.9)$$

$$\frac{d}{dr} \left| \frac{\partial p_s}{\partial r} \right| = \frac{1}{\left| \frac{\partial p_s}{\partial r} \right|} \left( \frac{\partial p_s}{\partial r} \right)^2 \frac{1}{r} \left[ b \left( \frac{r_{v_m}}{r} \right)^b - b - 1 \right] \quad (3.10)$$

The determination of the Holland's scale parameter  $b$ , as well as the expected radius of maximum winds on a hypothetical storm, can be performed from the statistical models developed by Vickery and Wadhwa,<sup>26</sup> which were estimated from databases of measurements from hurricanes in the Atlantic Ocean and the Gulf of Mexico. The selected models from those studies correspond to the expressions:

$$b = 1.833 - 0.326 \sqrt{f_c r_{v_m}} \quad (3.11)$$

$$\ln(r_{v_m}) = 3.015 - 6.291 \times 10^{-5} \Delta p_s^2 + 0.0037 \phi \quad (3.12)$$



where  $\phi$  represents the latitude angle. The models presented in Equations 3.11 and 3.12 have reported standard deviations of  $\sigma_b = 0.221$ ; and  $\sigma_{\ln(r_{vm})} = 0.448$ , for  $\Delta p_s \leq 87$  hPa, values of  $\sigma_{\ln(r_{vm})} = 1.137 - 0.00792\Delta p_s$  for  $87 \text{ hPa} < \Delta p_s \leq 120$  hPa, and  $\sigma_{\ln(r_{vm})} = 0.186$  for  $\Delta p_s > 120$  hPa. Moreover, it is important to remark that Equation 3.11 assumes that  $r_{vm}$  is introduced in meters, whereas  $r_{vm}$  is given in km in Equation 3.12, according to the original publication.<sup>26</sup>

The importance of the pressure deficit  $\Delta p_s$  as one of the parameters that determine the intensity of the storm is remarked, and its magnitude needs to be properly associated with other storm parameters. Values of  $\Delta p_s$  are reported in many studies regarding tropical cyclones. However, its dependency on other intensity measures of the storm is by no means a straightforward deduction. Some studies have centered on its relation with other intensity parameters, like near-surface wind speed,<sup>27,28</sup> and also empirical models have been proposed to estimate its decay once a tropical cyclone has made landfall.<sup>29</sup> However, an alternative approach that allows its inclusion in the wind field simulation without the need for elaborate models or information on the storm is described next.

As presented in Table 2.1, the central pressure is also a measure of tropical cyclone intensity, and a classification of the storm in the Saffir-Simpson scale can be performed from such a value. Therefore,  $\Delta p_s$  can be determined from the central pressure ranges listed in Table 2.1 and the value of the far-field surface pressure, i.e., the standard atmospheric pressure at sea level ( $\sim 1013$  hPa). This simplification can be adopted in case there is no available information on the value of the surface pressure at the outermost isobar. This assumption has also been made in other studies, e.g., by Georgiou et al.,<sup>30</sup> and by Vickery.<sup>29</sup> Thus, by subtracting the values of  $p_{cs}$  reported in Table 2.1 to 1013, i.e.,  $\Delta p_s = 1013 - p_{cs}$ , ranges of  $\Delta p_s$  can be determined according to a cyclone classification, and can also be associated with other intensity measures of the storm. Moreover, as studied by Georgiou et al.,<sup>30</sup> the marginal random behavior of  $\Delta p_s$  can be characterized by a Weibull probability distribution. The lognormal distribution has also been found to represent fairly the random behavior of  $\Delta p_s$ .<sup>30,31</sup> The former is determined by a scale parameter  $C$ , and a shape parameter  $k$ ; whereas the latter is characterized by the parameters  $\mu$ , and  $\sigma$ . That is, the cumulative distribution function (CDF) of  $\Delta p_s$  can be expressed from the aforementioned distributions, respectively, as:

$$F(\Delta p_s|C, k) = 1 - \exp \left[ - \left( \frac{\Delta p_s}{C} \right)^k \right] \quad (3.13a)$$

$$F(\Delta p_s|\mu, \sigma) = \Phi \left[ \frac{\ln(\Delta p_s) - \mu}{\sigma} \right] \quad (3.13b)$$

where  $\Phi(\cdot)$  represents the standard-normal CDF. With this in mind, by assuming that the minimum ( $\Delta \check{p}_s$ ) and maximum ( $\Delta \hat{p}_s$ ) values computed for  $\Delta p_s$  from Table 2.1 represent two values of probability, say,  $P_1$  and  $P_2$ , respectively, the distribution parameters for a Weibull-distributed  $\Delta p_s$  can be estimated as:

$$C = \frac{\Delta \check{p}_s}{-\ln(1 - P_1)^{1/k}} = \frac{\Delta \hat{p}_s}{-\ln(1 - P_2)^{1/k}} \quad (3.14)$$

$$k = \frac{\ln[\ln(P_1)/\ln(P_2)]}{\ln(\Delta \hat{p}_s/\Delta \check{p}_s)} \quad (3.15)$$

Analogously, the distribution parameters for a lognormal-distributed  $\Delta p_s$  can be estimated as:

$$\mu = \frac{\ln(\Delta \check{p}_s) - \ln(\Delta \hat{p}_s) \frac{\Phi^{-1}(P_1)}{\Phi^{-1}(P_2)}}{1 - \frac{\Phi^{-1}(P_1)}{\Phi^{-1}(P_2)}} \quad (3.16)$$

$$\sigma = \frac{\ln(\Delta\check{p}_s) - \mu}{\Phi^{-1}(P_1)} = \frac{\ln(\Delta\hat{p}_s) - \mu}{\Phi^{-1}(P_2)} \quad (3.17)$$

Thus, if the values of  $P_1$  and  $P_2$  are assumed to be (for example), respectively, 0.05 and 0.95, the corresponding parameters for the distribution of  $\Delta p_s$  result as summarized in Table 3.1.

**Table 3.1:** Pressure differences deduced for the Saffir-Simpson classification of tropical cyclones, and their distribution parameters

Category	$\Delta p_s$ [hPa]	Maximum Gust Speed	Weibull parameters		Lognormal parameters	
		(Over Land, $z_0 = 0.03$ m) [m/s]	C [hPa]	$k$ [-]	$\mu$ [-]	$\sigma$ [-]
TD <sup>a</sup>	6.0 - 7.0	< 18.6	6.7149	26.386	1.8688	0.047
TS <sup>b</sup>	14.0 - 18.0	18.6 - 36.8	16.8202	16.184	2.7647	0.076
I <sup>c</sup>	24.0 - 33.0	36.8 - 48.1	30.2835	12.772	3.3372	0.097
II	34.0 - 48.0	48.1 - 58.1	43.7363	11.795	3.6988	0.105
III	49.0 - 68.0	58.1 - 69.7	62.2472	12.412	4.0557	0.100
IV	69.0 - 93.0	69.7 - 85.5	85.8052	13.626	4.3834	0.091
V <sup>d</sup>	94.0 - 123.0	> 85.5	114.3942	15.127	4.6777	0.082

<sup>a</sup> A range of 1006-1007 hPa was assumed for  $p_{cs}$  to approximate the value presented by Kantha.<sup>32</sup>

<sup>b</sup> A range of 995-999 hPa was assumed for  $p_{cs}$  to satisfy the condition  $p_{cs} < 1000$  hPa.<sup>32</sup>

<sup>c</sup> A range of 980-989 hPa was assumed for  $p_{cs}$  to satisfy the condition  $p_{cs} \geq 980$  hPa.<sup>33</sup>

<sup>d</sup> A range of 890-919 hPa was assumed for  $p_{cs}$  to satisfy the condition  $p_{cs} < 920$  hPa.<sup>33</sup>

The distribution parameters presented in Table 3.1 assume that 90% of the tropical cyclones that classify within a certain category will display values of  $\Delta p_s$  within the proposed boundaries. Therefore, some implications from this assumption must be pointed out regarding the values presented in Table 3.1: (i) At the categories of lower intensities, values of  $p_{cs}$  had to be assumed in order to satisfy the magnitudes of the storm parameters indicated in the literature. (ii) The maximum value of the pressure difference assumed in Table 3.1 is of the order of the maximum pressure differences reported in noted references, e.g., Vickery and Wadhera.<sup>26</sup> Nevertheless, historical data indicates that greater pressure differences might be observed.<sup>34</sup> That is, statistical verification of these assumptions from a large database of hurricane observations remains a task for further studies.

It is possible to develop simulations of mean speed profiles displaying characteristics of the TCBL at a specific site by means of the presented models and deductions. For that purpose, the probability parameters of the pressure deficit distribution allow accounting for the variability in that parameter. The models for  $r_{vm}$ , and  $b$ , also serve that purpose. This is insofar since the uncertainty from those models was reported in the original reference,<sup>26</sup> and their errors can be assumed as normally-distributed random variables of zero means and standard deviations  $\sigma_{\ln(r_{vm})}$ , and  $\sigma_b$ , respectively. Uncertainty in the model describing the height of maximum winds  $\delta$  was omitted by their authors.<sup>24</sup> However, the random behavior of wind speed can be captured adequately from the uncertainties reported in the employed models.

### 3.2.2 Turbulence in the TCBL

A consensus on the characterization of turbulence during tropical cyclones is yet to be reached. However, relevant field and numerical studies continue to provide insight into this phenomenon. In this case study, the criteria adopted for the turbulent characterization of the wind field attend recent recommendations derived from studies based on numerical simulations of the TCBL. On that matter, Worsnop et al.<sup>18</sup> have proposed modifications to the parameters that characterize the functional form of the Kaimal turbulence spectrum as proposed in the IEC 61400-1.<sup>4</sup> According to this standard, the conventional Kaimal spectrum, and the suggested coherence function, are respectively represented by:

$$\frac{nS_i(z, n)}{\sigma_i^2} = \frac{A_K n L_{i,K} / \bar{U}}{[B_K + C_K n L_{i,K} / \bar{U}]^{5/3}} \quad (3.18)$$

$$\text{Coh}(s, n) = \exp \left[ -A_c \sqrt{(ns/\bar{U})^2 + (B_c s / 8.1 \Lambda_1)^2} \right] \quad (3.19)$$

where the sub-index  $i$  stands for the turbulent components  $u$ ,  $v$ , or  $w$ , and  $A_K = 4$ ,  $B_K = 1$ , and  $C_K = 6$  in the Kaimal turbulence model suggested by the IEC standard.<sup>4</sup> In Equation 3.19,  $s$  is the separation distance normal to the along-wind direction between two points in space, whereas  $A_c$  and  $B_c$  are given values of 12 and 0.12, respectively.

In their publication, Worsnop et al.<sup>18</sup> estimated the values of  $A_K$ ,  $B_K$ , and  $C_K$  from LESs of tropical-cyclone wind flows. The adjusted values correspond to Tropical-Storm, Category-I, and Category-IV winds. Nevertheless, they give recommended values of  $A_K$ ,  $B_K$ , and  $C_K$ , for all cyclone categories, which correspond to values of 8.7, 2, and 6, respectively. Moreover, they also estimate the values of  $A_c$  and  $B_c$  for the same storm categories. However, the values presented in the original publication vary as a function of the spatial separation  $s$ . Individual values of  $A_c$  and  $B_c$  are reported for each particular storm category and evaluated spatial separation. Nonetheless, a general recommendation is omitted, resulting in limitations for the implementation of the estimated values presented in their work. Notwithstanding, based on the original values reported by Worsnop et al.,<sup>18</sup> the following functional forms are proposed in this work for the coherence coefficients of Equation 3.19:

$$A_c = 0.2047s + 0.5339 \quad (3.20)$$

$$B_c = 0.2585 \exp(-0.05146s) \quad (3.21)$$

Equations 3.20 and 3.21 have been estimated from the values reported by Worsnop et al.,<sup>18</sup> and they have been validated by comparing the resulting coherence values against the ones displayed in the original publication for different radial positions and wind speeds. The comparisons gave very resemblant results.

According to Worsnop et al.,<sup>18</sup> the coherence model as suggested in the IEC 61400-1<sup>4</sup> tends to underpredict the coherence values during tropical cyclones at most of the frequencies and separations evaluated in their work. This is because the coherence values decay too promptly in the standard coherence expression, compared to the observed coherence from their simulations. In the original reference,<sup>18</sup> this has been attributed to the structure of the TCBL. Figure 3.1 displays a comparison between the turbulence spectra computed with the conventional parameters suggested in the IEC 61400-1,<sup>4</sup> and the ones suggested for the tropical cyclone wind field.<sup>18</sup> A comparison between the coherence function from the standard model, and the one adjusted as proposed in this work is also displayed.

The cases presented in Figure 3.1 assume a reference wind speed of 50 m/s at a height of 90 m, and a turbulence intensity  $I_u = 0.18$ . From the figure, it can be observed a shift toward high frequencies in the cyclone turbulence spectra, as well as higher spectral ordinates. Further, higher coherence values at all the evaluated frequencies are displayed. These features are consistent with TCBL studies from LES<sup>19</sup> and have also been observed in other studies on the topic centered on field measurements.<sup>10</sup>

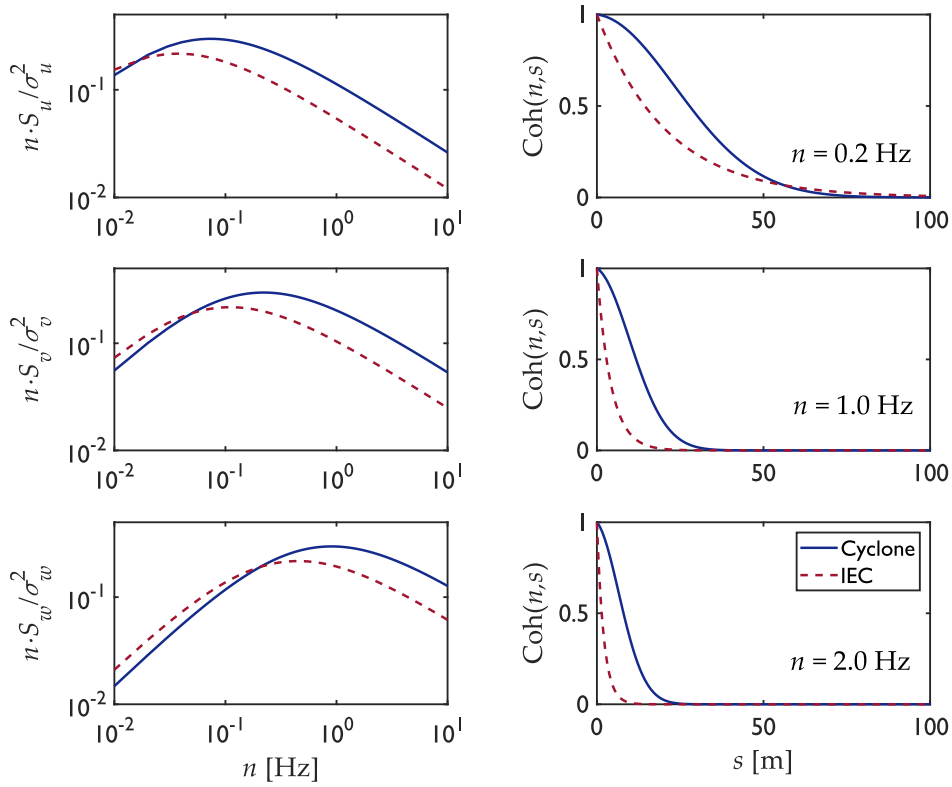


**Figure 3.1:** Comparison between tropical cyclone turbulence field and conventional values (Left: normalized turbulence spectra, Right: coherence values)

### 3.2.3 Simulations

As mentioned at the beginning of the section, two sites with different tropical cyclone hazard have been selected to evaluate the structural response and reliability of a reference wind turbine. The sites correspond to hypothetical locations in the Mexican state of Oaxaca and the Yucatan peninsula. For the former, a latitude angle  $\phi = 16.720^\circ$  was assumed, whereas for the latter  $\phi = 21.130^\circ$ . The latitude coordinate plays a consequential role in the estimation of the wind speed profile during a tropical cyclone, as summarized in Section 3.2.1. Moreover, according to the Manual of Civil Works<sup>35</sup> of the Mexican Federal Electricity Commission (CFE), the 3-s gust mean wind speed at 10-m height for the selected sites is 41.91 and 59.17 m/s, respectively, for a 200-year return period (as specified for wind turbines in the aforementioned reference).

According to Tables 2.1 and 3.1, the gust wind speeds for the two selected sites correspond to tropical cyclones classified as Hurricane Category I, and Hurricane Category III, for the site at Oaxaca, and the Yucatan site, respectively. A gust factor of 1.425 can be applied to those wind speeds to represent a 10-min averaged wind speed, i.e.,  $\bar{U}_3 = 1.425\bar{U}_{600}$  (where the sub-indexes indicate the averaging time in seconds). Therefore, the 10-min mean wind speed values for the Oaxaca, and Yucatan sites are, respectively, 29.42 and 41.54 m/s. The gust-factor value has been determined from the Durst plot presented in the CFE standard.<sup>35</sup> However, it is also consistent with mean values reported from field measurements of typhoons and hurricanes for various cyclone categories, as well as for various terrain roughness lengths.<sup>15</sup> In this regard, the terrain category assumed to define the mean wind speed profile is considered as open terrain for both sites. This implies that, according to the CFE standard,<sup>35</sup> a power-law exponent  $\alpha = 0.14$  must be assumed to define the variation of the 10-min mean wind speed with height. This value of  $\alpha$  is slightly superior to the 0.11 value suggested in the IEC 61400-1 for the extreme turbulence model.<sup>4</sup> Nonetheless, the greater variation in the simulated mean speed

profile is the product of the supergradient wind model of the TCBL. Moreover, a turbulence intensity  $I_u = 18\%$  was assumed for the two sites, which is also slightly superior to the 16% value suggested as a reference in the IEC standard. However, as defined in the same standard, its reference values are unintended for tropical cyclone wind intensities, thus a greater value is used for this case study. Table 3.2 summarizes the mean wind speed and terrain parameters assumed for the wind field simulations at the two sites.

**Table 3.2:** Mean wind speed and turbulence parameters for flow-field simulations

Site	$\phi$ [°]	$\bar{U}_{600}(10)$ [m/s]	$\alpha$ [-]	$z_0$ [m]	$I_u$ [-]
Oaxaca	16.720	29.420	0.14	0.02	0.18
Yucatan	21.130	41.537	0.14	0.02	0.18

From the values summarized in Table 3.2, and from the equations presented in Subsections 3.2.1 and 3.2.2, a set of 50 three-dimensional wind field simulations was performed for each site by means of the spectral representation method.<sup>36</sup> To simulate the wind speed intensity concordant to the TCBL, a Weibull distribution was assumed for the central pressure deficit. 50 Monte Carlo simulations for each site were performed to avail of a different value of  $\Delta p_s$  in each analysis. Analogously, a radial position from the center of the storm was assumed as a uniformly-distributed random variable in each simulation, covering a range of values [0, 200] in km. The rest of the parameters were also computed by means of Monte Carlo simulations, adding a random error to the estimated values from their respective models. The random errors were assumed as normal variables of zero mean, and standard deviation equal to the uncertainty reported in each model. These criteria imply that each wind field simulation accounts for different positions with respect to the center of the storm and, therefore, also different mean wind speed profiles. Figure 3.2 displays the simulated values of the parameters that characterize the tropical cyclone wind field, according to the models employed for the purpose of the simulation. The resultant mean speed profiles simulated for each site are also included. A comparison with the conventional synoptic power-law mean speed profile is included as a reference.

From Figure 3.2 some observations originate: (i) for both sites, the height of maximum winds  $\delta$  occurs at altitudes superior to 500 m. Further, the value of  $\delta$  tends to increase outward the radial position with respect to the center of the storm. This implies greater wind speed intensity for structures near the storm center. (ii) A parameter that can give a direct notion of the intensity of the tropical cyclone is the central pressure deficit  $\Delta p_s$ . This parameter displays greater values for the Category III simulation (i.e., the Yucatan site). This is caused by the assumptions of the probable values of  $\Delta p_s$ . (iii) Regarding the magnitude of  $r_{v_m}$ , overall greater values are observed for the Category I simulations (i.e., the Oaxaca site). This is concordant with the coefficients of Equation 3.12, which implies an inversely proportional relation between  $r_{v_m}$  and  $\Delta p_s$ . This behavior is reasonable since a more-intense tropical cyclone is expected to display greater wind intensity nearer the center of the storm. (iv) Lastly, from the mean speed profiles displayed in Figure 3.2, a greater structural response can be anticipated from the tropical cyclone simulations than from a synoptic-wind assumption analysis. This also represents considerable load effects for high-rise structures. However, the variability of the dynamic structural response is yet to be studied.

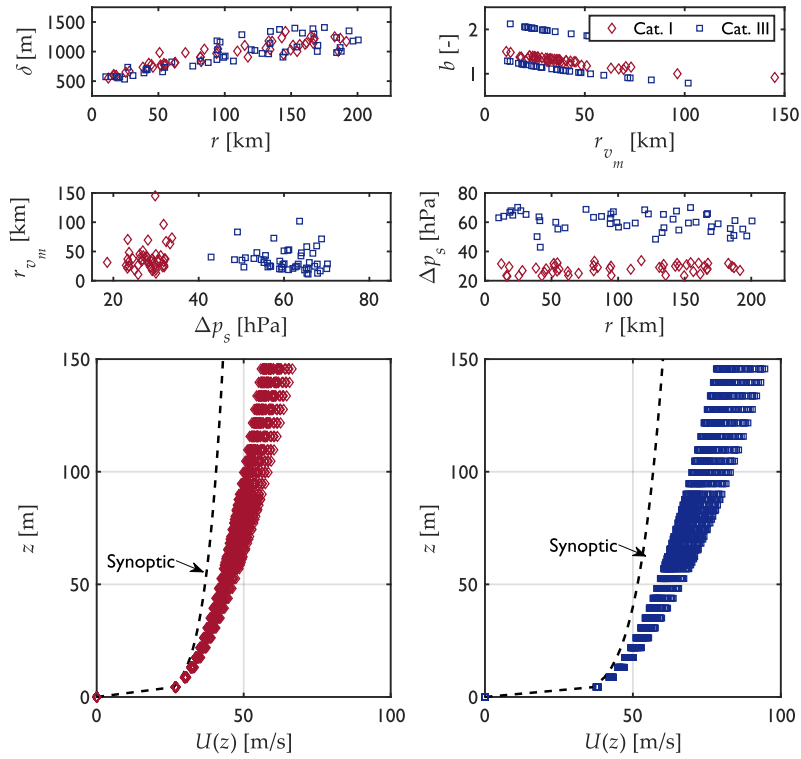


Figure 3.2: Simulated tropical cyclone parameters and mean speed profiles for the two selected sites

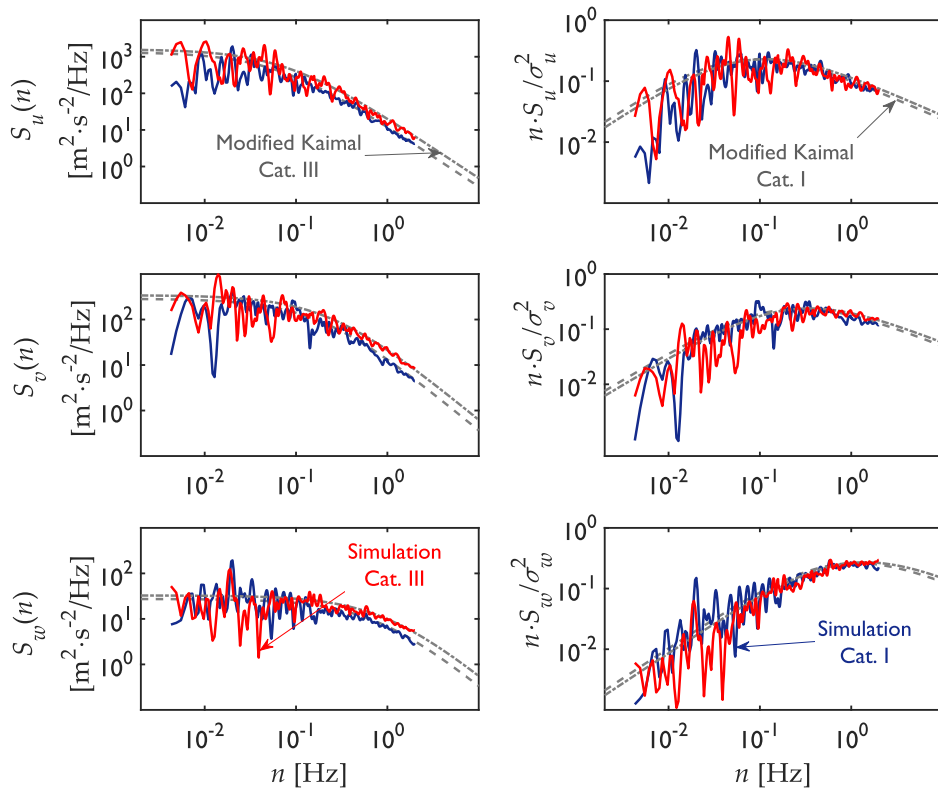


Figure 3.3: Turbulence spectra from the wind field simulations, for a height  $z = 150$  m

A sampling frequency of 10 Hz was employed to perform the stochastic wind field simulations, whereas the total length of each signal was set to 630 s. This is insofar as the structural-response signals will be trimmed to avoid the inclusion of numerical inaccuracies at the start of the analyses. Thus, the final response signals are intended to be 10-min long. For the two selected sites, and the total number of simulations, the Modified Kaimal spectra were employed (Equation 3.18, with the adjusted TCBL coefficients<sup>18</sup>). Equation 3.19 was used to model the spatial coherence among the signals, employing the coherence coefficients presented in Equations 3.20 and 3.21. The spatial distribution of points in the three-dimensional wind field simulation is taken according to the coordinates of the structural model of the selected HAWT for the analysis (described in Section 3.3). Figure 3.3 presents the turbulence spectra for one of the three-dimensional simulations at a point with  $z = 150$  m, for each of the two selected sites. A fair approximation in the distribution of turbulent energy is appreciated from the spectra, which suggests that the wind field simulations successfully represent the employed models.

### 3.3 Model description

Many of the structural analyses of wind turbines are performed on specialized aero-servo-hydro-elastic software. Notwithstanding the flexibility allowed by those codes, which enable many possibilities of standard analyses, a fair degree of programming skills is needed to develop different analyses under non-conventional load conditions. Different alternatives to solve the problem of analyzing a HAWT structure under a specific wind field condition are, for example, the coupled analyses from computational fluid dynamics with finite element analysis (FEA). However, such approaches require higher computational costs and are still encumbered with assumptions in the modeling of the flow field, as well as the FSI. This section describes a practical alternative to perform the aeroelastic analysis of a HAWT under the cyclone flow field. The analyses are performed in a commercial FEA software, which is a powerful and versatile tool.

A finite element model (FEM) of the benchmark NREL 5 MW wind turbine<sup>37</sup> was developed in the FEA software ANSYS.<sup>38</sup> The general description of the turbine, and the developed FEM, are detailed in this section. The employed criteria for the aeroelastic analysis are also described.

#### 3.3.1 Description of the turbine

The 5-MW reference wind turbine of the National Renewable Energy Laboratory (NREL) is a complete structural and servo-mechanical conceptual model HAWT developed to enable the research and technological studies of offshore wind energy.<sup>37</sup> It is widely used in wind-energy-related research for offshore analyses, and also to analyze HAWTs in onshore conditions. It is a conventional three-blade HAWT that operates in upwind conditions, and its dimensions and characteristics are based on real data from commercial wind turbines and technical tendencies from its time. The main general characteristics that describe the structure of the 5-MW reference HAWT are summarized in Table 3.3.

##### *Blade's description*

The blades are the more aerodynamically complex elements in a wind turbine. The geometric configuration and characteristics of these elements are intended to extract the greatest-possible kinetic energy from the wind stream. This is done by means of the lift force generated on the blades during the diverse operation conditions of the turbine. Thus, the geometrical configuration of these elements governs the aerodynamic forces on the structure of the HAWT during operation conditions, as well as contributes when the turbine is parked and it needs to withstand extreme-wind events.<sup>6</sup>

The blades of the 5-MW reference wind turbine are composited from six different airfoils at the outer span of the blade, which transition to a circular section at its root, i.e., at the hub connection. The aerodynamic profiles that characterize the blade of the reference wind turbine are summarized in Table 3.4. The default pitch angle  $\beta$  of the blade section, and its chord  $c$ , at diverse radial stations

**Table 3.3:** General properties of the NREL 5-MW Baseline HAWT

Rated power	5.0 MW
Number of blades	3
Rotor diameter	126.0 m
Hub diameter	3.0 m
Hub height	90.0 m
Tower height	87.6 m
Cut-in wind speed	3.0 m/s
Rated wind speed	11.4 m/s
Cut-out wind speed	25.0 m/s
Rated rotor speed	12.1 rpm
Shaft tilt angle	5.0°
Precone angle	2.5°
Rotor mass	110,000.0 kg
Nacelle mass	240,000.0 kg
Tower mass	347,460.0 kg

are also presented. In Table 3.4, the variable  $r$  stands for the radial coordinate at the blade span, by no means it must be confused with the radial position in a tropical cyclone wind field.

**Table 3.4:** Distribution of the aerodynamic properties of the blade for the 5-MW reference wind turbine

$r$ (m)	$\beta$ (°)	$c$ (m)	Airfoil
03.00	13.308	3.542	circular
08.33	13.308	4.167	circular
11.75	13.308	4.557	DU40-A17
18.85	11.480	4.652	DU35-A17
24.05	09.011	4.249	DU30-A17
32.25	06.544	3.748	DU25-A17
36.35	05.361	3.502	DU21-A17
44.55	03.125	3.010	NACA 64-618
62.00	00.150	1.400	NACA 64-618

The different airfoils that form the blades display different aerodynamic-force coefficients for lift ( $C_L$ ), drag ( $C_D$ ), and moment ( $C_M$ ). How these static coefficients vary with respect to the angle of attack  $\alpha$  is displayed in Figure 3.4. The angle of attack  $\alpha$  of the blade is measured from its chord axis and, in this context, it must be distinguished from the power-law exponent that describes the wind speed variation with height. Moreover, in the case of the circular profiles, a value for  $C_D = 1.0$  is assumed, whereas the lift and moment coefficients are assumed null for circular sections.

### 3.3.2 Structural model

A FEM was developed in the ANSYS parametric design language (APDL) to analyze the selected reference wind turbine. Since an intricate model would imply futile computing time expense, given the compendious nature of the selected HAWT, a model with gratuitous features was avoided. The developed model consisted mainly of beam and lumped-mass elements. How these elements were configured is described in the following, as well as a comparison of the realized dynamic properties of the structure with the ones reported in the original reference.<sup>37</sup>



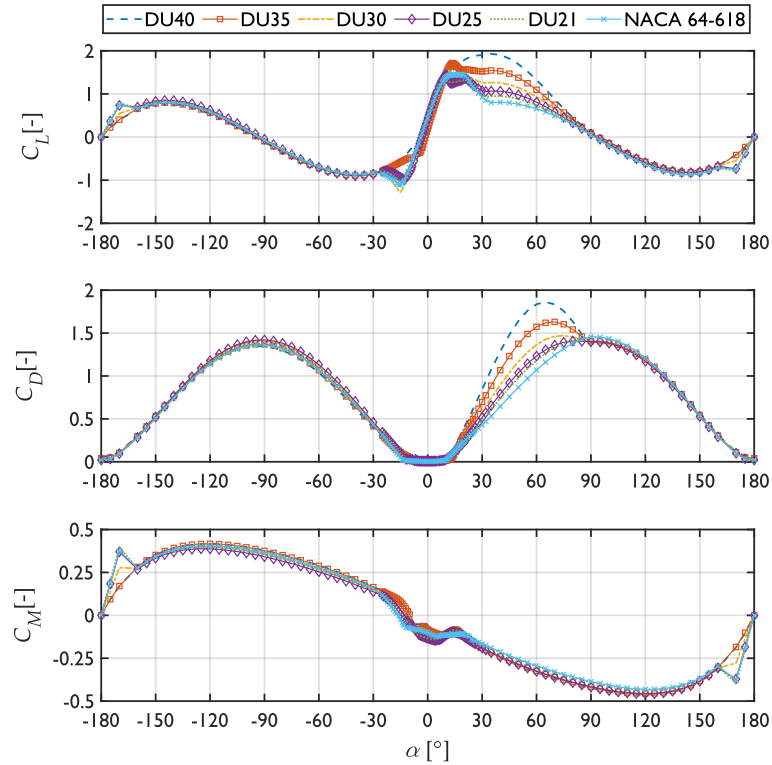


Figure 3.4: Aerodynamic coefficients for the airfoils that define the blade of the reference wind turbine

### Blade modeling

According to the original reference of the NREL,<sup>37</sup> each blade of the selected HAWT has a total mass of 17,740 kg. The structural damping ratio of 0.477% is reported for all structural modes of the blade element. Nevertheless, the natural frequencies of vibration in the edge-wise, flap-wise, or twist, directions are omitted. No details about the materials or the structural configuration of the blades are provided in the NREL document since the blade properties were based on another reference model. However, the stiffness values in the different directions are reported at several span coordinates of the blade.

The blades of the selected HAWT were modeled in APDL by means of the element BEAM188, accounting for the reported stiffness values from the original reference.<sup>37</sup> The chosen element accounts for six degrees of freedom (DOFs) at each end and can support material nonlinearities if an adequate material model is provided. However, in the present case study only the elastic behavior of the structural elements is accounted for. Regarding the discretization of the blades in the model, these were subdivided into 48 elements. The computed natural frequencies for the first 5 modes of a single blade are listed in Table 3.5. As mentioned previously, in the original reference no natural frequency is provided for the blades alone. However, further references that centered on the definition of the structural properties, and in an elaborate FEM of the same reference blade, reported comparable values.<sup>39</sup> The comparison is included in Table 3.5, where resembling values can be appreciated regardless of the simplifications adopted for the present study.

**Table 3.5:** Blade dynamic properties computed from the APDL model

Mode	Description	Frequency (this study) [Hz]	Frequency (SANDIA model) <sup>39</sup> [Hz]
1	1st flap-wise	0.7034	0.87
2	1st edge-wise	1.1046	1.06
3	2nd flap-wise	2.0414	2.68
4	2nd edge-wise	4.1432	3.91
5	3rd flap-wise	4.7876	5.57

### *Nacelle and hub modeling*

The hub mass is specified in the original report to be 56,780 kg, whereas the nacelle, as presented in Table 3.3, is assumed to be 240,000 kg. These components of the turbine were represented in the FEM by lumped masses, modeled by means of the element MASS21, which can account for the mass and inertia in six DOFs. The rotational inertia of the nacelle around the yaw axis was considered as 2,607,890 kg·m<sup>2</sup>, as specified in the original report.<sup>37</sup> Moreover, the connection between these elements, and the rest of the structural components was performed in the APDL model by means of the element MPC184, which was defined as a rigid beam connecting the tower to the nacelle element, and the latter to the hub. The blade-hub connection was also modeled by means of the element MPC184. This was made for the sake of simplification, disregarding the dynamic contribution of the nacelle-yaw actuator and drive-train connecting these elements. However, as presented in Table 3.6, the dynamical similitude among the models was by no means depleted by these assumptions.

### *Tower modeling*

The structural response of most HAWTs is often governed by the first bending modes of the tower. According to the original report,<sup>37</sup> the tower of the selected wind turbine is a hollow conical steel section, with an outer diameter at its bottom equal to 6 m, and 3.87 m at its higher end. The thickness of the tower is reported to be equal to 2.7 cm at the bottom, and 1.9 cm at the top, varying linearly along the tower height. Nevertheless, in the original report,<sup>37</sup> it is also mentioned that these values had to be augmented by 30% to achieve bending-stiffness values comparable to the ones reported for another reference wind turbine which served as a base model for the definition. Details on the structural configuration of the tower are omitted in the original report<sup>37</sup> since it is intended as a conceptual model. However, the material density suggested in the aforementioned reference is 8,500 kg/m<sup>3</sup>, thus the weight of stiffeners and connection elements along the tower (e.g., welding and bolts) can be accounted for in the model. The elastic modulus of the material is assumed as 210 GPa. The tower was modeled in APDL by means of the BEAM188 element, defining a tapered hollow section, and dividing it into 20 elements.

Figure 3.5 displays a rendered scheme of the developed model, whereas a comparison of the dynamic characteristics of the tower against the ones covered in the original report<sup>37</sup> is presented in Table 3.6. According to the modal analysis performed on the FEM, the first bending mode of the tower represents more than 80% of the total mass contribution, in both the fore-aft and side-to-side directions. From Table 3.6 it can be seen a fair similitude in the computed frequencies of the structure, notwithstanding the simplifications adopted to develop the model. Moreover, the structure displays very flexible dynamic behavior, a feature that can make it significantly sensitive to wind-induced buffeting forces.

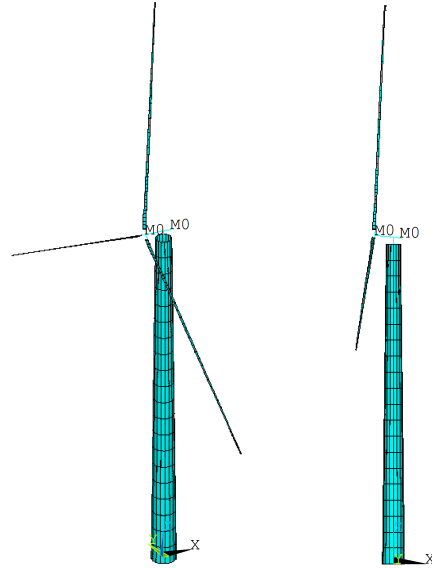


Figure 3.5: Finite element model for the 5-MW reference wind turbine

Table 3.6: Dynamic properties of the 5-MW reference wind turbine

Mode	Description	Frequency (this study) [Hz]	Frequency (NREL model) <sup>37</sup> [Hz]
1	1st Tower side-to-side	0.3219	0.3120
2	1st Tower fore-aft	0.3252	0.3240
3	1st Drivetrain torsion	0.6868	0.6205
4	1st Blade flap-wise yaw	0.7022	0.6664
5	1st Blade flap-wise pitch	0.7152	0.6675
6	1st Blade edge-wise yaw	0.9305	1.0898
7	1st Blade edge-wise pitch	1.0565	1.0793
13	2nd Tower fore-aft	3.0282	2.9003
14	2nd Tower side-to-side	3.2820	2.9361

Note: the numbering and sorting in the modes follow the computed results for the present model under the assumptions described in the text.

### 3.3.3 Aeroelastic modeling

Flexible structures subjected to flow-induced loads are often capable of exhibiting large deformations. These deformations can alter the pressure distribution product of the fluid flow over the body of the structure, and therefore, the magnitude of flow-induced loads. Moreover, the structural responses, such as accelerations or velocities, can be significant compared to the incident flow motion. This accentuates the importance of regarding the structural response in the determination of the flow-induced forces. The forces involved in the structural motion of a flow-excited structure can be classified into three types according to their origin: (i) Elastic forces, which are dependent on the structural response, (ii) Flow-induced forces, which can be categorized into diverse types, according to the flow mechanism or phenomenon originating them, and (iii) Inertial forces, induced by the acceleration of the structure.<sup>40</sup>

The flow-induced forces can be classified into several categories, depending on the phenomena behind their origin. In the present case study, the buffeting force due to the turbulent wind flow on the structure is considered. Phenomena like vortex shedding, or flutter, are disregarded in the present analysis due to the lack of the necessary aerodynamic information on the geometry of the model.

Thus, taking into consideration the above statements, the equation of motion of a multi-DOF system under a flow-induced excitation  $\mathbf{f}_f$  is expressed as:

$$\mathbf{M}_s \ddot{\mathbf{d}}(t) + \mathbf{C}_s \dot{\mathbf{d}}(t) + \mathbf{K}_s \mathbf{d}(t) = \mathbf{f}_f(t) \quad (3.22)$$

where  $\mathbf{M}_s$ ,  $\mathbf{C}_s$ , and  $\mathbf{K}_s$  represent the structural mass, damping, and stiffness matrices, respectively. The structural response is represented by the vector  $\mathbf{d}$ , and the over-dots denote time differentiation. If the flow-induced excitation is a stationary process, the force vector  $\mathbf{f}_f$  can be separated into three parts: a quasi-static force component  $\bar{\mathbf{f}}_a$ , a buffeting component  $\mathbf{f}_a(t)$  dependent on time, and a self-excited force component which depends on the structural response, that is:

$$\mathbf{f}_f(t) = \bar{\mathbf{f}}_a + \mathbf{f}_a(t) - \mathbf{M}_a \ddot{\mathbf{d}}(t) - \mathbf{C}_a \dot{\mathbf{d}}(t) - \mathbf{K}_a \mathbf{d}(t) \quad (3.23)$$

where the terms  $\mathbf{M}_a$ ,  $\mathbf{C}_a$ , and  $\mathbf{K}_a$  are the added mass, fluid damping, and fluid rigidity matrices, respectively. These terms can be rearranged to the left side of Equation 3.22, resulting in:

$$(\mathbf{M}_s + \mathbf{M}_a) \ddot{\mathbf{d}} + (\mathbf{C}_s + \mathbf{C}_a) \dot{\mathbf{d}} + (\mathbf{K}_s + \mathbf{K}_a) \mathbf{d} = \bar{\mathbf{f}}_a + \mathbf{f}_a \quad (3.24)$$

where the indication of time dependence has been omitted for brevity. The added mass term is disregarded in the present case study. This is insofar since the density of the structure is several orders of magnitude greater than the air density, and the contribution of the latter is easily outweighed by the mass of the structure itself. The fluid damping, and the fluid rigidity, were estimated from the quasi-steady assumption, as deduced and summarized in Appendix B. It must be observed that *aerodynamic instability* can be modeled from this approach if the elements within  $\mathbf{C}_a$  and  $\mathbf{K}_a$  result in negative values. Informed FSI-modeling criteria must be adopted for the estimation of these matrices. In this regard, quasi-steady aerodynamics appears disparaged in late publications centered on the subject of structural aerodynamics. This is due to its simplicity, and its incapability to model the frequency-dependent behavior of wind-induced loads. As displayed in some references,<sup>7,41</sup> the outcomes from quasi-steady assumptions tend to provide overestimated response results, however, these quantities can be assumed to fall within acceptable boundaries of tolerance for high wind-speed intensities.

The structural damping was considered assuming viscous damping of 1% of the critical damping value, and Rayleigh-damping coefficients proportional to the mass and stiffness of the structure were defined in the analyses. The frequencies adopted for the computation of these coefficients correspond to the first and second bending frequencies of the tower in the fore-aft direction. The fluid damping and fluid rigidity matrices were included in the APDL model by means of the element MATR1X27. This is a two-node element capable of providing a six-DOF matrix at each end. Thus, it can be incorporated into a structural model as an additional mass, damping, or stiffness matrix. Its implementation in APDL for an aeroelastic simulation is summarized in Appendix B. Figure 3.6 displays a schematic of the APDL model with the inclusion of the fluid damping and rigidity elements.

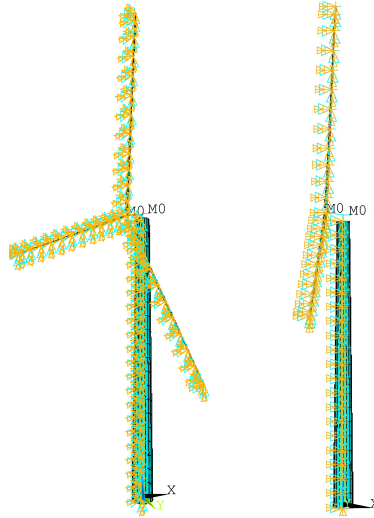


**Figure 3.6:** Finite element model for the 5-MW reference wind turbine including added damping and rigidity elements

## 3.4 Results

The sets of 50 wind field simulations were analyzed for each site. Due to the lack of necessary information on the aerodynamics of the nacelle, all the analyses consider that the turbine is aligned to the main wind direction, assuming that the yaw mechanism of the turbine was still in operation at the time the hypothetical storm falls at the site. This assumption narrows the cases covered in the present case study. However, it adds to the avoidance of epistemic uncertainties in the results. A similar criterion has also been adopted in other studies on the subject.<sup>7,12</sup>

The pitch angle of the blades was assumed in  $90^\circ$ , i.e., with the chord of the blades oriented normally to the rotor plane. This orientation is logical, for the rotor would generate lower drag forces during strong winds with the adopted orientation. A comparison with the structural response disregarding aerodynamic damping is included by means of spectral analyses of the wind-induced dynamic response.

### 3.4.1 Exploration of the results

The structural responses evaluated in this case study correspond to the displacements at the top of the tower ( $d_x$ ,  $d_y$ ), and the stress product of the bending moments at its base ( $M_x$ ,  $M_y$ ). A total of 100 aeroelastic time-history analyses were performed on the HAWT model to study its dynamic response. According to the quasi-steady criterion summarized in Appendix B, the fluid damping and fluid rigidity matrices are dependent on the mean wind velocity incident on the structure. Therefore, each analysis considers a different value of aerodynamic damping and aerodynamic rigidity. The blades of the turbine are the main contributors to these quantities, given the values of their aerodynamic coefficients. On the contrary, a constant drag coefficient was assumed for the tower, with negligible aerodynamic- lift and twisting coefficients. These assumptions might imply lower or higher contribution from the fluid matrices on the structural response to a certain degree, depending on the criteria adopted for the pitch configuration of the blades.

Figures 3.7 and 3.8 display a statistical summary of the power spectral density functions (PSDFs) of the evaluated responses for the Cat. I simulations. The results of 20 analyses that disregard the effects of fluid damping, and rigidity, are compared with the ones from 20 analyses performed under the FSI assumptions summarized in the previous section.

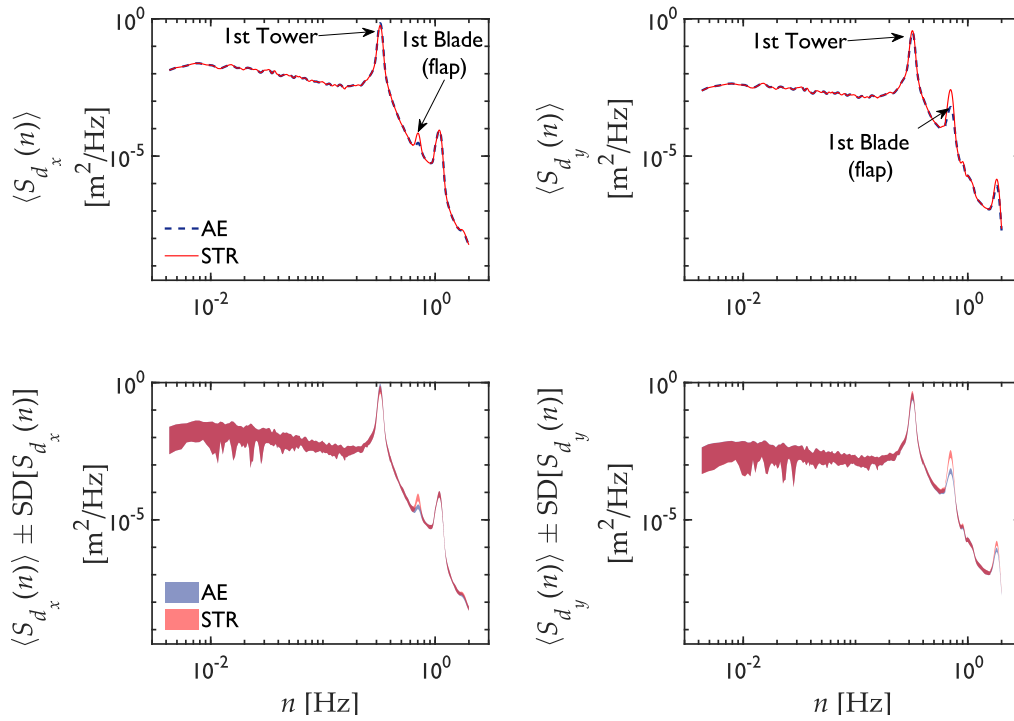


**Figure 3.7:** Spectral comparison between aeroelastic (AE) and non-aeroelastic (STR) time-history tower displacements

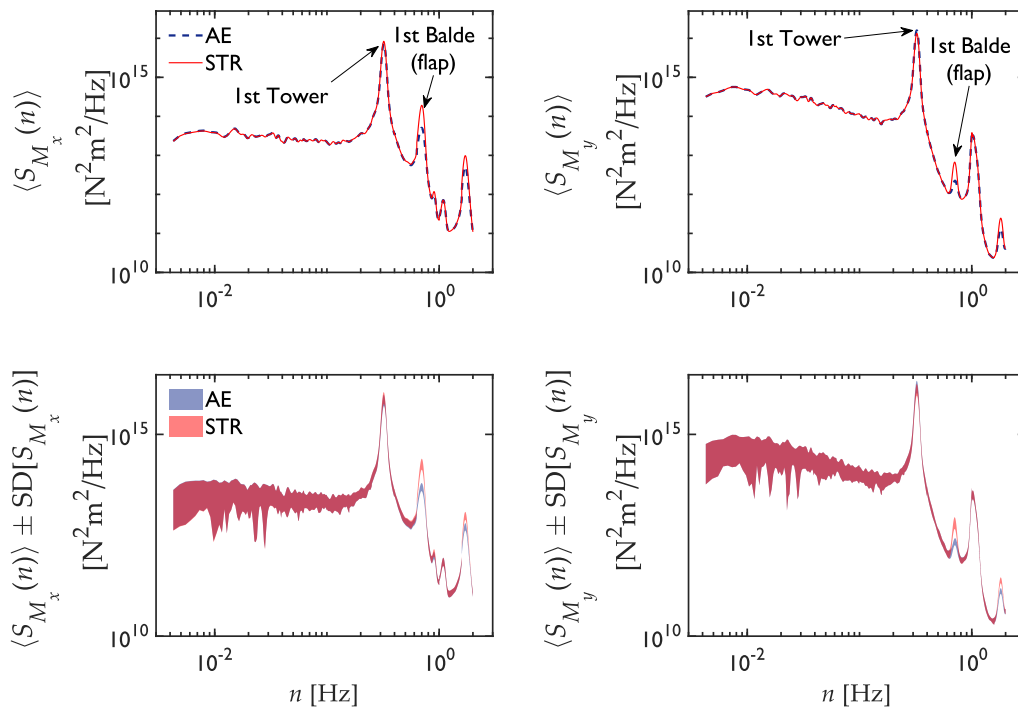


**Figure 3.8:** Spectral comparison between aeroelastic (AE) and non-aeroelastic (STR) time-history tower-base moments

From Figure 3.7 the ensemble average of the displacement spectra is denoted as  $\langle S_{d_i} \rangle$ , where the sub-index  $i$  represents either the along-wind ( $x$ ) or across-wind ( $y$ ) direction. This is analogous to the moment spectra in Figure 3.8. From both figures, it can be seen that the fluid damping appears to contribute little to the stochastic component of structural response at the first bending-mode frequency of the tower. Even more, some spectral ordinates at this frequency appear to be slightly higher for the aeroelastic spectra than the non-aeroelastic ones. These observations have two main explanations: (i) As mentioned in Section 3.3.2, the tower-bending modes contribute more than 80% to the dynamic response. Given the assumed aerodynamic characteristics of the tower (i.e., constant drag coefficient, and no lift or twist contributions), the motion of the tower adds no damping to the structure. (ii) Because the blades are assumed to be along-wind oriented, their aerodynamic contribution in the along-wind (drag) direction is rather minute (see Figure 3.4). Moreover, the existent coupling in the fluid damping and fluid rigidity matrices with other aerodynamic DOFs can incorporate negative contributions to the drag component (see Appendix B). This causes a slight increase in the dynamic response amplitude in the along-wind direction. Contrarily, the structural responses associated with the blade-lift DOFs are more likely to display positive values of fluid damping. This last statement can be justified by looking at frequencies where the aerodynamic DOF in the lift direction of the blade has greater participation. For example, at the frequencies associated with the flapping modes of the blades. At these frequencies, lower spectral amplitudes from the aeroelastic analyses are observed in Figures 3.7 and 3.8.

Despite the slight differences observed in the PSDFs of structural response, the inclusion of fluid damping and fluid rigidity is consequential in the probabilistic characterization of the response maxima. This assertion can be justified by looking at the probability plots from the maxima computed from 20 aeroelastic analyses, and their non-aeroelastic counterparts. Figure 3.9 displays these representations for data from the Category-III analyses. The  $p$ -values from a two-sample Kolmogorov-Smirnov test are also displayed in the figure. A normal-distribution fit is also included as a reference. From Figure 3.9 it can be seen that the negative (and minute) damping contribution in the along-wind direction is significant for the estimation of the probability distribution of response maxima. The null hypothesis implying that the two samples come from the same distribution would be rejected at a 5% significance level. For the across-wind displacements, the situation is the opposite: fluid damping and rigidity contribute to the response diminution, but with no sufficiency to regard an alteration in the probability distribution of the structural-response maxima.

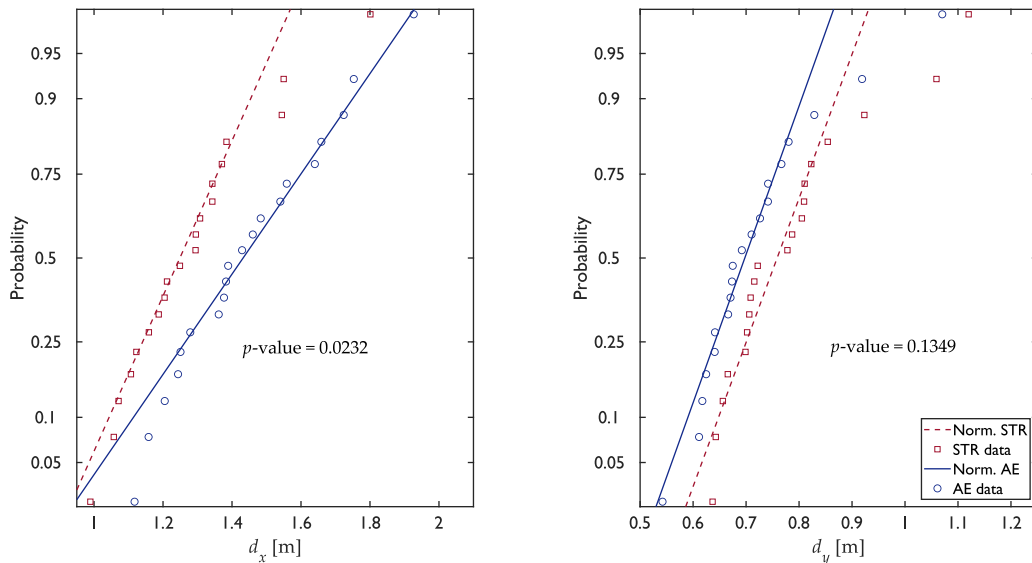


**Figure 3.9:** Normal-distribution probability plot of displacements from aeroelastic (AE) and non-aeroelastic (STR) analyses

Furthermore, the response coupling is increased due to the aerodynamic damping and rigidity. This effect can be appreciated by looking at the measured correlation between the response histories from a set of 20 analyses that account for FSI, and comparing these values with estimations from analyses that disregard it. Figure 3.10 displays values of linear correlation for the structural response of the HAWT in the along-wind and across-wind directions. A greater degree of association is displayed from the analyses that account for the fluid damping and rigidity matrices.

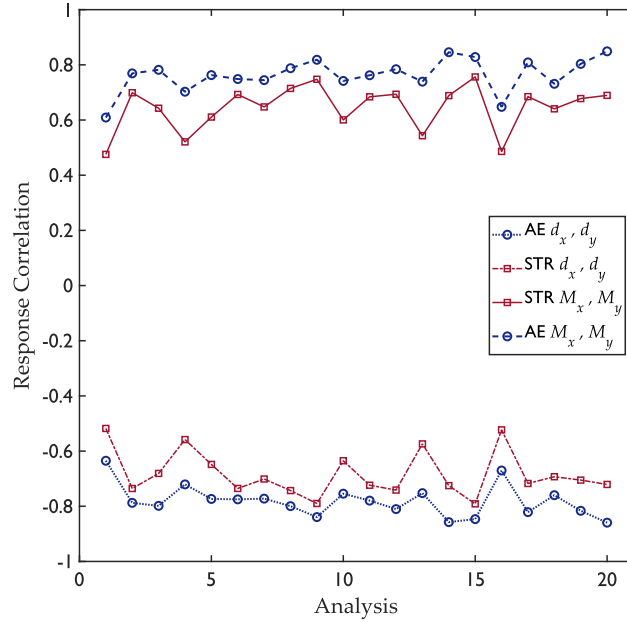


Figure 3.10: Measured linear correlation coefficients from aeroelastic (AE) and non-aeroelastic (STR) analyses

### 3.4.2 Peak factor

The maximum response of any wind-sensitive structure is of interest when it is analyzed under the action of extreme wind events. Professor Alan Davenport developed the theoretical formulations to estimate the maximum response of wind-excited structures under gusty winds. The assumptions adopted for his derivations are that both the wind excitation and the structural response are stochastic Gaussian processes.<sup>42</sup> These expressions are adopted by virtually all wind-engineering standards and references. For example, the expression provided by the Manual of Civil Works from Mexican CFE<sup>35</sup> states that the quasi-static response of wind turbines must be multiplied by the following factor to account for the probable maximum in a 10-min time interval:

$$F_{RR} = 1 + 2k_p I_u(z_s) \sqrt{B^2 + R^2} \quad (3.25)$$

where  $B$  and  $R$  stand for the background and resonant components of the response, respectively.  $I_u$  represents the turbulence intensity in the along-wind direction,  $z_s$  is the reference height (the hub height, in the case of HAWTs), and  $k_p$  is the *peak factor* as deduced originally by Davenport.<sup>42</sup>

The values of  $B$  and  $R$  are estimated from approximations of the structural response spectra, which, as can be seen in Figures 3.7 and 3.8, show resemblances between the non-aeroelastic and the aeroelastic results for the assumptions of this study. Moreover,  $k_p$  is determined from the statistical properties of the response histories. The conventional expression for the peak factor is stated as<sup>42</sup>:

$$k_p = \sqrt{2 \ln(\nu T)} + \frac{\gamma}{\sqrt{2 \ln(\nu T)}} \quad (3.26)$$



where  $\gamma$  is the Euler's constant ( $\approx 0.5772$ ),  $\nu$  is the rate of up-crossings from the response history, and  $T$  is the length of the response signal.

Given the degree of coupling between the components of structural response in the  $x$ - and  $y$ - directions, aggrandized by the fluid damping and rigidity, the assumption of *Gaussianity* might be of no application in the estimation of the extreme values of the structural response. This can imply over- or underestimation of the response maxima. To verify the validity of these assumptions, an exploration of the probabilistic characterization of the structural response is presented in the following sections.

#### Characterization of response amplitudes

The evaluation of the amplitude distribution of structural responses was carried out to determine if it is adequately represented by a Gaussian process. A Gaussian distribution is characterized by being symmetric and having a kurtosis of 3. The first examination carried out on the data was by estimating the skewness and kurtosis of the response amplitudes from each simulation. Figure 3.11 displays the values of these parameters from each analysis for the displacements in the  $x$ - and  $y$ -directions. The corresponding values for base moments around these axes are also displayed, as well as the skewness and kurtosis for the vector sum of the response components.

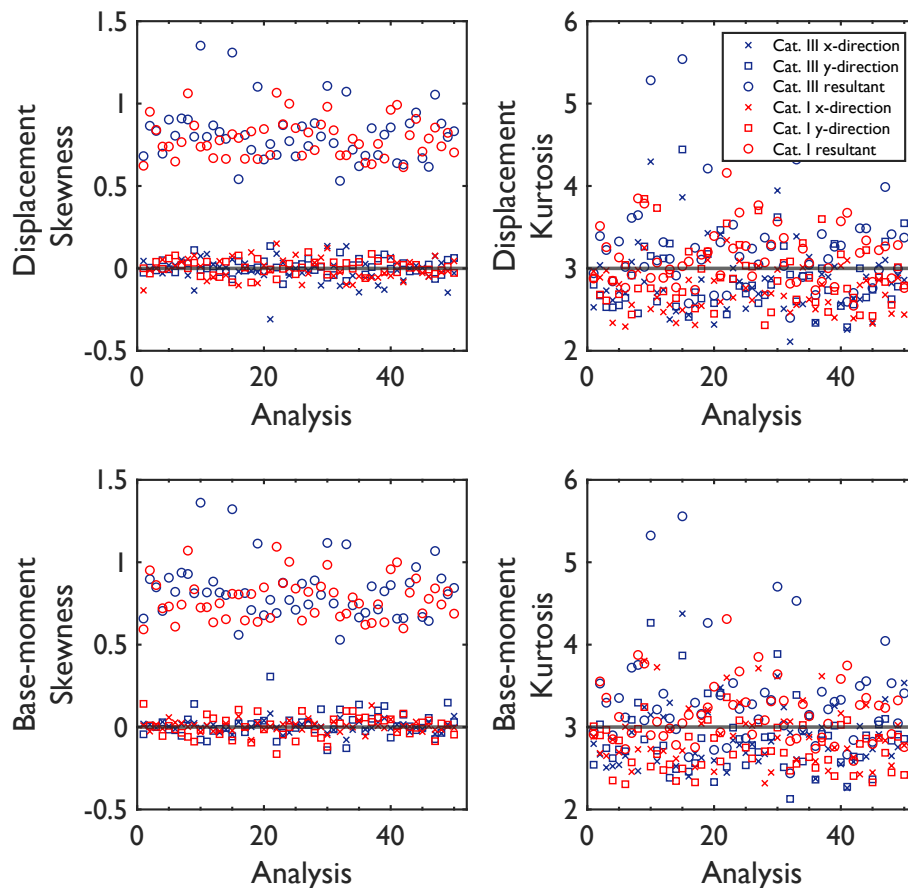


Figure 3.11: Skewness and kurtosis from structural responses

From Figure 3.11 it is seen that, overall, the responses in the  $x$ - and  $y$ -directions are symmetric to a certain degree. On the other hand, the resultant responses have positive skewness in all cases. Moreover, the kurtosis from all responses is more or less dispersed around 3. However, the greater part of

the data seems to behave like a *soft* process, i.e., it displays values of kurtosis less than three. This can be visualized more clearly in Figure 3.12, where box plots from the distribution of the kurtosis of the data are presented.

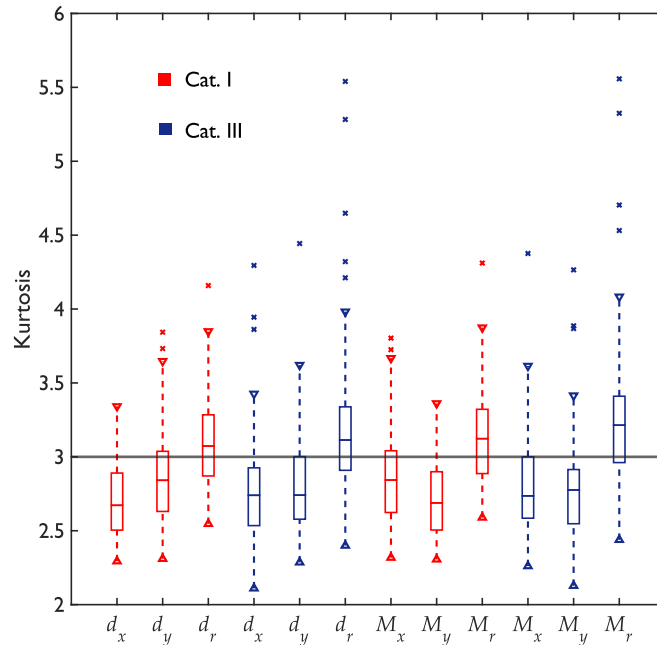
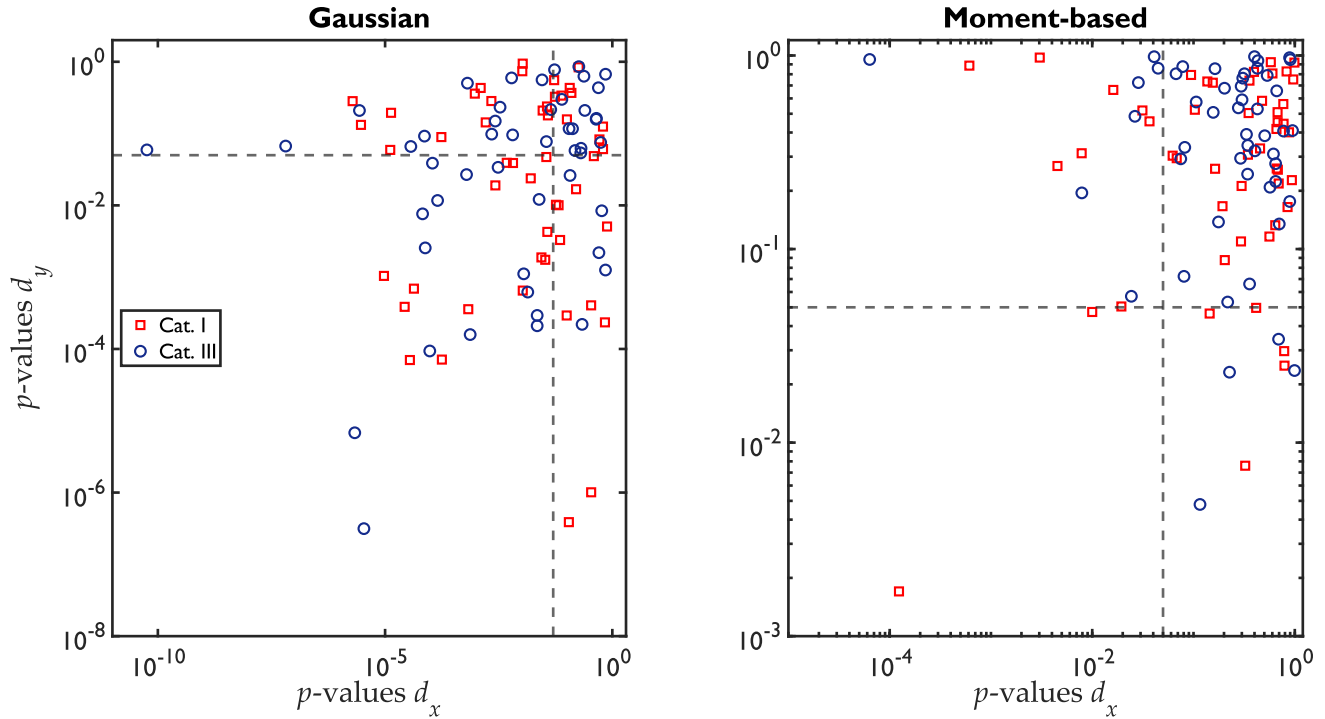


Figure 3.12: Kurtosis values from structural responses

Given the presented examinations the following premises can be stated: (i) the structural response can be fairly represented by a Gaussian distribution in the  $x$ - and  $y$ -directions since the amplitude distribution of the data appears to be fairly symmetrical. However, the kurtosis of these responses deviates from Gaussianity in the majority of cases. Therefore, a quantitative evaluation of the adequateness of a Gaussian distribution is pertinent. (ii) Conventional structural analyses are centered on the determination of the structural response in the along- and across-wind directions, whereas the resultant vector of structural response might differ from these directions. It is seen from Figures 3.11 and 3.12 that the distribution of resultant amplitudes might display complicated features. If the amplitudes of displacement in the along- and across-wind directions were to behave as independent Gaussian processes, the resultant displacement could be represented by a Rayleigh distribution. However, given the strong correlation displayed by the components of the response, a more uncommon distribution is necessary for its probabilistic representation. Therefore, the probabilistic features of the resultant response will be explored only incipiently in the present study.

Regarding the first premise from the previous paragraph, Kolmogorov-Smirnov tests were performed on the normalized distributions of displacement amplitudes. The distributions considered for the evaluation of the implied hypotheses were a standard-normal distribution and non-Gaussian distributions as estimated from diverse moment-based models. These models account for processes with kurtosis other than three.<sup>43,44</sup> Figure 3.13 displays the  $p$ -values computed from these tests for the along- and across-wind displacements of each analysis. The conventional 5% significance level to reject the null hypothesis of the test is included as a reference.

Regarding Figure 3.13, the observations that fall in the southwest quadrant are responses in which neither  $d_x$  nor  $d_y$  were fairly represented by the selected distributions. The southeast quadrant holds responses where only the  $x$ -component displays a fair probability of being represented by the selected distribution; this is analogous to the  $y$ -component of response but in the northwest quadrant. Lastly,



**Figure 3.13:** Evaluation of goodness of response amplitude distributions

the northeast quadrant holds the observations in which the responses in both the  $x$ - and  $y$ -directions display a fair probability of being represented by the selected distributions. It can be inferred from the figure that the amplitudes of displacements display a rather non-Gaussian behavior. Whether the considerations currently adopted by common standards are adequate is briefly discussed in the following section.

#### *Peak factor evaluation*

The peak factors associated with the maximum values of response measured from each analysis for both the Cat. I and Cat. III events are displayed in Figure 3.14. Moreover, the peak factor measured from the vector sum of displacement components, i.e., from  $d_r^2 = d_x^2 + d_y^2$  is also displayed. The peak factors computed according to Equation 3.26 in the two main components are also presented in the figure. As can be seen from Figure 3.14, the conventional peak factors for  $d_x$  and  $d_y$  tend to over-predict the measured values. However, this is a conservative criterion that adds to the safety of the structures designed under this assumption. This overestimation is attributed in this work to the general tendency in the response data towards a soft process. Notwithstanding, the peak factors measured from the resultant responses display larger values. This can underestimate important responses in symmetrical structures, like HAWT towers. The approach proposed here to estimate a safe value for a 'combined-response' peak factor comes from the evaluation of  $k_{p,r}^2 = k_{p,x}^2 + (0.8k_{p,y})^2$ . This value for  $k_{p,r}$  is displayed in Figure 3.14 as a dashed line. The constant of 0.8 has been defined intuitively given the correlation values displayed by the components of the response. It is given a value lower than unity since the maximum response in the  $x$ -direction is unlikely to occur at the same time that the maximum response in the  $y$ -direction. However, the definition of more detailed criteria is out of the scope of the present work.

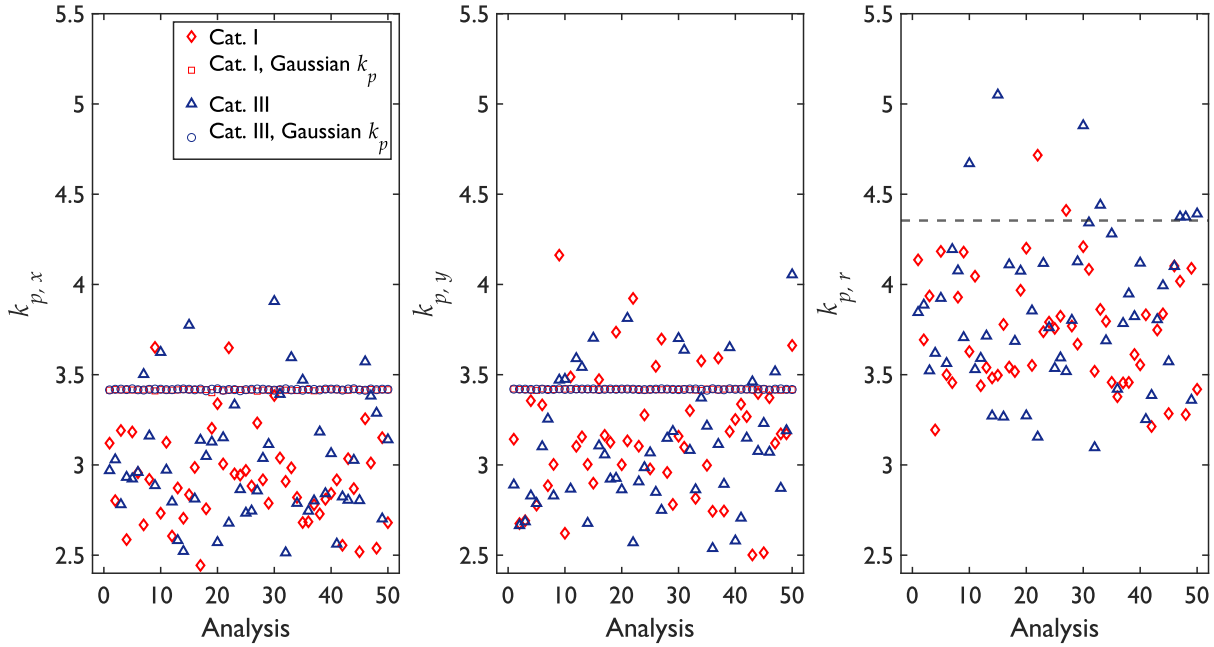


Figure 3.14: Peak factors computed from the structural response

### 3.4.3 Reliability evaluation

The main structural component of a HAWT is the tower, thus it is of major importance to determine its performance during extreme wind events. Other studies that have served as a basis for the present work have defined different performance levels for this element.<sup>45</sup> In this study, two performance thresholds are evaluated. The former corresponds to the probability of a residual displacement of  $\sim 0.1\%$  of the tower height to be produced by the cyclone event. The latter corresponds to the probability of reaching the nominal capacity of the tower section at its base. The residual displacement is evaluated as a function of the tower-tip displacement. In this study, it is assumed that this level is reached at a displacement of  $1.5\%$  of the tower height.<sup>45</sup> As for the determination of the section capacity, it is defined from expressions presented in documents for recommended practice for the structural design of HAWT structures.<sup>46</sup> These recommendations suggest the following threshold to estimate the tower capacity from the stress at its walls:

$$\phi_c F_{cr} \geq \frac{P_u}{A} + \frac{M_u}{S} \quad (3.27)$$

where  $\phi_c$  is the capacity reduction factor for combined axial load and bending (assumed as 1.0 in this study).  $P_u$  and  $M_u$  are the axial force and bending moment acting on the structure, respectively; and  $A$  and  $S$  are the cross-section area and elastic section modulus, respectively. The stress  $F_{cr}$  is computed from the expression:

$$F_{cr} = \begin{cases} F_y & \text{if } \frac{D_c}{t_c} \leq \frac{0.11E}{F_y} \\ \frac{0.038E}{(D_c/t_c)} + \frac{2}{3}F_y & \text{if } \frac{0.11E}{F_y} < \frac{D_c}{t_c} \leq \frac{0.357E}{F_y} \\ \frac{0.276E}{(D_c/t_c)} & \text{if } \frac{0.357E}{F_y} < \frac{D_c}{t_c} \leq 330 \end{cases} \quad (3.28)$$

where  $F_y$  is the yielding stress of the material, and  $t_c$  is the thickness of the tower wall. In this case study  $F_y$  was assumed as 350 MPa, whereas the value of  $t_c$  accounts for the increased stiffness for the present model, as mentioned in Section 3.3.2.

The probability of failure is defined by the following expression:

$$P_f = \int_{g(\mathbf{x}) \leq 0} f_{\mathbf{x}}(\mathbf{x}) d\mathbf{x} \quad (3.29)$$

where  $g(\mathbf{x})$  is a performance function that describes the limit state being evaluated, and  $\mathbf{x}$  is a vector of random variables that intervene in the structural capacity. These random variables often include as uncertain quantities the load acting on the system, as well as the material properties and structural dimensions, among other possible sources of uncertainty. In the present case study, the loads on the tower and its capacity are assumed uncertain. The joint PDF of the random variables that intervene is represented by  $f_{\mathbf{x}}(\mathbf{x})$ . Moreover, the function  $g(\mathbf{x})$  can be defined as  $g(\mathbf{x}) = R - S$ , where  $R$  represents the resistance of the structural system, whereas  $S$ , in this context, represents the loads acting on it. Accounting for the aforementioned assumptions, the probability of failure can also be expressed as:

$$P_f = \int_{\text{all } x} F_R(x) f_S(x) dx \quad (3.30)$$

where  $F_R$  and  $f_S$  are the CDF and PDF of structural capacity and loads, respectively. In this regard, the structural capacity was assumed to be represented by a lognormal distribution, with a coefficient of variation of 20%, for both the displacement and tower stress. On that matter, the values of  $0.015z_s$  and  $F_{cr}$  were assumed as the mean of the response capacity for the levels of performance under evaluation. These criteria have reduced the problem to the determination of the PDF that adequately describes the behavior of the response maxima. Direct integration was performed to evaluate the probability of exceeding the maximum displacement, as well as the exceedance probability of  $F_{cr}$ . The following section elaborates on this subject.

#### *Characterization of response maxima*

The resultant stress at the bottom walls of the tower was computed by means of Equation 3.27 for each of the 100 aeroelastic analyses performed. Subsequently, the maximum value from those response histories was identified. Different PDFs were fitted to the data separated into the Cat. I and Cat. III analyses. This was analogous to the displacement in the along-wind, and resultant directions. The PDF fittings that were evaluated correspond to the following distributions: Normal, Lognormal, Generalized Extreme Value (GEV), Weibull, and the moment-based distribution computed from the statistical moments of the samples.<sup>43,44</sup> Table 3.7 displays the  $p$ -values estimated from a Kolmogorov-Smirnov test performed on the estimated distributions of the data.

**Table 3.7:** Evaluation of adequacy ( $p$ -values) of various distributions for the response maxima on the tower

Distribution	Cat. I			Cat. III		
	$d_x$	$d_r$	Stress	$d_x$	$d_r$	Stress
Normal	0.7378	0.9831	0.9791	0.9685	0.6913	0.8069
Lognormal	0.9455	0.9934	0.9997	0.9900	0.9267	0.9761
GEV	0.7766	0.9957	0.9785	0.9826	0.9516	0.9498
Weibull	0.3478	0.6216	0.5670	0.6355	0.2872	0.3648
Moment-Based	0.8127	0.9953	0.9804	0.9110	0.8466	0.8014

From Table 3.7 it is seen that the hypothesis stating that the response maxima (either displacement or stress) come from the evaluated distributions is rejected for none of them at conventional signif-

icance levels. It is also seen that the Lognormal distribution displays the greatest similitude with the data. Notwithstanding, the behavior of the distribution at its 'tail' is of significant importance. Figures 3.15 and 3.16 display the probability distributions fitted to the stress data, along with the probability of exceedance of stress maxima estimated for the Lognormal, GEV, and moment-based (M-B) distributions, for the Cat. I and Cat. III results, respectively. The probability of exceeding a certain level of stress once in 200 years is marked in both figures as reference. It can be observed the sensitivity of the response values to the tail-behavior characterization for the required levels of reliability, even for distributions that represent the data as adequately as the ones displayed.

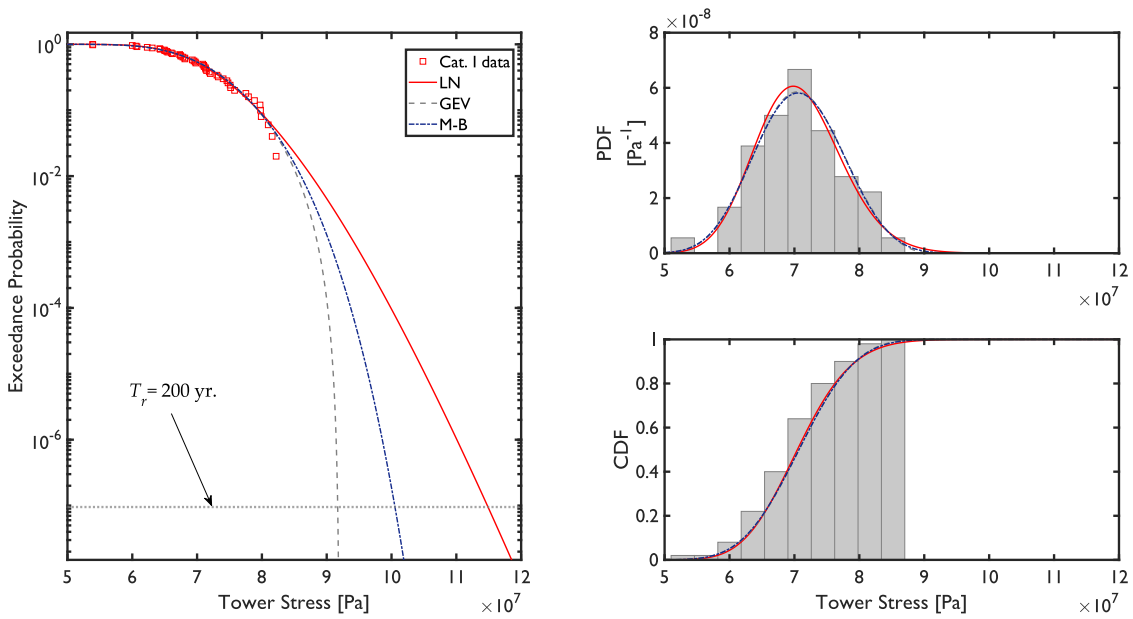


Figure 3.15: Probability distribution of tower stress maxima for the Category I analyses

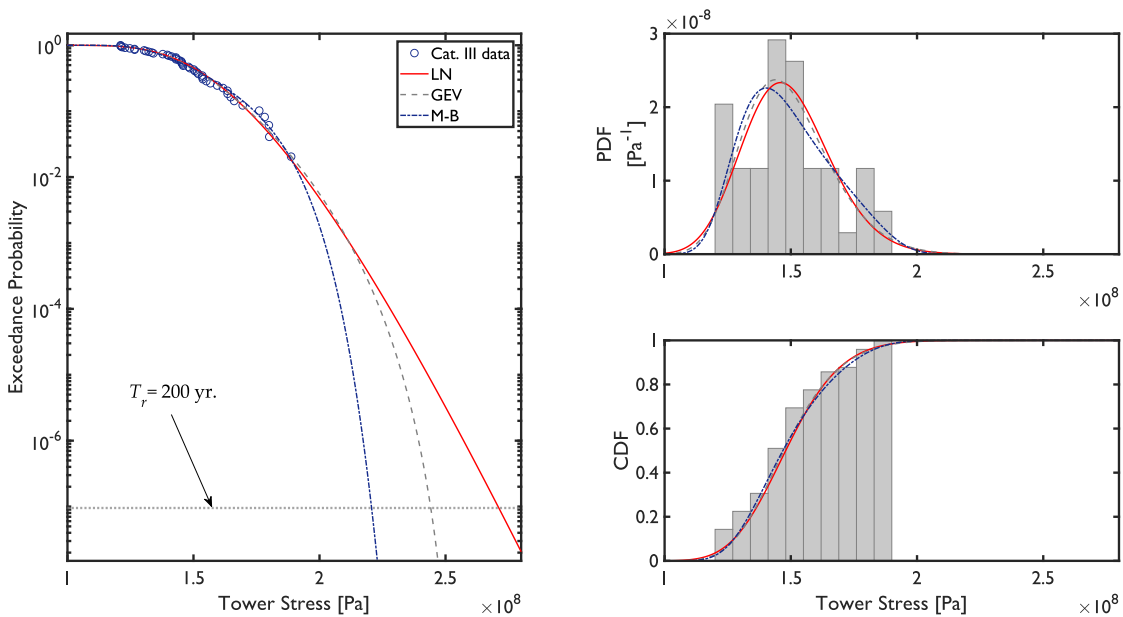


Figure 3.16: Probability distribution of tower stress maxima for the Category III analyses

### Probability of failure

Various probability distributions that represent fairly the behavior of the response maxima have been estimated. Based on these estimations, the probability of failure as defined in Equation 3.29 is evaluated for the two sites assumed in this case study. According to Equation 3.28, the mean resistant stress of the tower at its base is 260.82 MPa, whereas the mean of the threshold defined for displacement is 1.125 m. The probability of failure is thus evaluated under all the assumptions described in this section. Table 3.8 displays the different values of  $P_f$  for the distributions displayed in Figures 3.15 and 3.16. Only the resultant displacement and stress are displayed in the table.

**Table 3.8:** Probability of failure for the two sites and performance levels evaluated

Distribution	Cat. I		Cat. III	
	Disp.	Stress	Disp.	Stress
Lognormal	0.0161	2.02E-09	0.9214	0.0086
GEV	0.0155	8.68E-10	0.9217	0.0087
Moment-Based	0.0159	1.07E-09	0.9207	0.0089

From Table 3.8 it can be seen that the selected HAWT displays a fair probability of reaching a residual displacement at a Category I hurricane. This damage state is almost certain for a Category III event. Moreover, the probability of exceeding the tower capacity once in a 200-year time interval (i.e., 9.51E-08) is unreachd for the Oaxaca site. Contrarily, it is widely surpassed for the Yucatan site, even for a shorter return period, such as the one suggested for extreme wind by the IEC 61400-1.<sup>4</sup>

## 3.5 Conclusions

The NREL 5-MW reference wind turbine is a widely employed model in wind energy research. Although it is a conceptual one, it is intended to represent the characteristics of real multi-megawatt turbines. The results from this study demonstrate that the criteria from technical recommendations for wind actions on structures currently adopted for Mexico permit the deployment of similar turbines for sites prone to low-category cyclone intensities. Notwithstanding, a great part of Mexican territory, as well as many other tropical regions, is prone to greater wind intensities due to cyclone hazard. This will demand the adequate characterization of extreme-event wind actions and structural response to continue the deployment of wind energy.

Lastly, the following summary displays the conclusions of the present study:

- Two sites prone to tropical cyclones, with different wind hazard levels, have been selected for the study of the structural response of a HAWT.
- The wind flow used for the analyses is concordant with models from observations and studies on the characteristics of the TCBL.
- The TCBL simulated from the used models displays significantly greater values than the synoptic profile as proposed in the CFE<sup>35</sup> and other wind-loading standards. This appears significant for structures as high as the one analyzed in this chapter.
- The parameters that characterize the probability distribution of the central pressure deficit have been defined for their application in flow-field simulations. Two different PDFs have been considered to model its behavior. Moreover, these parameters have been associated with conventional tropical cyclone classifications.
- An aeroelastic FEM that allows the possibility of analyzing the structure under diverse phenomena considering the FSI was defined. Although the analyses on the model were elastic, further studies from this approach can consider the inelastic behavior of its structural components.

- The FSI, as considered in this study, represents negligible differences in the spectral analysis of the structural response. However, it spawns considerable differences in terms of its probability distribution. Moreover, the fluid damping and rigidity represent greater values of coupling in the structural response.
- The peak factor in the combined direction represents greater response values than the ones in the along-wind direction. Notwithstanding, an elaborate analysis of the peak factors in the combined direction remains a task for further studies.
- The peak factors as suggested in common wind standards, such as the CFE provisions,<sup>35</sup> are adequate for single-direction analyses in which the aerodynamic effects induce no non-linearities in the structural response. However, in symmetrical structures, the greater displacements appear in a coupled direction. Thus, a rudimentary alternative to cover this omission was proposed. Further analyses on this matter fall out of the scope and temporal frame of the study.
- For the site with a lower cyclone hazard (Cat. I), significant probabilities of reaching a residual displacement in the tower were found, whereas this damage state is virtually certain for the Cat. III analyses.
- For the Category-I events, the probability of tower failure is lower than the probability associated with a failure occurrence with a 200-year return period. For the Category-III events, it is several orders of magnitude greater, even if the failure occurrences are compared to a 50-year return period.

## References

1. Hangan, H., Romanic, D. & Jubayer, C. Three-dimensional, non-stationary and non-Gaussian (3D-NS-NG) wind fields and their implications to wind–structure interaction problems. *Journal of Fluids and Structures* **91**, 102583 (2019). doi: 10.1016/j.jfluidstructs.2019.01.024.
2. Kossin, J. P., Hall, T., Knutson, T., *et al.* in (eds Wuebbles, D. J., Fahey, D. W., Hibbard, K. A., *et al.*) 257–276 (U.S. Global Change Research Program, Washington, USA, 2017). doi: 10.7930/J07S7KXX.
3. Appendini, C. M. *et al.* Effect of climate change over landfalling hurricanes at the Yucatan Peninsula. *Climatic Change* **157**, 469–482 (2019). doi: 10.1007/s10584-019-02569-5.
4. IEC. *Wind turbines – Part 1: Design requirements* 3rd ed. International Electrotechnical Commission (Geneva, Switzerland, 2005).
5. Ma, Y., Martinez-Vazquez, P. & Baniotopoulos, C. Wind turbine tower collapse cases: a historical overview. *Proceedings of the Institution of Civil Engineers – Structures and Buildings* **172**, 547–555 (2019). doi: 10.1680/jstbu.17.00167.
6. Chen, X. & Xu, J. Z. Structural failure analysis of wind turbines impacted by super typhoon Usagi. *Engineering failure analysis* **60**, 391–404 (2016). doi: 10.1016/j.engfailanal.2015.11.028.
7. Amirinia, G. & Jung, S. Along-wind buffeting responses of wind turbines subjected to hurricanes considering unsteady aerodynamics of the tower. *Engineering Structures* **138**, 337–350 (2017). doi: 10.1016/j.engstruct.2017.02.023.
8. Amirinia, G. & Jung, S. Buffeting response analysis of offshore wind turbines subjected to hurricanes. *Ocean Engineering* **141**, 1–11 (2017). doi: 10.1016/j.oceaneng.2017.06.005.
9. Kaimal, J. C., Wyngaard, J. C., Izumi, Y. & Coté, O. R. Spectral characteristics of surface-layer turbulence. *Quarterly Journal of the Royal Meteorological Society* **98**, 563–589 (1972).
10. Li, L., Xiao, Y., Kareem, A., Song, L. & Qin, P. Modeling typhoon wind power spectra near sea surface based on measurements in the South China sea. *Journal of Wind Engineering and Industrial Aerodynamics* **104**, 565–576 (2012). doi: 10.1016/j.jweia.2012.04.005.



11. Yu, B., Chowdhury, A. G. & Masters, F. J. Hurricane wind power spectra, cospectra, and integral length scales. *Boundary-Layer Meteorology* **129**, 411–430 (2008). doi: 10.1007/s10546-008-9316-8.
12. Hallowell, S. T. *et al.* Hurricane risk assessment of offshore wind turbines. *Renewable Energy* **125**, 234–249 (2018). doi: 10.1016/j.renene.2018.02.090.
13. Jonkman, J. M. & Buhl Jr., M. L. *FAST User's Guide* National Renewable Energy Laboratory (Golden, Colorado, 2005). NREL/EL-500-29798.
14. Isherwood, R. A revised parameterisation of the Jonswap spectrum. *Applied ocean research* **9**, 47–50 (1987). doi: 10.1016/0141-1187(87)90030-7.
15. Li, L., Kareem, A., Xiao, Y., Song, L. & Zhou, C. A comparative study of field measurements of the turbulence characteristics of typhoon and hurricane winds. *Journal of Wind Engineering and Industrial Aerodynamics* **140**, 49–66 (2015). doi: 10.1016/j.jweia.2014.12.008.
16. Li, L. *et al.* Turbulence spectra for boundary-layer winds in tropical cyclones: a conceptual framework and field measurements at coastlines. *Boundary-Layer Meteorology* **154**, 243–263 (2015). doi: 10.1007/s10546-014-9974-7.
17. Bryan, G. H., Worsnop, R. P., Lundquist, J. K. & Zhang, J. A. A simple method for simulating wind profiles in the boundary layer of tropical cyclones. *Boundary-Layer Meteorology* **162**, 475–502 (2017). doi: 10.1007/s10546-016-0207-0.
18. Worsnop, R. P., Bryan, G. H., Lundquist, J. K. & Zhang, J. A. Using large-eddy simulations to define spectral and coherence characteristics of the hurricane boundary layer for wind-energy applications. *Boundary-Layer Meteorology* **165**, 55–86 (2017). doi: 10.1007/s10546-017-0266-x.
19. Ma, T. & Sun, C. Large eddy simulation of hurricane boundary layer turbulence and its application for power transmission system. *Journal of Wind Engineering and Industrial Aerodynamics* **210**, 104520 (2021). doi: 10.1016/j.jweia.2021.104520.
20. Kapoor, A. *et al.* Hurricane eyewall winds and structural response of wind turbines. *Wind Energy Science* **5**, 89–104 (2020). doi: 10.5194/wes-5-89-2020.
21. Jonkman, B. J. & Buhl Jr, M. L. *TurbSim user's guide* tech. rep. (National Renewable Energy Laboratory, Golden, USA, 2006).
22. IEA. *Projected costs of generating electricity* <https://www.iea.org/reports/projected-costs-of-generating-electricity-2020>.
23. Farfán, L. M., D'Sa, E. J., Liu, K.-b. & Rivera-Monroy, V. H. Tropical cyclone impacts on coastal regions: the case of the Yucatán and the Baja California Peninsulas, Mexico. *Estuaries and Coasts* **37**, 1388–1402 (2014). doi: 10.1007/s12237-014-9797-2.
24. Snaiki, R. & Wu, T. A semi-empirical model for mean wind velocity profile of landfalling hurricane boundary layers. *Journal of Wind Engineering and Industrial Aerodynamics* **180**, 249–261 (2018). doi: 10.1016/j.jweia.2018.08.004.
25. Holland, G. J., Belanger, J. I. & Fritz, A. A revised model for radial profiles of hurricane winds. *Monthly weather review* **138**, 4393–4401 (2010). doi: 10.1175/2010MWR3317.1.
26. Vickery, P. J. & Wadhera, D. Statistical models of Holland pressure profile parameter and radius to maximum winds of hurricanes from flight-level pressure and H\*Wind data. *Journal of Applied Meteorology and Climatology* **47**, 2497–2517 (2008). doi: 10.1175/2008JAMC1837.1.
27. Knaff, J. A. & Zehr, R. M. Reexamination of tropical cyclone wind–pressure relationships. *Weather and Forecasting* **22**, 71–88 (2007). doi: 10.1175/WAF965.1.
28. Chavas, D. R., Reed, K. A. & Knaff, J. A. Physical understanding of the tropical cyclone wind–pressure relationship. *Nature communications* **8**, 1–11 (2017). doi: 10.1038/s41467-017-01546-9.
29. Vickery, P. J. Simple empirical models for estimating the increase in the central pressure of tropical cyclones after landfall along the coastline of the United States. *Journal of Applied Meteorology* **44**, 1807–1826 (2005). doi: 10.1175/JAM2310.1.

30. Georgiou, P., Davenport, A. G. & Vickery, B. Design wind speeds in regions dominated by tropical cyclones. *Journal of Wind Engineering and Industrial Aerodynamics* **13**, 139–152 (1983). doi: 10.1016/0167-6105(83)90136-8.
31. Hong, H. P., Li, S. H. & Duan, Z. D. Typhoon wind hazard estimation and mapping for coastal region in mainland China. *Natural Hazards Review* **17**, 04016001 (2016). doi: 10.1061/(ASCE)NH.1527-6996.0000210.
32. Kantha, L. Time to replace the Saffir-Simpson hurricane scale? *Eos, Transactions American Geophysical Union* **87**, 3–6 (2006). doi: 10.1029/2006EO010003.
33. FEMA. *Hazus Hurricane Model Technical Manual* Federal Emergency Management Agency (Mar. 2021).
34. Dunnavan, G. M. & Diercks, J. W. An Analysis of Super Typhoon Tip (October 1979). *Monthly Weather Review* **108**, 1915–1923 (1980). doi: 10.1175/1520-0493(1980)108<1915:AAOSTT>2.0.CO;2.
35. INEEL & CFE. *Manual de Obras Civiles, Diseño por Viento* tech. rep. (Instituto Nacional de Electricidad y Energías Limpias, México, July 2020). (In Spanish).
36. Shinozuka, M. & Jan, C.-M. Digital simulation of random processes and its applications. *Journal of sound and vibration* **25**, 111–128 (1972). doi: 10.1016/0022-460X(72)90600-1.
37. Jonkman, J., Butterfield, S., Musial, W. & Scott, G. *Definition of a 5-MW Reference Wind Turbine for Offshore System Development* tech. rep. NREL/TP-500-38060 (National Renewable Energy Laboratory, Golden, USA, Feb. 2009).
38. *ANSYS Mechanical APDL Release 19.0* ANSYS Inc. (2018).
39. Resor, B. R. *Definition of a 5MW/61.5m Wind Turbine Blade Reference Model* tech. rep. SAND2013-2569 (Sandia National Laboratories, Albuquerque, USA, Apr. 2013).
40. Meseguer Ruiz, J., Sanz Andrés, Á., Perales Perales, J. M. & Pinado Carrión, S. *Aerodinámica Civil: Cargas de viento en las edificaciones* (McGraw Hill, Madrid, Spain, 2001). (in Spanish).
41. Clobes, M. & Peil, U. Unsteady buffeting wind loads in the time domain and their effect on the life-cycle prediction of guyed masts. *Structure and Infrastructure Engineering* **7**, 187–196 (2011). doi: 10.1080/15732471003588783.
42. Davenport, A. G. Note on the distribution of the largest value of a random function with application to gust loading. *Proceedings of the Institution of Civil Engineers* **28**, 187–196 (1964). doi: 10.1680/iicep.1964.10112.
43. Winterstein, S. R. & Kashaf, T. Moment-based load and response models with wind engineering applications. *J. Sol. Energy Eng.* **122**, 122–128 (2000). doi: 10.1115/1.1288028.
44. Ding, J. & Xinzhong, C. Moment-based translation model for hardening non-Gaussian response processes. *Journal of Engineering Mechanics* **142**, 06015006 (2016). doi: 10.1061/(ASCE)EM.1943-7889.0000986.
45. Martín del Campo, J. O. & Pozos-Estrada, A. Multi-hazard fragility analysis for a wind turbine support structure: An application to the Southwest of Mexico. *Engineering Structures* **209**, 109929 (2020). doi: 10.1016/j.engstruct.2019.109929.
46. ASCE & AWEA. *Recommended Practice for Compliance of Large Land-based Wind Turbine Support Structures* tech. rep. (American Society of Civil Engineers and American Wind Energy Association, 2011).

## Chapter 4

# Fragility evaluation of typical wind-turbine structures under cyclone-induced loads

According to the Climatescope survey from 2017,<sup>1</sup> developing countries represented about 60% of the total greenhouse gas emissions. This has encouraged the deployment of wind energy projects with the objective of cleaner energy production in these countries. According to the said survey, Mexico was among the countries with the most ambitious target for the reduction of greenhouse gas emissions, which had been one of the main motivations for the growth of wind energy in that country. By 2010 it was estimated that Mexico held an onshore wind potential of about 70 GW.<sup>2</sup> These arguments motivated the development of wind power plant projects along the country, and encourage the continuation of the production of energy from wind resources in a reliable manner.

This section covers the definition of three hypothetical wind turbine structures which are assumed to represent the ones currently installed in Mexico. The dimensions of these structures have been defined based on the characteristics of real turbines, and their structural response is estimated from cyclone-induced loads. Moreover, structural reliability concepts are applied to a fragility analysis of the three turbines.

### 4.1 Wind farms in Mexico

Wind energy has experienced rapid growth in recent decades due to the constant technological development on the subject. This has allowed a reduction in the cost of manufacturing, deployment, and grid integration of wind farms. In the case of onshore wind farms, the cost diminution was estimated to be ~25% from 2010 to 2017,<sup>3</sup> which has contributed to the recent growth of wind farms worldwide, including in developing countries.

Since the construction of the first wind farm in Mexico in 1994, with a capacity of ~1.5 MW,<sup>4</sup> Mexico has experienced considerable growth in wind energy. In 2020 it was within the 5 countries of the Americas with greater installed wind capacity. Moreover, according to the IEA, Mexico was among the countries members of the said association with greater wind energy capacity growth in 2017.<sup>3</sup>

The wind turbines currently installed in Mexico are medium-sized.<sup>3</sup> Their average rated power is 2.1 MW, whereas the average height is 78.2 m.<sup>4</sup> This can be appreciated from the histograms displayed in Figure 4.1, which consider the information on the existing Mexican wind farms until 2019 (also displayed previously in Figure 1.3).

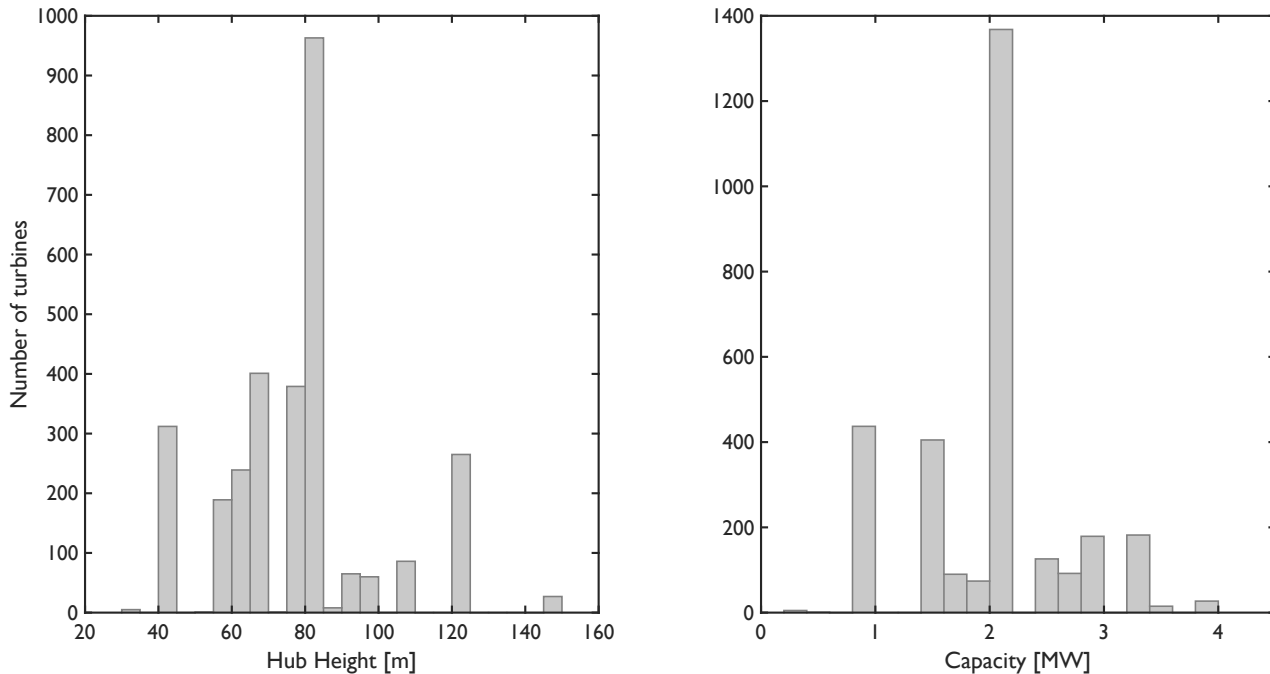


Figure 4.1: Wind turbines in Mexico (2019)

As can be seen from Figure 4.1, two parameters have been selected for the characterization of the existing wind turbines. The hub height is an important parameter, because the tower governs the dynamic response of the structure, as displayed in the structural analyses performed in Chapter 3. Another important parameter is the nominal capacity of the turbine. This is due to the direct dependency of the power extracted by the turbine on the dimension of its main components, like the rotor.

Inasmuch as Mexico is a country exposed to a wide variety of natural hazards, which include tropical cyclones, the need for adequate assessment of wind-farm risk metrics becomes peremptory. Regarding risk assessment, the *vulnerability functions* are key tools that allow relating the intensity of a particular phenomenon acting on a structure with a measure of its probable consequence, given the structural performance. This consequence can be measured, for example, as losses (social or economic).<sup>5</sup> It is thus convenient to evaluate in terms of probability the performance of the structural system under study. In that regard, the *fragility functions* have become a key element in risk analyses, since they relate the intensity of a physical phenomenon with the probability of reaching or exceeding a level of physical damage of the structure. The literature covering the definition of fragility functions on civil structures is wide in earthquake engineering, however, it is scarce on wind engineering topics. Some authors have applied these concepts to the study of the structural performance of buildings under wind action.<sup>6,7</sup> There are also some studies that have investigated the application of fragility functions on wind turbines.<sup>8-14</sup> However, flow-field conditions concordant with tropical cyclones have been disregarded by most of the references found in the literature on the subject.

In the next sections, three turbines are defined based on the more common parametric dimensions summarized in Figure 4.1. These turbines are analyzed under several intensities of cyclone-induced wind action on them, and a fragility analysis is performed considering different performance levels.

## 4.2 Definition of hypothetical wind turbine structures

According to the information displayed in Figure 4.1, three different heights were selected to model representative turbines. To cover a wider range of heights accounting for the existing number of tur-

bines, these heights were selected as 44, 80, and 100 m. Based on these values, a nominal capacity was assumed for each turbine height, respectively: 1.0, 2.5, and 3.3 MW. These capacities were guided from the dimensions displayed in catalogs of one of the manufacturers with the greater number of turbines installed in Mexico. Furthermore, they are fairly concordant with the distribution of capacities summarized in Figure 4.1.

Due to the fact that the analyses described in this chapter correspond to cyclone-induced loads, the turbines were assumed to be in fully-parked position, such as in the cases studied in Chapter 3. This allows simplifying the definition of the turbines to their main components involved in the aerodynamic loads on the structure and its dynamic response. That is, the definition of the turbines is centered on the description of the aerodynamic and structural characteristics of the blades, the tower, and the nacelle.

The analyses on the turbines were performed by means of finite element modeling. The FEM was developed in APDL, and a criterion similar to the one described in Chapter 3 was adopted for the definition of the models. However, an important difference in the modeling procedure adopted for the three turbines is the aerodynamic damping, since it was disregarded in the present analysis. This criterion was adopted because the aerodynamic characteristics of the turbines account for many assumptions, as described ahead in this section, and it would be futile to detail the contribution of aerodynamic damping in the flow-induced forces and structural behavior. Moreover, as performed in the analyses developed in Chapter 3, the yaw actuator and drive train are assumed as rigid elements. The following subsections describe the criteria adopted for the dimension definition of the turbines and the development of their respective FEMs for structural analyses.

#### 4.2.1 Definition of blades and nacelle

Based on the selected hub heights for the hypothetical turbines (44, 80, and 100 m), three nominal capacities were assumed for each of them, respectively, 1, 2.5, and 3.3 MW. These capacities were selected based on the commercial information from one of the wind turbine manufacturers with the greater number of turbines deployed in Mexico. The relevance of the selection of the turbine capacities stands in the definition of rotor diameters. According to the information from the same manufacturer, the rotor diameters for the aforementioned capacities are, respectively, 50, 90, and 114 m. These rotor dimensions were selected to define the properties of the turbines to be analyzed, and a hub radius equal to 1.5 m was assumed for the three cases.

The National Renewable Energy Laboratory has published aids and tools for the estimation of costs of, onshore and offshore, wind energy. These tools are mainly based on the sizes of turbine components,<sup>15</sup> and the information from these models derives from industry data. The reports include models for the estimation of wind-turbine component cost and dimension, and the input variables are mainly rotor sizes, among other parameters that describe the turbine. From one of the models published by the NREL,<sup>15</sup> the masses for the blades were estimated, respectively as: 1,897.14; 8,699.09; and 12,808.28 kg.

The dynamic properties of these blades were approximated based on a model fitting the fundamental frequency values of three wind turbine blades as reported by other studies.<sup>16</sup> From this information, the blade frequencies in the flap-wise direction were estimated as 1.85, 1.20, and 0.94 Hz, in ascending order of blade length. In the case of the edge-wise frequencies, these were estimated in an analogous manner respectively as 2.15, 1.60, and 1.38 Hz. To satisfy these dynamic characteristics in the FEM, a constant rectangular cross-section (of cross-section area  $b \times h$ ) was assumed along the beam elements composing the blades of the turbines. For the FEM, an elastic modulus of 38 GPa was assumed for the blades. All the aforementioned assumptions are summarized in Table 4.1.

Analogously as performed for the blade characteristics, the masses for the nacelle and hub of the three turbines were approximated from fittings performed to values displayed in other references

**Table 4.1:** Summary of blade properties for the three wind turbines

Rated Power (MW)	Blade Length (m)	Flap-wise frequency (Hz)	Edge-wise frequency (Hz)	Total mass (kg)	Distributed mass (kg/m)	$b$ (m)	$h$ (m)
1.0	23.50	1.85	2.15	1,897.14	80.73	0.525	0.600
2.5	43.50	1.20	1.60	8,699.09	199.98	0.950	1.250
3.3	55.50	0.94	1.38	12,808.28	230.78	1.075	1.600

from the NREL.<sup>17</sup> The nacelle and hub masses were estimated as summarized in Table 4.2. The hub and nacelle were modeled by means of the element MASS21 in APDL. These elements were assumed as lumped masses at the top of the tower, linked to the tower elements by means of the element MPC184. This criterion is analogous to the one described in Section 3.3.2. The blades were modeled by means of the element BEAM4, assuming a rectangular cross-section. The modeling of the tower for the three turbines is described in the following section.

**Table 4.2:** Summary of hub and nacelle properties for the three wind turbines

Rated Power (MW)	Hub mass (kg)	Nacelle mass (kg)
1.0	22,531.75	28,444.55
2.5	40,577.14	72,237.31
3.3	51,372.38	126,362.73

#### 4.2.2 Definition of the tower

In reality, each wind turbine tower structure has its peculiarities. For the present study, due to the fact that the hypothetical turbines are based only on overall dimensions, the definition of the tower structure followed a criterion based on the scaling of an already-defined wind turbine support structure. The wind turbine tower prototype presented in the work of Bazeos et al.<sup>18</sup> is described in great detail, thus, it was selected for its scaling for the three wind turbines. The original steel structure is nearly 38.0 m high and is defined from three main hollow cylindrical sections of three different diameters and several thicknesses, connected by hollow truncated conical sections for the transition between the tower elements. The proportions of the sections composing the geometry of the steel tower have been scaled holding the same thickness-to-diameter ratios from the original reference,<sup>18</sup> following the selected heights for the hypothetical wind turbines. The overall dimensions for the three hypothetical turbines are summarized in Table 4.3.

**Table 4.3:** Overall dimensions of the modeled wind turbine towers

Property	Rated Power [MW]		
	1.0	2.5	3.3
Hub height [m]	44.00	80.00	100.00
Tower bottom diameter [m]	3.20	5.90	7.40
Tower top diameter [m]	2.10	3.80	4.80
Tower bottom thickness [mm]	19.00	32.00	45.00
Tower top thickness [mm]	13.00	22.00	25.00

Analogously to what has been described in Section 3.3.2, the tower structure was modeled in APDL by means of the element BEAM188, assuming an elastic modulus of 210 GPa and a Poisson

modulus of 0.33 for the material. Moreover, as performed similarly for the case analyzed in Section 3.3.2, the density for the tower material was assumed as  $8,243 \text{ kg/m}^3$  to account for additional mass involved in the weight of the tower from stiffeners, welding, and other possible connection elements.

The FEM of the turbines was developed under the assumptions described previously. Their identified dynamic properties are summarized in Table 4.4. Note that, although no elaborate structural design was performed on the defined structures, their natural frequencies are comparable to the values reported for benchmark wind turbines, such as those defined for the project WindPACT of the NREL.<sup>19</sup> Moreover, their structural capacities are expected to resemble those of a commercial wind turbine support structure, inasmuch as their structural density per unit height is comparable to the values displayed by the aforementioned reference turbines.<sup>19</sup> This claim can be sustained considering that the ultimate strength of a structural element is strongly related to the quantity of material used for its construction, and the cross-section geometries from the hypothetical turbines and the ones from the WindPACT project are similar. Figure 4.2 displays a schematic comparison between the values computed for the developed models and the ones from the aforementioned reference turbines, including also the values for the reference turbine analyzed in Chapter 3.<sup>20</sup> Furthermore, a comparison between the elastic and plastic section moduli of the NREL turbines, and the ones defined in this study is presented in Figure 4.3. The compared values are particular to locations at the base of the towers, and a fraction of 0.3 times their height. A fair resemblance between the structural characteristics of the turbines defined in this study and the ones from the reference studies can be appreciated from both figures.

**Table 4.4:** Dynamic properties of the modeled wind turbine towers

Property	Rated Power [MW]		
	1.0	2.5	3.3
Hub height [m]	44.00	80.00	100.00
Tower mass [kg]	21,718.65	122,844.04	231,630.99
Frequency (Side-to-Side) [Hz]	0.479	0.383	0.338
Frequency (Fore-Aft) [Hz]	0.484	0.390	0.344

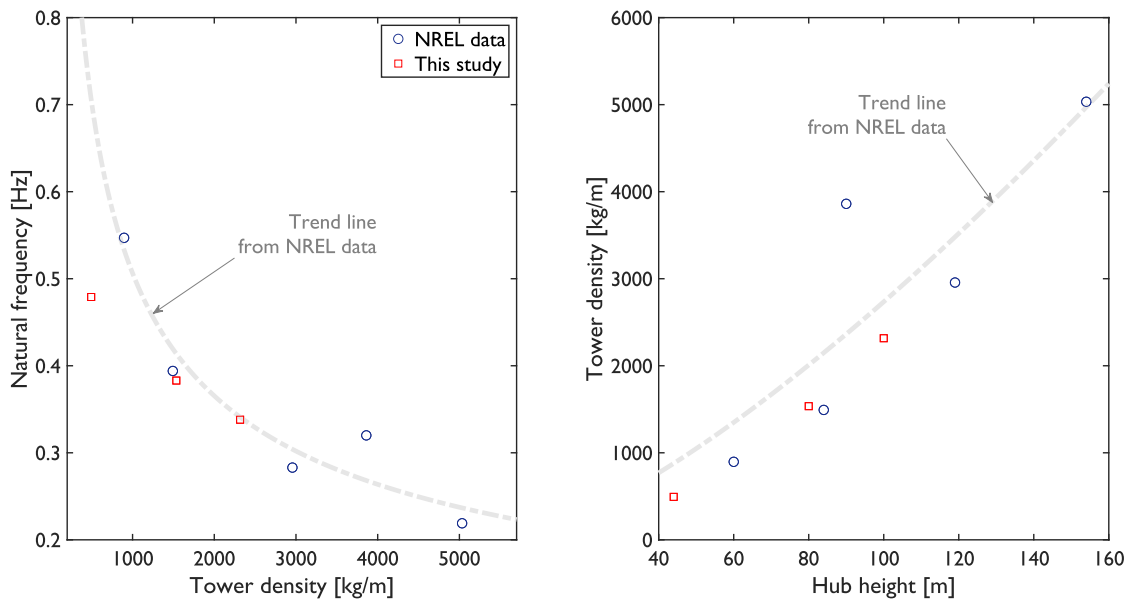


**Figure 4.2:** Structural summary of the hypothetical and reference wind turbines

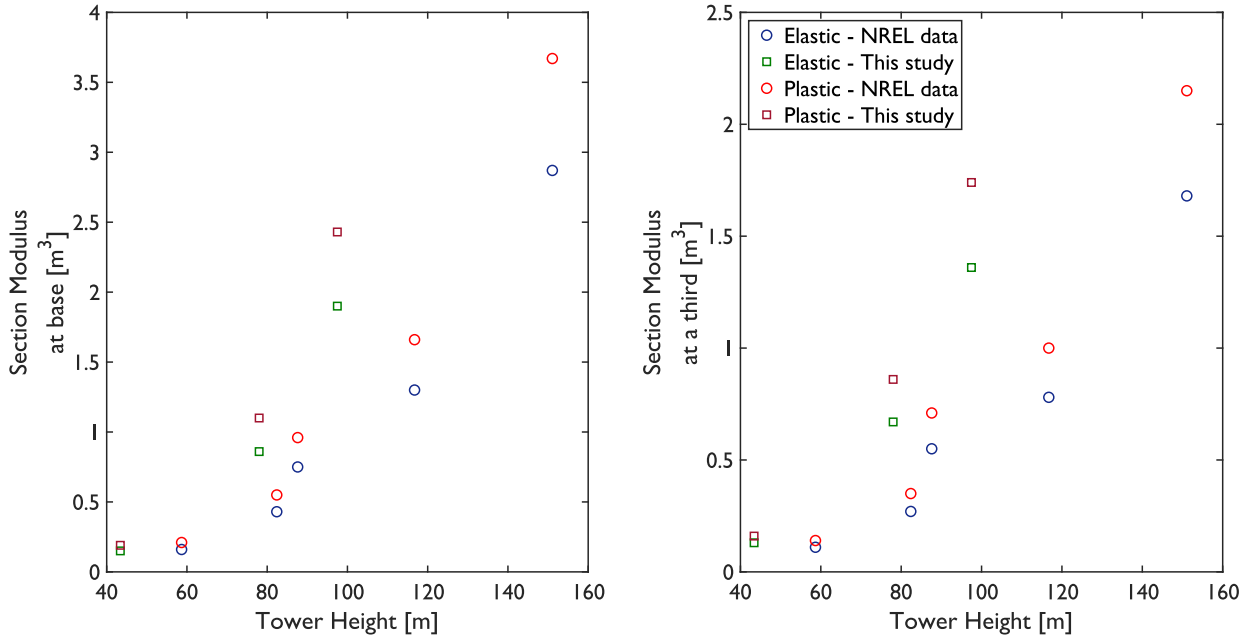


Figure 4.3: Section moduli of the hypothetical and reference wind turbines

### 4.3 Wind loads

The criteria adopted for the computation of the loads on the structures for their fragility analyses are described in this section. These include the aerodynamic assumptions for the modeled structures, as well as the flow-field characteristics.

#### 4.3.1 Wind field simulation

The wind field assumed for the present analyses is concordant to tropical-cyclone conditions. The same models and procedures described in Section 3.2.1 for the simulation of the tropical cyclone boundary layer were employed for all the analyses. Due to the actual distribution of wind farms in Mexico, the assumptions adopted for the present analyses consider a hypothetical site located in the Mexican state of Oaxaca. Dissimilarly to the conditions assumed for the studies carried out in Chapter 3, only one site was considered for the present analyses. This is due to the number of time-history computations necessary for the fragility analysis of the three turbines.

As commented in previous paragraphs, a fragility analysis describes the probability of a structural system to reach or exceed a certain performance level (or damage state) under the action of a specific phenomenon given an intensity level of it. In the present study, the phenomenon is cyclone-induced wind action on the wind turbines. To determine the damage probability, a set of flow-field simulations was performed for every intensity level considered for the analysis of each structure. The mean wind speed measured at a height of 10 m was selected as the intensity measure for the fragility analyses. Moreover, recalling some of the assumptions necessary for the implementation of the models summarized in Chapter 3, a latitude angle equal to  $16.581^\circ$  was considered for all the simulations.

To cover the wide range of intensities necessary for the evaluation of the structural response, and dissimilarly to the criteria adopted for the analyses performed in Chapter 3, a probability distribution for the surface pressure deficit  $\Delta p_s$  was disregarded for the present study. Due to this assumption,  $\Delta p_s$  was premised as a uniform random variable ranging from values from 15 to 150 hPa for each wind-field simulation. As for the radial position for the site under analysis with respect to the center



of the storm, the same assumptions adopted for the analyses described in Chapter 3 were used, i.e., the radial position was assumed as a random variable with uniform distribution in each simulation, assigning it a random value between 0 and 200 km.

The range of intensities covered for the simulations consists of 20 levels. These intensity levels assume values of mean wind speed at 10 m height from 30 to 70 m/s, in increments of 2 m/s. A total of 30 wind field simulations, or *seeds*, were considered for each intensity level for each of the turbines. Figure 4.4 displays some of the values computed of the mean wind speed profiles simulated for the 1 MW wind turbine, along with some of the values of the parameters involved in the simulation of the TCBL.

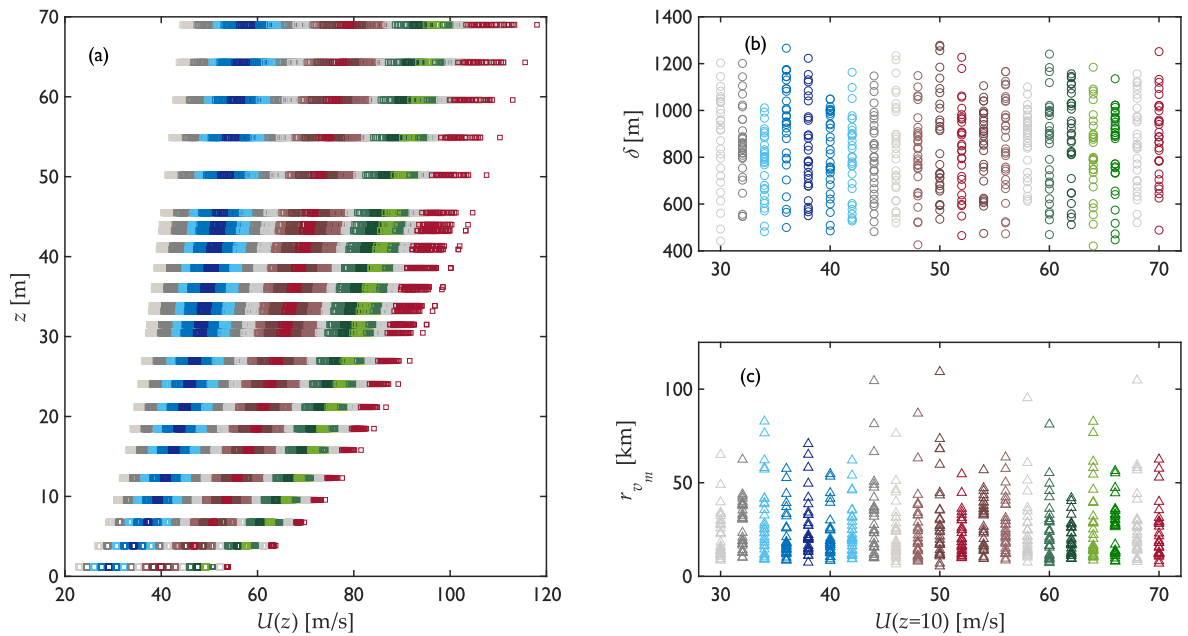


**Figure 4.4:** TCBL flow-field simulations for the 1 MW wind turbine: (a) Mean velocity profile, (b) Height of maximum wind, (c) Radius of maximum wind

### 4.3.2 Aerodynamic loads

As mentioned before in this chapter, due to the fact that the turbines are hypothetical, the aerodynamic properties of their blade elements are assumed to be represented by an airfoil common for wind energy purposes. However, an elaborate aerodynamic definition of these elements is out of the scope of the analyses. Moreover, the conditions assumed for the present study are similar to the ones described in Chapter 3, where the main aerodynamic contribution to the loads on the structure is the tower element. Therefore, an elaborate aerodynamic definition and an aeroelastic analysis of the structure are disregarded.

The blades of the three turbines were assumed to be represented by a NACA 63-415 airfoil. The chord of these blades was assumed to vary linearly along each one, from 0.11 times the blade length at a fraction of 0.18 the blade length (disregarding the hub radius), to 0.04 times the blade length at the outer rotor radius. The aerodynamic coefficients of the assumed blades at a Reynolds number of  $1E6$  are displayed in Figure 4.5. Moreover, analogously to the assumptions regarded in the analyses performed in Chapter 3, the blades were assumed to be oriented with the chord parallel to the wind direction. The root of the blade was assumed as a circular section, and the aerodynamic coefficients

at radial positions between the root and the position at 0.18 times the blade length were assumed to vary linearly. Lastly, the tilt angle and pre-cone of the blades were disregarded on the models.

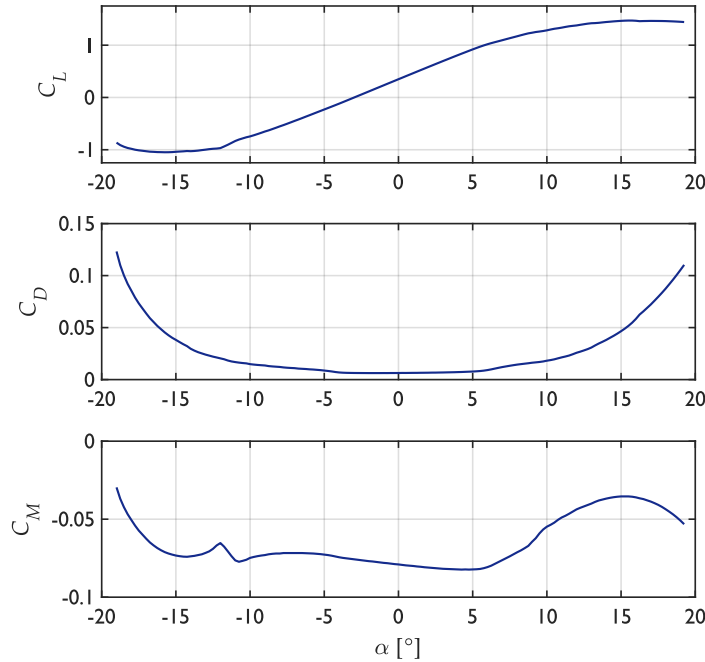


Figure 4.5: Aerodynamic coefficients of the assumed blades

The circular sections were assumed to produce only drag forces, and any other aerodynamic phenomenon (e.g., vortex shedding) was disregarded. The drag coefficients of all circular sections involved in the model were assumed to be 1.2. Thus, the forces per unit length applied to the FEM were computed from the conventional equation of flow-induced forces, expressed as (e.g., for the drag force):

$$D = \frac{1}{2} \rho U^2 c_i C_D \quad (4.1)$$

where  $c_i$  represents the characteristic length of the element where the force is being applied, e.g., the diameter of the tower section, or the blade chord. The lift force and aerodynamic moments were computed analogously, considering their respective aerodynamic coefficients.

#### 4.4 Results and fragility analyses

Structural risk is often evaluated in terms of the probability of exceeding a value of a decision variable of interest.<sup>21</sup> This decision variable is an attribute that can be measured and that reflects the structural performance of a particular system, e.g., economic losses. The level of performance of a particular structure can be defined through thresholds of damage, referred often as *limit states*, or *damage thresholds*. The limit state can be understood as the boundary between two different damage conditions, which are often called *damage states*.<sup>5</sup> Fragility functions, or fragility curves, provide information necessary in risk assessment of any kind of hazard, as they allow to estimate the probability of reaching a certain limit state, given the occurrence of a phenomenon that affects the structure with a certain level of intensity. The intensity of the phenomenon is expressed in terms of an intensity measure, which must characterize adequately the phenomenon, and correlate with the structural response.

#### 4.4.1 Response histories

A total of 30 turbulent wind field simulations were performed for each wind intensity and each of the modeled turbines. Each of the simulations considered a total duration of 600 s. A total of 1,800 time-history analyses were performed. To save computing time, these analyses were elastic. The analyses could be carried out in either the frequency or the time domain, however, the time-domain approach was adopted for a simpler definition and characterization of the time series and systematic analyses in the APDL code. A damping ratio of 1% of the critical damping was considered for the analyses, assuming Rayleigh damping coefficients from the first two bending frequencies of the tower. Figure 4.6 displays an example of the displacement histories for the three wind turbines, for a wind intensity  $\bar{U}(10) = 38$  m/s. Note that the first 50 s from the signal were disregarded to avoid the inclusion of numerical inaccuracies from the start of the analysis.

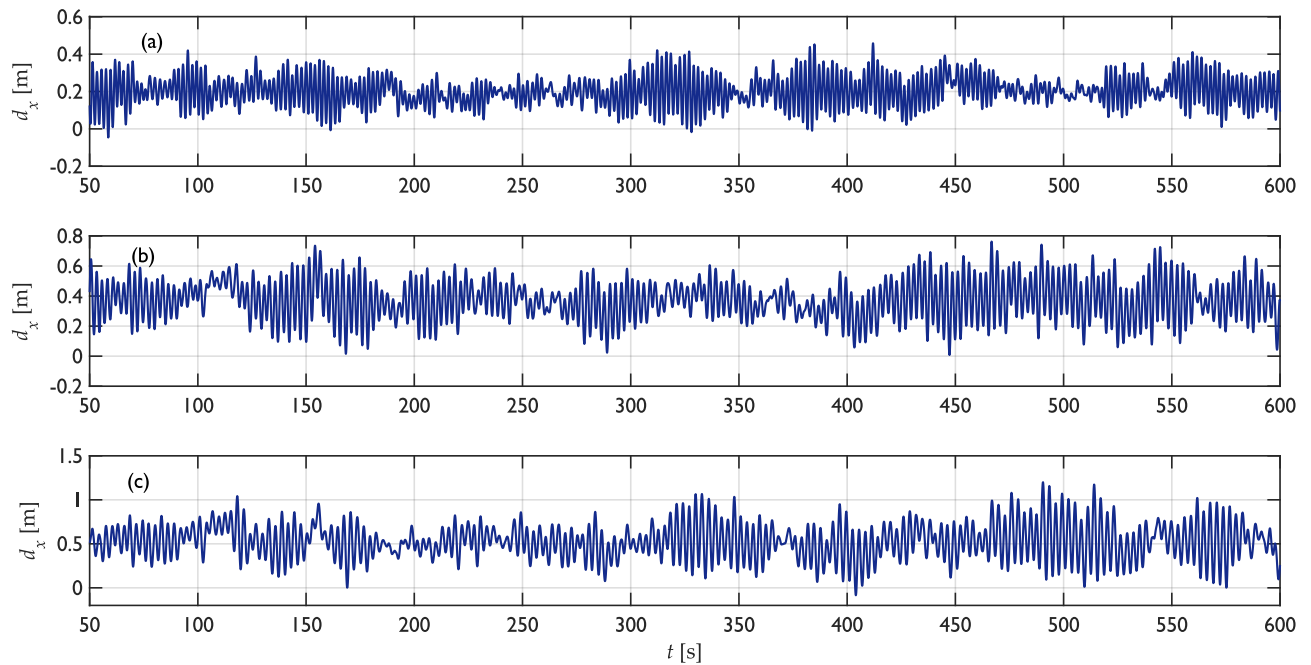


**Figure 4.6:** Along-wind displacement at the top of the tower: (a) for the 1MW turbine, (b) for the 2.5MW turbine, (c) for the 3.3MW turbine

#### 4.4.2 Damage states

In the present analysis, as mentioned previously, the intensity measure selected for the fragility evaluation of the turbines is the mean wind speed measured at 10 m height,  $\bar{U}(10)$ . This intensity measure was selected because it delivers in terms of practicality, for it holds a direct correlation with the flow-induced forces on the structure, and therefore, with the structural response. This measure also allows the analytic evaluation of the mean annual exceedance rate of the decision variable, as exemplified in publications related to this study.<sup>4</sup>

As for the evaluated levels of performance, in the present analyses, three damage states were considered. These damage states can be associated with the occurrence of minor, moderate, and complete damage (collapse) on the wind turbine support structure. The thresholds for these damage states are defined in the following.

### *Tower top displacement*

Design standards for common civil structures often establish displacement limits for specific actions. These limits are defined as an attempt to avoid physical damage of the structure, as well as to avoid collision between other bodies that might be near, to avoid an unstable configuration of the system, damage to the non-structural elements, or excessive vibration. Wind turbines are no exception to these kinds of problems. However, in common wind turbine standards, there is no specification on this criterion.

The fragility evaluation of the support structure of a wind turbine under seismic action performed by Nuta was published in 2011.<sup>22,23</sup> Among the diverse damage measures explored in their work is the maximum horizontal displacement at the top of the tower. Moreover, Nuta et al.<sup>23</sup> considered as damage state a residual displacement of the tower. They regarded criteria for the erection of steel structures, which defined values of recumbence between 0.1% and 0.2% of the tower height. According to the analyses performed on an elaborate FEM by the aforementioned authors, the appearance of a residual displacement of 0.2% occurred at an average lateral displacement of 2.50% of the tower height.<sup>22</sup>

On this basis, for this study, a lateral displacement of 1.25% was assumed as a limit state to consider the occurrence of a residual displacement on the tower structure. Note that the analyses performed by Nuta<sup>22</sup> assume earthquake action on the structure. However, the structure analyzed in the aforementioned work holds sufficient dynamic resemblances with the turbines assumed for this study to consider the adopted assumptions as reasonable ones.

### *Nominal capacity of the tower*

The large slenderness ratios of steel tubular sections, such as those displayed by most wind turbine support structures, encouraged the publication of recommendations for the structural design of these elements.<sup>24</sup> According to experimental tests performed on a natural-scale wind turbine tower,<sup>25</sup> the expressions presented by the ASCE and AWEA in their recommendations<sup>24</sup> provided an adequate prediction of the bending capacity of the tested element at the evaluated positions.

The nominal flexural strength capacity as specified in the ASCE recommendations<sup>24</sup> has been summarized in Equations 3.27 and 3.28. As can be seen in those expressions, the flexural capacity of the tower is defined by the yield stress of the material (assumed as 350 MPa in the present analysis), the linear section modulus, and the elastic modulus of the material. The nominal resistance of the tower structure is represented by the critical stress  $F_{cr}$ , also known as 'buckling stress'. Notwithstanding the relevance of the aforementioned expressions for the estimation of  $F_{cr}$ , the collapse of the tower (i.e., the buckling of the section) might also be adequately represented by other responses measured at the tower, as described next.

### *Buckling of the tower*

As pointed out by Jay et al.,<sup>26</sup> the conventional stress-based design expressions for thin shell structures suggested in many standards are often over-conservative for slender tubular sections. In the same reference is remarked that some structural standards, such as the Eurocode 3, allow the estimation of the buckling capacity from FEMs of the shell structure.

Despite the geometric similarities among the hypothetical structures modeled for this study, a detailed numerical analysis of them was omitted to avoid the spending of computational resources in the analysis of structures, the properties of which have been extrapolated. However, the analysis in pure bending to estimate the flexural capacity of the NREL 5MW reference wind turbine<sup>20</sup> has been performed in several references. From a non-linear analysis performed on the aforementioned turbine,<sup>13</sup> as well as from other studies related to the buckling capacity of tubular shell structures,<sup>27</sup> values of section curvature ( $\kappa_s$ ) and flexure capacity were analyzed.

The normalized curvature at which the flexural capacity of the tower section drops was identified from the non-linear numerical analyses performed on the support structure of the NREL 5-MW reference wind turbine.<sup>13</sup> This value of structural response was normalized with respect to the plastic curvature  $\kappa_p$  of the steel section. The plastic curvature is defined as  $\kappa_p = M_p/EI$ , where  $M_p$  is the plastic moment of the tower section, and  $I$  is its second area moment. At a curvature of approximately  $0.75\kappa_p$ , the drop of flexural resistance was identified, which is of the order of values observed from experimental tests performed on tubular elements of comparable diameter-to-thickness ratios.<sup>27</sup> On these bases, the limit state was defined from the aforementioned value of the plastic curvature. The defined limit and damage states for the fragility analyses are summarized in Table 4.5.

**Table 4.5:** Damage states defined for the fragility analyses

Damage State	Description	Damage threshold
DS1	Residual displacement of the tower	$d_x = 0.0125H$
DS2	Nominal moment of the tower	$M_y = M_n$
DS3	Collapse by buckling	$\kappa_s = 0.75\kappa_p$

#### 4.4.3 Fragility functions

From each of the response histories, such as those displayed in Figure 4.6, and for each of the turbines under all the evaluated levels of intensity, the maximum values of response were identified. The probability distribution that represented better these extremes was determined from a Kolmogorov-Smirnov test, considering the normal (NR), lognormal (LN), and generalized extreme value (GEV) distributions. Figure 4.7 displays a summary of the computed  $p$ -values from these tests for the three turbines and their responses representing the defined damage states. From Figure 4.7 it can be seen that all the evaluated distributions have a high probability to represent the random behavior of the response maxima. However, the GEV distribution displayed higher  $p$ -values for the majority of cases. Notwithstanding, a comparison between the fragility estimates computed when considering the GEV and the lognormal distribution for all the responses is presented in the following.

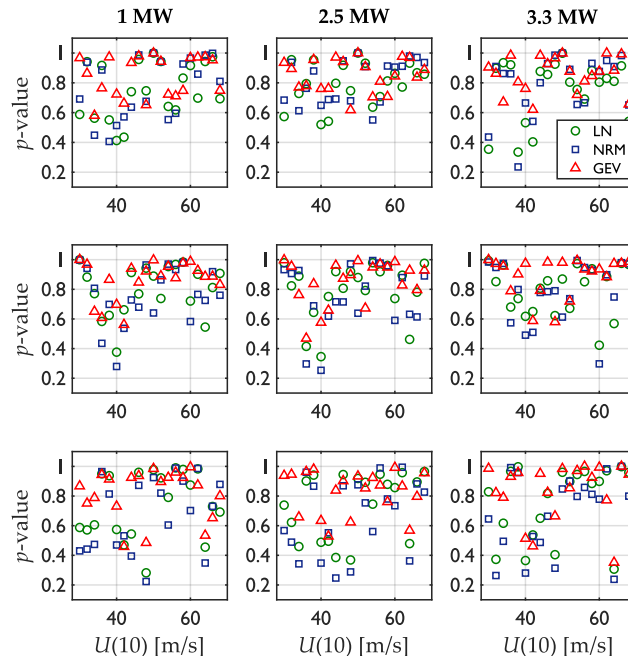


**Figure 4.7:** Summary from goodness-of-the-fit tests performed on the response maxima (from the top row to the bottom row: for DS1, DS2, and DS3)

Fragility functions are commonly expressed as a lognormal cumulative distribution function (CDF), defined from its parameters  $\mu_i$ , and  $\sigma_i$ , as in the following equation:

$$F_i(IM) = \Phi \left[ \frac{\ln(IM) - \mu_i}{\sigma_i} \right] \quad (4.2)$$

where  $\Phi(\cdot)$  represents the standard-normal CDF,  $IM$  the intensity measure describing the probability of failure (in the present study  $\bar{U}(10)$ ), and the sub-index  $i$  stands for the damage state under evaluation.

The values of probability of failure can be computed from the evaluation of Equation 3.29 at each intensity level. However, if the resistance of the structure is assumed as deterministic, the probability of failure can be computed from the complement of probability of the CDF representing the response maxima, evaluated at the limit state. Once the probability of failure at each evaluated intensity is found for each of the structures, the parameters defining the fragility function can be determined by means of a linear fitting of Equation 4.2. Table 4.6 summarizes the parameters  $\mu_i$  and  $\sigma_i$  computed for each of the damage states for the three turbines. These values include the estimations considering cases where either a GEV distribution or a lognormal distribution represent the behavior of the data.

**Table 4.6:** Parameters for the fragility functions

		GEV		LN	
		$\mu$	$\sigma$	$\mu$	$\sigma$
1 MW	DS1	3.7653	0.0528	3.7706	0.0421
	DS2	3.9411	0.0443	3.9476	0.0420
	DS3	4.0293	0.0558	4.0319	0.0449
2.5 MW	DS1	3.6799	0.0662	3.7038	0.0498
	DS2	3.7603	0.0659	3.7884	0.0471
	DS3	3.9327	0.0478	3.9540	0.0478
3.3 MW	DS1	3.6286	0.0477	3.6527	0.0521
	DS2	3.7258	0.0504	3.7584	0.0499
	DS3	3.8486	0.0564	3.8897	0.0505

Note that the parameters identified assuming that the maxima of the structural response are represented by a GEV distribution are considerably similar to those computed assuming a lognormal distribution. For the sake of a clearer visualization of the influence of these values on the estimation of the probability of failure, a comparison between the implied fragility functions is displayed in Figure 4.8.

## 4.5 Conclusions

The study of three hypothetical wind turbines under cyclone-induced action has been presented in this chapter. The results from this study have been applied to a fragility analysis, and subsequent vulnerability and risk analysis, as has been presented in archived publications.<sup>4</sup> Moreover, the following comments and considerations regarding the described analyses can be made:

- The selected hub heights, as well as the rated power of the turbines, are concordant with the data available from Mexican wind energy plants. This can be observed by comparing the selected values with the data displayed in Figure 4.1. Moreover, the definition of the three hypothetical turbines follows models established from commercial data. Therefore, the selected dimensions are, with rational sustenance, assumed to be representative of the wind turbines built in reality.
- A detailed structural design and the determination of the structural capacity of the selected support structures have been omitted in the present analysis for the sake of computing-time

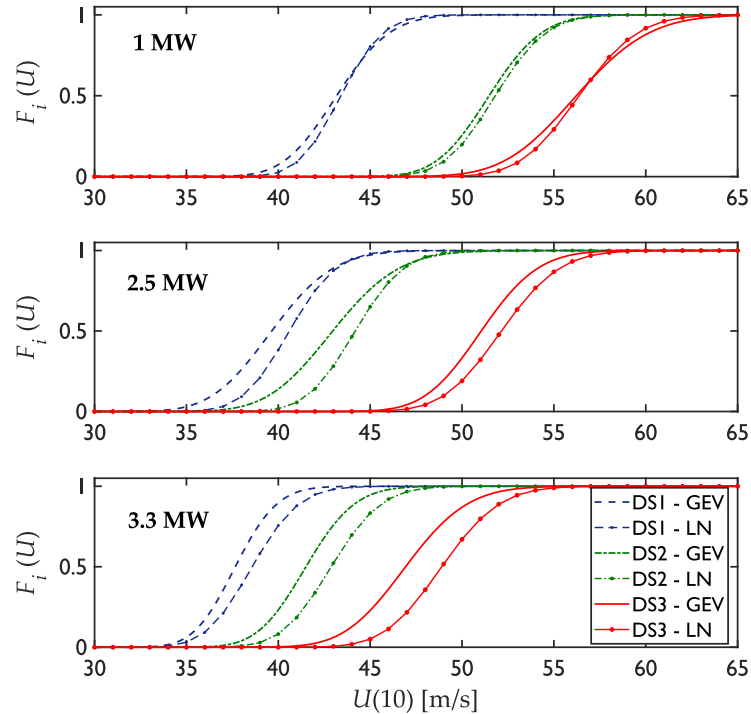


Figure 4.8: Fragility functions for the analyzed wind turbines under cyclone-induced action

economy. However, structural characteristics (such as dynamic properties, and material density per unit height) from the hypothetical wind turbines analyzed are comparable to the ones from benchmark wind turbines that have been derived from commercial data. Insofar as the structural capacity of an element is strongly related to the quantity of material employed for its construction, it appears logical to assume that the hypothetical wind turbines will display a similar tendency in structural capacity to that of an actual structure. This assumption is supported by the section moduli of the structures. Moreover, the aforementioned benchmark wind turbines are structures derived from data of turbines from the early 2000s, which is consistent with the age of existing wind farms in Mexico, whose earliest wind energy plant dates from the same period of time.

- Tropical cyclones are a natural phenomenon capable of producing serious damage to civil infrastructure. Wind farms located in cyclone-prone regions are vulnerable to their actions. Recent studies on available measurements from the TCBL have been proposed in the literature, and have been applied in this study to determine the impact of cyclone-induced loads on wind turbines. Moreover, inasmuch as wind turbines are wind-sensitive structures that can cover a high extent of the TCBL, the consideration of differences in the mean velocity profile and turbulent-energy distribution during tropical cyclones is pertinent. The flow-field simulations performed in this study represent the particular conditions of cyclonic wind flow. For the implementation of the aforementioned expressions in the simulation of the TCBL, a hypothetical location of the wind energy plants was assumed in the Mexican state of Oaxaca, which holds the greater part of the installed capacity from wind energy sources in Mexico.
- Three damage states were defined to perform the fragility analyses of the structures. These were defined by structural responses that determine the performance of the tower. The probability of failure at each wind intensity was evaluated from the respective structural response associated with each damage state. The goodness-of-the-fit tests performed on the maximum values of structural responses considered three CDFs. All the evaluated distributions displayed a fair probability of representing the randomness of the response maxima. However, the gener-

alized extreme value distribution displayed a higher probability of representing the structural responses for the greater part of the cases.

- Among the limit states defined for the fragility analyses, the buckling stress of the tower (as defined in recommendations for the structural design of wind turbine support structures) is more likely to occur than the selected fraction of the plastic curvature of the sections. This is consistent in the three analyzed structures. However, this fact is also concordant with the observation from other authors who have described the stress-criterion design of slender tubular structures as ‘over-conservative’.<sup>26</sup> Further studies on wind turbine structures more elaborately detailed and properly defined are necessary to provide more insights into such an assertion.
- For the sake of visualization of the influence of probability distribution selection and its representation of the response maxima, two distributions were considered when estimating the parameters for the fragility functions. Despite the resemblances displayed in the parameters of  $F_i(IM)$  obtained with either of the evaluated CDFs, evident differences in the values of fragility exist in some of the damage states considered.
- In the case of the 1-MW wind turbine, the differences found in the fragility estimates considering two different probability distributions for the structural response can be assumed negligible. However, some of the estimates of the probability of failure for the other turbines can be significant. Overall, the assumption of a GEV distribution describing the random nature of the response maxima displayed greater fragility estimates. Notwithstanding, the differences found between the real distribution of the structural response maxima and the lognormal distribution can be considered of no statistical significance.

## References

1. Climatescope. *Climatescope 2020* <https://global-climatescope.org/results/mx#power-market>. (accessed: 11.08.2021).
2. INEEL. *Project “Wind Atlas for Mexico (AEM)”* <https://aems.ineel.mx/aemdata/About.aspx>. (accessed: 12.08.2021).
3. IEA-Wind. *IEA Wind Technology Collaboration Programme 2017 Annual Report* tech. rep. (International Energy Agency, 2017). <https://iea-wind.org/iea-publications/#ut-portfolio-details-wrap-101>.
4. Jaimes, M. A., García-Soto, A. D., Martín del Campo, J. O. & Pozos-Estrada, A. Probabilistic risk assessment on wind turbine towers subjected to cyclone-induced wind loads. *Wind Energy* **23**, 528–546 (2020). doi: 10.1002/we.2436.
5. Ptilakis, K., Crowley, H. & Kaynia, A. M. *SYNER-G: Typology Definition and Fragility Functions for Physical Elements at Seismic Risk* (eds Ptilakis, K., Crowley, H. & Kaynia, A. M.) chap. 1 (Springer, 2014).
6. Cui, W. & Caracoglia, L. A unified framework for performance-based wind engineering of tall buildings in hurricane-prone regions based on lifetime intervention-cost estimation. *Structural safety* **73**, 75–86 (2018). doi: 10.1016/j.strusafe.2018.02.003.
7. Lima-Castillo, I. F., Gómez-Martínez, R. & Pozos-Estrada, A. Methodology to develop fragility curves of glass façades under wind-induced pressure. *International Journal of Civil Engineering* **17**, 347–359 (2019). doi: 10.1007/s40999-018-0360-6.
8. Quilligan, A., O’Connor, A. & Pakrashi, V. Fragility analysis of steel and concrete wind turbine towers. *Engineering Structures* **36**, 270–282 (2012). doi: 10.1016/j.engstruct.2011.12.013.
9. Mensah, A. F. & Dueñas-Orsorio, L. Improved reliability of wind turbine towers with tuned liquid column dampers (TLCDs). *Structural safety* **47**, 78–86 (2014). doi: 10.1016/j.strusafe.2013.08.004.



10. Wei, K. *et al.* *Performance Levels and Fragility for Offshore Wind Turbine Support Structures during Extreme Events in Structures Congress 2015* (2015), 1891–1902.
11. Asareh, M.-A., Schonberg, W. & Volz, J. Fragility analysis of a 5-MW NREL wind turbine considering aero-elastic and seismic interaction using finite element method. *Finite Elements in Analysis and Design* **120**, 57–67 (2016). doi: 10.1016/j.finel.2016.06.006.
12. Fitzgerald, B., Sarkar, S. & Staino, A. Improved reliability of wind turbine towers with active tuned mass dampers (ATMDs). *Journal of Sound and Vibration* **419**, 103–122 (2018). doi: 10.1016/j.jsv.2017.12.026.
13. Martín del Campo, J. O. & Pozos-Estrada, A. Multi-hazard fragility analysis for a wind turbine support structure: An application to the Southwest of Mexico. *Engineering Structures* **209**, 109929 (2020). doi: 10.1016/j.engstruct.2019.109929.
14. Yuan, C., Li, J., Chen, J., Xu, Q. & Xie, Y. Study on the Influence of Baseline Control System on the Fragility of Large-Scale Wind Turbine considering Seismic-Aerodynamic Combination. *Advances in Civil Engineering* **2020** (2020). doi: 10.1155/2020/8471761.
15. Fingerish, L., Hand, M. & Laxson, A. *Wind Turbine Design Cost and Scaling Model* tech. rep. NREL/TP-500-40566 (National Renewable Energy Laboratory, Golden, United States, Dec. 2006).
16. Ashwill, T. D. *Cost Study for Large Wind Turbine Blades* tech. rep. SAND2003-1428 (Sandia National Laboratories, Albuquerque, USA, May 2003).
17. Guo, Y., Parsons, T., King, R., Dykes, K. & Veers, P. *An Analytical Formulation for Sizing and Estimating the Dimensions and Weight of Wind Turbine Hub and Drivetrain Components* tech. rep. NREL/TP-5000-63008 (National Renewable Energy Laboratory, Golden, USA, June 2015).
18. Bazeos, N. *et al.* Static, seismic and stability analyses of a prototype wind turbine steel tower. *Engineering Structures* **24**, 1015–1025 (2002). doi: 10.1016/S0141-0296(02)00021-4.
19. Rinker, J. & Dykes, K. *WindPACT Reference Wind Turbine* tech. rep. NREL/TP-5000-67667 (National Renewable Energy Laboratory, Golden, USA, Apr. 2018).
20. Jonkman, J., Butterfield, S., Musial, W. & Scott, G. *Definition of a 5-MW Reference Wind Turbine for Offshore System Development* tech. rep. NREL/TP-500-38060 (National Renewable Energy Laboratory, Golden, USA, Feb. 2009).
21. Ciampoli, M. & Petrini, F. Performance-based Aeolian risk assessment and reduction for tall buildings. *Probabilistic Engineering Mechanics* **28**, 75–84 (2012). doi: 10.1016/j.probengmech.2011.08.013.
22. Nuta, E. *Seismic Analysis of Steel Wind Turbine Towers in the Canadian Environment* MA thesis (University of Toronto, 2010).
23. Nuta, E., Christopoulos, C. & Packer, J. A. Methodology for seismic risk assessment for tubular steel wind turbine towers: application to Canadian seismic environment. *Canadian Journal of Civil Engineering* **38**, 293–304 (2011). doi: 10.1139/L11-002.
24. ASCE & AWEA. *Recommended Practice for Compliance of Large Land-based Wind Turbine Support Structures* tech. rep. (American Society of Civil Engineers and American Wind Energy Association, 2011).
25. Sim, H.-B., Prowell, I., Elgamal, A. & Uang, C.-M. Flexural tests and associated study of a full-scale 65-kW wind turbine tower. *Journal of Structural Engineering* **140**, 04013110 (2014). doi: 10.1061/(ASCE)ST.1943-541X.0000924.
26. Jay, A. *et al.* Spirally welded steel wind towers: Buckling experiments, analyses, and research needs. *Journal of Constructional Steel Research* **125**, 218–226 (2016). doi: 10.1016/j.jcsr.2016.06.022.
27. Elchalakani, M., Zhao, X. L. & Grzebieta, R. Bending tests to determine slenderness limits for cold-formed circular hollow sections. *Journal of Constructional Steel Research* **58**, 1407–1430 (2002). doi: 10.1016/S0143-974X(01)00106-7.

[This page intentionally left blank]

## Chapter 5

# Reliability enhancement of wind turbine structures with passive damping devices

Reflecting upon the history of the study of mechanical vibrations, it is an alluring fact that something so elemental in human culture, such as music, has become the nascency of an engaging and sometimes mathematically complex scientific subject. The interest of mankind in mechanical vibrations has been strongly marked by music. Possibly, earlier humans became interested in the sound coming from an object that accidentally became a whistle or a drum, and the first musical instruments were born. The sound of a musical instrument originates fundamentally from the structural vibration of its strings or its structure at certain frequencies and amplitudes, and a melody comes from their modulation — when it is played with sufficient masterfulness. Thereafter, the texture of a musical phrase being played is changed by the inclusion of the adequate amount of damping on the string vibration, as in e.g., some effects achieved from some string instruments. The control of structural vibrations is quite similar in that regard. In order to reduce structural vibrations produced by earthquakes, wind action, or the mere operation or service of a structure, we seek to modify its rigidity, mass, damping, or shape. Thus passive or active counter-forces are provided in the system.<sup>1</sup>

This chapter covers an exploratory study on the enhancement in the probability of structural failure on three wind turbines representative of the ones installed in Mexico. Such an enhancement is achieved by means of supplementary damping devices added to the turbines. As will be described ahead, the studies in the literature centered on the vibration control of operating wind turbine structures or components are ample. However, no reference has centered on the evaluation of the reduction in the probability of failure under cyclone-induced forces achieved with the use of passive damping devices. This subject is covered in the following pages.

### 5.1 Introduction

Due to the low frequencies dominating the structural behavior of wind turbine support structures, these become highly sensitive to wind action. Strong-wind events, such as cyclones and storms, represent one of the driving conditions for their structural design. According to different surveys, the greater part of collapses observed in these types of structures owes to these phenomena.<sup>2,3</sup> Moreover, insofar as a marked tendency towards offshore wind energy infrastructure is observed in many countries, the action of tropical cyclones on offshore structures becomes a relevant area of risk and hazard studies. There is a large number of publications in the literature from the last decade concerning structural studies on cyclone-induced actions on offshore wind structures.<sup>4-8</sup> Notwithstanding, land-based turbines are also vulnerable to these actions.<sup>9-11</sup>

Tropical cyclones are the natural phenomena that represent the greater damages worldwide, in terms of both population and cost of infrastructure.<sup>12</sup> The increasing number of yearly cyclones in

tropical latitudes<sup>13–15</sup> impels the need for novel studies on the subject. Among the studies that concern wind- and structural engineering are the measures to mitigate the cyclone-induced losses from civil structures and infrastructure, such as the inclusion of supplementary damping devices on the structures for the abatement of their response.

Supplementary damping for control of structural vibrations can be broadly classified into three major types: (i) Passive energy dissipation systems, which are the simplest inasmuch as they have constant parameters, and need no power supply to operate. They environ a broad variety of materials and devices for the improvement of structural characteristics such as damping, stiffness, or strength.<sup>1</sup> (ii) Active control systems use actuators to regulate the restoring forces supplied on the structure. Moreover, these systems require a power supply to function. (iii) Hybrid and semiactive control systems are capable of enhancing the performance of the structure via active devices, however, passive control devices can be included to reduce the energy used to operate the system.<sup>1</sup>

Among the most popular passive supplementary damping devices are the systems known as *tuned mass dampers* (TMDs), and tuned liquid column dampers (TLCDs). The former consist of a mass connected to the structure through a spring and a dashpot (usually represented by a viscous damper). The TMD dissipates energy through the damper when the structure is deformed due to external excitation. The natural frequency of the damping device must be close to the frequency of vibration from the modal shape which needs to be controlled in the structure, thus they receive the adjective of *tuned*. Figure 5.1 presents a schematic of the concept on which the TMDs operate in a structure with stiffness  $k_s$ , damping  $c_s$ , and mass  $m_s$ ; whereas these respective properties of the TMD are  $k_d$ ,  $c_d$ , and  $m_d$ .

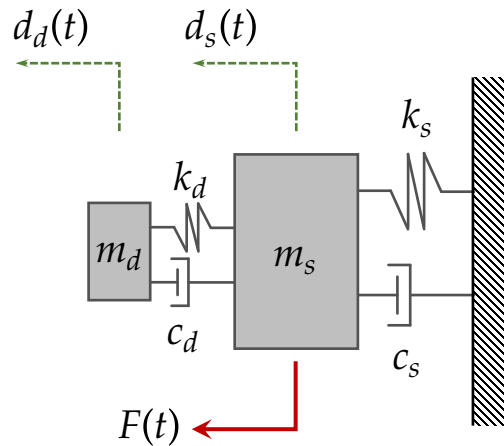


Figure 5.1: Modeling of a structure with a TMD

TMDs have been used for several decades in the vibration control of civil structures. Their efficiency in controlling the wind-induced vibration of tall buildings has been extensively studied.<sup>16,17</sup> Moreover, the use of passive<sup>18</sup> and active<sup>19</sup> TMDs also has been documented in various types of structures for the aforementioned purpose, even during tropical cyclones. The implementation of active or passive TMDs on wind turbines, as well as other types of damping devices, has still to reach maturity. However, there are some studies in the literature concerning the subject. A brief survey of some recent and noteworthy research on the subject of supplementary damping and reliability studies on wind turbines is presented in the following subsection.

### 5.1.1 Passive devices and wind turbines

A review of recent research focused on the applications of diverse vibration control methods on wind turbines can be found in the publications by Rahman et al.,<sup>20</sup> and Zuo et al.<sup>21</sup> However, notwithstanding the relevance of many studies found in the literature, only some of them concerned to supplementary-damping devices on wind turbines are referenced in the following.

The study of passive damping devices on the structural response of wind turbines has been a subject for nearly 30 years. One of the earliest studies performed on wind turbine support structures fitted with TMDs is presented in the work of Enevoldsen and Mørk.<sup>22</sup> In their work, an analytic study of a 40-m-height wind turbine fitted with a single TMD is carried out. Due to the reduced structural response achieved with the implementation of TMDs on the structure, it is expected to see also a reduction in the cost of the structure itself. This is insofar as less material volume is needed for its construction without dissatisfying safety requirements. The effectiveness of the TMD installed on the turbine was evaluated from the material volume that the structural design implies for both operation and extreme conditions. Considerable reductions were reported by the aforementioned authors.<sup>22</sup>

A great part of the studies and analyses on wind turbines are performed mainly from numerical models. In that regard, the employment of codes developed for the specific purpose of aero-servo-hydro-elastic analysis of wind turbines is common. Lackner and Rotea<sup>23</sup> developed numerical tools for the inclusion of supplementary damping devices in the aero-servo-hydro-elastic code FAST.<sup>24</sup> The applications of the developments by the aforementioned authors on operation analyses of offshore floating wind turbines demonstrated fatigue-equivalent load reductions with the employment of either passive or active devices.<sup>25</sup> Among the observations made in their work, Lackner and Rotea remark on the fact that the active devices result in greater load reduction on the structure, inasmuch as the operating conditions of the turbine are above-rated. This is insofar as the power consumption from the active damping device implies energy costs that are of no recoupment.<sup>25</sup> Further studies on the modeling of the actuator dynamics from active damping devices on the structural response of floating offshore wind turbines were performed by Stewart and Lackner,<sup>26</sup> and Namik et al.<sup>27</sup>

Notwithstanding all the analytic advances achieved in tools for numerical evaluation, experimental tests on supplementary damping devices are aye pertinent. This is also a relevant subject for wind turbine studies. Albeit the real conditions affecting wind turbine structures are difficult to measure and replicate, many of the experimental studies of supplementary damping devices reported in recent literature have endeavored to replicate multiple actions on scaled offshore wind turbine models.<sup>28,29</sup> However, the structural response of land-based wind turbines has also been regarded by recent experimental research.<sup>30,31</sup> Furthermore, the oft-growing developments in computational tools broaden the experimental capabilities for structural studies. This is regarded, for example, in the performance of experimental tests with the inclusion of real-time control of the dynamic properties of the damping device installed in the wind turbine.<sup>28,32</sup> Also, the performance of hybrid tests on the real-time response of physical models of the supplementary damping device, aided by numerical models of the wind turbine structure, reflects these advancements as well.<sup>31</sup>

The auspicious potential of offshore wind energy motivates presently the development of research focused on offshore infrastructure. Thus, a great part of wind energy studies is centered on heeding problems related to the deployment of wind turbines offshore. This fact includes the research addressing the enhancement of the dynamic response of offshore-HAWT structures by means of 'conventional' passive damping devices. In the literature from recent years, a considerable number of studies can be found centered on the implementation of TMDs and TLCs on offshore wind turbines,<sup>29,33–36</sup> whereas less frequent studies are reported for land-based wind turbines.<sup>31,37</sup> However, onshore wind energy still has the potential to be exploited worldwide, including in areas where the wind hazard differs from the established international standards.<sup>38</sup> Therefore, there are still gaps in the research on onshore wind energy that have to be filled.

The enhancement of the dynamic behavior of wind turbine structures, by means of supplementary damping implementation, alludes that the benefits of such devices can impact the reliability of HAWT structures under the diverse phenomena acting upon them. However, counted published studies are found in the archived literature dealing with that particular subject.

### *Fragility evaluation*

The above-referred literature illustrates the broadly documented use of supplementary damping devices, and how these can improve the structural response of wind turbines under both operational and extreme ambient conditions. These improvements have been expressed in the surveyed studies in terms of structural response, and sometimes in a measure of damage. Notwithstanding the previous observations, wind turbines can be subjected to different hazards that characterize the site of their installation. There are studies in the literature that have centered on the reliability and risk assessment of wind turbine structures. Adequate risk evaluation must rely on results of structural performance expressed in terms of reliability, i.e., of the probability of damage. Although such studies are less common than the ones mentioned above, it is counterfactual to assert them as non-existent.

Some of the said hazard-focused research has centered on the evaluation of structural performance under seismic action, by means of fragility evaluation of the wind turbine support structures.<sup>39,40</sup> Furthermore, multi-hazard studies have been conducted from numerical models to research the fragility of both onshore<sup>41,42</sup> and offshore<sup>43</sup> wind turbine support structures. However, few studies concern specifically the actions of tropical cyclones on wind turbines for risk or fragility estimation.<sup>7,10</sup>

A subject covered even more infrequently by research on the topic is the evaluation of reliability enhancement of wind turbines by the use of supplementary damping. Among the surveyed works are the studies reported by Mensah and Dueñas-Osorio,<sup>44,45</sup> who presented the results from numerical models of onshore wind turbines fitted with TLCDs. In their work, a fragility analysis, and subsequent risk evaluation, are performed to assess the reliability enhancement achieved with different configurations of the TLCDs. The analyses included the measurement of the tower-top displacement of the operating wind turbine at diverse wind intensities. The enhancement in reliability is expressed in terms of the reduced conditional and annual probability of failure.

Fitzgerald et al.<sup>46</sup> performed the fragility analysis on an operating 5-MW land-based wind turbine. The main objective of their work was to study the improvement in the structural response achieved when the turbine is fitted with active TMDs. Such an improvement is evaluated in terms of the probability of damage estimated from the tower displacement, where a considerable reduction of this quantity is seen when the structure is fitted with the active TMDs.

The numerical analyses of a monopile-supported offshore wind turbine, considering the actions of earthquake, wind, waves, as well as soil-pile interaction, were performed by Hemmati et al.<sup>47</sup> The implementation of a single TLCD on the structure is also analyzed, and the improvement achieved with the supplementary damper is determined from a fragility analysis of the results. The performance states analyzed in the study are defined from levels of acceleration at the nacelle. Differences up to 13% in terms of fragility were reported by the authors when comparing the cases with and without tuned damper.

Three main topics have been identified as gaps to be filled from the extensive survey performed from the research referenced above : (i) studies on onshore wind turbines have been unattended in recent research. As commented in previous paragraphs, this is insofar as there is a large wind energy potential to be exploited from offshore sources. However, there are numerous regions worldwide where onshore wind potential is either of relevance, or offshore resources are unavailable. Moreover, in countries where wind energy development has yet to reach maturity, such as Mexico, the totality of the installed HAWTs is land-based. (ii) Cyclone-induced action on wind turbines has been either disregarded or misassumed. A synoptic wind profile has been assumed in a great part of the

research that has studied wind intensities comparable to those observed in tropical cyclones. This assumption is of no consequence when the structure under analysis is of low height. However, as observed from the simulations and analyses performed in Chapter 3, the difference in mean speed can be of significance, even at altitudes that represent just a fraction of the height of maximum winds. (iii) The assessment of reliability enhancement considering the previous two implications has been performed in no study surveyed in this work, evidently. In view of these observations, the following sections elaborate on the fragility evaluation of three land-based wind turbines representative of those installed in Mexico, and fitted with TMDs. The structures under study have been defined and studied in Chapter 4. Furthermore, the assessment of reliability enhancement is performed for the three turbines. Comments on the determination of the optimal parameters for the TMDs are also covered.

## 5.2 Passive damping devices

As commented previously in this chapter, the employment of passive TMDs has been widely studied in civil structures, as the former are devices commonly employed to reduce the mechanical response of the latter. TMDs are convenient to enhance the structural behavior in service states,<sup>16,17</sup> however, the benefits of passive TMDs can also contribute to extending the ultimate limit states of structural performance.<sup>48,49</sup>

A TMD consists fundamentally of a mass connected to the main structural system through a spring and a damper in parallel (see Figure 5.1). The criteria adopted for the development of finite element models (FEMs) including the installation of the TMDs on the three turbines defined previously in Chapter 4, as well as the determination of their optimal parameters, are described in this section.

### 5.2.1 Description of numerical models

The finite element models developed for the analyses of the three turbines described previously in Chapter 4 were the ones employed for the present study. However, the modeling of the TMD at the nacelle of each of the structures was implemented by means of the element COMBIN14 in APDL. This element represents a combination of spring and damper in parallel. It is a two-nodes element capable of representing uni-axial tension or compression effects up to three degrees of freedom (DOFs). Among other characteristics of the element is the possibility of representing non-linear damping when the appropriate coefficients are defined for its damping part. Nevertheless, in the present study, only linear damping is analyzed. Furthermore, the element has no mass by itself, thus, an additional mass must be modeled to represent the mass of the tuned damper. This is achieved in APDL by means of the element MASS21, which can be associated with one of the nodes of the element COMBIN14. Figure 5.2 displays a schematic of how the elements COMBIN14 and MASS21 are included in the structural model to represent the participation of a TMD.

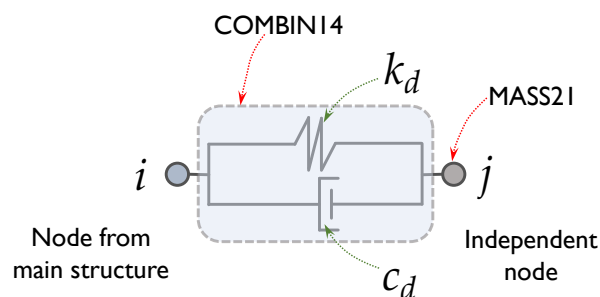


Figure 5.2: Modeling of a TMD for finite element analysis

The stiffness and damping constants of the TMD are represented in Figure 5.2 as  $k_d$  and  $c_d$ , respectively. In order for the TMD to reduce adequately the structural response, its mass must be determined as a significant fraction of the structural mass. The value of  $k_d$  is defined subsequently from the natural frequency of the TMD necessary to control the vibration mode of interest. Whereas the value of  $c_d$  will depend on these two parameters. Therefore, it is evident that all these values will be different for each of the three turbines under analysis, although their parametric ratios with respect to the main structural properties might be similar. One of the common procedures to estimate the optimal values of these parameters is described in the following, as well as the criterion adopted in the present study.

### 5.2.2 Modal parameters of the main structure

Consider the two-DOFs system illustrated in Figure 5.1, and let the following relations between the parameters displayed in the figure be defined:

$$\omega_s = \sqrt{\frac{k_s}{m_s}} \quad (5.1)$$

$$\omega_d = \sqrt{\frac{k_d}{m_d}} \quad (5.2)$$

$$\mu_d = \frac{m_d}{m_s} \quad (5.3)$$

$$\varphi_d = \frac{\omega_d}{\omega_s} \quad (5.4)$$

$$\zeta_d = \frac{c_d}{2\sqrt{k_d m_d}} \quad (5.5)$$

where  $\omega_i$  is the natural angular frequency of either the structure ( $i = s$ ) or the damper ( $i = d$ );  $\mu_d$ ,  $\varphi_d$ , and  $\zeta_d$  are called *mass ratio*, *frequency ratio*, and *damping ratio*, respectively.

There are several approaches defined in the literature to determine the ‘optimal’ parameters of the TMD, that is, the values of the frequency and damping ratios that produce the lower structural response. Some of these approaches assume that the excitation of the structure is characterized as either a harmonic force<sup>50,51</sup> or a white-noise excitation.<sup>51–53</sup> Depending on the structural response that it is sought to optimize (i.e., displacement, force, or acceleration) the results of this optimization hold different expressions. The ‘classical’ solution for the displacement optimization of an undamped structure under harmonic excitation is summarized in the following.

If a low damping coefficient for the structure can be assumed, as it is common in many civil structures (and particularly in wind-sensitive ones), the damping coefficient  $c_s$  can be disregarded with negligible implications. Moreover, if  $F(t)$  is a harmonic function, the equations of motion of the 2-DOF system from Figure 5.1 can be expressed as:

$$m_s \ddot{d}_s + k_s d_s + k_d (d_s - d_d) + c_d (\dot{d}_s - \dot{d}_d) = F_0 \sin(\omega t) \quad (5.6a)$$

$$m_d \ddot{d}_d + k_d (d_d - d_s) + c_d (\dot{d}_d - \dot{d}_s) = 0 \quad (5.6b)$$

The solution of Equations 5.6a and 5.6b is complex and, after the pertinent algebraic procedure, it can be found that the frequency ratio that produces the lowest possible amplitude of response in the structure is<sup>50</sup>:



$$\varphi_{\text{opt}} = \frac{1}{1 + \mu_d} \quad (5.7)$$

whereas the average damping ratio that produces the lowest maxima in the response curves of the structure results in<sup>50</sup>:

$$\zeta_{\text{opt}} = \sqrt{\frac{3\mu_d}{8(1 + \mu_d)^3}} \quad (5.8)$$

Thus, the parameters defined in Equations 5.7 and 5.8 are expressed as a function of the mass ratio  $\mu_d$ . This parameter ( $\mu_d$ ) has to be defined from a mass sufficiently large to participate in the motion of the structure, and sufficiently small to imply trivial reinforcements or strengthening of it. Typical values of  $\mu_d$  range from 0.01 to 0.1,<sup>16</sup> however, greater values are plausible. Moreover, it is important to note that  $\mu_d$  is commonly expressed as a fraction of the modal mass of the structure, as is the case in the present study. The modal properties of the three turbines under analysis were estimated. Table 5.1 summarizes the results from the modal analyses performed on the three turbines.

**Table 5.1:** Modal properties of the modeled wind turbine towers

Parameter (1st mode)	Rated Power [MW]		
	1.0	2.5	3.3
Frequency [Hz]	0.484	0.390	0.344
Effective mass [kg]	62,876	174,752	282,659
Effective-to-total mass ratio	0.809	0.677	0.642
Modal mass [kg]	12,927	30,669	51,831

From Table 5.1 it can be seen that the first mode of vibration represents the participation of the greater portion of mass from the structure. Higher modes of vibration represented effective-mass ratios up to 6.2, 10.7, and 12.2%, for the 1, 2.5, and 3.3 MW turbines, respectively. The modal mass was extracted from the APDL models directly. However, corroboration of that value was performed with a MATLAB code, considering the stiffness and mass matrices as defined in the FEM. Differences up to 4% were found among the values of the modal mass computed from the different codes.

In order to define the adequate values for the TMD parameters on the structures, including the masses of the dampers, parametric analyses have been performed in the literature,<sup>49</sup> performing a series of time-step analyses and analyzing the response histories from the TMD-fitted structure. The approach adopted in this study relies on the performance of a set of harmonic analyses on the full models of the structures, varying at each analysis one of the parameters involved in the definition of the TMD. The following subsection describes the approach in greater detail.

### 5.2.3 Harmonic analyses

The concept of a harmonic analysis can be understood as a set of computations of the structural response product of a harmonic excitation, performed at several individual frequencies governing said excitation. The maximum response amplitudes obtained from the set of analyses are plotted subsequently against the values of their respective frequency of excitation. Thus, the frequencies that could produce resonant responses on the structure can be identified. In mathematical terms, this can be expressed from the equation of motion of a multi-DOF system:

$$\mathbf{M}_s \ddot{\mathbf{d}}(t) + \mathbf{C}_s \dot{\mathbf{d}}(t) + \mathbf{K}_s \mathbf{d}(t) = \mathbf{f}(t) \quad (5.9)$$

where  $\mathbf{M}_s$ ,  $\mathbf{C}_s$ , and  $\mathbf{K}_s$  are the mass, damping, and stiffness matrices of the structure, respectively. The vector  $\mathbf{d}$  contains the structural displacement at every DOF, and the dots denote differentiation with respect to time  $t$ . The vector  $\mathbf{f}$  contains the forces exciting the structure.

Hence, if  $\mathbf{f}$  represents a harmonic excitation, defining the variable  $\omega$  as the angular frequency, and  $i$  as the imaginary unit, it can be stated that  $\mathbf{f}(t) = \mathbf{f}_h(\omega) \exp(i\omega t)$ , and  $\mathbf{d}(t) = \mathbf{d}_h(\omega) \exp(i\omega t)$ . The  $j$ -th elements at vectors  $\mathbf{f}_h(\omega)$  and  $\mathbf{d}_h(\omega)$  are defined as  $f_j = F_j \exp(i\vartheta_j)$  and  $d_j = D_j \exp(i\varphi_j)$ , respectively.  $F_j$  and  $D_j$  are the peak force and displacement amplitudes on the  $j$ -th DOF at frequency  $\omega$  and phase angles  $\vartheta_j$  and  $\varphi_j$ , respectively.<sup>54</sup>

Thus, substituting the force and displacement vectors in Equation 5.9, and dividing by  $\exp(i\omega t)$ , it can be expressed in the frequency domain as:

$$\left(-\omega^2 \mathbf{M}_s + i\omega \mathbf{C}_s + \mathbf{K}_s\right) \mathbf{d}_h(\omega) = \mathbf{f}_h(\omega) \quad (5.10)$$

From Equation 5.10, the unknown elements are the peak amplitudes composing the vector  $\mathbf{d}_h(\omega)$ . This can be solved in APDL, which computes the solution by either direct elimination or iterative methods.<sup>55</sup> Other alternatives, like mode superposition, are also available in APDL. However, no discussion on the methods for the solution of these equations will be addressed in this work.

Definition of  $\mathbf{C}_s$  is necessary to avoid resonance asymptotes in the results. For this purpose, Rayleigh damping coefficients were computed from the frequencies of the two tower modes with greater participation in a single direction, assuming a damping ratio of 1%. Moreover, the definition of the frequency range of the analysis, as well as the amplitudes of the forces, are necessary to perform the harmonic analysis. The phase angles are also necessary when multiple out-of-phase loads are applied, however, this parameter was disregarded for the purposes of the approximation of optimal TMD parameters.

The harmonic analyses were performed by modeling the elements COMBIN14 and MASS21 at the nacelle of the turbines. A force on each of the nodes from the models of the main structure was applied assuming a distribution as would be produced by a synoptic power-law wind-speed profile on each structure. The power-law exponent assumed an open-terrain exposure category, whereas the drag coefficients were assumed as specified in the analyses of Chapter 4. The tower-top displacement was used as the response to evaluate the harmonic excitation. Furthermore, a frequency sweep from 0.01 to 10 Hz was considered for the harmonic analyses, performed with increments of 0.01 Hz. For each turbine, ranges of  $\mu_d$ ,  $\zeta_d$ , and  $\phi_d$  of [0.1,0.2], [0.025,0.2], and [0.95,1.05], respectively, were considered for the study of the TMD. These criteria are summarized in Table 5.2.

**Table 5.2:** Parameters for harmonic analyses and TMDs

Parameter	$n$ [Hz]		$\mu_d$		$\zeta_d$		$\phi_d$	
	min	max	min	max	min	max	min	max
Value	0.01	10.00	0.10	0.20	0.025	0.200	0.95	1.05

Figure 5.3 illustrates the moduli of the peak amplitudes measured from the harmonic analyses for all the values of the TMD parameters evaluated. The undamped response of the wind turbines is included as well, where the peaks at the first bending mode frequency can be identified. Moreover, the damper case which produced the lower peak in the vicinity of the natural frequency of the structure was identified and is displayed in the figure with a red line. This combination is referred as ‘expected optimum’. An asseveration of these parameters as optimal is still omitted inasmuch as the greater reduction in structural response might be produced by a different parametric combination, due to the contribution of wide-band frequency content from turbulent wind-speed signals. Moreover, insofar as the mean wind profile used for the final analyses is different in every cyclonic wind-field simulation performed, a different force distribution on the models is applied. However, the identification of these values aids in the reduction of possible combinations to evaluate the structural response under wide-band actions.

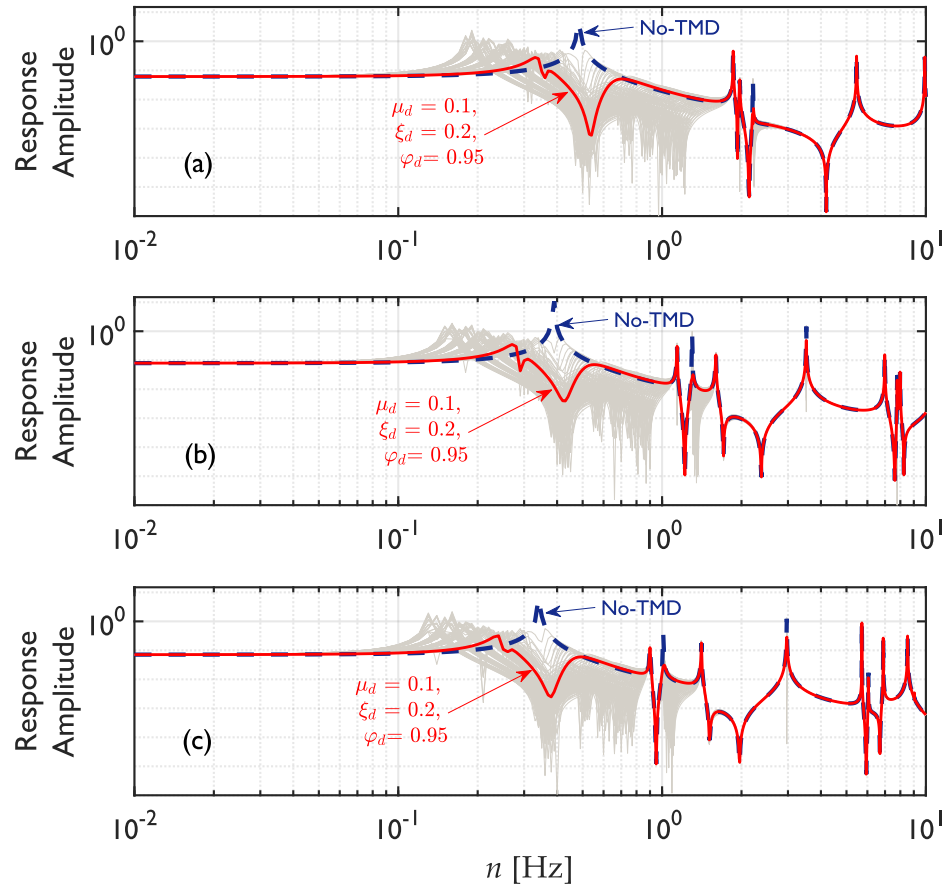


**Figure 5.3:** Results from harmonic analyses of the structures with a TMD: (a) for the 1MW turbine, (b) for the 2.5MW turbine, and (c) for the 3.3MW turbine

From Figure 5.3 some observations are pertinent: (i) The curve identified as ‘expected optimum’ is non-correspondent to the lowest amplitudes reached near the target frequency. Rather, the criterion for the identification of an optimal configuration of damper parameters is driven by the lowest values of the peaks that are formed near the said frequency. This owes to the objective of employing TMDs for reducing the maximum response at the greatest bandwidth, rather than reaching the lowest value of amplitude at (or near) a particular frequency. (ii) The two crests displayed from the damped curves at the left and right of the first modal frequency of the structure are a common feature in these types of devices. These summits have been displayed also in similar plots from experimental measurements.<sup>29</sup> The formation of these crests owes to the contribution of the TMD, and their magnitude depends on the damping of the device. Due to this, the TMD will produce resonance in the response of the structure at either  $c_d = 0$  or  $c_d = \infty$ .<sup>50</sup> (iii) The reduction of amplitude due to the incorporation of a TMD can also be appreciated at other peaks of the plots. However, according to the modal analyses, the main contribution of the structural vibration comes from the first bending mode. Thus, a reduction in the structural response at different frequencies due to this effect might be negligible for a wide-banded excitation.

### 5.3 Results

The turbulent wind field signals simulated in Chapter 4 were used for the present study. This permitted a direct comparison of the response signals and, therefore, a prompter visualization of the effects of the TMDs on the turbines in the time domain. Nevertheless, the number of analyses was reduced

to 15 per wind intensity, instead of the 30 analyses per intensity performed in Chapter 4. This owes to the fact that eight different parametric combinations of TMDs were evaluated for intensities of  $\bar{U}(10)$  from 30 to 70 m/s, in increments of 2 m/s. The combination of TMD parameters evaluated from time-step dynamic analyses corresponds to values of  $\mu_d$  equal to 0.1 and 0.15,  $\zeta_d$  equal to 0.15 and 0.2, and  $\varphi_d$  equal to 0.95 and 1.00.

Figure 5.4 displays a comparison between three displacement signals for each of the three turbines. In a similar way to what was performed in the analyses from Chapter 4, the displacement was measured at the top of the tower. Other structural responses, such as tower rotation, and bending moment were extracted from the analyses. However, a graphical depiction of these is omitted to avoid figure redundancy. The displayed signals correspond to displacements under the undamped case, as well as parametric configurations  $[\mu_d, \zeta_d, \varphi_d]$  of  $[0.10, 0.20, 0.95]$  and  $[0.15, 0.15, 0.95]$ . The displacement histories correspond to a wind intensity of  $\bar{U}(10) = 50$  m/s for the three structures. Note that the first 50 s from the start of the signals have been omitted. This was performed in order to avoid the inclusion of numerical inaccuracies at the start of the solution. The last 50 s from the 600-s-length signals are hidden in the figure for the mere purpose of a better graphical presentation.

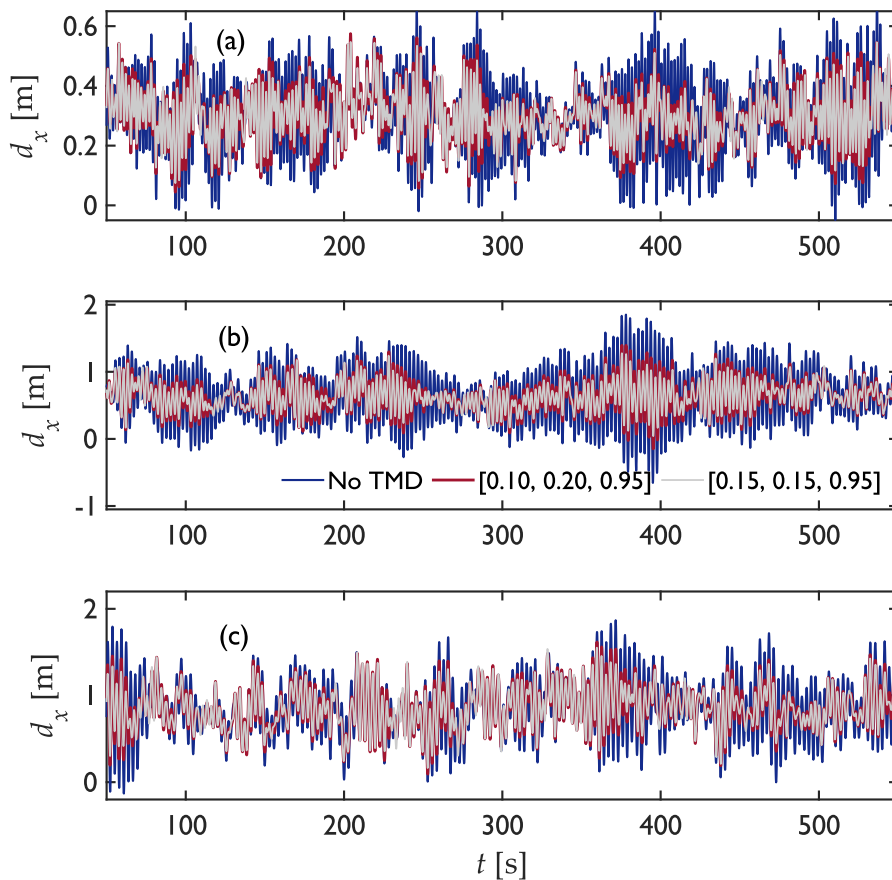


**Figure 5.4:** Displacement histories for the three turbines with and without TMD: (a) for the 1MW turbine, (b) for the 2.5MW turbine, and (c) for the 3.3MW turbine

From Figure 5.4 an evident reduction in the amplitude of displacement is displayed for the three turbines when a TMD is included. Furthermore, contrasting the results from the harmonic analyses, the TMD configuration  $[0.15, 0.15, 0.95]$  appears to achieve greater reductions of the structural response — for the three structures — than the combination identified as the expected optimum. This implies that, although a fair approximation to the optimal TMD parameters is achieved from the har-

monic analyses, the determination of an optimal configuration requires further information on the dynamic nature of the excitation. This might be attributed to the differences in the distribution of forces on the structure, which are different from the ones produced by a synoptic wind profile. In addition, the reduction achieved in each signal for a specific damping-parameter definition is variable at every analysis. Comparisons to other TMD parametric combinations are omitted to avoid saturation and redundancy of figures. Nevertheless, a summary of the average response reductions achieved, in terms of both the peak and root-mean-square (RMS) value of the response, is presented for the three turbines in Table 5.3 for each of the analyzed combinations of TMD parameters.

**Table 5.3:** Average response reduction achieved with the TMDs

Rated Power	1 MW		2.5 MW		3.3 MW	
	Peak	RMS	Peak	RMS	Peak	RMS
$\mu_d = 0.10, \xi_d = 0.15, \varphi_d = 0.95$	0.791	0.919	0.808	0.929	0.794	0.923
$\mu_d = 0.10, \xi_d = 0.15, \varphi_d = 1.00$	0.791	0.919	0.809	0.929	0.795	0.924
$\mu_d = 0.10, \xi_d = 0.20, \varphi_d = 0.95$	0.805	0.923	0.824	0.933	0.810	0.928
$\mu_d = 0.10, \xi_d = 0.20, \varphi_d = 1.00$	0.806	0.924	0.826	0.934	0.812	0.929
$\mu_d = 0.15, \xi_d = 0.15, \varphi_d = 0.95$	0.762	0.911	0.777	0.921	0.763	0.916
$\mu_d = 0.15, \xi_d = 0.15, \varphi_d = 1.00$	0.764	0.912	0.780	0.922	0.766	0.917
$\mu_d = 0.15, \xi_d = 0.20, \varphi_d = 0.95$	0.775	0.915	0.792	0.925	0.778	0.919
$\mu_d = 0.15, \xi_d = 0.20, \varphi_d = 1.00$	0.777	0.916	0.796	0.926	0.780	0.921

From Table 5.3 it can be seen that the combination that produces the greater response reduction for the three turbines is the case  $\mu_d = 0.15$ ,  $\xi_d = 0.15$ , and  $\varphi_d = 0.95$ . This combination holds for either the peak or the RMS value of the response. Furthermore, the combination expected to be the optimum displayed the second smallest reductions, despite being the combination that showed the lower maxima in the plots from the harmonic analyses. Nevertheless, as mentioned in paragraphs before, these have served as an approximation to reduce the number of analyses necessary to determine the optimal TMD parameters, inasmuch as a great number of time-history analyses would have been necessary to cover the same number of evaluated combinations otherwise. Having stated the previous observations, the combination [0.15, 0.15, 0.95] will be referred as 'optimal' in the remaining of this chapter.

### 5.3.1 Spectral comparisons

The visualization of the response reduction achieved with the TMDs on the structures can also be appreciated in the frequency domain. The power spectral density functions (PSDFs) of the displacement signals shown in Figure 5.4 were estimated, and are displayed in Figure 5.5. In this figure, from top to bottom are displayed the PSDFs of tower-top displacement for the 1, 2.5, and 3.3 MW turbines, respectively. The curves at the left show the spectral estimation, whereas the ones at the right display the normalized estimations (with respect to the variance of the signals).

It can be observed in Figure 5.5 that the TMD contributes to the reduction of the structural response only at the dominant frequency. That is, the reduction is observed only at the peak of the spectral density, displayed at the first bending mode of the tower. No differences are observed in the spectral amplitudes at frequencies far from the natural frequencies of the structures. Moreover, corroboration to what Figure 5.4 and Table 5.3 state is provided in Figure 5.5, and a greater reduction at the dominant frequency is seen from the combination [0.15, 0.15, 0.95]. Regarding the normalized spectral plots, lower frequency is seen for the undamped case. This is justified in the reduction of the RMS value of structural response when the TMD is provided to the structure. That is,

insofar as the RMS value is related to the variance of the signal, and the spectra from TMD cases are normalized to lower variances, the normalized spectral amplitudes of the damped cases are greater. This can also be observed by comparing the slightly-superior normalized amplitudes for the optimal configuration to the red line displayed in the figure.

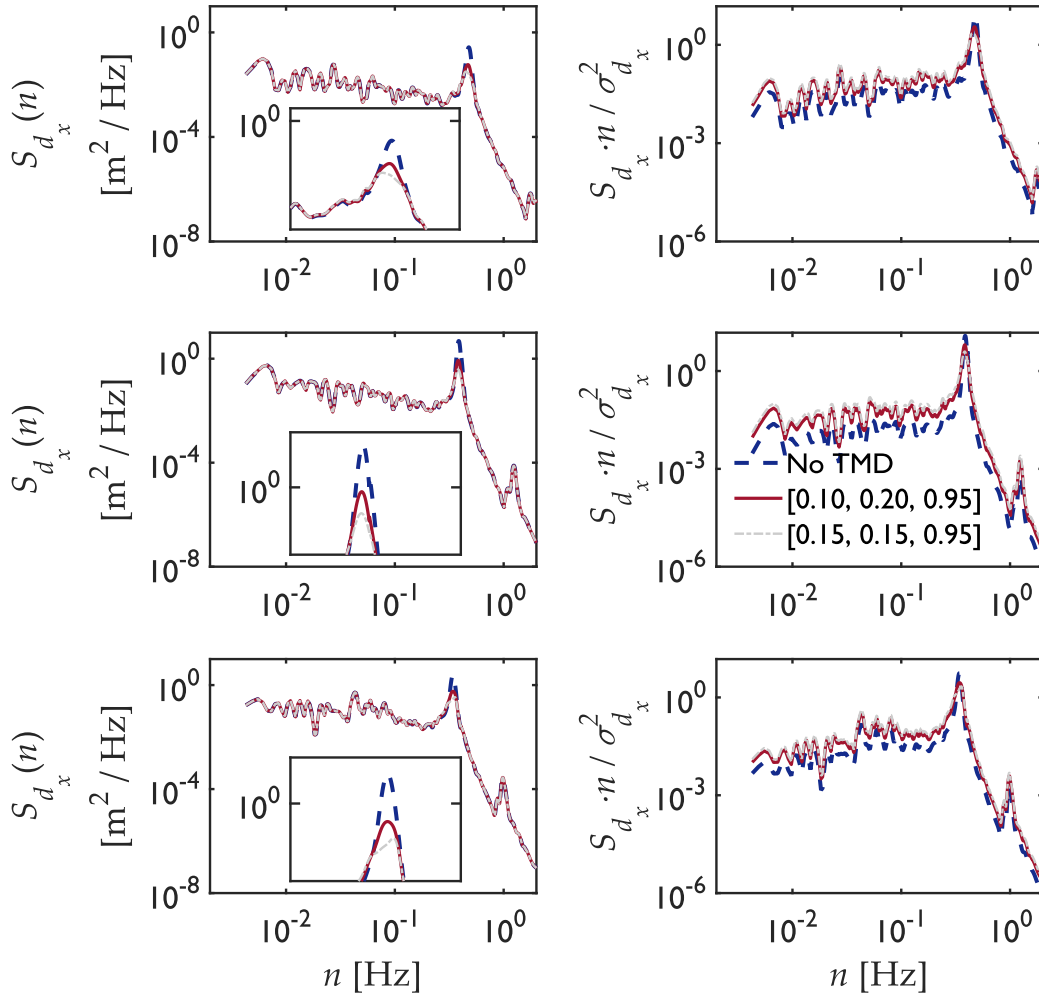


**Figure 5.5:** Spectral densities of tower-top displacement for  $\bar{U}(10) = 50$  m/s. From top to bottom: for the 1, 2.5, and 3.3 MW wind turbines

## 5.4 Fragility analysis

As performed in Chapter 4, the probability of failure of the three turbines was evaluated for the cyclone-induced action on them. The same damage states (DSs) defined in Chapter 4 were considered, with the same damage thresholds. Nevertheless, aside from the determination of the reliability enhancement achieved from the use of TMDs, an important difference in how the fragility was evaluated is found in this study with respect to what was presented in Chapter 4. The difference is centered on the fact that, in Chapter 4, the parameters that define the fragility function as a log-normal distribution are assessed from a foregoing estimation of the exceedance probability of the defined structural responses. In this study, the fragility is determined from a model describing the median of the structural response used to evaluate the DS. This value, evidently, is different for each of the

combinations of the TMD parameters analyzed. However, the models proposed for this evaluation allow estimating the fragility by accounting for these differences.

#### 5.4.1 Characterization of structural response maxima

According to the definition of probability of failure, presented in Equation 3.29 and elicited here for convenience, it can be defined as:

$$P_f = \int_{g(\mathbf{x}) \leq 0} f_{\mathbf{x}}(\mathbf{x}) d\mathbf{x} \quad (5.11)$$

where  $g(\mathbf{x})$  is the function that describes the structural performance, and  $f_{\mathbf{x}}(\mathbf{x})$  is the probability distribution function of the involved variables. The performance function can be briefly defined in a linear manner as  $g(\mathbf{x}) = R - S$ , where  $R$  represents the resistance of the structural system, and  $S$  the loads acting on it. In this regard, it can be seen that values of  $g(R, S)$  lower than zero imply a failure of the structural system, i.e., that the loads surpass the structural resistance. Under the assumption that both  $R$  and  $S$  are independent variables with normal distribution, a reliability index  $q$  can be defined as<sup>56</sup>:

$$q = \frac{E[R] - E[S]}{\sqrt{\text{Var}[R] + \text{Var}[S]}} \quad (5.12)$$

where  $E$  and  $\text{Var}$  denote the expectation operator and variance, respectively. Considering Equation 5.12, the probability of failure can be expressed as<sup>56</sup>:

$$P_f = P[g(R, S) \leq 0] = \Phi[-q] \quad (5.13)$$

where  $\Phi(\cdot)$  represents the standard-normal cumulative distribution function (CDF). From Equation 5.13, if the actions on the structure are expressed from a demand parameter  $DP_i$ , and the resistance as a damage threshold  $dt_i$  (both conveniently assumed log-normally distributed), for an  $i$ -th level of structural performance, Equation 5.13 takes the form of Equation 4.2, and can be expressed as:

$$P_f = \Phi \left[ \frac{\ln \left( \widehat{DP}_i \right) - \ln(dt_i)}{\sigma_i} \right] = F_i(IM) \quad (5.14)$$

where the symbol  $\widehat{DP}_i$  denotes the median of the demand parameter chosen to evaluate the structural performance at level  $i$  as a function of the intensity measure  $IM$ . The uncertainty involved in both the structural demand and capacity has been abbreviated in  $\sigma_i$ . Thus, a model describing the relation between the medians of  $DP$  and  $IM$  is required for the evaluation of Equation 5.14.

Recalling what has been presented in Chapter 4, the responses studied for the fragility analyses were: (i) displacement ( $d_x$ ), (ii) bending moment ( $M_y$ ), and (iii) structural rotation ( $\kappa_s$ ), all measured at the tower of the wind turbines and each one representing a different DS. An exploration of the results of these responses suggested that a fair approximation of their median, evaluated as a function of the intensity measure  $\bar{U}(10)$ , was achieved from models with the form  $y = a \exp(bx)$ . This form proved to represent fairly the response at all the evaluated TMD parametric combinations. Nevertheless, instead of performing eight different models for a single TMD-parameter combination per structural response, a single model involving the TMD parameters was developed for each DS considered and each wind turbine. The procedure for the development of the models is briefly summarized next.

Linear regression models can express the relation between a variable  $y_i$  and predictor variable  $x_i$  in general form as:

$$y_0 = \mathbf{X}_0 \mathbf{b} + \varepsilon \quad (5.15)$$

where  $\mathbf{y}_0$  is the vector containing the response variables,  $\mathbf{X}_0$  is the design matrix,  $\mathbf{b}$  is the vector of parameters that define the model, and  $\boldsymbol{\varepsilon}$  is the error-terms vector. If the natural logarithm of the explored functional form (mentioned in the previous paragraph) is applied to Equation 5.15,  $\mathbf{y}_0$  will contain the values of  $\ln(y_i)$ , whereas the  $i$ -th row of the design matrix will be formed by  $[1, x_i]$ , and  $\mathbf{b} = \{\ln(a), b\}^T$ . This was performed for each group of results corresponding to each one of the TMD combinations. From the results, the values of  $\ln(a)$  were different in the regression performed for each TMD-parameter combination, whereas the values of  $b$  appeared to remain almost constant. Availing of this behavior from the results, the value of  $b$  was *fixed* in the models, and an average of the values estimated for this parameter from each damper combination was used at each DS. Thus, holding the linearity of the model, the coefficients associated with each of the (TMD) parameters involved in the structural response were estimated from models with the form :

$$\mathbf{y}_1 = \mathbf{X}_1 \mathbf{a} + \boldsymbol{\varepsilon} \quad (5.16)$$

where the  $i$ -th element of the response vector  $\mathbf{y}_1$  are formed by  $y_i / \exp(bx_i)$  (note that this time the response variable shows no translation to logarithmic space), whereas the  $i$ -th row of the response matrix  $\mathbf{X}_1$  are formed by  $[\mu_{d,i}, \xi_{d,i}, \varphi_{d,i}, 1]$ , and  $\mathbf{a} = \{a_1, a_2, a_3, a_4\}^T$ . Thus, the model describing the median of the demand parameters for each case is:

$$\widehat{DP}(IM) = (a_1 \mu_d + a_2 \xi_d + a_3 \varphi_d + a_4) \exp(bIM) \quad (5.17)$$

From this model, the median of the undamped response can be estimated assuming the TMD parameters equal to zero. Figure 5.6 displays the results from the linear regression performed to the median of the three demand parameters evaluated for the fragility analyses. Only results from intensities  $\bar{U}(10) \geq 44$  m/s are included, as well as only the 'optimal' and undamped cases are displayed. This is done for the sake of better visualization. The resulting estimators for the models for each turbine and each DS are summarized in Table 5.4.

Furthermore, an important element involved in Equation 5.14 is the uncertainty from both the actions on the structure and the structural resistance. In the present study, neither the damage thresholds nor the parameters of the TMDs have been assumed as uncertain. Further studies considering them as such would represent relevant findings, inasmuch as the TMD parameters have a strong influence on the structural response of the wind turbine support structure. However, these considerations are out of the scope of the present study. In view of this, the uncertainty expressed in Equation 5.14 can be simplified to the uncertainty from the structural response representing the demand parameters. This can be determined from the standard deviation of the residuals from the model. Nevertheless, due to the assumption of a log-normal distribution characterizing the random behavior of the structural response, the residuals have to be measured from the natural logarithm of Equation 5.17, that is:

$$\ln(\widehat{DP}) = \ln(a_1 \mu_d + a_2 \xi_d + a_3 \varphi_d + a_4) + bIM + \sigma_{\ln DP} \epsilon \quad (5.18)$$

where  $\epsilon$  is the normalized error, i.e., it is conveniently assumed as a zero-mean and unit-variance normally-distributed random variable. The uncertainty  $\sigma_{\ln DP}$  is obtained from the residuals of Equation 5.18 from the whole set of observations. Figure 5.7 displays a schematic of the observed values from the optimal TMD case against the respective values of Equation 5.18. The area covered by one standard deviation around the median is also presented in the figure.



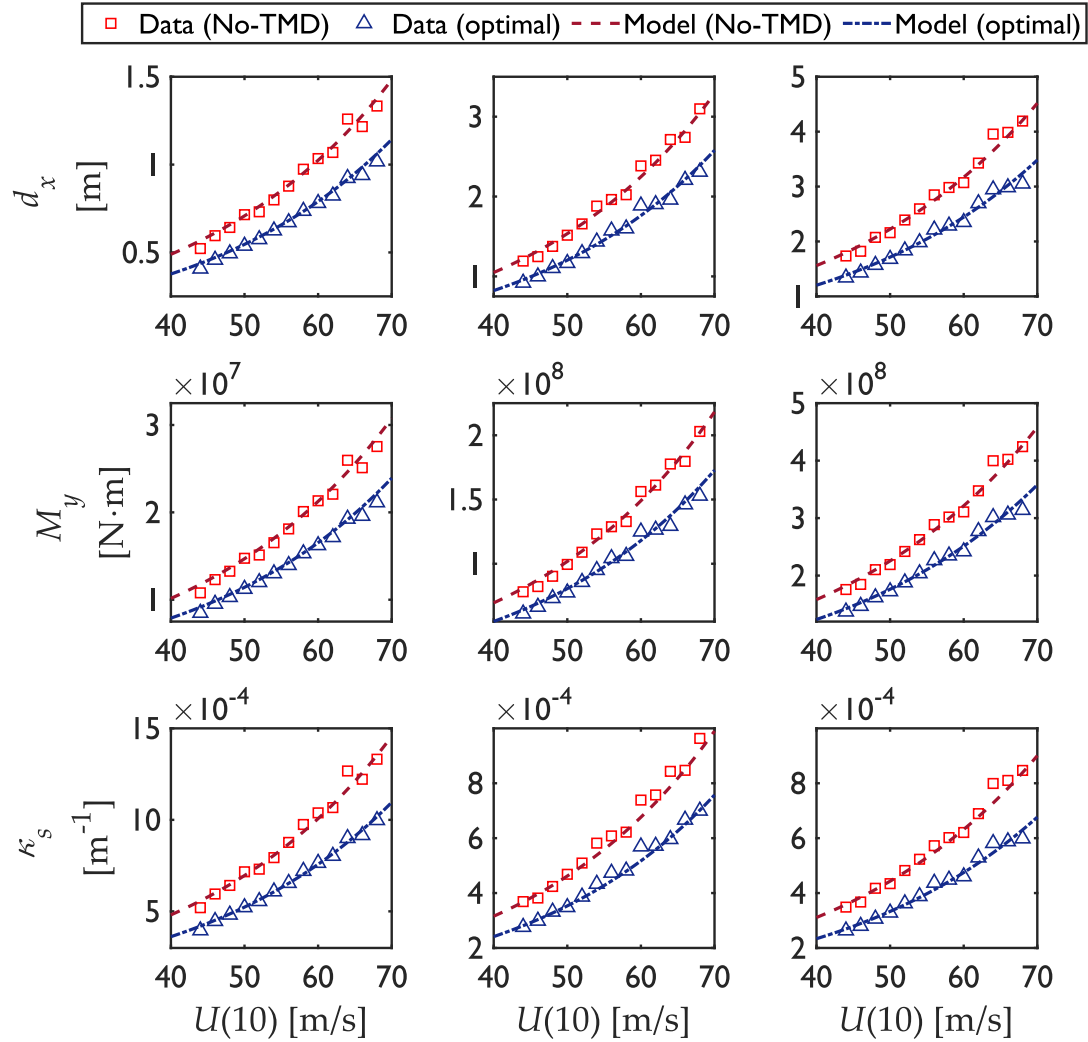


**Figure 5.6:** Fittings for the median of the demand parameters for the undamped and optimal cases. From left to right: for the 1, 2.5, and 3.3 MW wind turbines

**Table 5.4:** Model estimators for the median structural response and uncertainties

Turbine	1 MW			2.5 MW			3.3 MW		
Parameter	DS1	DS2	DS3	DS1	DS2	DS3	DS1	DS2	DS3
$a_1$	-0.0670	-1.340E+06	-7.199E-05	-0.1430	-9.071E+06	-4.708E-05	-0.2489	-2.408E+07	-5.361E-05
$a_2$	0.0272	5.455E+05	2.893E-05	0.0618	3.925E+06	2.015E-05	0.1062	1.033E+07	2.273E-05
$a_3$	-0.0206	-4.166E+05	-2.182E-05	-0.0391	-2.500E+06	-1.277E-05	-0.0686	-6.656E+06	-1.485E-05
$a_4$	0.1116	2.316E+06	1.097E-04	0.2284	1.514E+07	6.873E-05	0.3781	3.835E+07	7.538E-05
$b$	0.0366	0.0366	0.0369	0.0381	0.0379	0.0386	0.0354	0.0354	0.0356
$\sigma_{\ln DP}$ (No TMD)	0.1104	0.1090	0.1152	0.1126	0.1106	0.1184	0.1228	0.1205	0.1276
$\sigma_{\ln DP}$ (With TMD)	0.0836	0.0828	0.0860	0.0979	0.0964	0.1018	0.1107	0.1092	0.1139

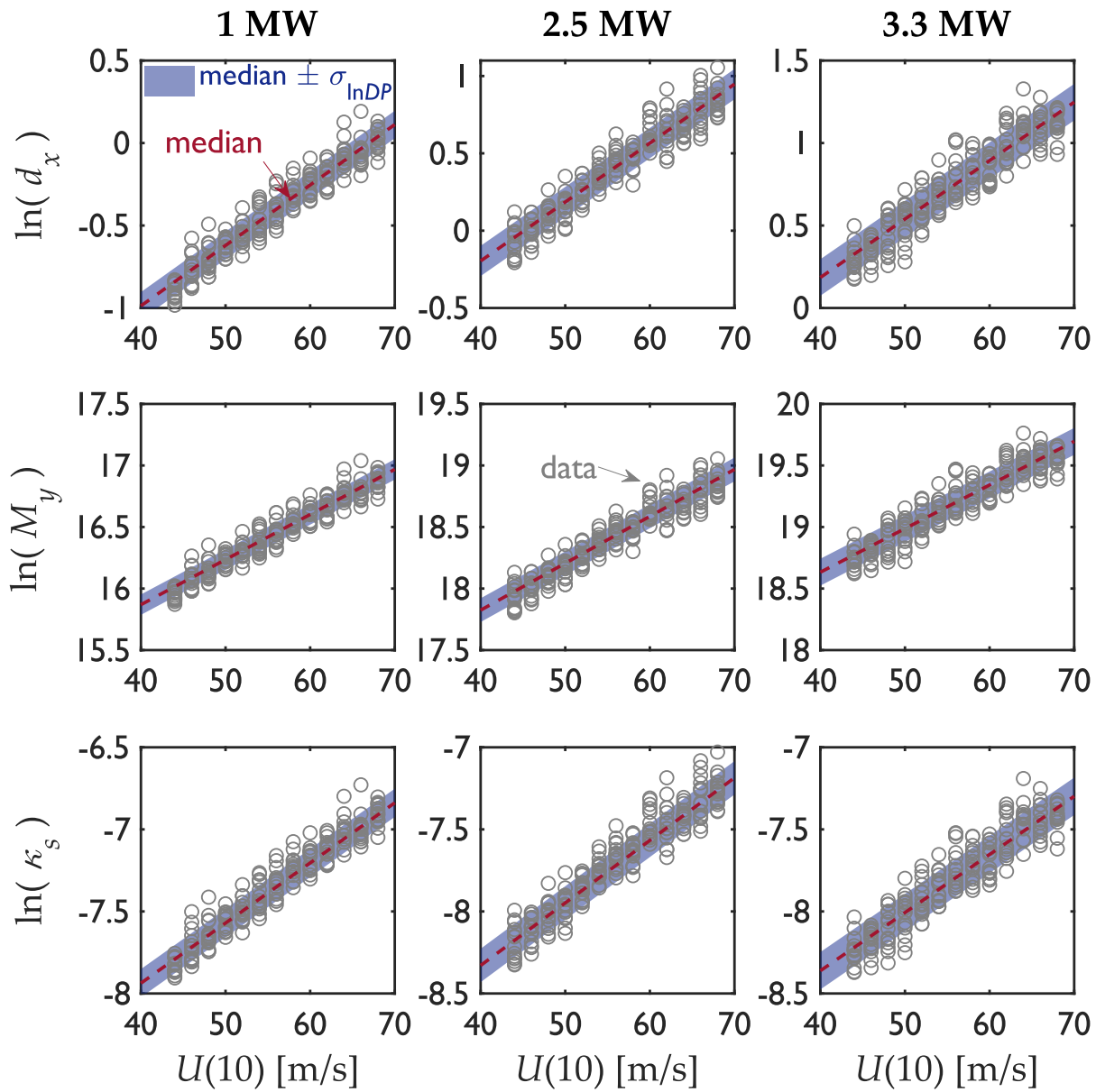


Figure 5.7: Fittings for the natural logarithm of the estimated median for the optimal cases, and observations

Moreover, the assumption of the normal distribution of the raw residuals is corroborated by means of probability plots performed on them, using response data from the numerical analyses. These probability plots are presented in Figure 5.8. Note from this figure that the residuals from the undamped case have been separated from those of the TMD cases. This owes to the fact that the undamped cases displayed larger values of uncertainty that were of relevance in the estimation of the fragility functions, which are described in the following subsection. The uncertainty estimated from the residuals of Equation 5.18 is also presented in Table 5.4, where the distinction between uncertainties of the damped and undamped cases is taken into account.

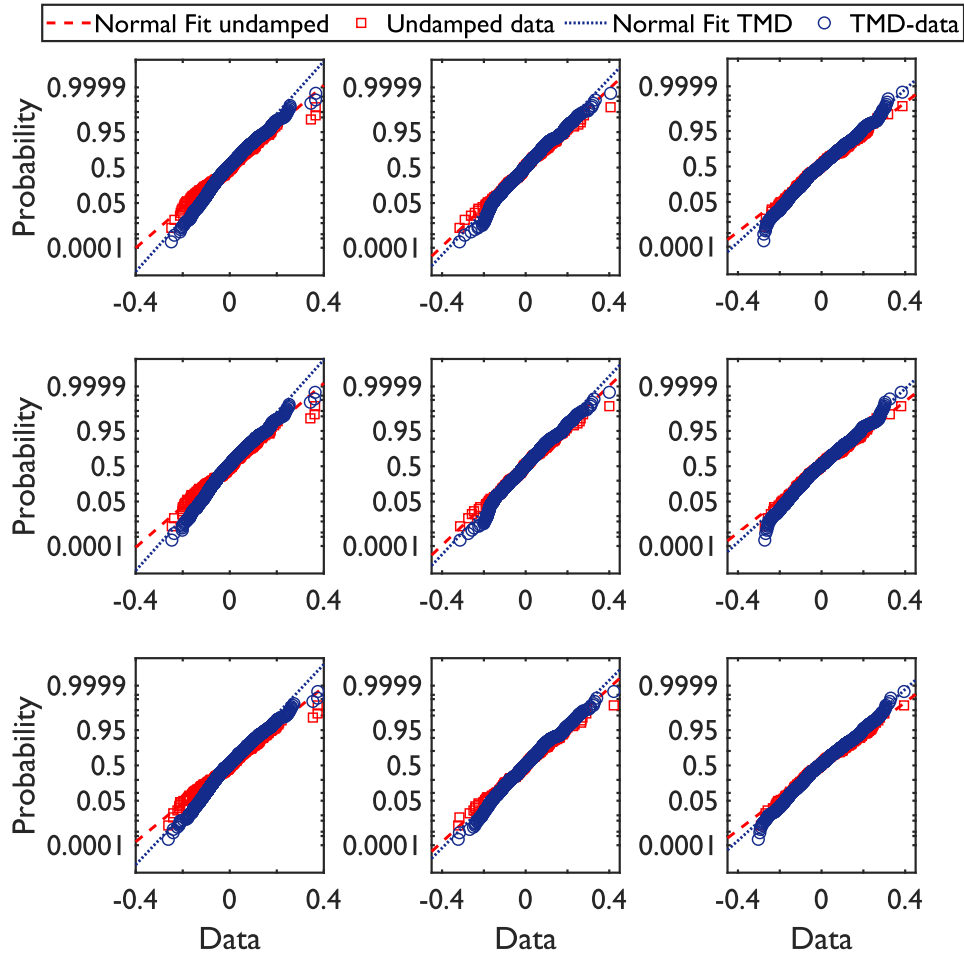


Figure 5.8: Probability plots of raw residuals of Equation 5.18

#### 5.4.2 Development of fragility functions

The DSs representing the structural performance of the wind turbine structures have been defined earlier in Chapter 4. Recalling these states, the damage levels have been defined to represent a residual displacement on the structure, the reaching of the nominal bending moment capacity of the section, and the buckling of the structure measured from the curvature of the tower. By means of the damage thresholds summarized in Table 4.5, and the estimators presented in Table 5.4, Equation 5.14 was evaluated and the structural fragility was estimated.

The fragility functions computed for each turbine and each DS are displayed in Figure 5.9. In the figure, the cases corresponding to the undamped and the 'optimal' case are selected de novo to illustrate the effects of the damping devices on structural fragility. From left to right the boxes in the figure display the fragility functions for the 1, 2.5, and 3.3 MW wind turbines. Whereas from top to bottom are presented the functions for the DSs 1 to 3.

From Figure 5.9 it can be seen a considerable reduction in the probability of failure for all the evaluated DSs when the structures are fitted with a TMD. Moreover, it can be seen that all the states of performance are reached within the ranges of intensity evaluated in the numerical analyses. In that regard, the structures appear to become more sensitive to wind action as they become more flexible. That is, the larger the turbine, the higher the probability of damage or collapse at any particular wind speed. Notwithstanding, the effects of the TMD on the structural response become notorious in every

case. As can be inferred from Equations 5.17 and 5.18, and from Table 5.4, different combinations of the TMD parameters would also produce a reduction in the probability of damage. However, the one selected as the optimal case from the time-history analyses produced the greatest reduction in fragility estimates. The following section discusses in more detail these reductions.

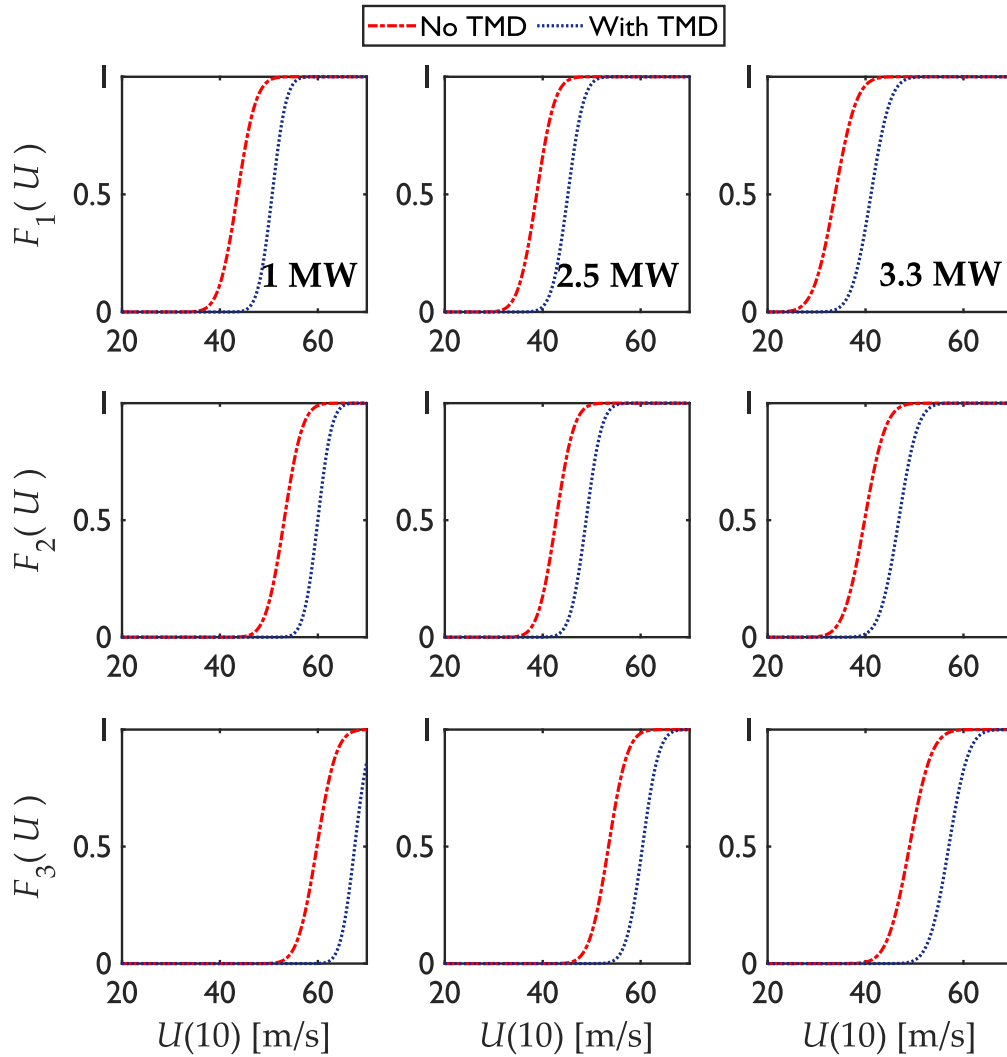


Figure 5.9: Comparison of fragility values for the studied wind turbines

## 5.5 Reliability enhancement

The use of passive damping devices on the structures diminishes the structural response in terms of the RMS value as well as the peak values. In the present study, the latter are the ones of interest due to the extreme values of intensities that represent the phenomena under evaluation, which are tropical cyclones. The evaluation of structural response enhancement presented in the literature survey is performed by comparison of the structural fragility at a particular value of wind intensity. However, as can be appreciated from Figure 5.9, it is unpractical to determine the differences in fragility straightforwardly at a single intensity value. A simple evaluation of this enhancement is performed in this section.

### 5.5.1 Quantification of reliability enhancement

As can be seen from Figure 5.9, the estimations of fragility are different for each DS, structure, and even the value of wind intensity. The enhancement of fragility can be visualized in a more practical manner by defining this enhancement as  $\Delta F(IM)$ . This value is proposed in this study to be computed from the subtraction of the fragility estimates when the structures are fitted with TMDs, to those without any passive damping device. That is,  $\Delta F(IM) = F_{\text{No TMD}}(IM) - F_{\text{TMD}}(IM)$ . Figure 5.10 displays the values of estimated reliability enhancement from the functions displayed in Figure 5.9. From top to bottom, these reductions are presented for the 1, 2.5, and 3.3 MW wind turbines, respectively.

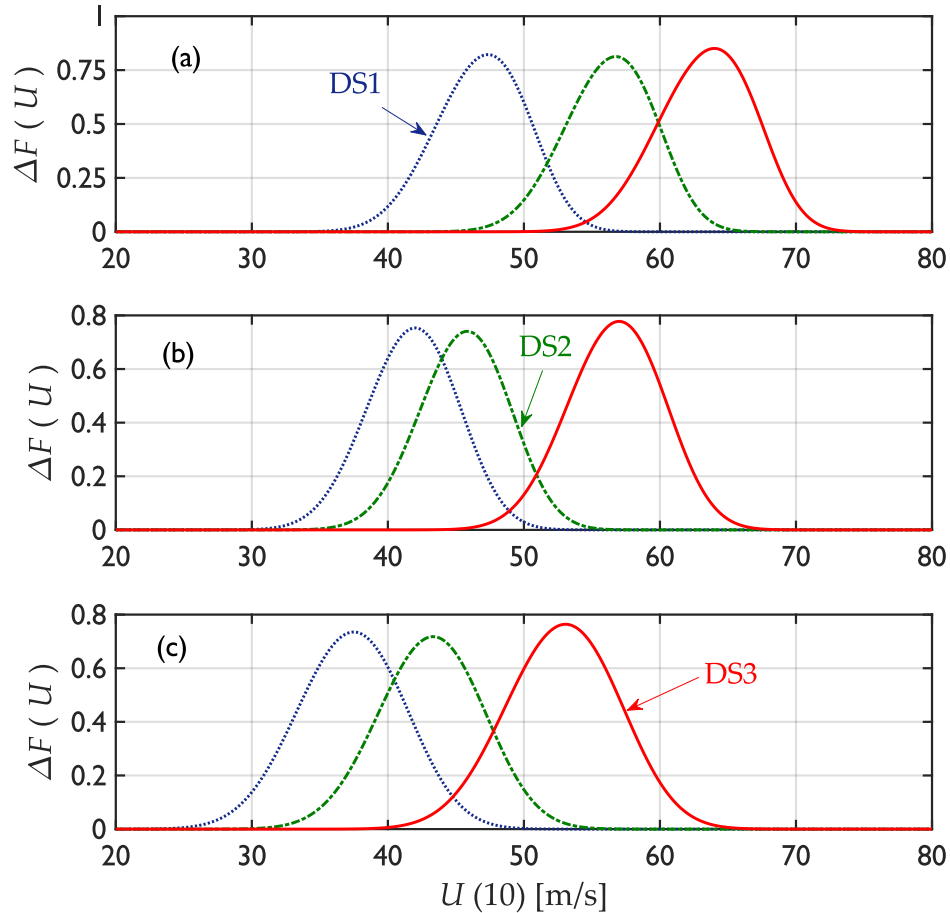


**Figure 5.10:** Fragility enhancement achieved with a TMD on the structures: (a) for the 1 MW wind turbine, (b) for the 2.5 MW wind turbine, and (c) for the 3.3 MW wind turbine

Figure 5.10 displays the fragility enhancement achieved for the three turbines analyzed under the action of cyclone-induced wind forces when a TMD is fitted to them. From this figure, it can be seen that the reduction in fragility estimates is variable along the wind intensity axis, and a maximum value of fragility reduction can be achieved at particular intervals of wind speed. Moreover, as mentioned previously, as the structures become more flexible, they become more sensitive to wind action. This can also be appreciated from Figure 5.10 by observing the leftward tendency of the location of the peaks of  $\Delta F$  on the intensity axis for the larger turbines.

The maximum reduction in fragility is  $\sim 80\%$  in all cases. That is, the greatest difference in fragility estimates is nearly 80% less probability of damage when the structures are fitted with a TMD. This is

mainly attributable to the contribution of a single mode dominating the structural response, inasmuch as the TMDs are effective in controlling a single modal form. Diverse studies of passive damping devices on wind-sensitive structures suggest that these devices are more effective in reducing the RMS values of structural response at low wind intensities. In this case, the greater enhancement in the probability of failure is seen at large wind speeds. However, for the analyzed structures, the range of intensities of this enhancement is limited and is of no contribution to the fragility estimates for extremely large wind speeds, i.e., for wind speeds of Category-IV cyclones or superior.

The structural reliability contribution of the passive damping devices can also be determined by accounting for a specific hazard context. This is dictated by the location of the structures under analysis. In the case of the present study, the turbines are assumed to be located in the Mexican state of Oaxaca. The following subsection displays a brief illustration of the structural risk enhancement achieved with passive damping devices, accounting for a concordant hazard context.

### 5.5.2 Risk enhancement

The implementation of TMDs on the structures represents a considerable reduction in the probability of structural failure. However, the cyclone hazard is site-dependent, that is, the wind intensities are unequally probable at a particular site. A brief and quick example of the enhancement achieved with TMDs in terms of annual probability of damage is presented in this part. For that purpose, the data presented in published research related to this dissertation is considered.

In the work of Jaimes et al.,<sup>10</sup> a probabilistic risk analysis is carried out for the three turbines analyzed in this study. However, in that reference, the turbines include no damping device. A comparison between the risk for two sites in Mexico is presented in the aforementioned reference.<sup>10</sup> One of the sites corresponds to the state of Oaxaca. As mentioned previously in this dissertation, this site is of relevance for wind turbine studies in the hazard context of Mexico, owing to the fact that the greater part of wind turbines in the country are installed on the aforementioned site. Thus, the hazard curve presented in the reference of Jaimes et al.<sup>10</sup> is used for the following example. The original curve is presented for 3-s gust values of maximum wind speed in km/h. However, these values have been transformed to 10-min averaged values in m/s. This has been performed assuming a gust factor of 1.425, as premised also for the analyses of Chapter 3. Therefore, the annual rate at which a wind-speed value measured at 10 m from the ground is equaled or exceeded ( $\lambda(\bar{U})$ ), for an arbitrary site in Oaxaca, is presented in Figure 5.11.

According to the law of total probability, the annual probability (or rather, the mean annual frequency) of physical damage on a structure, associated with an  $i$ -th DS of performance with damage threshold  $dt_i$ , is given by<sup>57</sup>:

$$P_{af,i} = \int P(DP_i \geq dt_i | im) \left| \frac{d\lambda(im)}{dim} \right| dim \quad (5.19)$$

The first term within the integral in Equation 5.19 is the fragility function such as those presented in Figure 5.9. Therefore, accounting for the annual exceedance rate as displayed in Figure 5.11, the annual probability of failure  $P_{af}$  computed for each of the turbines and their DSs is summarized in Table 5.5.

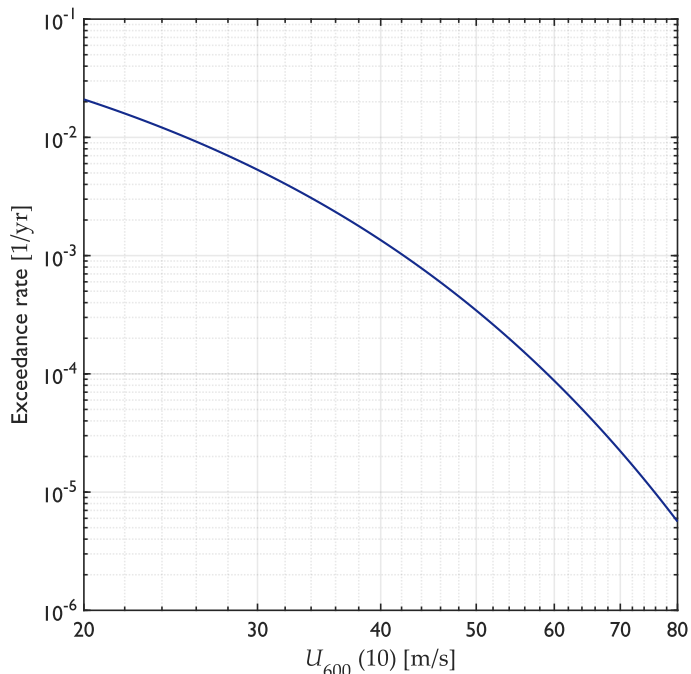


Figure 5.11: Annual exceedance rate for a site in Oaxaca, according to Jaimes et al.<sup>10</sup>

Table 5.5: Annual probability of structural failure due to tropical cyclones

Turbine	1 MW	2.5 MW	3.3 MW
Case	$P_{af}$ [1/yr]	$P_{af}$ [1/yr]	$P_{af}$ [1/yr]
DS1 (No TMD)	8.96E-04	1.73E-03	3.54E-03
DS1 (with TMD)	3.23E-04	7.05E-04	1.26E-03
Ratio	2.774	2.459	2.802
DS2 (No TMD)	2.38E-04	1.00E-03	1.54E-03
DS2 (with TMD)	8.60E-05	4.21E-04	5.78E-04
Ratio	2.764	2.385	2.666
DS3 (No TMD)	9.25E-05	2.29E-04	4.40E-04
DS3 (with TMD)	2.70E-05	8.28E-05	1.39E-04
Ratio	3.425	2.764	3.163

As can be seen from the information summarized in Table 5.5, the risk reduction achieved with the use of a TMD on the structures is considerable for the hazard context assumed for this rapid evaluation. In the table, the ratio between the values of  $P_{af}$  achieved with no TMD to those achieved with the implementation of a passive damping device is also presented. These values indicate that the mean annual probability of failure is nearly three times lower when a passive damping device is added to the structures. However, different TMD configurations, as well as different hazard contexts, can produce different ratios. Notwithstanding, risk reduction would still be expected with the implementation of TMDs, which can imply considerable gains in the lifetime extension of wind turbine support structures.

## 5.6 Conclusions

The fragility analyses, and prompt risk analysis, of three wind turbines subjected to cyclone-induced action, and fitted with tuned mass dampers, have been presented in this chapter. Different combi-

nations of the parameters that define the TMDs have been studied from harmonic analyses on FEMs of the three structures, as well as from time-history analyses that account for cyclonic wind field. An optimal combination of the parameters that define the TMD has been determined, and comparisons between the structural response accounting for that combination and without the inclusion of the TMDs have been carried out. From the results, the efficacy of the use of TMDs on the structure in reducing the probability of failure has been determined. A simple evaluation of structural risk enhancement has been performed accounting for the hazard context of the site premised for the analyses.

Part of the results displayed in the present chapter has been published in an archived journal.<sup>58</sup> In that publication, the earthquake action on the structures is also accounted for, as well as the combined action of cyclonic wind and earthquake. Earthquake-induced responses of the structures have been disregarded in the present chapter, inasmuch as these fall out of the scope of the present dissertation. However, the interested reader is referred to the work of Martín del Campo et al.<sup>58</sup> for further details on the results from the earthquake and multi-hazard cases.

Regarding the procedures and analyses presented in the present chapter, the following comments are noteworthy:

- Regarding the literature surveyed for the present study, it is a noticeable fact that most of the studies on wind turbines and damping devices are of numerical nature. No study or report was found where the response was measured from real structures, other than the ones performed experimentally. Notwithstanding the relevance of the surveyed experimental studies, these accounted for simplified models representing the wind turbine structures. Thus, a research gap involving the field measurements of the structural response of wind turbines fitted with supplementary damping devices is identified.
- A great part of recent studies is centered on the use of active and semi-active TMDs. This is attributed in part to the liabilities identified from passive TMDs compared to the aforementioned devices. Among these debits mentioned in diverse references, in the mild opinion of the author, perhaps the one of greatest consequences might be the mistuning of the passive TMD. Howbeit, passive TMDs are a consolidated solution to reduce the structural response and, as has been presented in this chapter, the numerical studies of their use indicate notable benefits in terms of structural reliability. Further studies accounting for physical problems that might be unattended numerically are of relevance for the validation of these findings.
- Among the surveyed publications for this study, it was noted that the ones accounting for earthquake action on the structures disregarded any consideration of site effects. That is, most of the surveyed studies analyzed the HAWT structures under the actions of ‘textbook’ ground-motion records, and no real measurements of ground motions from sites near, or similar, to real wind farm locations were used in those studies.
- The TMD parameters determined as optimal from the time-history analyses imply lower ratios than the values predicted by conventional expressions. However, these expressions, as well as the results from harmonic analyses, are useful to determine a premier approximation to the optimal values.
- Greater uncertainty values can be observed in Table 5.4 for the undamped cases than for the cases that account for the implementation of a TMD on the structures. This is attributed to the reduction of the RMS value of the structural response. This metric was disregarded for the present study, however, a lower RMS value of response is concordant with measurements from other TMD-centered studies.



- For the present study, no probability distribution other than the log-normal distribution has been considered to represent the structural response maxima. Nevertheless, the disregard of other probability distributions owes to the fact that log-normally distributed variables are assumed for the estimation of structural fragility from the median of the structural response.
- A better estimation of the uncertainty involved from the parameters that define the TMDs could be achieved by the use of *mixed-effects* models. The uncertainties accounted by means of these models could be the structural damping and the detuning of the TMD. Moreover, a more elaborate residual analysis is necessary when these models are applied. However, these are out of the scope of the present work.
- The curves displaying the enhancement of probability of failure can be availed for reliability-based optimization problems. That is, the maximum fragility enhancement can be studied and targeted for specific levels of intensity measure, in order to achieve the lowest failure rates during a risk analysis. Nevertheless, these activities are beyond the reach of this work.

## References

1. Housner, G. W. *et al.* Structural control: past, present, and future. *Journal of Engineering Mechanics* **123**, 897–971 (1997). doi: 10.1061/(ASCE)0733-9399(1997)123:9(897).
2. Chou, J.-S. & Tu, W.-T. Failure analysis and risk management of a collapsed large wind turbine tower. *Engineering Failure Analysis* **18**, 295–313 (2011). doi: 10.1016/j.engfailanal.2010.09.008.
3. Ma, Y., Martinez-Vazquez, P. & Baniotopoulos, C. Wind turbine tower collapse cases: a historical overview. *Proceedings of the Institution of Civil Engineers – Structures and Buildings* **172**, 547–555 (2019). doi: 10.1680/jstbu.17.00167.
4. Hong, L. & Möller, B. An economic assessment of tropical cyclone risk on offshore wind farms. *Renewable Energy* **44**, 180–192 (2012). doi: 10.1016/j.renene.2012.01.010.
5. Rose, S., Jaramillo, P., Small, M. J., Grossmann, I. & Apt, J. Quantifying the hurricane risk to offshore wind turbines. *Proceedings of the National Academy of Sciences* **109**, 3247–3252 (2012). doi: 10.1073/pnas.1111769109.
6. Amirinia, G. & Jung, S. Buffeting response analysis of offshore wind turbines subjected to hurricanes. *Ocean Engineering* **141**, 1–11 (2017). doi: 10.1016/j.oceaneng.2017.06.005.
7. Hallowell, S. T. *et al.* Hurricane risk assessment of offshore wind turbines. *Renewable Energy* **125**, 234–249 (2018). doi: 10.1016/j.renene.2018.02.090.
8. Kapoor, A. *et al.* Hurricane eyewall winds and structural response of wind turbines. *Wind Energy Science* **5**, 89–104 (2020). doi: 10.5194/wes-5-89-2020.
9. Amirinia, G. & Jung, S. Along-wind buffeting responses of wind turbines subjected to hurricanes considering unsteady aerodynamics of the tower. *Engineering Structures* **138**, 337–350 (2017). doi: 10.1016/j.engstruct.2017.02.023.
10. Jaimes, M. A., García-Soto, A. D., Martín del Campo, J. O. & Pozos-Estrada, A. Probabilistic risk assessment on wind turbine towers subjected to cyclone-induced wind loads. *Wind Energy* **23**, 528–546 (2020). doi: 10.1002/we.2436.
11. Wang, H., Ke, S. T., Wang, T. G. & Zhu, S. Y. Typhoon-induced vibration response and the working mechanism of large wind turbine considering multi-stage effects. *Renewable Energy* **153**, 740–758 (2020). doi: 10.1016/j.renene.2020.02.013.
12. Klotzbach, P. J., Bowen, S. G., Pielke, R. & Bell, M. Continental U.S. hurricane landfall frequency and associated damage: Observations and future risks. *Bulletin of the American Meteorological Society* **99**, 1359–1376 (2018). doi: 10.1175/BAMS-D-17-0184.1.

13. Suzuki-Parker, A. *Uncertainties and Limitations in Simulating Tropical Cyclones* PhD thesis (Georgia Institute of Technology, Atlanta, USA, Aug. 2011). doi: 10.1007/978-3-642-25029-3.
14. Kossin, J. P., Hall, T., Knutson, T., *et al.* in (eds Wuebbles, D. J., Fahey, D. W., Hibbard, K. A., *et al.*) 257–276 (U.S. Global Change Research Program, Washington, USA, 2017). doi: 10.7930/J07S7KXX.
15. Appendini, C. M. *et al.* Effect of climate change over landfalling hurricanes at the Yucatan Peninsula. *Climatic Change* **157**, 469–482 (2019). doi: 10.1007/s10584-019-02569-5.
16. Pozos-Estrada, A. *Reliability of wind-sensitive buildings: a service reliability design consideration* PhD thesis (University of Western Ontario, London, Canada, 2009).
17. Pozos-Estrada, A. & Hong, H. P. Sensitivity analysis of the effectiveness of tuned mass dampers to reduce the wind-induced torsional responses. *Latin American Journal of Solids and Structures* **12**, 2520–2538 (2015). doi: 10.1590/1679-78251856.
18. Sun, Z., Zou, Z., Ying, X. & Li, X. Tuned mass dampers for wind-induced vibration control of Chongqi bridge. *Journal of Bridge Engineering* **25**, 05019014 (2020). doi: 10.1061/(ASCE)BE.1943-5592.0001510.
19. Zhou, K., Zhang, J.-W. & Li, Q.-S. Control performance of active tuned mass damper for mitigating wind-induced vibrations of a 600-m-tall skyscraper. *Journal of Building Engineering* **45**, 103646 (2022). doi: 10.1016/j.jobe.2021.103646.
20. Rahman, M., Ong, Z. C., Chong, W. T., Julai, S. & Khoo, S. Y. Performance enhancement of wind turbine systems with vibration control: A review. *Renewable and Sustainable Energy Reviews* **51**, 43–54 (2015). doi: 10.1016/j.rser.2015.05.078.
21. Zuo, H., Bi, K. & Hao, H. A state-of-the-art review on the vibration mitigation of wind turbines. *Renewable and Sustainable Energy Reviews* **121**, 109710 (2020). doi: 10.1016/j.rser.2020.109710.
22. Enevoldsen, I. & Mørk, K. J. Effects of a vibration mass damper in a wind turbine tower. *Journal of Structural Mechanics* **24**, 155–187 (1996). doi: 10.1080/08905459608905260.
23. Lackner, M. A. & Rotea, M. A. Passive structural control of offshore wind turbines. *Wind Energy* **14**, 373–388 (2011). doi: 10.1002/we.426.
24. Jonkman, J. M. & Buhl Jr., M. L. *FAST User's Guide* National Renewable Energy Laboratory (Golden, Colorado, 2005). NREL/EL-500-29798.
25. Lackner, M. A. & Rotea, M. A. Structural control of floating wind turbines. *Mechatronics* **21**, 704–719 (2011). doi: 10.1016/j.mechatronics.2010.11.007.
26. Stewart, G. M. & Lackner, M. A. The effect of actuator dynamics on active structural control of offshore wind turbines. *Engineering Structures* **33**, 1807–1816 (2011). doi: 10.1016/j.engstruct.2011.02.020.
27. Namik, H., Rotea, M. & Lackner, M. *Active structural control with actuator dynamics on a floating wind turbine* in *51st AIAA Aerospace Sciences Meeting Including the New Horizons Forum and Aerospace Exposition* (2013), 455. doi: 10.2514/6.2013-455.
28. Lian, J. *et al.* Application of an eddy current-tuned mass damper to vibration mitigation of offshore wind turbines. *Energies* **11**, 3319 (2018). doi: 10.3390/en1123319.
29. Zhao, B., Gao, H., Wang, Z. & Lu, Z. Shaking table test on vibration control effects of a monopile offshore wind turbine with a tuned mass damper. *Wind energy* **21**, 1309–1328 (2018). doi: 10.1002/we.2256.
30. Chen, J. & Georgakis, C. T. Tuned rolling-ball dampers for vibration control in wind turbines. *Journal of Sound and Vibration* **332**, 5271–5282 (2013). doi: 10.1016/j.jsv.2013.05.019.
31. Zhang, Z., Basu, B. & Nielsen, S. R. Real-time hybrid aeroelastic simulation of wind turbines with various types of full-scale tuned liquid dampers. *Wind Energy* **22**, 239–256 (2019). doi: 10.1002/we.2281.
32. Caterino, N. Semi-active control of a wind turbine via magnetorheological dampers. *Journal of Sound and Vibration* **345**, 1–17 (2015). doi: 10.1016/j.jsv.2015.01.022.

33. Si, Y., Karimi, H. R. & Gao, H. Modelling and optimization of a passive structural control design for a spar-type floating wind turbine. *Engineering Structures* **69**, 168–182 (2014). doi: 10.1016/j.engstruct.2014.03.011.
34. Zuo, H., Bi, K. & Hao, H. Using multiple tuned mass dampers to control offshore wind turbine vibrations under multiple hazards. *Engineering Structures* **141**, 303–315 (2017). doi: 10.1016/j.engstruct.2017.03.006.
35. Sun, C. Semi-active control of monopile offshore wind turbines under multi-hazards. *Mechanical Systems and Signal Processing* **99**, 285–305 (2018). doi: 10.1016/j.ymsp.2017.06.016.
36. Hemmati, A., Oterkus, E. & Khorasanchi, M. Vibration suppression of offshore wind turbine foundations using tuned liquid column dampers and tuned mass dampers. *Ocean Engineering* **172**, 286–295 (2019). doi: 10.1016/j.oceaneng.2018.11.055.
37. Brodersen, M. L., Bjørke, A.-S. & Høgsberg, J. Active tuned mass damper for damping of offshore wind turbine vibrations. *Wind Energy* **20**, 783–796 (2017). doi: 10.1002/we.2063.
38. IEC. *Wind turbines – Part 1: Design requirements* 3rd ed. International Electrotechnical Commission (Geneva, Switzerland, 2005).
39. Kim, D. H., Lee, S. G. & Lee, I. K. Seismic fragility analysis of 5 MW offshore wind turbine. *Renewable Energy* **65**, 250–256 (2014). doi: 10.1016/j.renene.2013.09.023.
40. Patil, A., Jung, S. & Kwon, O.-S. Structural performance of a parked wind turbine tower subjected to strong ground motions. *Engineering Structures* **120**, 92–102 (2016). doi: 10.1016/j.engstruct.2016.04.020.
41. Asareh, M.-A., Schonberg, W. & Volz, J. Fragility analysis of a 5-MW NREL wind turbine considering aero-elastic and seismic interaction using finite element method. *Finite Elements in Analysis and Design* **120**, 57–67 (2016). doi: 10.1016/j.finel.2016.06.006.
42. Martín del Campo, J. O. & Pozos-Estrada, A. Multi-hazard fragility analysis for a wind turbine support structure: An application to the Southwest of Mexico. *Engineering Structures* **209**, 109929 (2020). doi: 10.1016/j.engstruct.2019.109929.
43. Katsanos, E. I., Sanz, A. A., Georgakis, C. T. & Thöns, S. Multi-hazard response analysis of a 5MW offshore wind turbine. *Procedia Engineering* **199**, 3206–3211 (2017). doi: 10.1016/j.proeng.2017.09.548.
44. Mensah, A. F. & Dueñas-Osorio, L. *Reliability analysis of wind turbines equipped with tuned liquid column dampers (TLCD)* in *Structures Congress 2012* (2012), 1190–1200. doi: 10.1061/9780784412367.107.
45. Mensah, A. F. & Dueñas-Osorio, L. Improved reliability of wind turbine towers with tuned liquid column dampers (TLCDs). *Structural safety* **47**, 78–86 (2014). doi: 10.1016/j.strusafe.2013.08.004.
46. Fitzgerald, B., Sarkar, S. & Staino, A. Improved reliability of wind turbine towers with active tuned mass dampers (ATMDs). *Journal of Sound and Vibration* **419**, 103–122 (2018). doi: 10.1016/j.jsv.2017.12.026.
47. Hemmati, A., Oterkus, E. & Barltrop, N. Fragility reduction of offshore wind turbines using tuned liquid column dampers. *Soil Dynamics and Earthquake Engineering* **125**, 105705 (2019). doi: 10.1016/j.soildyn.2019.105705.
48. Wong, K. K. & Harris, J. L. Seismic damage and fragility analysis of structures with tuned mass dampers based on plastic energy. *The Structural Design of Tall and Special Buildings* **21**, 296–310 (2012). doi: 10.1002/tal.604.
49. Pozos-Estrada, A. & Gómez, R. Parametric study of the use and optimization of tuned mass dampers to control the wind-and seismic-induced responses of a slender monument. *The Structural Design of Tall and Special Buildings* **28**, e1633 (2019). doi: 10.1002/tal.1633.
50. Den Hartog, J. P. *Mechanical Vibrations* 4th ed. (Dover Publications, New York, USA, 1985).

51. Warburton, G. B. Optimum absorber parameters for various combinations of response and excitation parameters. *Earthquake Engineering & Structural Dynamics* **10**, 381–401 (1982). doi: 10.1002/eqe.4290100304.
52. Chang, C. C. Mass dampers and their optimal designs for building vibration control. *Engineering Structures* **21**, 454–463 (1999). doi: 10.1016/S0141-0296(97)00213-7.
53. Bakre, S. V. & Jangid, R. S. Optimum parameters of tuned mass damper for damped main system. *Structural Control and Health Monitoring* **14**, 448–470 (2007). doi: 10.1002/stc.166.
54. Adams, M. L. J. *Rotating Machinery Vibration: from analysis to troubleshooting* (Marcel Dekker, Inc., 2001).
55. *ANSYS Mechanical APDL Theory Reference* ANSYS Inc. (2018).
56. Ditlevsen, O. & Madsen, M. H. *Structural Reliability Methods* (Wiley New York, 2005).
57. Cornell, C. A., Jalayer, F., Hamburger, R. O. & Foutch, D. A. Probabilistic basis for 2000 SAC federal emergency management agency steel moment frame guidelines. *Journal of structural engineering* **128**, 526–533 (2002). doi: 10.1061/ASCE:0733-9445(2002)128:4(526)
58. Martín del Campo, J. O., Pozos-Estrada, A. & Pozos-Estrada, O. Development of fragility curves of land-based wind turbines with tuned mass dampers under cyclone and seismic loading. *Wind Energy* **24**, 737–753 (2021). doi: 10.1002/we.2600.

## Chapter 6

# Simplified evaluation of the structural response of wind turbines

The development of computational tools for the performance of difficult mathematical calculations has enabled the solution of numerous problems in physics and engineering. Structural engineering has also benefited from the advancements in these tools. For example, problems that demanded laborious calculations that could take days to solve 'by hand' 30 years ago, are solved in a matter of seconds with contemporary domestic computational power. These advances have permitted more detailed analyses of structural systems under a wide variety of load cases and combinations. In the case of some structures, these load cases imply the combination of several environmental variables that influence the structural response — and consequently the structural reliability — to a large extent. State-of-the-art approaches rely on massive time-history simulations and analyses for the estimation of the structural response under diverse load conditions. Notwithstanding the modern numerical capabilities, these approaches are sometimes prohibitive due to their large computational expense.

This chapter presents a simplified method for prompt evaluation of wind turbine support structures. The method is no substitute for a detailed model of the wind turbine structure. Rather, the simplification is intended to be of application for prompt reliability analyses, inasmuch as it allows to replicate response values relying fundamentally on stochastic and probabilistic information of the loads acting on the structural component under analysis.

### 6.1 Introduction

The wind-loading chain, as first proposed by Professor Alan G. Davenport, defines the assessment of wind action on a particular structure from the combined effects of the links composing the chain (see Figure 6.1): (i) wind climate, (ii) terrain influence, (iii) aerodynamic characteristics, (iv) dynamic response, and (v) design criteria.<sup>1</sup> Although these elements are defined as deterministic in common wind-engineering standards, each of them is, in reality, stochastic,<sup>2</sup> and might even display a certain degree of statistical dependence. This symbolism was originally explained by Professor Davenport to describe the steps of reliable wind load evaluation on wind-sensitive civil structures, such as bridges or high-rise buildings. However, the concepts summarized in that train of thought can be extrapolated to different kinds of systems, such as horizontal axis wind turbines (HAWTs).

The first and second links of the chain (i.e., the environmental parameters) determine in great part the magnitudes and effects of the loads on the structure under study and are of major significance for its lifetime. Published studies specific to wind turbine structures have centered on the probabilistic characterization of the diverse environmental parameters that intervene in the wind loads on them. In the case of onshore wind turbines, among the studied parameters are often: the mean wind speed in the prevailing direction  $\bar{U}(z)$ , the standard deviation of wind speed (i.e., turbulence)  $\sigma_u$ , the power-

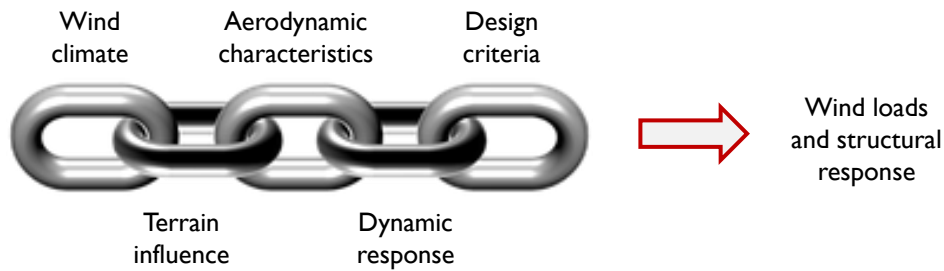


Figure 6.1: Wind loading chain

law exponent that defines the mean-speed profile  $\alpha$ , the turbulence length scale  $L_u$ , the air density  $\rho$ , and the flow incidence angle, among other ambient or turbine-related parameters.<sup>3,4</sup> Whereas, in the case of offshore structures, the definition of uncertainties from the ocean environment is of large importance as well.<sup>5</sup>

The third link in the chain corresponds to the aerodynamic characteristics of the structure. In the case of common civil structures, their aerodynamic characteristics are driven mainly by the geometry of the structure with respect to the incidence angle of the flow. Whereas in the case of operating wind turbines, the greater aerodynamic-load contributions are originated from the rotor (see Section 2.2). In this regard, the aerodynamic force coefficients on which the rotor operates vary considerably with wind speed. This is insofar as the turbine is provided with mechanisms to ensure optimal extraction of energy from the wind stream. This makes the aerodynamic evaluation of an operating wind turbine more intricate than that of a static structure. Furthermore, ambient conditions such as wind turbulence ( $\sigma_u$ ) are considerably affected within wind farms by the operating wind turbines.<sup>6</sup> Thus, one of the environmental parameters of greater importance for the wind-induced actions on a specific turbine is dependent on the aerodynamic characteristics of upwind-adjacent turbines operating within the wind power plant. The influence of uncertainties in this turbine-affected parameter (as well as in other environmental parameters) on the structural reliability of HAWTs has received attention from studies in the literature.<sup>7</sup>

Due to the oft-growing size of wind turbines and their components, the determination of their dynamic characteristics becomes of greater relevance. Some main wind-turbine elements are flexible structures susceptible to aerodynamic excitation, which asserts the importance of the fourth link in Davenport's chain. Wind-sensitive structures are generally prone to display low structural damping, and this is likewise for HAWTs. Furthermore, due to the operation of the turbine, aerodynamic damping plays a significant and variable contribution in the determination of the structural response under aerodynamic loads. Dynamic characteristics of the structure of the turbine — such as stiffness and mass — may be assumed to display less uncertain participation in the dynamic response of the HAWT, when compared to conventional civil structures. This is reasonable due to the high-quality control present in the fabrication of wind turbine elements.<sup>8</sup> However, aerodynamic damping is affected by many parameters of random nature, thus its assessment is a rather intricate subject. The aerodynamic and structural damping on wind turbine structures has been studied from various approaches in experimental research.<sup>9–12</sup> These studies comport with the difficulties of damping assessment due to the complicated interactions between structural vibration modes and diverse elements of the structure. Other approaches for disquisition on damping, such as numerical and analytic methods, have studied the estimation of aerodynamic damping on operating wind turbines. These studies have researched aerodynamic damping either from deductions based on the blade element momentum (BEM) theory<sup>13,14</sup> or from wavelet analysis of the structural response signals.<sup>8,15</sup> In summary, any survey of research that has centered on the aerodynamic damping estimation of operating wind turbines asserts that it is an issue neither trivial nor facile. Thus, the adopted approach for its

account in the structural response is driven by the complexity and accuracy demanded by the problem under analysis.<sup>12</sup>

Wind-excited elements of a HAWT, such as the blades or the tower, are continuously subjected to structural vibrations during their entire lifetime due to the operation of the turbine. That is, the design of these elements has to account for the cycles of load reversals that are expected to occur during their entire lifetime. Therefore, fatigue damage is an important design condition that has to be assessed for the whole service life of the turbine. This condition belongs to the fifth element of Davenport's chain for wind turbine structures. Regarding structural lifetime, the service life of wind turbines goes, on average, from 20 to 40 years.<sup>16</sup> This implies a large number of possible combinations of environmental and operational conditions for a single HAWT during this time, which have to be evaluated for the assessment of fatigue damage. As mentioned previously in this chapter, modern approaches for this assessment rely on samples of aeroelastic time-history analyses of the operating HAWT. These are performed for a large number of environmental and operational combinations, which typically demand long computing times. In this regard, inasmuch as surrogate models are tools for prompt and inexpensive solutions to physical problems of random nature, recent research has begun to study the use of these models for the assessment of fatigue-driven structural reliability of wind turbines.<sup>4,7,17-20</sup> This has been performed through different techniques, aiming for the definition of the limit state function for different load cases. Furthermore, regarding the lifetime of HAWTs, insofar as many of the currently-deployed wind turbines are about to reach (or exceed) their service life, the planning of the end of the latter is of relevance. Little research has been conducted to assess the technological, environmental, and economic issues associated with the end of service life of wind turbines.<sup>16</sup> However, re-powering of wind turbines that are still in condition to extend their service life is a feasible option economically.<sup>16,21</sup> The lifetime extension of wind turbines is expected to become an important part of the wind energy industry, inasmuch as an extension of up to 25% of the original service life is plausible in optimal cases.<sup>21</sup> These scenarios are directing research on structural health monitoring for the development of lifetime-extension strategies,<sup>21,22</sup> which mainly focus on the reliable assessment of fatigue damage on structural components of existing wind turbines. For this purpose, such strategies account for the incorporation of health-monitoring data and numerical models,<sup>23,24</sup> among other things.

The issues discussed above make it evident that the structural response of operating wind turbines is an intricate subject. Thus, in order to approach this issue, the use of numerical models and computational simulations for the evaluation of the structural reliability of wind turbines is undisputed. In that regard, non-parametric models for the evaluation of the structural response of wind turbines from large databases are a current tendency. Nevertheless, the adequate consideration of uncertainty in the structural response of HAWTs is still prohibitive, even with modern computational tools. This owes to the large number of numerical simulations needed to cover the ample possibilities of combinations regarding the parameters involved in the analyses. To contribute to that need, a simplified method for the determination of signals describing the response of the support structure of HAWTs is proposed and described in this chapter. The method is unintended as a replacement for detailed analyses from other numerical approaches for the assessment of structural response, such as elaborate finite element modeling (FEM). Rather, it is proposed as a feasible and computationally economical solution for prompt analyses, enabling to cover a wider range of operation and environmental conditions. This solution is useful for the development of structural reliability analyses. The method relies fundamentally on spectral characteristics of the loads and responses of the wind turbine structure, as well as on the probabilistic characteristics of their amplitudes. Details on the bases of the method are provided next.

### 6.1.1 Summary of the simplified methodology

The simplified strategies commented herein are intended for the evaluation of the maximum structural response, as well as for the determination of fatigue damage on a structural element. The examples covered in this chapter represent stages of power production during the normal operation

of wind turbines. That is, the methodology and examples presented in this chapter assume uninterrupted and constant power-production conditions from 10-min-length stochastic simulations, as accepted by the IEC 61400-1.<sup>25</sup> However, the methodology can be extrapolated to other cases of operation and other structures, if the proper criteria are adopted. Furthermore, in this chapter, it is assumed a linear distribution of stresses in the cross-section of the element under analysis. Thus, the histories of structural responses are assumed to be representative of the elastic linear behavior of the support structure.

As briefly described in Section 2.2, the dynamic forces acting on the support structure of a HAWT in operation are defined mainly from the thrust force on the rotor, and its associated aerodynamic moments. This can be availed for a reduction in the number of data needed to represent the structural behavior of the turbine tower. Moreover, the spectral characteristics of these actions will determine the frequency content, maximum amplitudes, and the number of load cycles. All these factors are of importance for fatigue evaluation. In that regard, the most commonly adopted procedure for cycle counting is the *rain-flow* algorithm,<sup>26</sup> in combination with the accumulated damage estimated from the S-N curve of the material. These criteria are accepted in conventional wind turbine standards and are accounted for the development of the present methodology.

What has been commented in the previous paragraphs serves as bases for the simplification discussed herein. Such a simplification can adopt two outlooks: (i) the simulation of aerodynamic forces for subsequent application to a reduced-order model of the wind turbine support structure, or (ii) the simulation of spectrally- and statistically-concordant structural response signals. For the two cases, the next steps can be followed for each combination of environmental and performance parameters involved in the structural response of a wind turbine:

- (i) Perform a representative sample of structural time-history analyses of the turbine functioning under specific environmental and operational conditions. These analyses must be performed on detailed models of the structure under study.
- (ii) Compute the first four statistical moments of the load or response signals of interest for each of the analyses in the sample.
- (iii) Estimate the cumulative distribution function (CDF) of the load or response amplitudes from the signals in the original sample.
- (iv) For each of the analyses in the sample, estimate the power spectral density function (PSDF) of the loads or the response produced by the operation of the wind turbine.
- (v) Perform a set of simulations of Gaussian signals with the frequency content dictated by the PSDF of load or response amplitudes for each of the elements that compose the original sample.
- (vi) Carry out the transformation of the Gaussian signals simulated in step (v), accounting for its respective CDF as estimated in step (iii).
- (vii) Compute the fatigue damage or the structural evaluation from the signals resulting from step (vi).

As can be observed from the list of steps just described, the statistical moments of the sample histories are mentioned as necessary. This owes to the fact that, inasmuch as the elastic structural response is directly proportional to the force acting on a system, the distribution of force-amplitude maxima is necessary to ensure the adequate representation of the maxima of responses. The following section provides more details on this subject. Moreover, a simplified four degree-of-freedom (DOF) model for structural analysis is also described in a subsequent section.



## 6.2 Simulation of non-Gaussian stochastic processes

Conventional simulation of wind turbulence in the neutral atmospheric boundary layer assumes that the amplitude distribution of turbulence is of Gaussian characteristics. This is a valid assumption for a wide variety of cases.<sup>27</sup> However, non-linearities introduced by, e.g., the combination of wind speed components, or the aerodynamic characteristics of a structure, can deviate the aerodynamic loads from a Gaussian distribution. For HAWTs, the intricate aerodynamic shapes of wind turbine blades, and the varying load decomposition originated by the operation of wind turbine rotors, are factors that induce significant non-linearities that can distort the probability distribution of force amplitudes acting on the structure. The distortion of load amplitudes thus influences greatly the ranges of stresses during a load sequence on the structural elements, as well as the extreme values of structural response expected in a determinate time interval. These distortions justify the definition of an adequate probability distribution of loads and responses as a matter of great relevance for structural reliability. An adequate probabilistic description of the load amplitudes acting on the structure facilitates the performance of stochastic process simulation. This simulated process can represent a physical one, but at a lower computing time compared to a full analysis of the structure. Elaboration on this subject is carried out in the following.

### 6.2.1 Translation models for non-Gaussian processes

There have been different methods proposed in the literature for the simulation of non-Gaussian stochastic processes. These methods rely on translation process theory, on which a non-Gaussian process can be related to a Gaussian one by means of a translation function. To elaborate on this, consider a stochastic stationary Gaussian process  $X(t)$ , the amplitudes of which can be represented by a standard-normal distribution. The process  $X(t)$  is thus to be translated into a non-Gaussian process  $Z(t)$ . However,  $Z(t)$  is conveniently normalized into the process  $Y(t)$ , which has zero mean and unit variance. Hence, the translation function  $g[X(t)]$  is defined form:

$$y(x) = F_Y^{-1}[\Phi(x)] = g(x) \quad (6.1)$$

In Equation 6.1,  $F_Y$  is the CDF of the normalized non-Gaussian process  $Y(t)$ ,  $\Phi(\cdot)$  the standard-normal CDF, and  $g(\cdot)$  the translation function. The latter must be devoid of memory and monotonically increasing for an adequate mapping of the processes.<sup>28</sup> According to the previous definitions, it can be asserted that  $g^{-1}[Y(t)] = X(t)$ . Furthermore, insofar as the amplitudes of  $X(t)$  are represented by a standard-normal distribution, the probability density function (PDF) of  $Y(t)$  can be expressed as  $f_Y(y) = \frac{d}{dy}F_Y(y) = \frac{dx}{dy}f_X(x)$ , that is:

$$f_Y(y) = \frac{1}{\sqrt{2\pi}} \exp\left[-\frac{x^2(y)}{2}\right] \frac{d}{dy}x(y) \quad (6.2)$$

Heretofore the relevance of the translation function has been indirectly expressed. In that regard, albeit Equation 6.1 is in practice evaluated numerically, in order to do so the form of  $g(X)$  is sought to be determined. For this purpose, an ingenious solution has been presented from the Hermite series expressing the non-Gaussian variable as<sup>29</sup>:

$$Y(t) = \sum_{n \geq 0} h_n He_n[X(t)] \quad (6.3)$$

$$He_n(x) = (-1)^n \exp(x^2/2) \frac{d^n}{dx^n} [\exp(-x^2/2)]$$

where  $He_n(\cdot)$  is the  $n$ -th Hermite polynomial, and the coefficients  $h_n$  are referred to as Hermite moments. This owes to the fact that they can be determined from the statistical moments of the variable  $Y(t)$ .<sup>29</sup> The relation between the variables expressed from the Hermite series can be applied also to their PDF, which results in<sup>30</sup>:

$$f_Y(y) = f_X(y) \left[ 1 + \sum_{n \geq 1} h_n He_n(y) \right] \quad (6.4)$$

where the Hermite moments  $h_n$  can be expressed as  $h_n = \frac{\alpha_n}{n!} - \frac{\alpha_{n-2}}{1!2(n-2)!} + \frac{\alpha_{n-4}}{2!4(n-4)!} - \dots$ , from the known statistical moments  $\alpha_n$ .<sup>30</sup> Equations 6.3 and 6.4 establish the base of one of the transformations of non-Gaussian processes more frequently used in structural engineering, as formerly published by Winterstein.<sup>30</sup> From this approach, recalling that the variable  $Y(t)$  has zero mean and unit variance, it can be truncately expressed from its third and fourth statistical moments and the Gaussian variable as  $Y = \kappa_w [X + \tilde{h}_3(X^2 - 1) + \tilde{h}_4(X^3 - 3X)]$ . Or rather, a value of  $X(t)$  and its correspondent derivative can be expressed from a value of the non-Gaussian variable as<sup>30</sup>:

$$x(y) = \left[ \sqrt{\tilde{\zeta}_w^2(y) + c} + \tilde{\zeta}_w(y) \right]^{1/3} - \left[ \sqrt{\tilde{\zeta}_w^2(y) + c} - \tilde{\zeta}_w(y) \right]^{1/3} - a \quad (6.5)$$

$$\frac{dx(y)}{dy} = \frac{b}{2\kappa_w \sqrt{\tilde{\zeta}_w^2(y) + c}} \left[ \left( \sqrt{\tilde{\zeta}_w^2(y) + c} + \tilde{\zeta}_w(y) \right)^{1/3} + \left( \sqrt{\tilde{\zeta}_w^2(y) + c} - \tilde{\zeta}_w(y) \right)^{1/3} \right] \quad (6.6)$$

where the parameters needed for the evaluation of the transformation are defined from<sup>30</sup>:

$$\tilde{\zeta}_w(y) = 1.5b \left( a + \frac{y}{\kappa_w} \right) - a^3 \quad (6.7a)$$

$$\kappa_w = \frac{1}{\sqrt{1 + 2\tilde{h}_3^2 + 6\tilde{h}_4^2}} \quad (6.7b)$$

$$a = \frac{\tilde{h}_3}{3\tilde{h}_4}, \quad b = \frac{1}{3\tilde{h}_4}, \quad c = (b - 1 - a^2)^3 \quad (6.7c)$$

In Equation 6.7, the coefficients  $\tilde{h}_3$  and  $\tilde{h}_4$  must be distinguished from the Hermite moments. Notwithstanding, these can also be defined from the third and fourth statistical moments of the non-Gaussian variable (i.e., from its *skewness* and *kurtosis*), as commented previously. A revised version of these coefficients presented optimized closed-form solutions with the form<sup>31</sup>:

$$\tilde{h}_3 = \frac{\alpha_3}{6} \left[ \frac{1 - 0.015|\alpha_3| + 0.3\alpha_3^2}{1 + 0.2(\alpha_4 - 3)} \right] \quad (6.8a)$$

$$\tilde{h}_4 = \tilde{h}_{40} \left[ 1 - \frac{1.43\alpha_3^2}{\alpha_4 - 3} \right]^{1-0.1(\alpha_4)^{0.8}} \quad (6.8b)$$

$$\tilde{h}_{40} = \frac{[1 + 1.25(\alpha_4 - 3)]^{1/3} - 1}{10} \quad (6.8c)$$

The model summarized above covers a wide variety of cases with application to structural engineering problems. However, it has been found rather inadequate for *hardening* stochastic processes, i.e., those with kurtosis less than three.<sup>32</sup> The moment-based translation model from Hermite polynomials presented is thus of application for cases where  $3 < \alpha_4 < 15$ . Moreover, in order for the translation function to be monotonic, the relation  $\alpha_4 \geq 3 + (1.25\alpha_3)^2$  must be ensured.<sup>32</sup>

To overcome the limitations of the model based on the Hermite polynomials, Ding and Chen developed translation models based on orthogonal polynomials. Their translation model is intended for processes with kurtosis less than three. From this approach, a value of the Gaussian process  $X(t)$  can be expressed from one of the non-Gaussian variable by<sup>32</sup>:

$$x(y) \approx b_2 y + b_3 (y^2 - \alpha_3 y - 1) + b_4 (y^3 - \alpha_4 y - \alpha_3) \quad (6.9)$$

$$\frac{dx(y)}{dy} \approx b_2 + 2b_3 y - b_3 \alpha_3 + 3b_4 y^2 - b_4 \alpha_4 \quad (6.10)$$

The derivative of  $X$  with respect to  $Y$  has also been presented in Equation 6.10, where the coefficients defining the model are determined from closed-form solutions dependent on the statistical moments:

$$b_2 = \varphi \left[ 1 - \frac{\alpha_3^4 + 1.2\alpha_3^2 - 0.18}{7.5 \exp(0.5\alpha_4)} \right] \quad (6.11a)$$

$$b_3 = - \frac{0.8\alpha_3^5 + \alpha_3^3 + 0.77\alpha_3}{(\alpha_4 - 1)^2 + 0.5} \quad (6.11b)$$

$$b_4 = - \varphi \left[ 0.04 - \frac{11.5\alpha_3^4 + 6.8\alpha_3^2 + 3.5}{(\alpha_4^2 + 0.4)^2 + 0.15} \right] \quad (6.11c)$$

$$\varphi = [1 - 0.06(3 - \alpha_4)]^{1/3} \quad (6.11d)$$

According to its authors,<sup>32</sup> a monotonic translation function is achieved from the model summarized in Equation 6.9 if the relation  $(1.35\alpha_3)^2 + 1.25 \leq \alpha_4$  is held.

Notwithstanding the relevance of the refined models described above, the statistical features displayed from loads of operating rotors on wind turbine structures are seldom described from these approaches. Howbeit, availing from the fact that wind load signals on wind turbines are often composed of large samples of data, a practical non-parametric transformation can be implemented to perform the transformation of a simulated Gaussian signal. Such a transformation is described in the following subsection.

## 6.2.2 Direct process translation

The applicability of the translation models described above is limited to certain intervals of values for the skewness ( $\alpha_3$ ) and kurtosis ( $\alpha_4$ ) of the non-Gaussian process. Although these models cover a wide range of cases of interest for structural engineering, the aerodynamic action on wind turbine structures often displays complicated features which are nontrivial in the evaluation of the structural response. A non-parametric approach is presented herein to outstrip these limitations.

For illustration purposes, consider a thrust force signal represented by the process  $Z(t)$  as displayed in Figure 6.2. The signal has been measured from an analysis performed in the aero-servo-elastic code FAST,<sup>33</sup> for the 5-MW reference turbine of the NREL,<sup>34</sup> which has also been described and analyzed in Chapter 3. The analysis considered that the turbine is operating within the normal specifications at a constant rotor speed with no variations of the blade pitch angle. Normal environmental conditions and operational wind speed levels were assumed. Further description of environmental and operational aspects assumed for the analysis of the turbine are irrelevant for the purposes of this example.

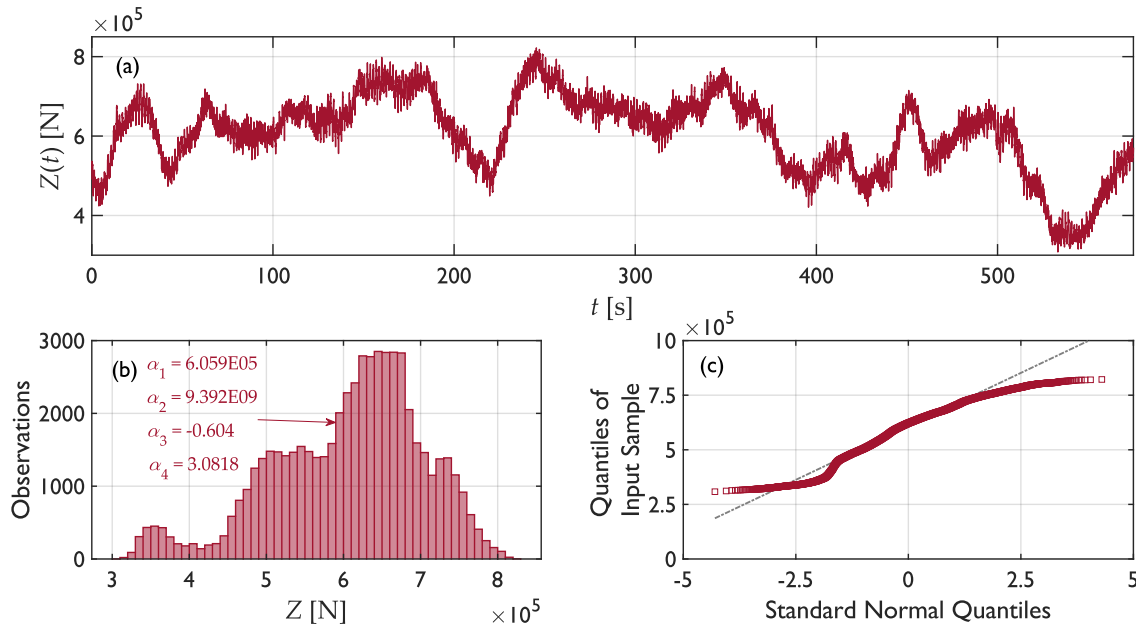


**Figure 6.2:** Non-Gaussian aerodynamic load signal: (a) Thrust force signal, (b) Amplitude histogram, (c) Q-Q plot of force amplitudes

From the quantile plot and the histogram displayed in Figure 6.2, it is evident that the amplitudes of forces deviate considerably from a Gaussian distribution. Moreover, it can be seen that the kurtosis of the force amplitudes is slightly superior to three. However, the condition  $\alpha_4 \geq 3 + (1.25\alpha_3)^2$  necessary for the application of the moment-based Hermite transformation is unsatisfied, whereas the condition  $(1.35\alpha_3)^2 + 1.25 \leq \alpha_4$  suggested for the model based on orthogonal polynomials is met. Notwithstanding this fact, a sort of multi-modality can be observed from the histogram of the force amplitudes. An accurate representation of such a feature in the PDF of the thrust force is unattainable by means of the transformations described above.

Due to the central limit theorem, a stochastic process simulated from the spectral representation method tends towards gaussianity as it is largely sampled.<sup>35</sup> In wind engineering applications it is common to simulate long wind speed signals. These are often simulated at a sampling frequency sufficiently high to cover a wide portion of the turbulence spectrum. Consequently, practical wind load signals often display large samples of data. This is the case of the signal displayed in Figure 6.2a, which was computed at a sampling frequency of 100 Hz. In this regard, it is a useful assumption premising that the empirical CDF computed from the non-Gaussian signal represents fairly the real distribution of the process  $Z(t)$ .

The simplified translation method presented in this subsection relies on the equivalence of cumulative distributions of the processes, such as the one expressed in Equation 6.1, but by means of their empirical CDFs. To elaborate on the matter, consider a Gaussian process  $X(t)$  of  $l$  elements simulated

from the spectral representation method.<sup>35</sup> The process  $X(t)$  displays the frequency content dictated by the PSDF of  $Z(t)$ , and has an empirical CDF expressed from:

$$\hat{F}_l(x) = \frac{1}{l+1} \sum_{k=1}^l \mathbf{1}_{X_k \leq x} \tag{6.12}$$

where  $\mathbf{1}_{(\cdot)}$  is the indicator function. The process  $X(t)$  is to be translated into the non-Gaussian process  $\tilde{Z}(t)$ .  $\tilde{Z}(t)$  must be described by the same probability distribution of  $Z(t)$ , which is formed by  $m$  elements. Therefore, the empirical CDF of  $Z(t)$  is defined as  $\hat{F}_m(z)$ . Thus, by means of interpolation of values, such as the one summarized in Figure 6.3, the translation of  $X(t)$  into  $\tilde{Z}(t)$  is performed. Note that this non-parametric transformation is based on the premise that all the involved processes are composed of samples sufficiently large to assume that their empirical CDFs approximate fairly their real cumulative distributions. Furthermore, if  $l > m$ , the values at the upper and lower tails of the distribution of  $\tilde{Z}$  must be computed from an interpolation with 0 or 1, and their corresponding nearest value from  $\hat{F}_m(z)$ .

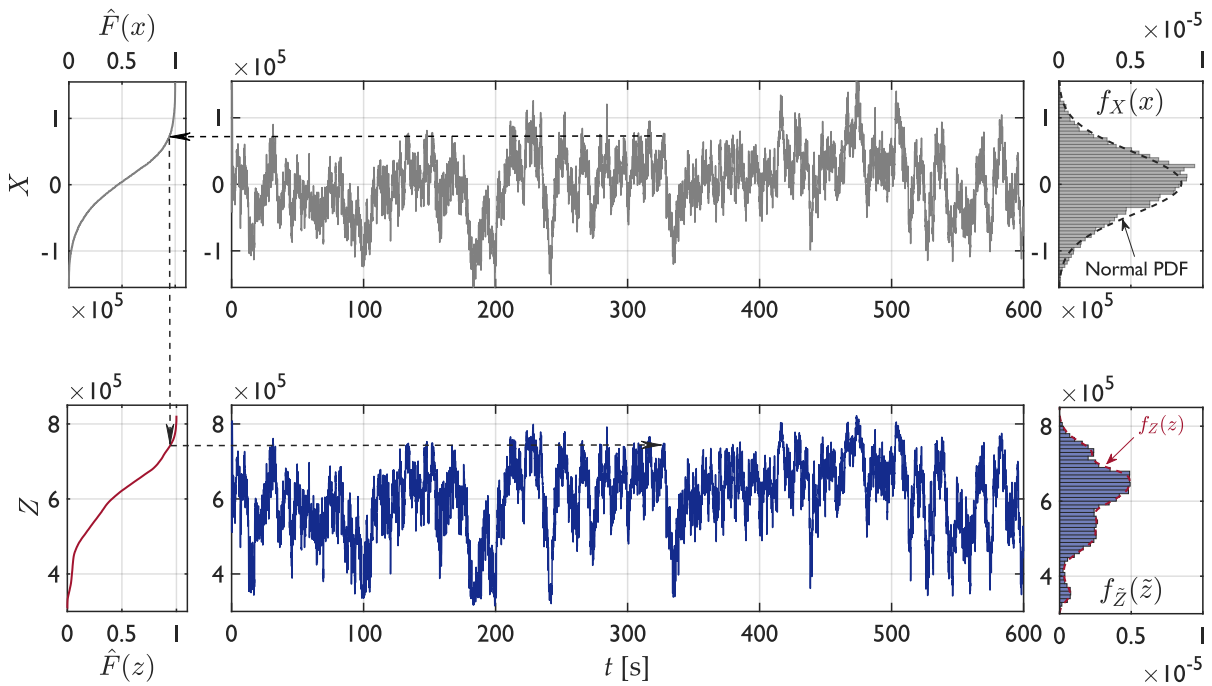


Figure 6.3: Direct translation of a stochastic process

The transformations that have been summarized herein can describe an ample variety of stochastic processes common in structural and wind engineering. A relevant premise for their application is that such transformations are valid for wide-banded processes, like wind action on structures, as it has been oftentimes presented in the literature. Moreover, any correlation among different signals has been disregarded hitherto for their translation. This is an availability of the simplified methodology described in this chapter, attainable inasmuch as the resultant aerodynamic loads on the wind turbine rotor display null values of association among different components. This permits a reduction of the DOFs necessary for a simplified structural model, as described in the following section.

### 6.3 Simplified wind turbine support-structure model

The abatement of long computing time for reliability analyses can be achieved by means of the reduction in the number of response signals needed for the representation of the structural behavior of the wind turbine support structure. A simplification of the structural model is pertinent for this purpose. Such a simplification can be implemented under the premise that the structural response of the support structure of the wind turbine is adequately described from the first bending mode of the tower. This section elaborates on this subject, it also provides details on the assumptions adopted for the performance of structural analyses.

#### 6.3.1 Four-DOF model

In previous chapters, the structural behavior of land-based wind turbine support structures was discussed. This was done either for the evaluation of the aeroelastic response under cyclone-induced loads or for the implementation of supplementary damping devices on the structure. Regardless of the objectives of the dynamic evaluation, the structural response of the support structures was observed to be dominated by the first bending mode of the tower. This permits several simplifications in its modeling. To expand on this simplification, consider the coordinate system with its origin at the nacelle of the wind turbine, as schematized in Figure 6.4. Please distinguish the coordinate axes indicated in the figure from the values of random variables employed to discuss the translation process theory in the previous section. The degrees of freedom that describe the response of the rotor-nacelle assembly are also illustrated in Figure 6.4.

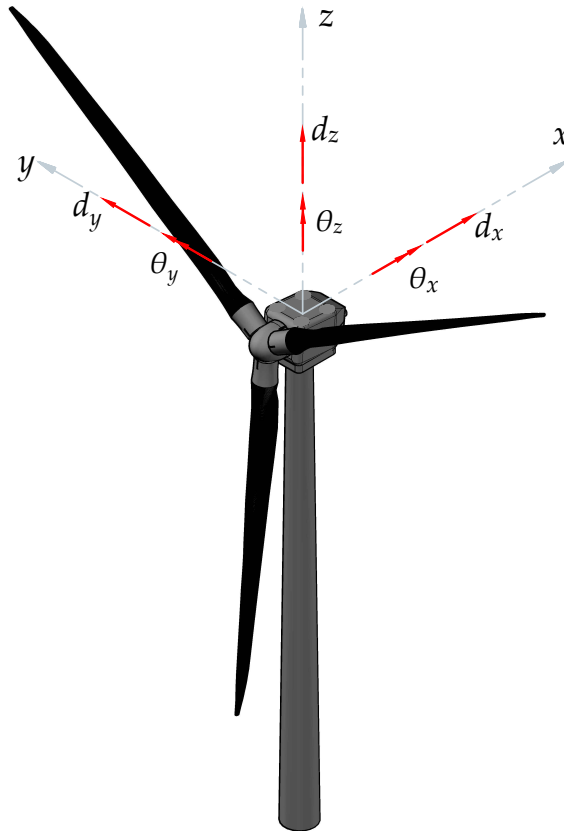


Figure 6.4: Degrees of freedom for the representation of a HAWT support structure

The dominance of the first bending mode of the turbine tower permits premising that the support structure can be modeled as a cantilevered beam. Whereas this cantilevered beam is assumed as massless, the rotor-nacelle assembly is treated as a lumped mass at the end of the tower. The lumped mass is represented by  $m_{\text{eq}}$  and is determined from  $m_{\text{eq}} = m_{\text{blades}} + m_{\text{hub}} + m_{\text{nacelle}} + (33/140)m_{\text{tower}}$ . These elements represent, in respective order, the masses of the blades, the hub, the nacelle, and a fraction of the mass of the tower. This last term assumes that the tower is represented by an element of constant cross-section and height  $H$ .<sup>36</sup>

Dynamic similitude can be maintained between the simplified (or equivalent) system and the turbine structure. For this purpose, the second area moments of the equivalent cross-section of the cantilevered element have to be defined from the natural frequencies of the real structure. This definition implies the following relation:

$$I_x = \frac{m_{\text{eq}}\omega_x^2 H^3}{3E} \quad (6.13a)$$

$$I_y = \frac{m_{\text{eq}}\omega_y^2 H^3}{3E} \quad (6.13b)$$

where  $\omega_j$  is the angular frequency of the first bending mode of the tower in the  $j$ -direction ( $j = x, y$ ), and  $E$  is the elastic modulus of the tower structure. Furthermore, disregarding the degrees of freedom (and consequently the vibration frequencies) associated with the  $z$ -direction, the stiffness matrix of the equivalent system can be expressed as:

$$\mathbf{K}_s = \frac{2E}{H^3} \begin{bmatrix} 6I_x & 0 & 0 & -3HI_x \\ 0 & 6I_y & 3HI_y & 0 \\ 0 & 3HI_y & 2H^2I_y & 0 \\ -3HI_x & 0 & 0 & 2H^2I_x \end{bmatrix} \quad (6.14)$$

Under the assumptions commented above, the equation of motion considering aerodynamic damping effects can be expressed as:

$$\mathbf{M}_s \ddot{\mathbf{d}}(t) + [\mathbf{C}_s + \mathbf{C}_a] \dot{\mathbf{d}}(t) + \mathbf{K}_s \mathbf{d}(t) = \mathbf{f}_a(t) \quad (6.15)$$

In Equation 6.15 the vector of structural responses is defined as  $\mathbf{d} = \{d_x, d_y, \theta_x, \theta_y\}^T$ , and the dots denote differentiation with respect to time.  $\mathbf{M}_s$  and  $\mathbf{C}_s$  represent the mass and damping matrices of the equivalent structure, whereas  $\mathbf{C}_a$  represents the aerodynamic damping matrix. The vector  $\mathbf{f}_a$  summarizes the aerodynamic loads due to the operation of the turbine on the equivalent system. These forces result from the integration of the aerodynamic loads on the operating rotor.

From Equation 6.14 note that the pairs of degrees of freedom  $d_x$  and  $\theta_y$ , and  $d_y$  and  $\theta_x$ , are coupled. These structural responses can be obtained from the solution of Equation 6.15. Notwithstanding that these DOFs represent the structural response measured at the nacelle, they can be assumed as equivalent to the response at the topmost height of the tower without relevant loss of accuracy.

### Stress histories

In most cases, when the structural response of the wind turbine support structure is of interest, measurements at the greatest height of the tower are sufficient. Regarding the structural response at intermediate coordinates between the base of the tower and its topmost extreme, it can be estimated from the responses at the higher location. This can be done by means of a shape function  $\psi_t(z)$ . Comparing with this, the structural response in the  $j$ -direction can be estimated as  $d_j(z, t) = \psi_t(z)d_j(t)$ , where  $d_j$  is the structural displacement at the end of the tower, as included in the vector  $\mathbf{d}$ .

In this regard, if the support structure is assumed to behave as a cantilevered Euler-Bernoulli beam, the bending moment in the  $j$ -direction at a particular height of the tower can be roughly approximated from the expression  $M_j(z, t) = EI(z)\partial^2 d(z, t)/\partial z^2 = EI(z)d_j(t)d^2\psi_t(z)/dz^2$ . In this case,  $I(z)$  represents the *real* second area moment of the cross-section of the tower at a determinate height and must be distinguished from the *equivalent* second area moments defined in Equation 6.13. This distinction owes to the fact that the moments of inertia presented in Equation 6.13 assume a constant cross-section of the tower. Thus, if the components of bending moment at a determinate height are known, under the premise of a linear stress distribution across the tower section the stress history is defined from:

$$\zeta(z, t) = \frac{[D_c(z) - t_c(z)] \sqrt{M_x^2(z, t) + M_y^2(z, t)}}{2I(z)} \quad (6.16)$$

where  $\zeta(z, t)$  represents the stress amplitude, and  $D_c(z)$  and  $t_c(z)$  are the tower outer diameter and thickness, respectively — assuming that the support structure is built as a hollow circular section.

#### Damping estimation

In Equation 6.15, the added mass and fluid rigidity that intervene in the fluid-structure interaction have been disregarded. Therefore, the aeroelastic effects on the equivalent structural system are reduced to the influence of the aerodynamic damping matrix. Insofar as wind turbine support structures are flexible mechanical systems of low structural damping, the amplitudes of structural responses are majorly influenced by this quantity. As has been commented in the introduction of this chapter, aerodynamic damping evaluation on operating wind turbines is a subject neither trivial nor facile. An elaborate identification of the aerodynamic damping falls out of the scope of the present study. However, a common procedure for the damping estimation is briefly summarized next.

The half-power-points method is a commonly employed procedure for the estimation of damping on mechanical systems.<sup>11,12,36</sup> Under this approach, the damping matrix can be defined from the assumption of a single load and a single response signal. That is, the force and response histories are necessary for the estimation of damping in each DOF, disregarding any coupling between them. The half-power-points method consists of the estimation of the damping ratio from the following expression:

$$\tilde{\zeta}_j = \frac{\omega_j^{(2)} - \omega_j^{(1)}}{2\omega_j} \quad (6.17)$$

Equation 6.17 defines the damping ratio  $\tilde{\zeta}_j$  from the angular frequency of the  $j$ -th mode of the structure. In the equation,  $\omega_j^{(k)}$  ( $k = 1, 2$ ) are defined as the half-power points. That is, the frequencies near the  $j$ -th mode peak in the frequency-response function (FRF) at which the following equality is met<sup>36</sup>:

$$\left| H(i\omega_j^{(1)}) \right| = \left| H(i\omega_j^{(2)}) \right| = \frac{1}{\sqrt{2}} |H(i\omega_j)| \quad (6.18)$$

where  $|H(i\omega)|$  is the modulus of the FRF that relates the PSDFs of force  $S_{\bar{f}}(\omega)$  and response  $S_q(\omega)$  as  $S_q(\omega) = |H(i\omega)|^2 S_{\bar{f}}(\omega)$ , and  $i$  is the imaginary unit.

In the previous lines, the PSDFs of forces and responses can either be estimated from their respective histories in physical coordinates or can also be computed in modal coordinates. The latter case implies that the vectors of forces and displacements in modal coordinates are determined, respectively, from:



$$\bar{\mathbf{f}}(t) = \boldsymbol{\phi}_j^T \mathbf{f}_a(t) \quad (6.19)$$

$$\mathbf{q}(t) = \boldsymbol{\phi}_j^T \mathbf{d}(t) \quad (6.20)$$

where  $\boldsymbol{\phi}_j$  represents the modal shape vector describing the  $j$ -th modal form. From these elements, the modal matrix  $\boldsymbol{\Phi}$  is defined. According to these definitions, by letting the damping matrix in modal coordinates be expressed as  $\bar{\mathbf{C}} = \boldsymbol{\Phi}^T \mathbf{C} \boldsymbol{\Phi}$ , and the modal mass matrix as  $\bar{\mathbf{M}} = \boldsymbol{\Phi}^T \mathbf{M} \boldsymbol{\Phi}$ , the damping contribution in physical coordinates can be expressed from<sup>37</sup>:

$$\mathbf{C} = \left( \mathbf{M} \boldsymbol{\Phi} \bar{\mathbf{M}}^{-1} \right) \bar{\mathbf{C}} \left( \bar{\mathbf{M}}^{-1} \boldsymbol{\Phi}^T \mathbf{M} \right) \quad (6.21)$$

Note that, if the force and response signals used to evaluate  $S_q(\omega)$  and  $S_{\bar{f}}(\omega)$  are measured from a numerical or physical model accounting for aeroelastic interaction between the flow and the structure, the elements composing  $\bar{\mathbf{C}}$  (which result from the evaluation of Equation 6.17) will account for the contribution of  $\mathbf{C}_a$  and  $\mathbf{C}_s$ . However, insofar as Equation 6.21 is governed by the modal matrix, the coupled elements resulting from such an evaluation will be the same as in Equation 6.14. Further studies on the description of aerodynamic damping and the coupling it induces on different DOFs demand a more elaborate evaluation. Nevertheless, the simplicity of the approach described herein is availed for the sake of demonstration.

## 6.4 Simplified method for simulation of stress signals

Reliable structural design is governed by the maximum expected values of loads on an element. In the case of fatigue damage, the maximum value might display no association with the occurrence of extreme values of load amplitude. Rather, the load range and the number of load cycles determine the fatigue damage on a structural element. Fatigue damage implies material deterioration which can affect significantly the lifetime of a mechanical system or structural component. For this reason, it is important to account for this effect in their design. This section describes an algorithm to simulate *equivalent* stochastic processes. These are called ‘equivalent’ insofar as they can produce similar values of fatigue damage to those from an original process computed from an elaborate numerical model of a wind turbine in operation.

The random nature of wind turbulence makes wind turbine fatigue a rather complicated phenomenon, as it is often the case of load conditions governed by random loading. Conventional criteria in wind turbine standards, such as the IEC 61400-1,<sup>25</sup> permit the evaluation of fatigue damage from synthetically-generated turbulent wind simulations. Common assumptions for these simulations are the stationariness of the wind speed in 10-min time lapses, the neutral stratification of the atmospheric boundary layer, and the logarithmic- or power-law wind profile. Notwithstanding these assumptions, further complications can unfold on the problem, as atmospheric turbulence is affected by the operation of wind turbines within a wind power plant.<sup>6</sup> These conditions can also be studied by means of the simplified approach discussed herein. However, inasmuch as the illustration of the method is the main objective of this chapter, only conventional cases are covered.

It is oft-suggested by common wind turbine standards to perform the evaluation of fatigue damage from the rule of Miner.<sup>25</sup> This criterion assumes that the damage on the material of a structural element due to fatigue accumulates linearly and independently in each load cycle during a load history. This can be represented by means of the equation:

$$D = \sum_k \frac{1}{N(\Delta\zeta_k)} \quad (6.22)$$

In Equation 6.22,  $N$  is the number of cycles needed for the structural element to fail at a stress range  $\Delta\zeta$  occurring at the  $k$ -th time step of the load history. The value of  $N$  is commonly defined from laboratory tests, where an element from the specified material is subject to repeated harmonic load cycles of constant amplitude. The number of cycles to failure is determined, and the test is repeated at a different load amplitude on another specimen of identical characteristics. This way a curve describing the fatigue behavior of the material is built, known as the S-N curve. The S-N curve of a material is commonly expressed from the stress ranges as  $N = K_r \Delta\zeta^{-m}$ , where both  $K_r$  and  $m$  are material constants.

According to the assumptions commented previously, the stress ranges and the number of load cycles during a load history are the main characteristics that govern fatigue damage. In stationary processes, these two characteristics can be related to the PSDF of the process itself. This owes to the fact that the spectral moments define the rate of crossings of the process as well as its amplitudes, and consequently, the number of load cycles in a time-lapse.<sup>38</sup> In this regard, the stress range at the  $k$ -th time step of a digitally-sampled stress signal can be expressed as  $\Delta\zeta(t_k) = |\zeta(t_k) - \zeta(t_{k-1})|$ . A signal sampled at a constant time step  $\Delta t$  will thus be composed of stress ranges that can be expressed as:

$$\Delta\zeta(t_k) = |\dot{\zeta}(t_k)| \Delta t \quad (6.23)$$

where  $\dot{\zeta}(t)$  is defined as  $d\zeta/dt$ . Thus, a load signal able to represent the fatigue damage of an original load history can be obtained by the simulation of the stochastic process  $\Delta\zeta(t)$ . Therefore, information on  $\Delta\zeta(t)$  is required. In that regard, the PSDF of the process  $\dot{\zeta}(t)$  can be estimated from the PSDF of  $\zeta(t)$  form:

$$S_{\dot{\zeta}}(n) = (2\pi n)^2 S_{\zeta}(n) \quad (6.24)$$

In Equation 6.24,  $n$  represents the temporal frequency. Moreover, the spectral density of stress amplitudes  $S_{\zeta}(n)$  can be estimated from the Fourier transform of the autocorrelation function of a stress signal computed from Equation 6.16. Thus, the steps for the simulation of stationary equivalent stress signals can be summarized as:

- (i) Perform a time-history analysis of a wind turbine operating under specific conditions.
- (ii) Compute the stress history  $\zeta(t)$  and its derivative  $\dot{\zeta}(t)$ , by means of Equation 6.16.
- (iii) Estimate  $S_{\dot{\zeta}}(n)$ , either directly or by evaluation of Equation 6.24.
- (iv) Perform the simulation of a number of zero-mean processes  $\dot{X}(t)$  from  $S_{\dot{\zeta}}(n)$ , in order for these to have adequate frequency content (Please distinguish in this context between the stochastic processes  $X(t)$  and the spatial coordinate  $x$ ).
- (v) Correct the amplitude distributions of the simulated processes  $\dot{X}(t)$ , in case the amplitude distribution of  $\dot{\zeta}(t)$  evinces non-Gaussian characteristics. This correction can be performed by any of the methods described in Section 6.2. (Let  $\dot{Z}(t)$  be the corrected signal homologous to  $\dot{X}(t)$ ).
- (vi) Perform numerical integration on each of the processes  $\dot{X}(t)$  (or  $\dot{Z}(t)$ , in case the amplitude distribution of these has been corrected).
- (vii) Correct any difference in the mean component of  $X(t)$  — or  $Z(t)$  — with respect to the mean of the original signal  $\zeta(t)$ .
- (viii) Count the cycles of the resulting simulated signals to evaluate fatigue damage.

The steps summarized above have been phrased for the simulation of stress signals for fatigue analyses. However, a similar procedure can be applied for the simulation of diverse phenomena based on the load or response amplitudes. For example, an analogous procedure can be adopted to directly simulate signals of bending moment at the base of the tower, or any other height. If this is done for the evaluation of response maxima, the range similarity between the resultant signals and the original can be disregarded (that is, the simulated process must be concordant in amplitude, rather than its derivatives). Furthermore, noting that the described methodology relies fundamentally on spectral and probabilistic characteristics of an ‘original’ process, its implementation can be easily extrapolated to diverse problems in engineering related to random vibrations. Notwithstanding these comments, the required information is more easily attained either from the numerical evaluation of an elaborate structural model or from experimental data. The following section is centered on the evaluation of the effectiveness and precision of the methodologies and criteria described above. Such an evaluation is performed from numerical analyses of an operating wind turbine.

## 6.5 Numerical example

A numerical example is carried out to illustrate the application of the criteria described previously in this chapter. The analyses are performed on the onshore 5-MW reference wind turbine of the NREL,<sup>34</sup> the overall dimensions of which have already been described in Chapter 3. The turbine selected for this case study is assumed to be operating at its rated rotor speed. Furthermore, the pitch angle of its blades is assumed to remain constant during the analyses, and no yaw variation is assumed in the wind flow or the rotor orientation. Although these premises represent a rather idealized scenario, they serve the purpose of identification of shortcomings and gaps of the method proposed herein. This is of high importance for the adequate application of the methodology to related problems. Furthermore, in order to avoid redundancy and saturation of data, only nine environmental cases are assumed for the analyses. These cases correspond to mean wind speed values measured at hub height ( $\bar{U}_{\text{hub}}$ ) of 10, 15, and 20 m/s; and three levels of turbulence intensity ( $I_u$ ), which are: 5, 10, and 20%. The Kaimal turbulence spectra and a power-law exponent as suggested in the IEC 61400-1<sup>25</sup> for normal operation conditions were assumed in all the analyses.

### 6.5.1 Description of the turbine

As has been briefly described in Chapter 3, the 5-MW reference wind turbine of the NREL<sup>34</sup> is a model widely employed for wind energy research. The characteristics of this turbine needed for the application of the simplifications discussed herein are displayed in Table 6.1.

**Table 6.1:** Parameters of the 5MW reference wind turbine<sup>34</sup> for the simplified analyses

Parameter	Value	Units
$m_{\text{blades}}$	53,220.0	kg
$m_{\text{hub}}$	56,780.0	kg
$m_{\text{nacelle}}$	240,000.0	kg
$m_{\text{tower}}$	347,460.0	kg
$m_{\text{eq}}$	431.9	Mg
$H$	90.0	m
$\omega_x$	2.036	rad/s
$\omega_y$	1.960	rad/s
$I_x$	2.071	m <sup>4</sup>
$I_y$	1.921	m <sup>4</sup>
$D_c(z = 0)$	6.0	m
$t_c(z = 0)^a$	2.7	mm

<sup>a</sup> In the original reference,<sup>34</sup> this quantity is explicit as 2.7 mm in the description of the structure. However, in the same reference, it is mentioned that the tower-wall thickness was increased to comply with the structural characteristics of a turbine from another reference.<sup>39</sup> In the present example, the values displayed in this table are held for all the computations.

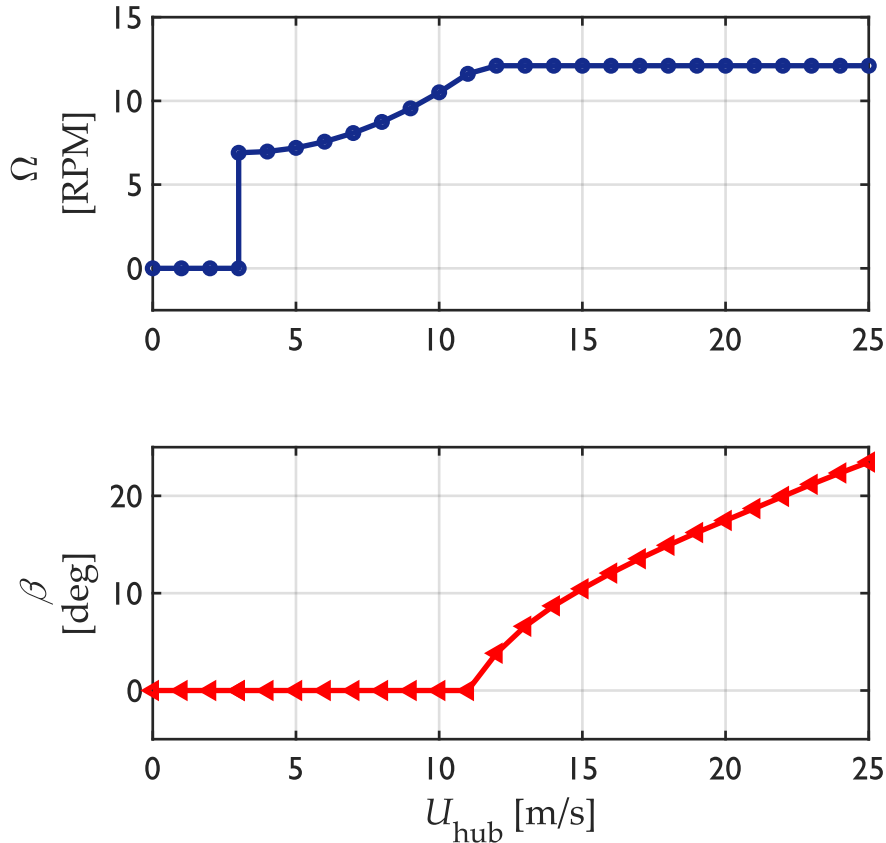


Figure 6.5: Rotor speed and pitch angle criteria of the 5MW reference wind turbine<sup>34</sup>

As summarized in Chapter 2, the rotor speed and the orientation of the blades are of major importance in the determination of the thrust coefficient on the rotor. That is, the forces on the structure are governed by these quantities, which depend on the operation of the turbine. Figure 6.5 summarizes the criteria defined for the operation of the turbine regarding the pitch angle ( $\beta$ ) and the rotor speed ( $\Omega$ ). Notwithstanding Figure 6.5, the rotor speed was assumed to be a constant value of 12.1 RPM in all the analyses. Note that, inasmuch as the determined values of  $\Omega$  for wind speeds of 15 and 20 m/s are indeed defined as 12.1 RPM in Figure 6.5, only its value for a wind speed of 10 m/s differs from what has been defined for the reference wind turbine. This was done for the sake of reducing the number of variables that intervene in the analyses. Trivial differences between this assumption and the real operation criterion are expected, insofar as the rotational speed at 10 m/s is slightly inferior to 12.1 RPM. Moreover, whereas the rotor speed was assumed constant for all the analyzed cases, the pitch angle of the blades  $\beta$  was taken as displayed in Figure 6.5. That is,  $\beta$  was set as 0, 10.45, and 17.47° for respective values of  $\bar{U}_{\text{hub}}$  equal to 10, 15, and 20 m/s.

### 6.5.2 Equivalent structural model

According to the premises commented in Subsection 6.3.1, aerodynamic load histories are necessary to perform the simplified analyses. The resultant load histories at the rotor in the  $x$ - and  $y$ -directions, as well as the resultant moments around the same directions, are the loads needed for the evaluation of the simplified 4-DOF model. A sample of these loads for each analyzed environmental condition was obtained from time-history analyses performed in the code FAST.<sup>33</sup> The operation conditions defined for these analyses have been stated in the previous subsection.

### Number of analyses

For the purposes commented above, the number of histories composing the samples must be defined. The definition of how ample must be the sample ensures an adequate representation of the processes without excessive computational expense. For this purpose, the standard errors from the mean values of the histories were explored. Figure 6.6 displays the standard error for mean thrust force ( $T$ ) and mean tower displacement in the  $x$ -direction ( $d_x$ ) for two of the cases covered. It can be inferred from the tendencies displayed in this figure that the standard error begins to ‘stabilize’ at 15 analyses.

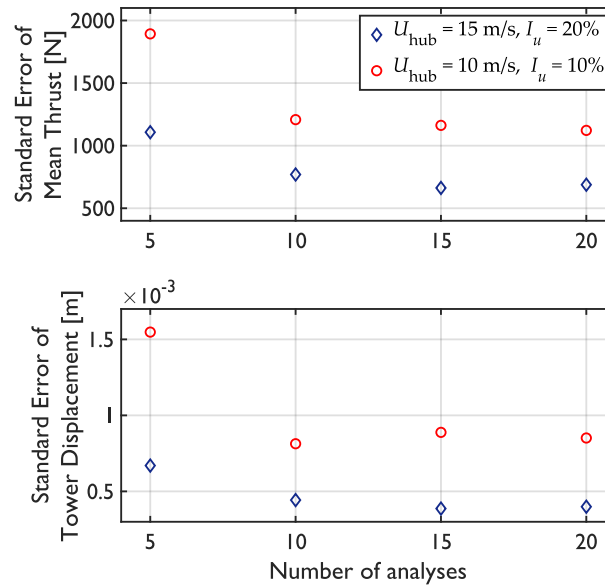


**Figure 6.6:** Standard errors measured for mean thrust force and mean tower displacement for  $\bar{U}_{\text{hub}}$  of 10 and 15 m/s, and  $I_u$  of 10 and 20%

Samples of 15 analyses per combination were used to carry out the stochastic simulation of force signals to analyze the equivalent structural model — hereafter referred to as ‘seed samples’. Five ‘replicas’ were performed from each of the elements of these samples, leading to a total of 75 equivalent load histories per combination. A sample of 20 additional analyses per combination was used for comparison purposes. The statistical characteristics of the force signals measured from this group — herein referred to as the ‘control sample’ — were explored. Figure 6.7 displays box plots of the skewness and kurtosis of the loads in two of the degrees of freedom evaluated for the control sample. These forces correspond to the displacement DOFs in the  $x$ - and  $y$ -directions, respectively. Further description of the forces in the rest of the DOFs was omitted for the sake of brevity.

Before any further description of the numerical study, some comments on the load statistics are pertinent. From Figure 6.7 it can be seen that the statistical moments of the load histories deviate from Gaussian characteristics to some degree. In the case of the thrust force  $T$ , no tendency is evident for the distribution of the skewness or kurtosis as either turbulence intensity or wind speed vary. Notwithstanding the ostensive dispersion of skewness of the thrust force around zero, it can be seen in Figure 6.7(a) that the greater part of the data is located on positive values. Whereas in the case of the fourth moment of  $T$ , the greater part of the kurtosis displays values lower than three, as in Figure 6.7(c). That is, the thrust force on the rotor is a rather *hardening* process. Regarding the statistical moments of the forces in-plane to the rotor, denoted as  $S$ , the skewness values from the data are also dispersed around zero. This can be appreciated in Figure 6.7(b). However, a tendency towards skewness diminishment can be appreciated in  $\alpha_3$  as wind speed increases. Moreover, it is evident from Figure 6.7(d) that the greater part of the data of  $S$  evinces a rather *hardening* behavior (i.e., with

kurtosis less than three). Notwithstanding, it is also evident that the process tends to *soften* as wind speed increases.

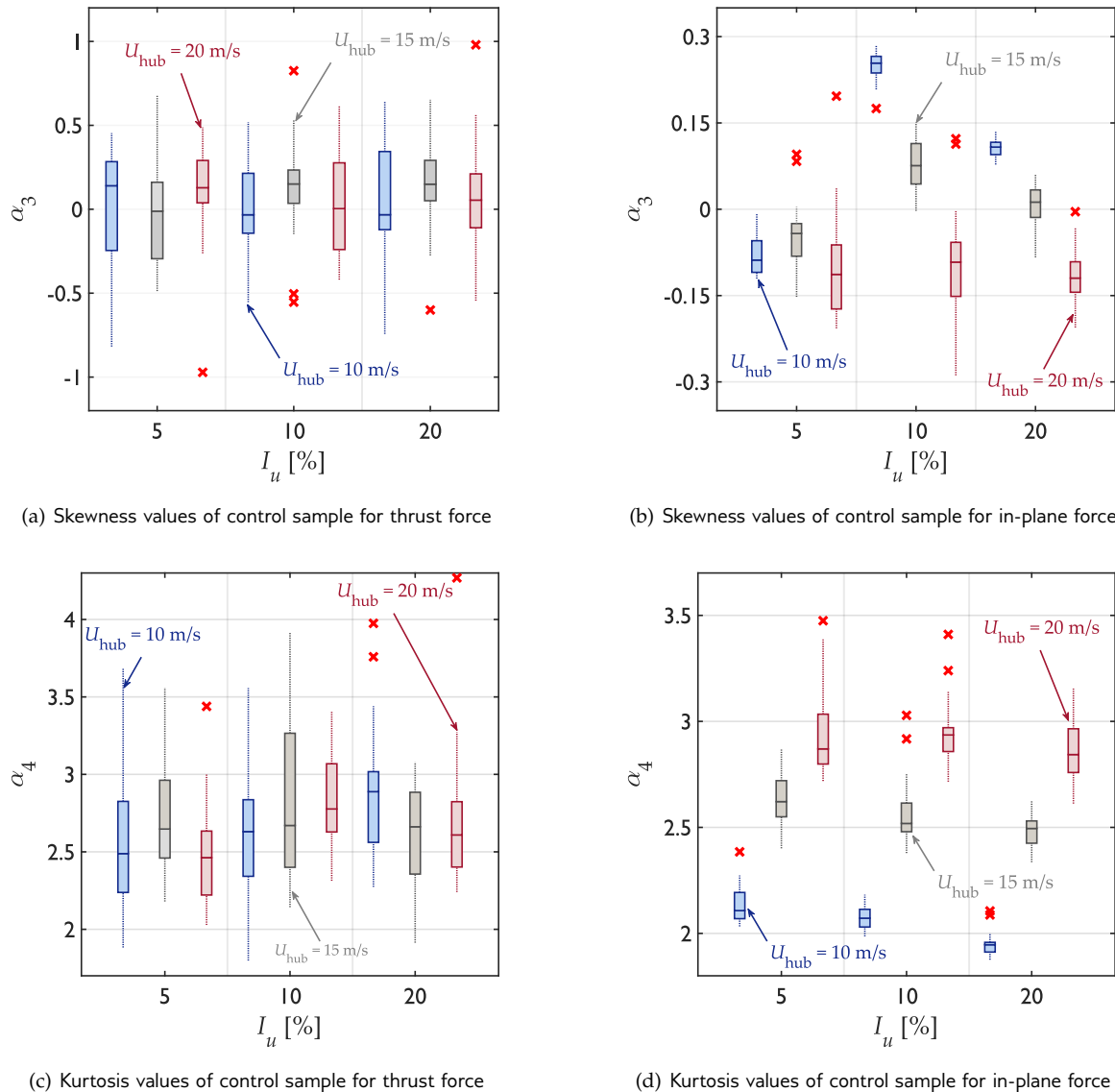


**Figure 6.7:** Statistical moments of aerodynamic forces on the operating rotor

### Simulation of force signals

As commented previously, the 4 DOF model proposed in Subsection 6.3.1 relies on the aerodynamic forces on the rotor in each degree of freedom representing the tower deflection. Stochastic simulation of forces on these DOFs was performed accounting for the characteristics displayed by the results from the full structural model. For this purpose, a foregoing exploration of the resulting forces from the seed samples was performed. From this exercise, it was observed that some of the load signals displayed considerable values of correlation (either positive or negative), whereas others displayed negligible correlation. Furthermore, the normalized spectral densities of the load signals that displayed correlation exhibited nearly identical ordinates. These facts were availed for the reduction of simulated signals for the simplified analyses. That is, for the simulation of equivalent processes, a

simplification can be assumed where only two uncorrelated signals are needed to perform the Gaussian simulation. The subsequent non-Gaussian translation is performed on these signals accounting for the respective amplitude distribution of their corresponding DOF. This simplification neglects non-unit values of correlation between some of the load histories in different degrees of freedom. Notwithstanding, the governing forces on the support structure are fairly represented from this assumption.

Figure 6.8 displays the values of correlation measured from the seed samples for the different loads. Some of the normalized PSDFs of the correlated loads are also displayed in their respective graphics. These similitudes in the spectral ordinates held for all the analyzed cases, a fact that aided in the simplification mentioned in the previous paragraph.

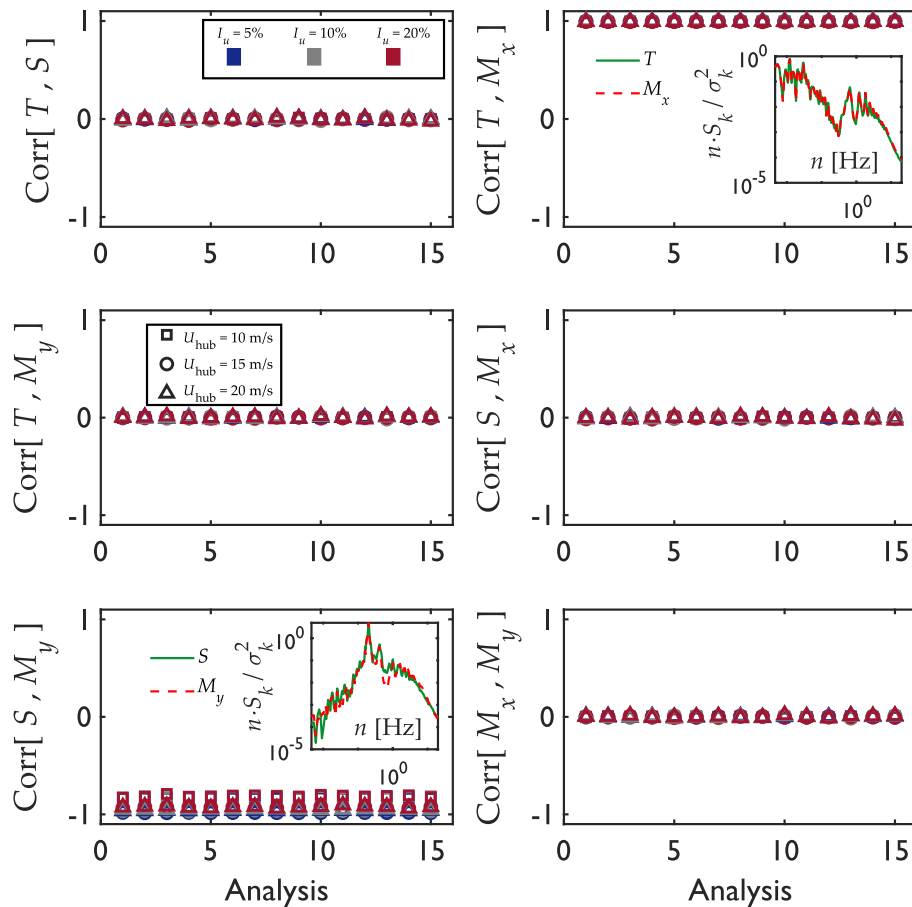
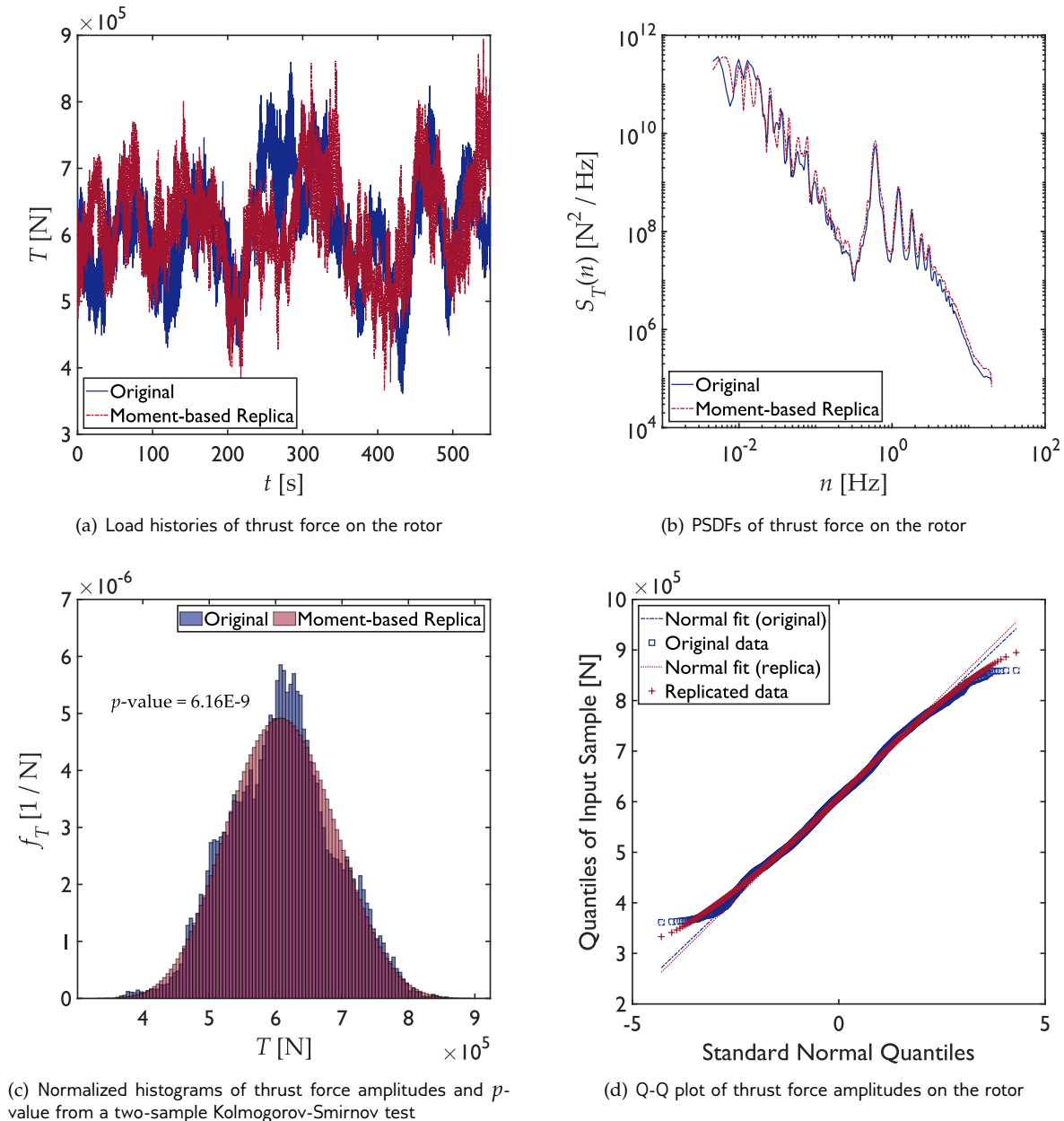


Figure 6.8: Measured correlation between the load histories in different DOFs for the seed sample

Let the scheme for the performance of the equivalent analyses be reiterated. The force signals to be applied to the 4-DOF model are simulated from the spectra estimated from the full-model (original) analyses in the seed sample. Subsequently, these simulated signals are translated into non-Gaussian processes, accounting for the amplitude distribution of the original load histories. In this regard, and as commented previously in this chapter, due to the elaborate decomposition of loads on the operating turbine some load histories displayed intricate characteristics. These characteristics are sometimes difficult to attain from the moment-based translation methods described above. To expand on such cases, two examples are displayed for the resulting aerodynamic forces in the  $x$ - and  $y$ -directions, i.e.,  $T(t)$  and  $S(t)$ , respectively.

Figure 6.9 displays some characteristics of an original load signal and its respective moment-based replica, which correspond to the thrust force  $T$ , whereas Figure 6.10 does it for the in-plane load  $S$ . Note that the length of the displayed time histories is 550 s. Recalling what has been stated previously in this chapter, conventional analyses assume 10-min length signals. That is, 50 s were trimmed out from the force signals displayed in Figures 6.9 and 6.10. This was done in order to avoid the inclusion of any numerical inaccuracies from the start of the aeroelastic analyses performed in FAST.

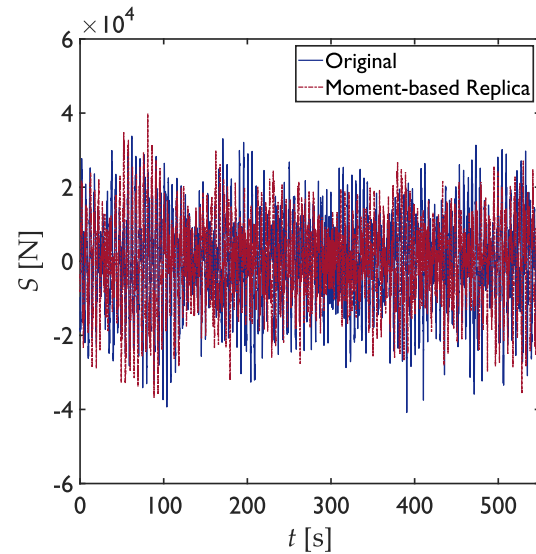


**Figure 6.9:** Moment-based simulated rotor thrust forces for application on the simplified model

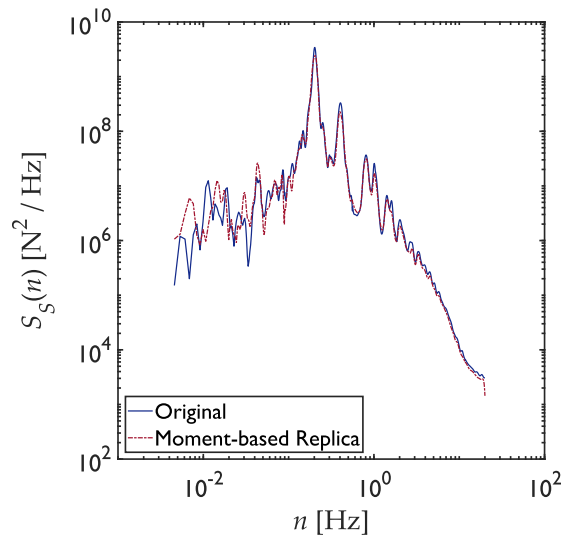
From Figures 6.9 and 6.10, note that the simulated forces exhibit significant resemblances to their respective originals. The PSDs of the thrust and in-plane forces are displayed, respectively, in Fig-



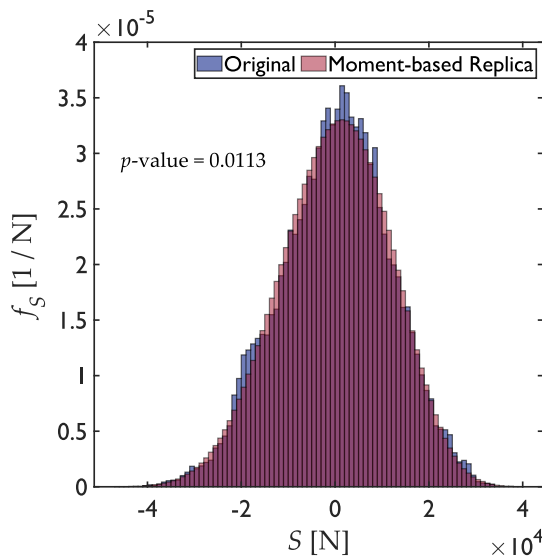
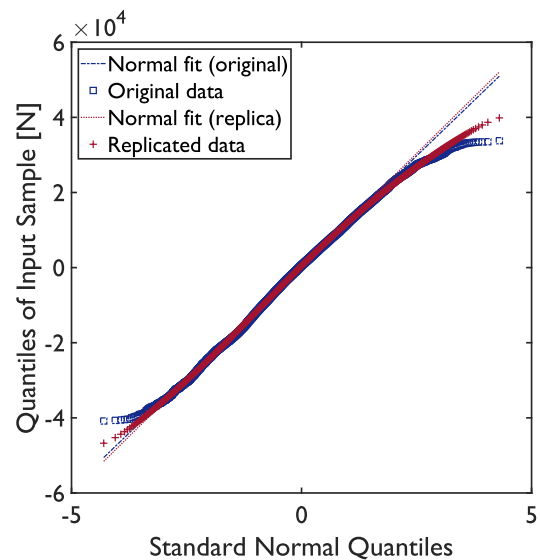
ures 6.9(b) and 6.10(b). In these figures, the spectral amplitudes from the replicas appear fairly comparable to their originals. Moreover, the quantile-quantile plots from the signals are also resemblant, as presented in Figures 6.9(d) and 6.10(d). Nevertheless, the  $p$ -values from a two-sample Kolmogorov-Smirnov test performed between the respective pairs of thrust forces are rather low. This implies that the hypothesis implying that each pair of samples come from the same distribution would be rejected at conventional significance levels. These values are displayed in Figures 6.9(c) and 6.10(c) for the thrust and in-plane forces, respectively.



(a) Load histories of in-plane force on the rotor



(b) PSDFs of in-plane force on the rotor

(c) Normalized histograms of in-plane force amplitudes and  $p$ -value from a two-sample Kolmogorov-Smirnov test

(d) Q-Q plot of in-plane force amplitudes on the rotor

**Figure 6.10:** Moment-based simulated rotor in-plane forces for application on the simplified model

As commented in Subsection 6.2.2, a non-parametric transformation can also be performed on the load signals. Again, for the sake of illustration, analogous information to the one displayed in Figures

6.9 and 6.10 is presented in Figures 6.11 and 6.12. However, the latter figures display information that has been replicated by applying the non-parametric approach described earlier. Further comments on the statistics achieved from this transformation to the simulated loads are presented next.

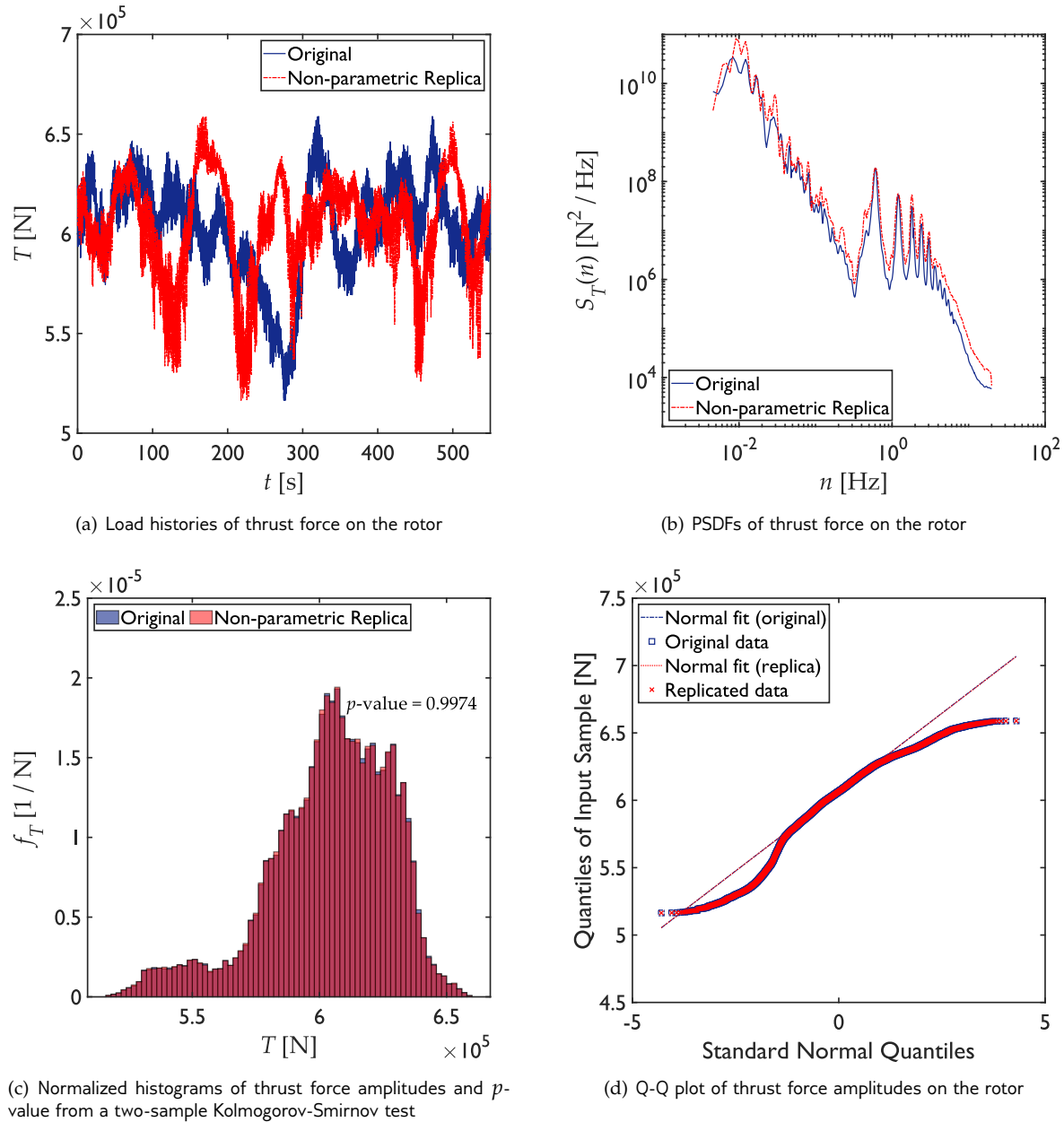


**Figure 6.11:** Non-parametrically transformed simulated rotor thrust forces for application on the simplified model

Analogously to the characteristics displayed by the moment-based transformations, the simulated signals transformed by the non-parametric scheme also exhibit significant similitude to their respective originals. However, as illustrated in Figure 6.11(b), the spectral amplitudes of non-parametrically-transformed thrust force are slightly overestimated at high frequencies, when compared to the moment-based transformed cases (c.f. Figure 6.9(b)). Notwithstanding, this is unanalogous to the in-plane

force spectra displayed in Figure 6.12(b), where a fair similitude in spectral amplitudes is observed between the original signal and its replica.

Moreover, in the histograms of amplitudes achieved from the replicas (Figures 6.11(c) and 6.12(c)), as well as in the quantile-quantile plots from them (Figures 6.11(d) and 6.12(d)), a nearly-identical representation of the original processes can be appreciated. This owes to the fact that the non-parametric transformation relies on the empirical CDF of the original process for the translation function. Therefore, a near-one  $p$ -value from a two-sample Kolmogorov-Smirnov test is obtained when this criterion for transformation is applied (see Figures 6.11(c) and 6.12(c)).

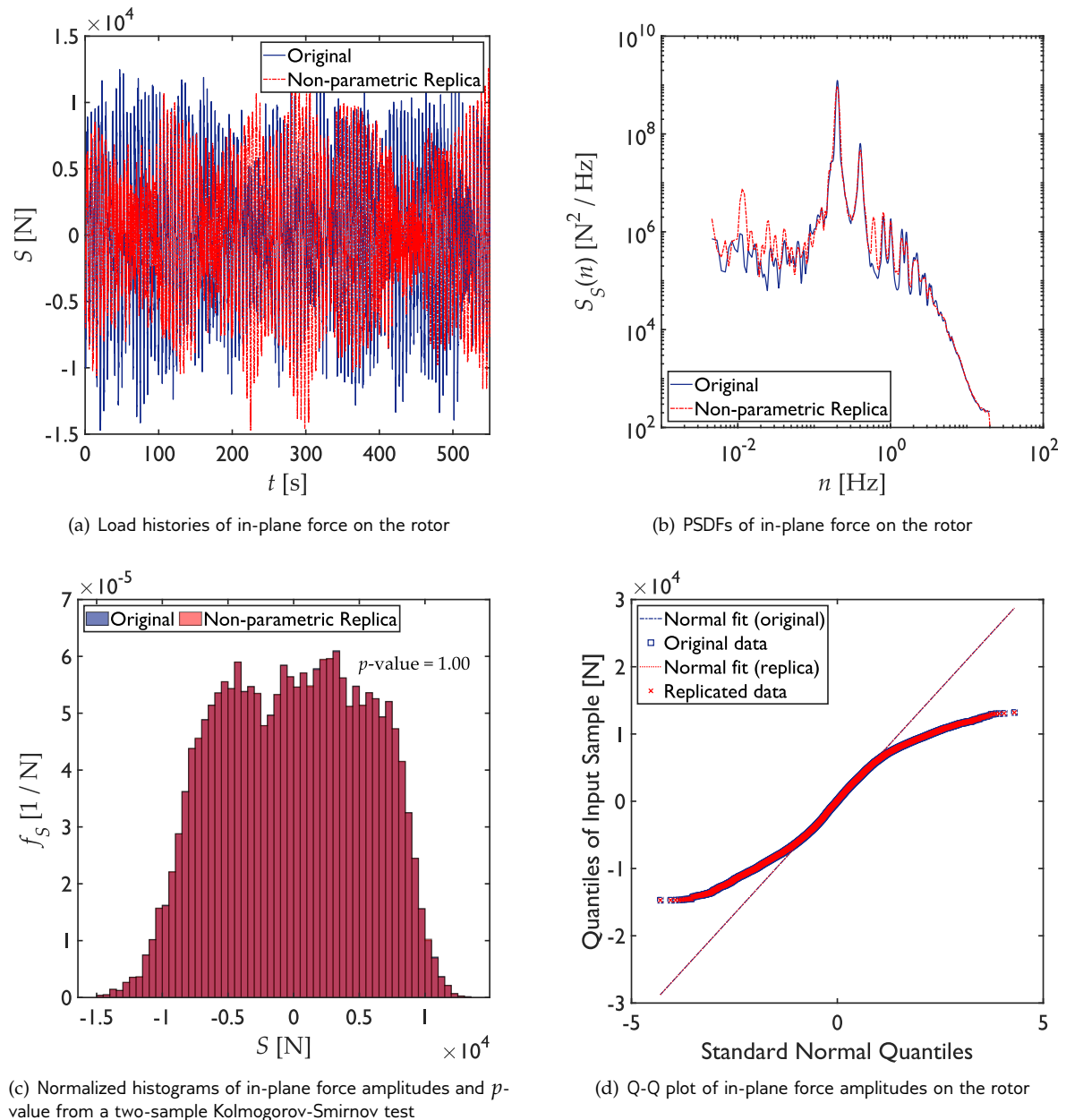


**Figure 6.12:** Non-parametrically transformed simulated rotor in-plane forces for application on the simplified model

Notwithstanding the advantages of the non-parametric transformation, the results from the analyses described in the following parts of this subsection account only for moment-based transformed signals. This decision owes to the fact that, inasmuch as force amplitudes control the response maxima, translated signals from the non-parametric approach would replicate the exact values of load maxima from the original analysis. Therefore, the randomness of the phenomenon under analysis might be misrepresented if the non-parametric transformation is used. Although the occurrence of the maxima in the uncorrelated DOFs is unlikely to appear at the same time in the simulations, the moment-based translation is elected for evaluation of the methods discussed herein.

### Damping identification

As commented in Section 6.1, there are several alternatives in the literature that suggest methods for the identification of damping from response signals. The one adopted for the present analyses is the commonly-named half-power-points method, as described in Subsection 6.3.1. This alternative implies that the damping is estimated as a fraction of the critical damping from the frequency-response function that relates the PSDFs of force and response. In this regard, the forces and responses associated with the four DOFs involved in the simplified equivalent structural model were analyzed. Figure 6.13 displays the moduli of the FRFs measured from the forces and responses in physical coordinates from each of the DOFs involved.

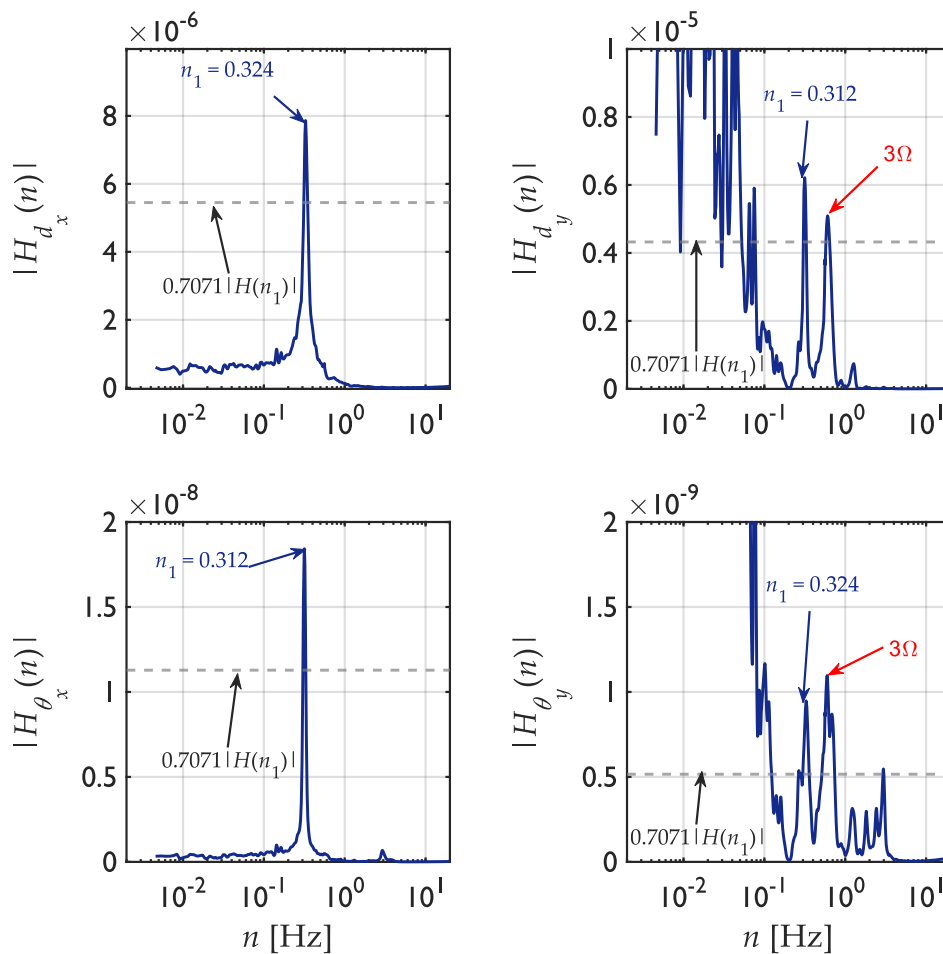


**Figure 6.13:** Moduli of the frequency-response functions in the four DOFs involved in the simplified structural model

Several observations are pertinent from Figure 6.13. In this figure, the peaks corresponding to the frequencies governing each response are evident. In the case of the function respective to the  $x$ -direction displacement, the peak is identified at the first bending mode of the tower in the fore-aft direction, i.e., at  $n_1 = 0.324$  Hz. This is analogous to the rotation around the  $x$ -axis, but with the peak displayed at the first bending frequency of the tower in the side-to-side direction, i.e., at  $n_1 = 0.312$  Hz. The value of the FRF moduli equal to  $|H(n_1)|/\sqrt{2}$  is also indicated in the figure. Thus, the damping in the direction of these responses was measured from the bandwidth displayed from these peaks.

Regarding the peaks displayed in the FRF moduli for the responses in the  $y$ -direction, and around the  $y$ -axis, several peaks are identified. This fact complicates to a certain degree the evaluation of damping in these directions. Notwithstanding, the peak corresponding to the first bending mode of the tower in the fore-aft and side-to-side directions can be identified in the moduli of the functions. These values are signaled in the rightmost plots displayed in Figure 6.13. The peak close to these frequencies (rightwards) corresponds to three times the passing frequency of the blades  $\Omega$ , which implies that the structural responses in these DOFs are highly influenced by the excitation produced by the rotor gyration. This assertion can be justified by recalling that the rotor speed was set to 12.1 RPM in all the analyses, which corresponds to a temporal frequency of 0.202 Hz. Due to the fact that the turbine under analysis is a three-bladed one, the actions on the structure due to a single blade passing will be recurrent at three times the passing frequency. Notwithstanding this behavior, the damping was measured from the bandwidth correspondent to the tower bending-mode frequencies, because the second peak has no relation to the structural characteristics of the tower.

In addition to what has been commented, the coupling between the displacement in the  $x$ -direction and the rotation around the  $y$ -axis can be inferred from Figure 6.13 by noting that the peak of each FRF moduli is formed at the frequency associated with the first bending mode in the fore-aft direction. This is analogous to the displacement in the  $y$ -direction and rotation around the  $x$ -axis, but with the peak displayed at the frequency associated with the first mode in the side-to-side direction. These observations support the coupling deduced in Equation 6.14.

Overall, similar characteristics were found in each of the FRF moduli in each of the analyses performed. Notwithstanding, the values of damping estimated in each combination showed variability to a certain degree. The damping estimates varied depending on the environmental condition evaluated, due to the different load characteristics of the implied operation state of the turbine. Moreover, as expected, the damping estimates in each DOF displayed different values. This variability is illustrated by box plots of the computed damping values from each of the elements in the sample used for the simulation of replicas. Figure 6.14 depicts these box plots.

Variability of the damping estimates is manifest, as depicted in Figure 6.14. From this figure, an overall tendency of damping variation with turbulence intensity is non-evident. However, some DOFs display a tendency of damping variation with wind speed. In this regard, observations on the variation of damping of each particular DOF are pertinent.

The damping estimated for the displacement in the  $x$ -direction (Figure 6.14(a)) displays that practically more than half of the estimates are correspondent to values from approximately 5 to 6.5%. This scatter is held practically for all the environmental and operational conditions evaluated. Whereas the damping ratios estimated for the displacement in the  $y$ -direction, as depicted in Figure 6.14(b), hardly surpass 5%. Notwithstanding, a general tendency towards higher values of damping in this DOF is observed as wind speed increases. Note that these damping estimates for displacement in the  $y$ -direction, although inferior to the estimates from displacement in the fore-aft direction, are superior to the 1% oft-suggested in the literature.<sup>10,13</sup> This could be attributed to a misestimation due to the diverse peaks displayed in the estimated FRF moduli. However, the peak in the site-to-side natural frequency of the tower is clearly defined in the FRF modulus correspondent to  $d_y$ , and is far from other peaks to be affected by them, as in, e.g., the case of the FRF modulus for the rotation around the  $y$ -axis (c.f. Figure 6.13 south-east graphic). In the case of this latter example, the modulus of the FRF

for  $\theta_y$  displays a wider bandwidth for the peak correspondent to the first bending mode of the tower. This implies a possible overestimation of the damping from this DOF, as is reflected in Figure 6.14(d).

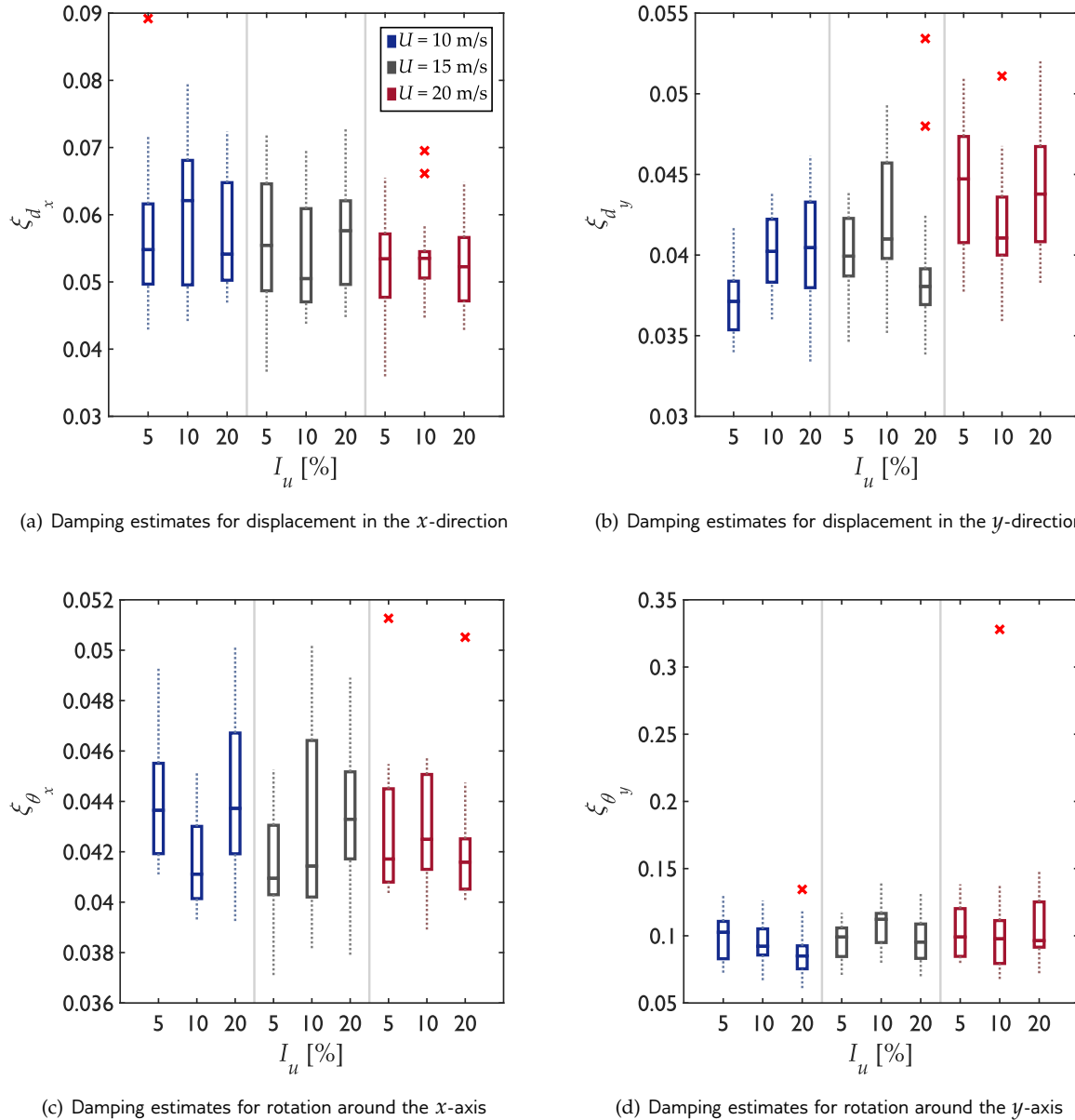


**Figure 6.14:** Damping estimates in each DOF from the samples used as seed

The uncertain determination of aeroelastic damping on the structure can be visualized from a different representation of the samples than that displayed in Figure 6.14. For that purpose, Figure 6.15 displays the kernel density estimation ( $k(\cdot)$ ) for the damping ratios from each DOF, and the different environmental and operational conditions. Insofar as the kernel density estimation is a non-parametric representation of the PDF of a sample, it can be availed for the visualization of the damping-ratio variation with either wind turbulence or wind speed, as illustrated in Figure 6.15.

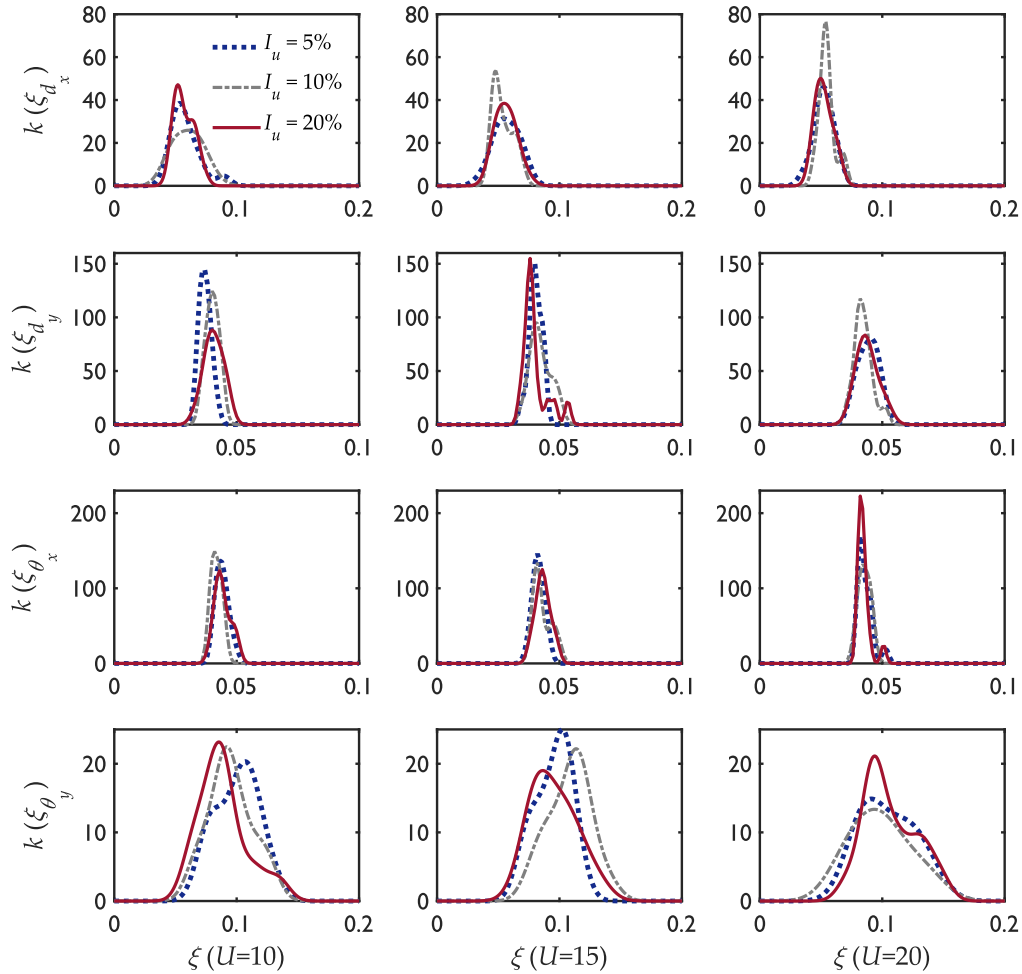


**Figure 6.15:** Kernel density estimations of damping values for the four DOFs needed for the simplified structural model

It can be inferred from Figure 6.15 that a damping ratio estimate for a certain DOF, given a wind speed, will very likely display close values regardless of the turbulence intensity. Such an assertion holds for all wind speeds and all DOFs, apart from the damping estimates associated with the rotation around the  $y$ -axis. In this last case, a greater variation of kernel density estimation with turbulence intensity is displayed, regarding the broadness of the represented PDF. This is attributed to the difficult bandwidth displayed in the FRF moduli for this DOF ( $\theta_y$ ). Notwithstanding these observations, the estimates for the rest of the DOFs appear less uncertain inasmuch as the kernel density estimates show more similitude for the different turbulence intensity values.

### Results

The control and seed samples were defined from analyses performed in FAST at a sampling frequency of 100 Hz, and under the operation and environmental criteria described previously in this chapter. Subsequent replicas of these original load histories in the four DOFs needed for the evaluation of the simplified model were obtained by means of the spectral representation method.<sup>35</sup> Some examples of the resulting histories of response obtained from the full model analyzed in FAST, as well as from the simplified 4-DOF model described herein, are presented in Figure 6.16. Their respective PSDFs are also included in the figure. For brevity, only one of the operation cases is displayed, which is correspondent to a mean wind speed of 15 m/s at the hub height, and a turbulence intensity of 15%.

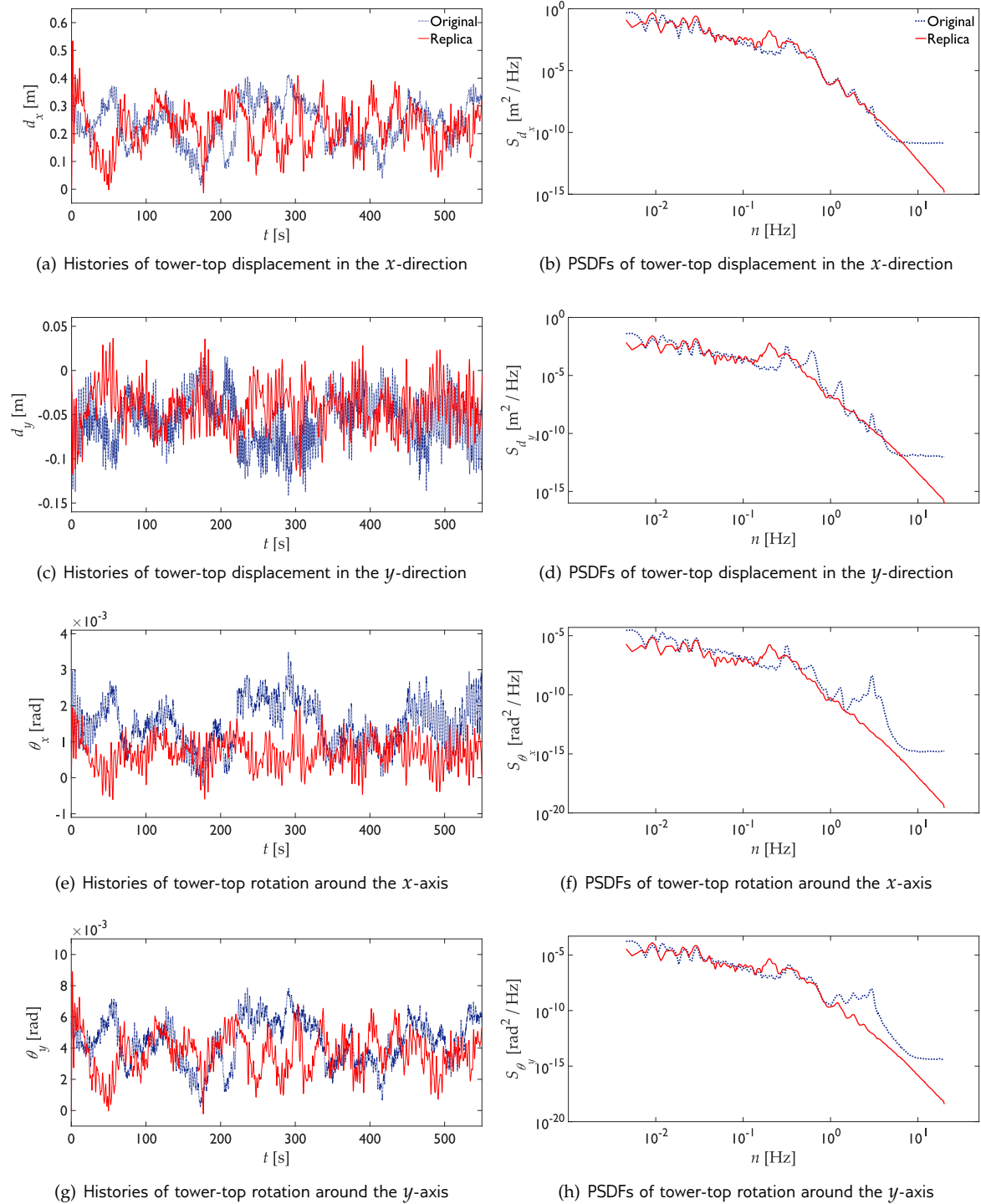


**Figure 6.16:** Response histories and their respective spectral densities for the four DOFs accounted for in the simplified evaluation



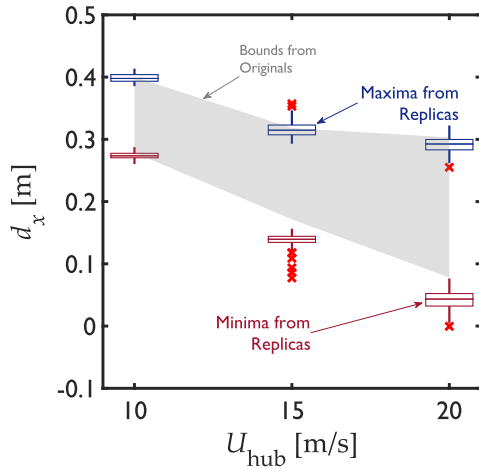
Before making further comments on the results from the simplified analyses, comments on the information displayed in Figure 6.16 are pertinent: (i) The response histories for a given DOF are resemblant to a certain degree. This is more clearly appreciated by looking at their PSDFs. The PSDFs for  $d_x$  are the ones displaying the greater similitudes between them (see Figure 6.16(b)). (ii) The PSDFs for rotation around the  $x$ - and  $y$ -axes show more dissimilitudes between the amplitudes from the originals and their respective replicas. A fact that is more notorious at higher frequencies (see Figures 6.16(f) and 6.16(h)). This is attributed to the neglect of higher modes of vibration associated with the aforementioned DOFs, and unattainable by the 4-DOF model. (iii) Some peaks in the PSDF of the replicas of  $d_y$  are disregarded with the simplified model. This might be attributed to the coupling between other DOFs and the displacement in the  $y$ -direction that is being neglected by the adopted criteria, possibly from the aerodynamic damping matrix. Notwithstanding these observations, the resemblance between the results from the simplified model and the ones from the full model appears satisfactory.

Inasmuch as the adopted criterion is intended for the provision of equivalent samples of structural response for the analysis of extreme values, it is pertinent the comparison between the maxima of the responses estimated with the simplified approach and those from the full-model analyses. For that purpose, Figure 6.17 illustrates a comparison between the bounds of maximum and minimum displacement displayed by the control sample, as well as box plots of maxima and minima displayed by the replicas obtained from the seed sample. For brevity, only the displacement in the  $x$ - and  $y$ -directions are presented.

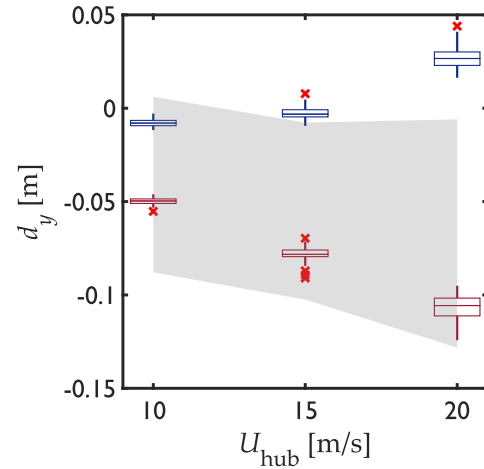
Note that either the results from the control sample, as well as from the replicas, display a diminishment in the along-wind displacement ( $d_x$ ) with wind speed. This is owed to the variation of the thrust coefficient of the rotor with wind speed. That is, inasmuch as the wind speed increases towards 20 m/s, the turbine approaches its cut-out speed (i.e., 25 m/s) and operates with a lower thrust coefficient. Moreover, the range of values covered by the data tends to widen as turbulence intensity increases. Overall the tendency from the maximum and minimum displacements in both the  $x$ - and  $y$ -directions displays similitude between the replicas and the control sample, as seen in Figure 6.17. However, many of the data miss the bounds demarcated by the full-model results. An *ideal* representation of the response maxima from the simplified analyses would display the outer whiskers of the box plots reaching the bounds of the original analyses from the inside. In the case of  $d_x$ , the greater part of the results converges within the bounds of the control samples for the maxima, whereas it diverges out of the bounds for the minima. Whereas for  $d_y$  the situation is the opposite. Notwithstanding that the tendencies displayed by the maxima and minima of responses are similar, the discrepancies displayed between the full-model analyses and the simplified ones can be attributed to the misestimation of coupling between the DOFs in the latter. This is also one of the possible causes of the spectral differences displayed in Figure 6.16(d), for example.

A better depiction of the behavior of the structural response from the simplified approach can be performed by looking at the probability distribution of the extremes. For that purpose, a comparison between the probability distribution of the maxima for the along-wind displacements from the control sample and the simplified model is presented in Figure 6.18.

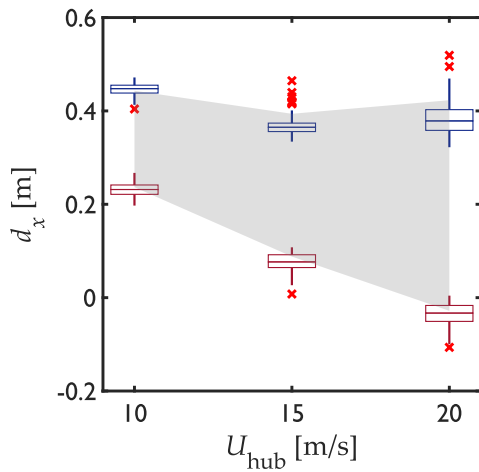
Fits of a normal probability distribution estimated from the data are also presented in Figure 6.18 merely as a reference. Results from goodness-of-the-fit tests are omitted in the figure, howbeit, all the samples of extreme responses from the full model appeared to be represented fairly by a normal probability distribution. Evaluation of other distributions was disregarded for the sake of brevity. The resemblance between the original samples and the replica is illustrated in Figure 6.18 and evaluated quantitatively by means of  $p$ -values from a two-sample Kolmogorov-Smirnov test performed on each pair. As depicted from the  $p$ -values computed from these tests, and displayed in Figure 6.18, inasmuch as wind speed and turbulence intensity increase, the resemblance between the probability distribution of the original and replicated samples also increases. It must be mentioned that the similitudes among the structural response in the  $y$ -direction are less notorious. Notwithstanding these ob-



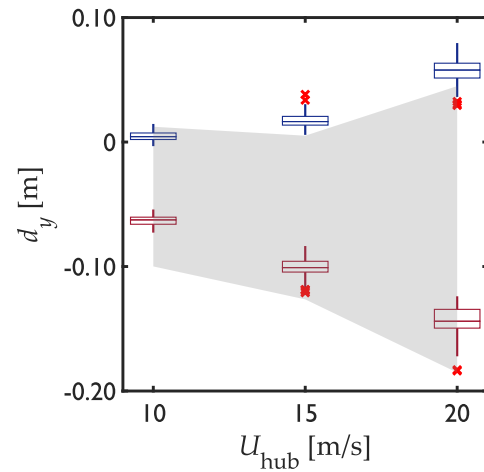
(a) Extreme values of tower-top displacement in the  $x$ -direction for  $I_u = 5\%$



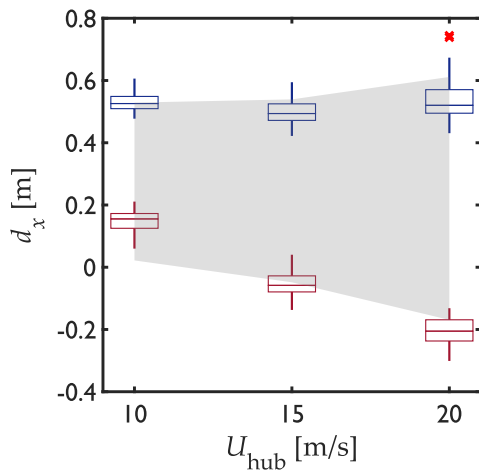
(b) Extreme values of tower-top displacement in the  $y$ -direction for  $I_u = 5\%$



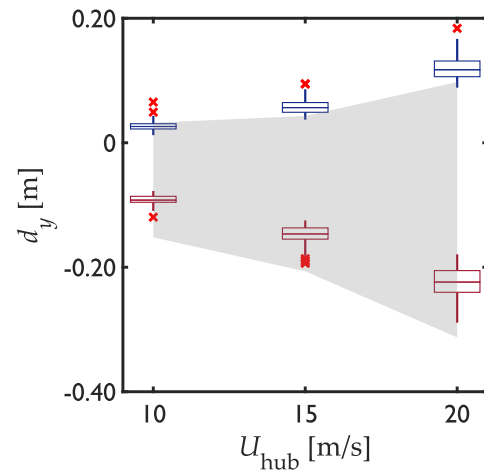
(c) Extreme values of tower-top displacement in the  $x$ -direction for  $I_u = 10\%$



(d) Extreme values of tower-top displacement in the  $y$ -direction for  $I_u = 10\%$



(e) Extreme values of tower-top displacement in the  $x$ -direction for  $I_u = 20\%$



(f) Extreme values of tower-top displacement in the  $y$ -direction for  $I_u = 20\%$

**Figure 6.17:** Maxima and minima of tower top displacement from simplified analyses

servations, a better representation of the structural response would be expected from the simplified model if a more sophisticated method for the identification of aeroelastic damping is used. This is premised inasmuch as a better assembly of the damping matrix would provide a better estimation of coupled responses in the simplified model. Unfortunately, further studies on the aforementioned hypotheses fall out of the temporal limits of the present study. Notwithstanding, a fair representation of samples of extreme values of structural response can also be achieved directly from the measured response signals, as described in the following subsection.

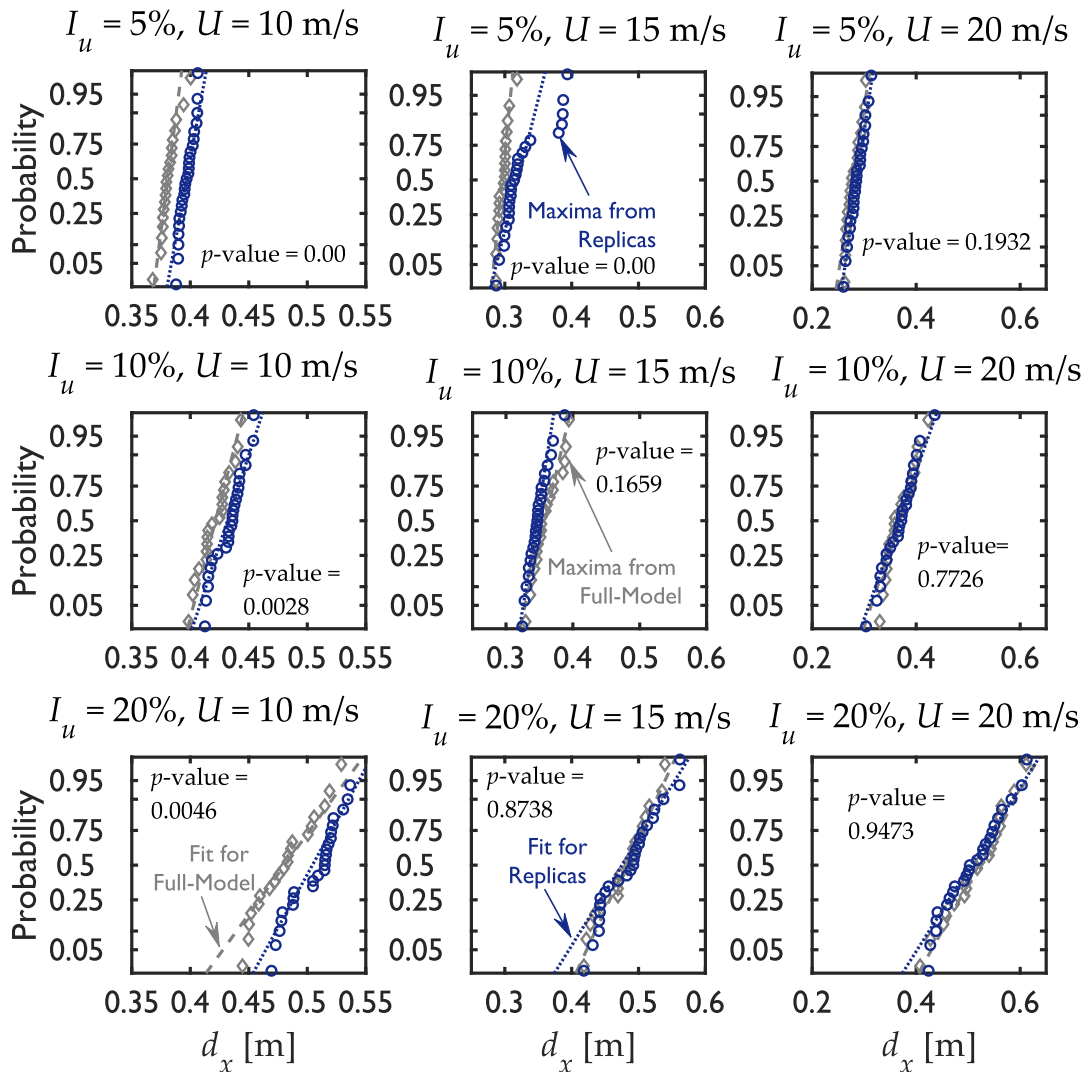


**Figure 6.18:** Probability plots and  $p$ -values from a two-sample Kolmogorov-Smirnov test from the control sample and replicated data

### 6.5.3 Simulation of response signals

Although the simplified model described in Subsection 6.3.1 (and evaluated in the foregoing paragraphs) emulated with a certain degree of similitude the behavior of an elaborate wind turbine structural model, it exhibited to be presumably dependent on the quality of the identification of aerodynamic terms in the equation of motion (Equation 6.15). However, in the same manner that the aforementioned simplified method relies on the statistical moments describing the amplitudes of forces on the structure, and on the spectral densities describing their frequency content, an economic criterion for the furnishment of structural response data is described in this subsection.

### Amplitude-based simulation

The simulation of non-Gaussian stochastic processes as described in Subsection 6.2.1 relies on the statistical moments of an original process, as well as on its spectral characterization. If these criteria are applied to simulate the response history of a structure, say, the displacement at the top of the tower of a wind turbine, it is imperative to determine adequately the probability distribution of the amplitudes of response. In that regard, an exploration of the statistical characteristics of the results from the seed sample was performed in order to determine if the moment-based translation models described in Subsection 6.2.1 are applicable. Figure 6.19 illustrates the relationship between the skewness  $\alpha_3$  and kurtosis  $\alpha_4$  of the structural displacements at the top of the tower for the different environmental combinations evaluated.

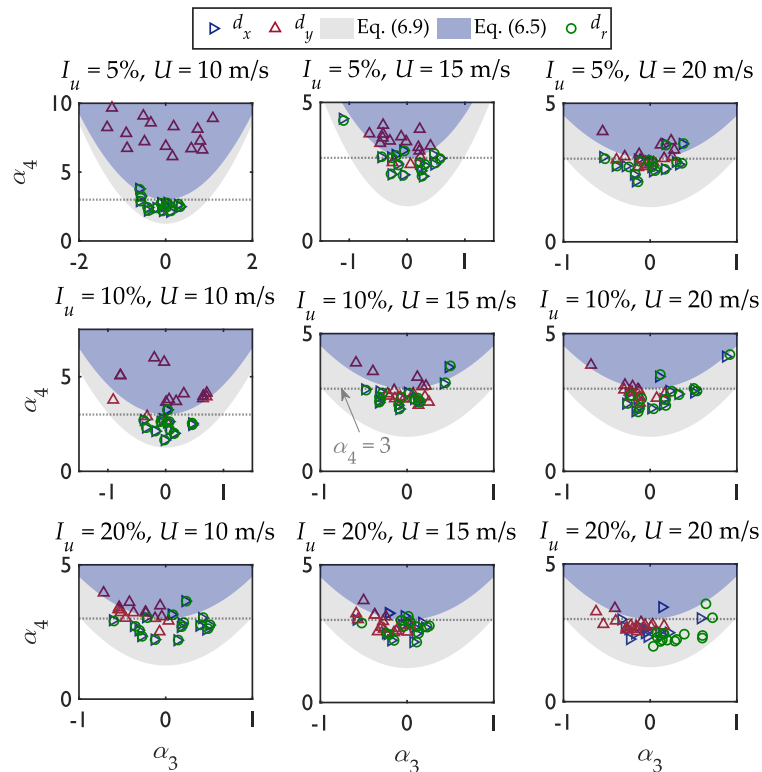


**Figure 6.19:** Values of skewness  $\alpha_3$  and kurtosis  $\alpha_4$  measured from the seed sample, and application regions for the moment-based translations models

Figure 6.19 illustrates the values of skewness and kurtosis for the displacement in both the  $x$ - and  $y$ -directions, as well as for the resultant displacement (computed as  $d_r^2(t) = d_x^2(t) + d_y^2(t)$ ). The regions of application for the translation models defined by Equations 6.5 and 6.9 are also displayed in the figure. These representations evince that the conditions for the application of the models described in Subsection 6.2.1 are satisfied. That is, the requirements for a monotonic translation function are met for the totality of the cases. Moreover, the greater part of the data appears to be suited for the application of the moment-based translation from Equation 6.9. Regarding the statistical characteristics of the data, the intricate behavior of the structural response can be appreciated by looking at how the statistical moments are dispersed across the quadrants of each of the plots. Furthermore, the resultant displacement  $d_r$  appears to display nearly-identical statistical moments as  $d_x$  for almost all the cases. Notwithstanding, inasmuch as  $d_r$  is (by definition) expected to be greater than  $d_x$ , it is, consequently, of greater interest for structural engineering purposes. Thus,  $d_r$  is selected for the illustration of the response signal simulation in the following paragraphs.

The statistical moments of the amplitudes of  $d_r$  satisfy the requirements of the translation models for a monotonic translation function. Regardless of these satisfied conditions, in order for the method discussed herein to be attractive for its application, the similarities in the probability distribution have to be sufficient. As can be inferred from the variation of the statistical moments of the amplitudes of responses, the probability distribution of  $d_r$  is expected to display complicated features. For the verification of this premise, the kernel density of the resultant-displacement amplitude, i.e.  $k(d_r)$ , was estimated for each element of the seed sample. Figure 6.20 illustrates these estimations for each one of the environmental combinations.

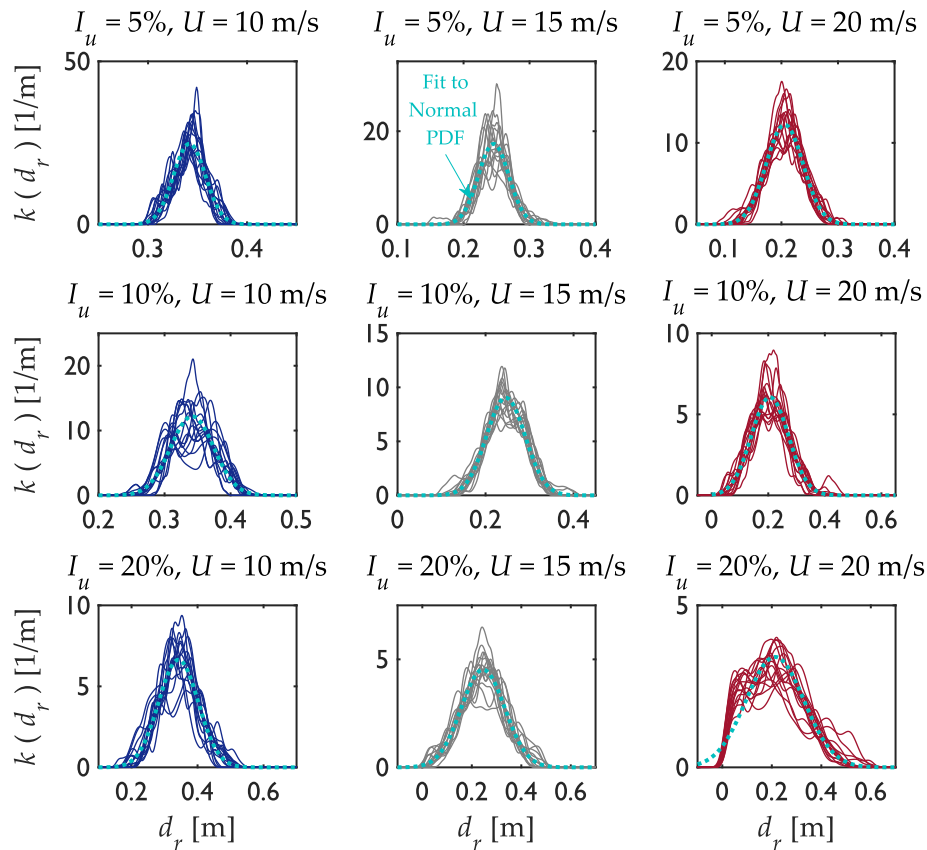
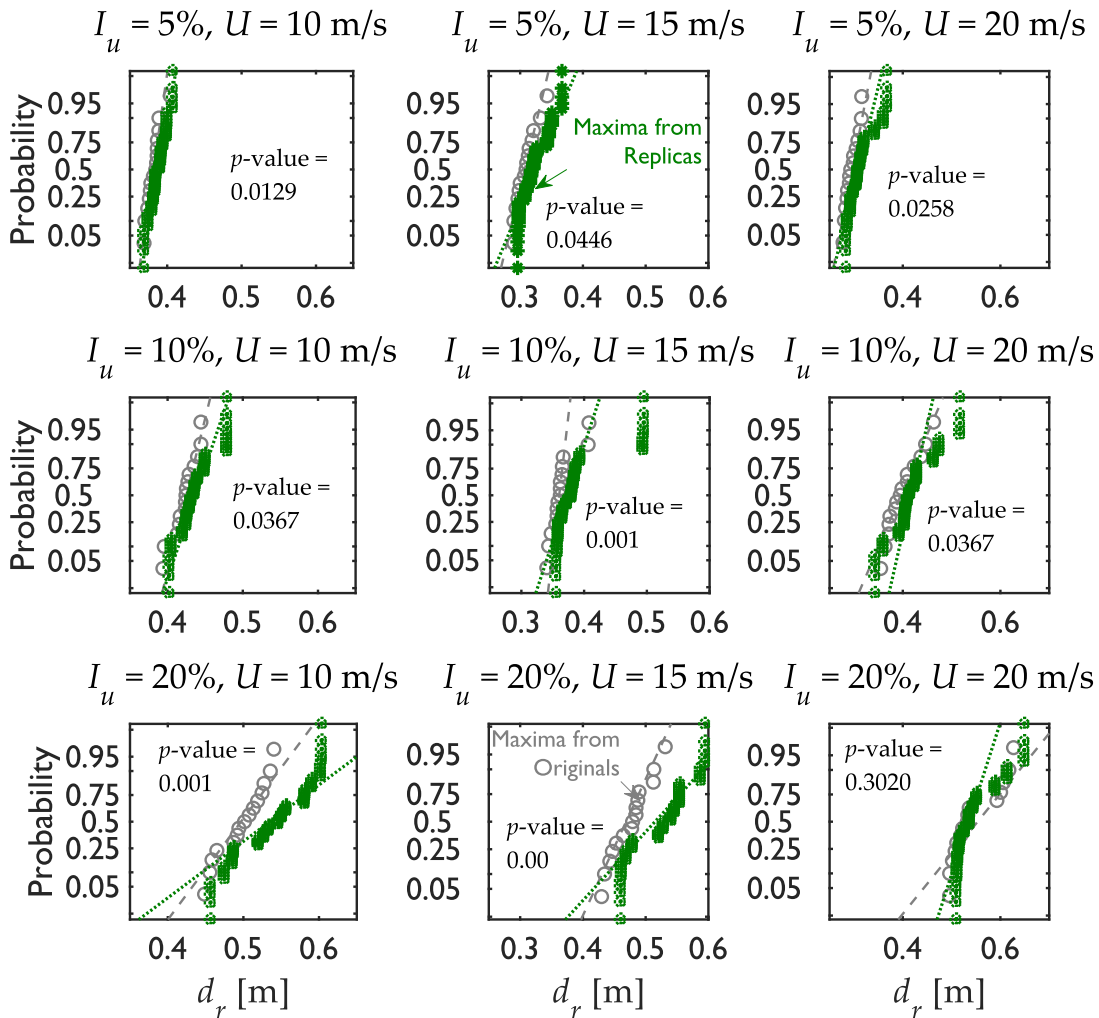


Figure 6.20: Kernel density estimations of the resultant displacement amplitude

The kernel estimations displayed in Figure 6.20 have been computed from samples of more than 50,000 data per estimation. That is inasmuch as each sample consists of response signals trimmed to 550 s, which result from structural analyses that have been performed at a sampling rate of 100 Hz. Notwithstanding the size of these samples, a great variation is evident in the approximated probability densities for all the cases. Complicated features such as multimodality can be appreciated in a great part of the estimations. Moreover, despite the fact that the greater part of the data has a rather *hardening* behavior (i.e., its kurtosis is less than three) as depicted in Figure 6.19, the greater part of the estimations of the PDF appears to be overall *leptokurtic*. That is, the approximations of the PDF from Figure 6.20 appear to be rather *sharpened* (a fit of a normal PDF to each set of data has been included in Figure 6.20 for comparison). From this behavior, a guess based on observation of the kernel estimations of the PDF would suggest values of kurtosis greater than three. However, the results presented in Figure 6.19 would contradict such a hypothesis. These observations serve as proof and provide details on the intricacy of the phenomenon under study. Moreover, despite the generally ‘adequate’ (in appearance) representation from a normal distribution, none of the samples displayed statistical significance when the amplitudes of  $d_r$  were tested for such a distribution.

Regardless of the intricate behavior of the probability distribution approximations from the resultant response amplitude, a simulation of response signals attempting to replicate the original  $d_r(t)$  signals was carried out. For that purpose, the PSDF of  $d_r$  was estimated from the results of the seed samples. A total of 15 replicas per original signal were simulated from these PSDFs of  $d_r$ . In this case, for the sake of lower computing time, instead of employing the spectral representation method,<sup>35</sup> as done for the analyses described so far in this chapter, an auto-regressive moving-average (ARMA) model was employed.<sup>40</sup> Furthermore, it must be mentioned that the sampling frequency of these replicas was set to 20 Hz, instead of the 100 Hz considered in the original signals and the simulations described previously. This was done also for the sake of the computing time economy from the simulations. Regarding the ARMA orders of the model, both the auto-regressive (AR) and moving-average (MA) orders of the model employed were set as 5. These values proved to be sufficient to capture adequately the spectral characteristics of the original signals. The amplitudes of the replicas were transformed into a non-Gaussian process by means of the moment-based methods described in Subsection 6.2.1 and in accordance with the results summarized in Figure 6.19. The maxima of these replicas were measured and compared to the maxima from the control sample. Figure 6.21 displays results analogous to those displayed in Figure 6.18, but for the simulated signals of  $d_r$ .



**Figure 6.21:** Normal probability plots of resultant response maxima, and  $p$ -values from a two-sample Kolmogorov-Smirnov test

From Figure 6.21 it is evident that the resemblance between the original samples and the replicas varies depending on each environmental condition. This is owed to the difficult probability characteristics displayed by the amplitudes of  $d_r$ . That is, despite the fact that the conditions for the application of the moment-based translation models described in Subsection 6.2.1 are satisfied, statistical significance was hard to achieve when the probability distribution of the original amplitudes was compared to the distributions estimated from the moment-based models. Results from these evaluations are omitted for the sake of brevity. Nevertheless, insofar as (for the present purpose) the relevant similitudes in the probability distribution are its extremes, the greater part of the results from the replicas translated by means of the moment-based models described in this chapter appeared to be satisfactory. This can be appreciated from Figure 6.21, where (for the greater part of the cases) there is no evidence to reject the null hypothesis that implies that each sample pair is represented by the same distribution at a significance level of 1% after a two-sample Kolmogorov-Smirnov test is performed.

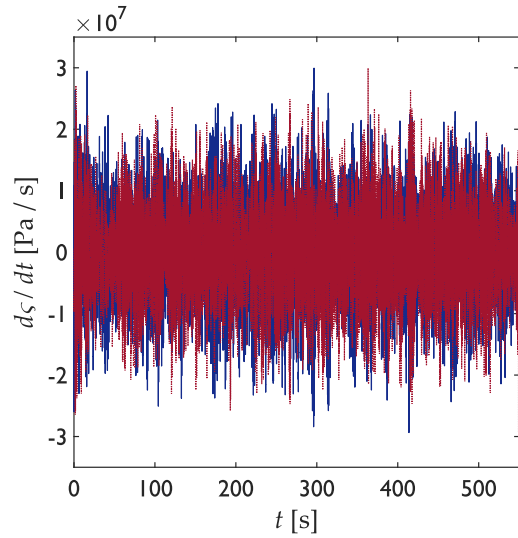
The cases discussed hitherto rely on the hypothesis that the extremes of structural response are of interest. However, some design conditions are governed by load cases where the adopted criterion must be different. This is the case of fatigue damage, for example. Explorations on approaches for the simulation of response signals for this purpose are described in the following.

#### *Range-based simulation for fatigue analysis*

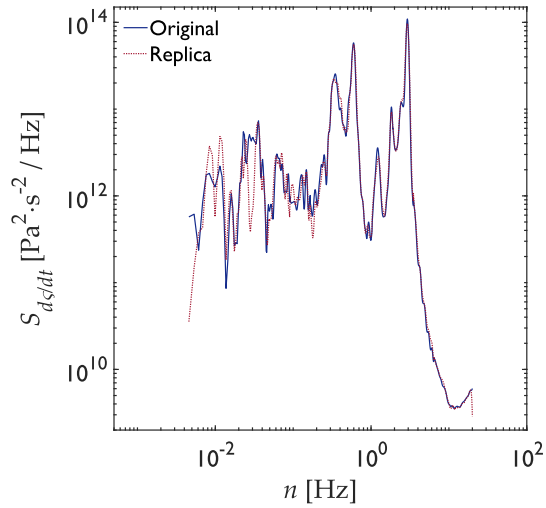
Fatigue damage is conventionally evaluated from cycle counting. One of the most widely accepted methods for this action is the one known as the *rain-flow* algorithm.<sup>26</sup> From this algorithm, a matrix of load cycles and ranges is constructed, and subsequent estimation of the fatigue damage produced from a load history can be obtained, usually from the rule of Miner. This criterion assumes that the fatigue damage accumulates linearly and independently at each load cycle (see Equation 6.22).

In order for the method discussed herein to be of application for fatigue analysis, replicas of the stress derivative  $\dot{\zeta}(t)$  with concordant amplitude distribution must be simulated. This is done for the sake of stress signals with an equivalent distribution of ranges, rather than amplitudes. The steps to obtain these signals are summarized in Subsection 6.1.1, and differently from what was performed for the simulation of signals for response amplitude maxima (Subsection 6.5.3), in the present cases, the direct transformation of non-Gaussian processes can be applied.

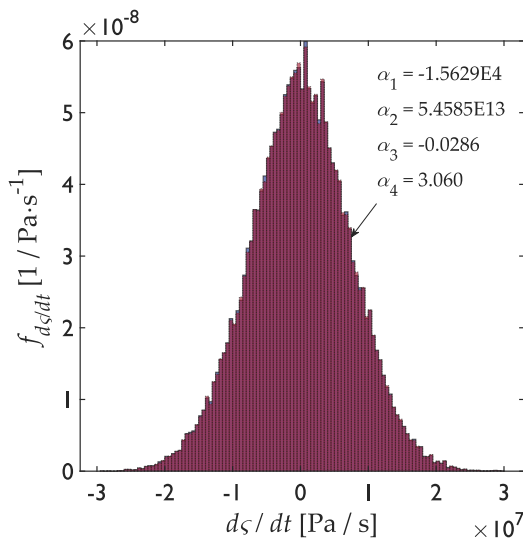
The resulting stresses at the base of the tower from each of the analyses performed in the software FAST<sup>33</sup> were computed in accordance with Equation 6.16. Conforming to the steps summarized in Subsection 6.1.1, the time derivative of the stress amplitude from the original analyses was computed. The PSDFs of these stress derivatives were estimated, and from these estimated functions a set of simulated signals with the same frequency content were obtained. Correction to the amplitude distribution was performed on the simulated signals used in this illustration, and they were subsequently integrated to obtain replicas of stress amplitudes. Figures 6.22 and 6.23 exemplify some of the replicas obtained from this approach, considering the spectral representation method<sup>35</sup> for their simulation, and a sampling frequency of 100 Hz.



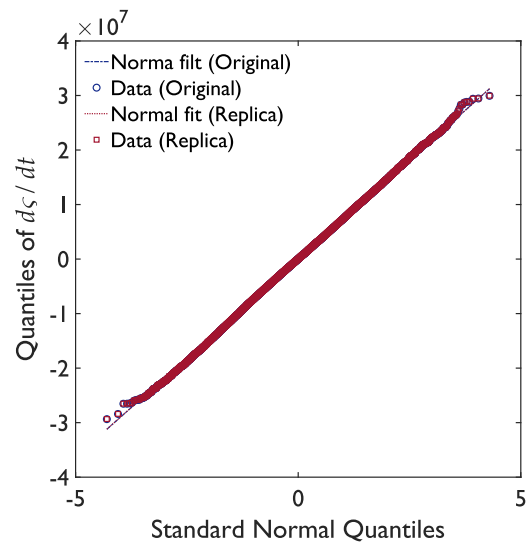
(a) Stress time derivatives for a case with  $\bar{U}_{\text{hub}} = 15$  m/s, and  $I_u = 5\%$



(b) PSDs of the stress derivatives displayed in Figure 6.22(a)



(c) Normalized histograms of amplitude for the stress derivatives displayed in Figure 6.22(a)



(d) Quantile-quantile plots of amplitude for the stress derivatives displayed in Figure 6.22(a)

**Figure 6.22:** Signals of stress derivatives, as well as their spectral and statistical characteristics

It is observed from Figure 6.22(b) that a fair similitude in frequency content is achieved from the spectrally-represented simulation.<sup>35</sup> Only a drop of spectral amplitude is barely visible at the highest frequencies in the spectrum from the replica. This drop is attributed to the treatment performed on the original signal for its spectral smoothing, inasmuch as this treated spectrum was employed for the simulation of the replica. Moreover, insofar as the non-parametric transformation described in Subsection 6.2.2 was employed on the signal, the normalized histograms of stress-derivative amplitudes shown in Figure 6.22(c) are nearly identical. This similarity can also be observed in Figure 6.22(d), where the markers of both the original and the replicated samples overlap. Moreover, from Figure 6.22(d) it is evident that the stress derivatives displayed are practically Gaussian. This observation is justified in the alignment displayed between the quantiles of the samples with fits to those from



a Gaussian distribution. The statistical moments presented in Figure 6.22(c) justify the observation as well. Exploration of the results from either the control or the seed samples showed that the stress derivatives displayed Gaussian characteristics generally. Only a small fraction of the results from both the seed and control samples displayed a bin intermittence in the histograms of  $\zeta$ , however, this caused no deviation from Gaussianity in the statistical moments of the samples. The illustration of such cases is disregarded for brevity. Furthermore, observe from Figure 6.22 that the signals of  $\zeta$  appear to be centered near zero. A characteristic that had to be held for the integration of the stress derivative signals. Moreover, it is important to consider that correction of the mean value of the simulated amplitude replicas after the integration of  $\zeta(t)$  needs to be performed, inasmuch as the integration would give a zero-centered signal. An example of the replicated signal of stress amplitude is presented in Figure 6.23.

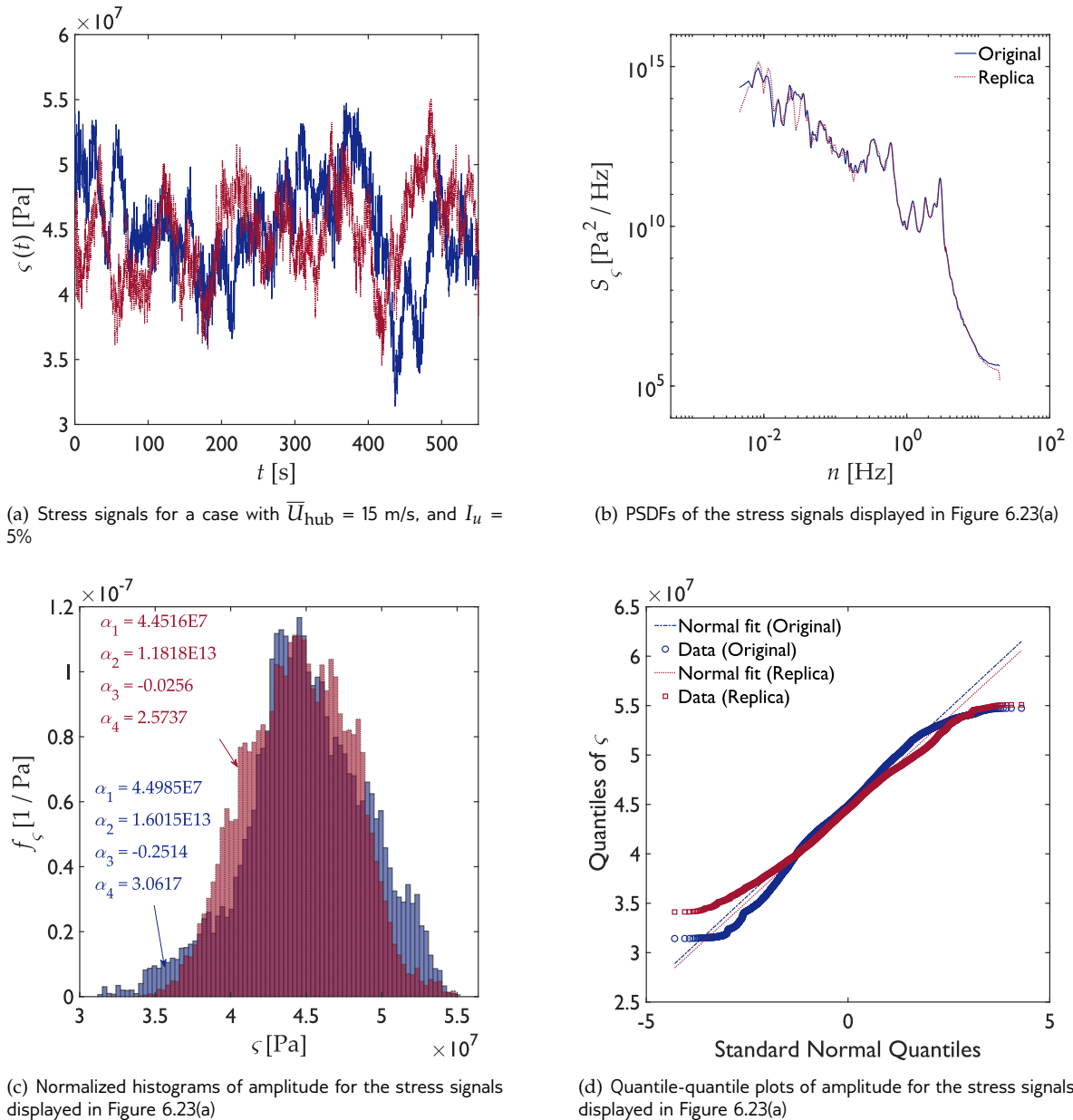


**Figure 6.23:** Signals of stress amplitudes, as well as their spectral and statistical characteristics

As in the case presented as an example for  $\dot{\zeta}(t)$ , the spectral amplitudes from the PSDF of stress at the base of the tower evince marked resemblances between the original and the replica. Analogously to the stress-derivative spectrum from the replica displayed in Figure 6.22(b), the PSDF estimated for the replicated stress-amplitude signal shows an amplitude drop barely visible at the highest frequencies in Figure 6.23(b). The more abrupt drop of spectral amplitude is attributed to the treatment performed on the original spectrum for its smoothing, whereas the gradual drop is caused by a loss of information at high frequencies from the time-domain integration of the simulated signal. Further comments on this latter observation are made ahead in the text. Regarding the statistical moments of the stress signals, evident differences are displayed in the two processes, as presented in Figure 6.23(c). From these histograms, it can be observed that neither of the two signals has Gaussian-distributed amplitudes, a fact that can be corroborated by the quantile-quantile plots displayed in Figure 6.23(d). Notwithstanding these differences, the resemblance of practical interest between the two signals must be displayed in the fatigue damage produced by either of them. This can be estimated from the cycle count performed on each signal. For that purpose, a histogram of cycles counted with the rain-flow<sup>26</sup> algorithm is presented in Figure 6.24.

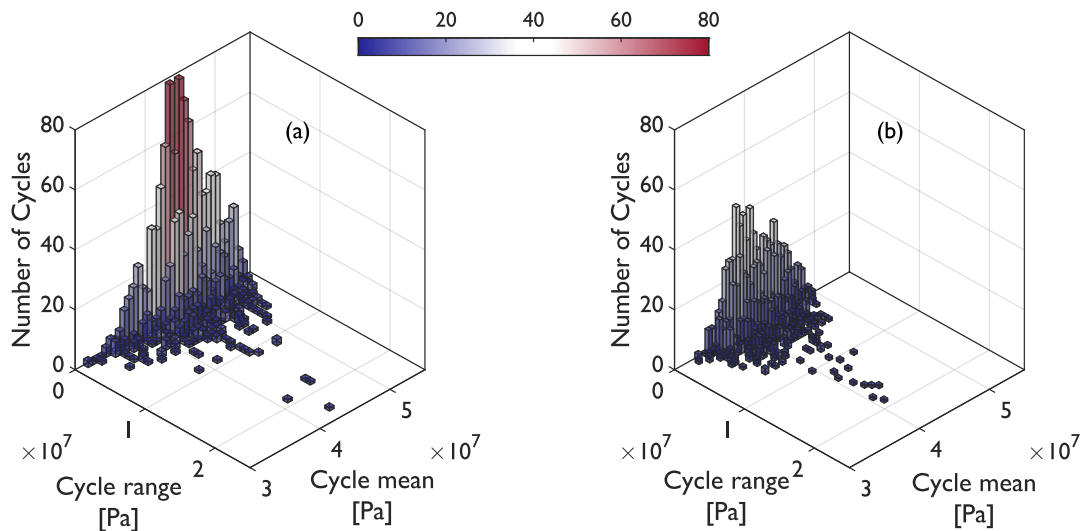


**Figure 6.24:** Rainflow histograms for stress histories at the base of the tower: (a) from a full-model signal, and (b) from a replicated signal

The replicated stress signal appears to have a lower number of cycles to fatigue, as displayed in Figure 6.24. However, this is merely apparent, inasmuch as both signals were sampled with the same time step (i.e., 0.01 s) and trimmed at the same length. Therefore, both signals hold the same number of observations, howbeit dispersed at different stress ranges and mean. From Figure 6.24(a) it is evident a significant contribution of low-range cycles from the original stress signal, whereas the replicated signal (Figure 6.24(b)) tends to display a distribution of stress cycles more concentrated at slightly higher ranges. A plausible overestimation of fatigue damage can be anticipated due to this fact. This hypothesis is justified in the fact that, since both signals have the same number of observations and identical frequency content at a considerable bandwidth, the observations that fall outside the 'low-range zones' have to be located at higher ranges and, consequently, will produce greater fatigue damage. In this regard, it must be mentioned that the original signal was differentiated and subsequently integrated with respect to time in order to filter out the high-frequency contributions commented in the previous paragraph. Such high-frequency contributions increased considerably the cycles counted at minute-range stresses. This process is of negligible effect for the fatigue damage evaluated from the rule of Miner, insofar as the cycles with larger ranges are the ones governing the damage.<sup>41</sup> Notwithstanding the de minimis contribution of the lost low-range stress cycles in the fa-

tigue damage, they were of consequence for the development of stress cycle histograms, such as the ones displayed in Figure 6.24. Thus, the high-frequency low-range contributions in the original signal were disregarded for the sake of a more direct comparison between the two signals. This comparison includes the kernel density estimation of the cycle range and mean, as depicted in Figure 6.25.

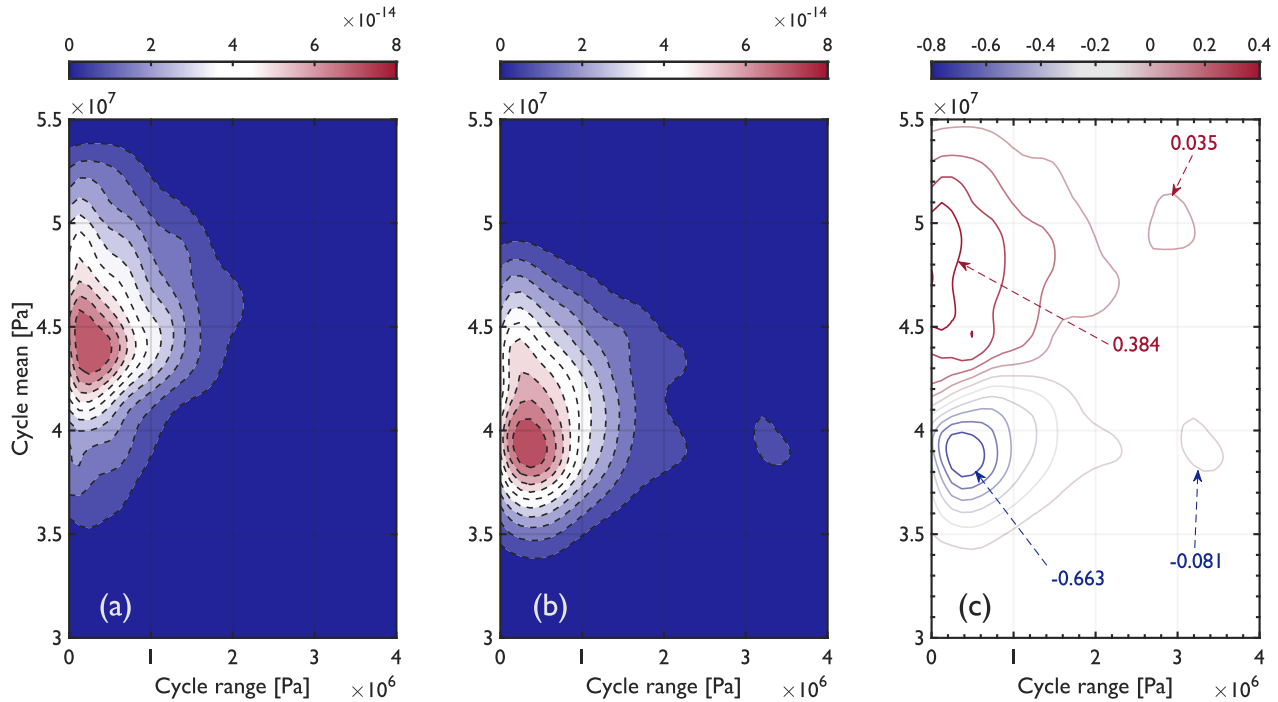


**Figure 6.25:** Kernel density estimations of range and mean of stress cycles: (a) from the full-model signal, (b) from the replicated signal, and (c) a normalized comparison of both

The kernel density estimations ( $k(\cdot)$ ), as depicted in Figure 6.25, are useful for the visualization of the distribution of stress range and mean of cycles from both the original and replicated signals. A comparison between these two approximations of the joint PDFs is presented in Figure 6.25(c). The contours displayed in Figure 6.25(c) were computed as  $(k_{\text{original}} - k_{\text{replica}}) / \max(k_{\text{original}})$ . Hence, positive values displayed in Figure 6.25(c) can be associated with underestimation of the joint PDF of mean and range of the stress cycles, whereas negative values would represent conservative results from the replicated signal. The greater differences in the kernel density estimations are signaled with arrows in the figure. From Figure 6.25(c), it is evident that the greatest underestimation occurs at stress ranges lower than 0.2 MPa for the case illustrated, whereas the greatest overestimation takes place at slightly higher stress ranges. Furthermore, the greatest underestimation of the approximated joint PDF of cycle range and cycle mean is about 38% of the original density, for the present case, whereas the greatest overestimation surpasses that quantity. Such a fact makes the replication approach rather conservative and, consequently, attractive for its implementation in preliminary and prompt revisions of fatigue on structural elements.

For a more complete visualization of the performance of the method proposed and discussed in this chapter, a comparison of fatigue damage estimated from stress signals from the control sample and replicated ones is performed. In a manner unanalogous to the signals described in the foregoing paragraphs, the signals employed for this comparison were simulated from an ARMA model.<sup>40</sup> The AR and MA orders of the model were set to 30 and 5, respectively, for the simulations. Furthermore, the sampling frequency of these signals was reduced to 20 Hz. These criteria were adopted for the sake of computing time economy, inasmuch as 50 replicas were performed, out from each of the 15 signals per environmental condition obtained from the seed sample. That is, a total of 750 replicas

per environmental combination were analyzed and compared to the results from the control sample. Regarding ARMA models, note that high AR orders in the simulation imply a longer coverage of the autocorrelation function of the process being simulated, howbeit, at a higher time of computation. On the other hand, the selection of a larger time step (in this case the time step is changed from 0.01 to 0.05 s) aids in the coverage of the same information from the autocorrelation function of the process employing lower AR orders. However, the loss of information at higher frequencies is the cost implied from this latter criterion. The study of the optimal AR and MA orders of the model is recommended before any analysis or application of the ARMA stochastic simulation, and it is particularly important in a subject as sensitive as fatigue evaluation. For the present study, an ARMA model with orders (30,5) sufficed for a fair spectral representation of the seed processes. Figure 6.26 illustrates one of the original stress signals from the seed sample, and a fraction of the 50-signals set integrated from the simulated stress derivatives. Some of the replicated signals are omitted in the figure to avoid saturation.

The resemblance between the original signal and its replicas can be appreciated in Figure 6.26(a), nevertheless, the estimated PDFs from the replicas are hardly resemblant. These dissimilarities can be observed in Figure 6.26(b), where the kernel density estimations from each of the replicas are included along with the normalized histogram from the original signal. Despite these differences, the spectral density estimated for each of the *cloned* signals resembles in a fair manner the estimated PSDF from the original signal. This behavior is illustrated in Figure 6.26(c). Regardless of the comparability between the spectral amplitudes from the original PSDF and the spectral density estimated from the *cloned* signals, which is evident at a fair bandwidth of frequencies, the peaks that characterize the original PSDF appear to be ‘smoothened’ for the spectral densities of the replicas.

To elaborate on the latter comment, consider the peaks displayed in the original PSDF from Figure 6.26(c), where a first peak in the spectral density is evident at the bending-mode frequency of the tower (i.e., near 0.32 Hz) and a second peak is displayed at three times the passing frequency of the blades (i.e., near 0.60 Hz). These two peaks are — by some means — merged into a peak around a frequency of  $\sim 0.5$  Hz in the spectral densities of the replicas. Furthermore, the group of peaks that appear in the original PSDF in the interval of the passing-frequency harmonics (i.e., between 6 and 9 times the passing frequency of the blades) is also ‘merged’ into a single peak near the frequency correspondent to 9 times the passing frequency of the blades (i.e., at 1.8 Hz) in the *cloned* signals.

This behavior is attributed to the criteria employed for the simulations. That is, for example, in the spectral representation method<sup>35</sup> a sweep of the spectral density is performed at each frequency where it is estimated, whereas a simulation from an ARMA model<sup>40</sup> considers the spectral characteristics of the signal in the time domain by means of its autocorrelation function. Inasmuch as the autocorrelation function of the process is obtained (in the present case) from the inverse Fourier transform of its PSDF, the former is estimated from the integration of a product of the spectral density at all the considered frequencies that define it. Moreover, owing to the fact that the time step selected for the ARMA simulation is five times that of the original signal, information from the autocorrelation function is lost when it is sampled, notwithstanding the AR order. In this regard, the use of time steps as small as the one from the original signal was explored, nevertheless, without success in finding the adequate AR and MA orders for a fair simulation of the process without the occurrences of numerical inaccuracies.

Fatigue damage was computed from the 750 replicas per environmental condition that were evaluated. This was done in accordance with the number of cycles counted and Equation 6.22. For that purpose, the material constants  $K_r$ , and  $m$  were assumed as  $3.9 \times 10^{12}$  (in  $\text{MPa}^m$ ), and 3, respectively, for  $N \leq 10^7$  cycles; and  $2.1 \times 10^{16}$  and 5 for  $N > 10^7$  cycles. Table 6.2 summarizes the mean values of fatigue damage computed from each sample and its standard deviation.

The mean values ( $E[D]$ ) and standard deviations ( $\sqrt{\text{Var}[D]}$ ) from the fatigue results are presented in Table 6.2. The resulting values of fatigue damage and its measures of dispersion are rather minute

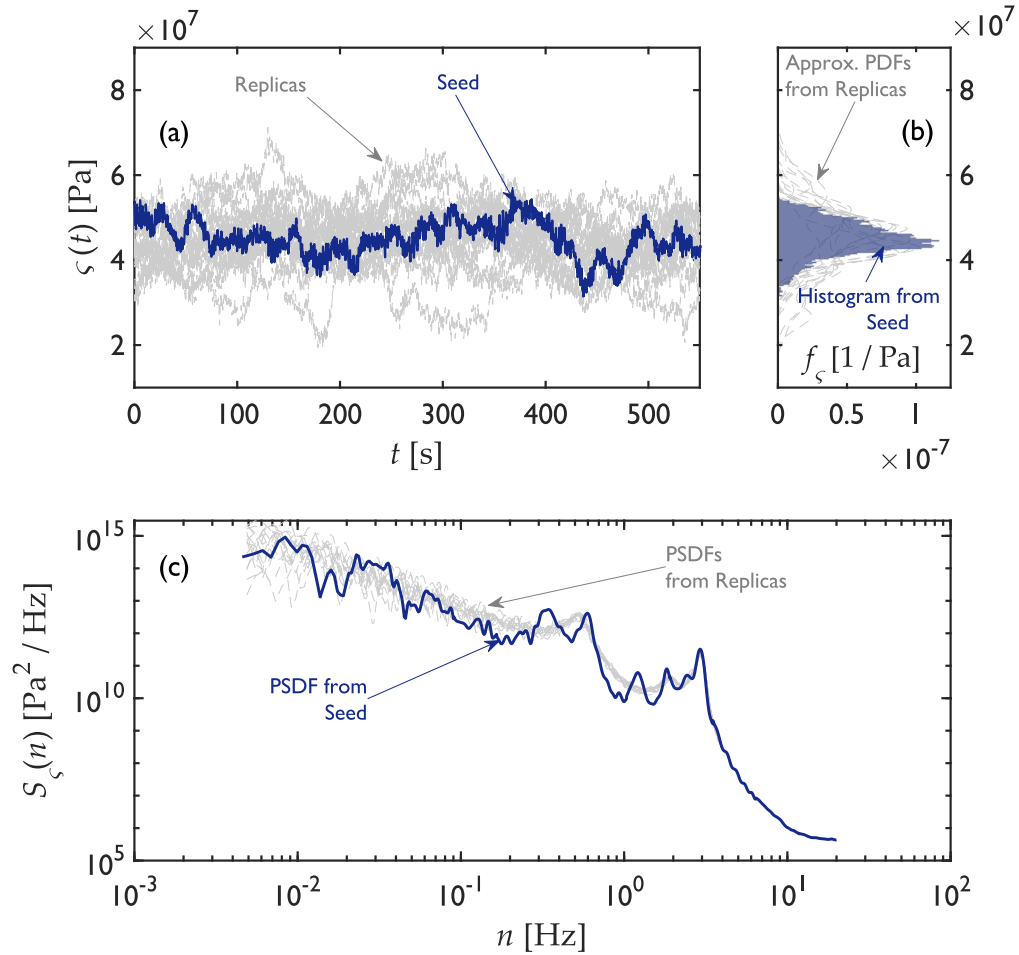


**Figure 6.26:** Stress signal from the seed sample and replicated signals (a), normalized histogram from the original stress signal and kernel density estimations from the replicas (b), and PSDFs from the original signal and its replicas (c)

**Table 6.2:** Summary of fatigue damage from the analyses performed in FAST and the replicated signals

Combination	$E[D]$		$\sqrt{\text{Var}[D]}$	
	Original	Replica	Original	Replica
$\bar{U}_{\text{hub}} = 10 \text{ m/s}, I_u = 5\%$	3.598E-09	2.896E-09	5.430E-10	8.179E-10
$\bar{U}_{\text{hub}} = 10 \text{ m/s}, I_u = 10\%$	2.259E-08	2.214E-08	2.789E-09	6.301E-09
$\bar{U}_{\text{hub}} = 10 \text{ m/s}, I_u = 20\%$	2.536E-07	1.686E-07	9.756E-08	4.395E-08
$\bar{U}_{\text{hub}} = 15 \text{ m/s}, I_u = 5\%$	1.140E-08	1.881E-08	1.160E-09	8.203E-09
$\bar{U}_{\text{hub}} = 15 \text{ m/s}, I_u = 10\%$	8.802E-08	1.354E-07	9.231E-09	4.317E-08
$\bar{U}_{\text{hub}} = 15 \text{ m/s}, I_u = 20\%$	8.374E-07	7.819E-07	1.271E-07	1.601E-07
$\bar{U}_{\text{hub}} = 20 \text{ m/s}, I_u = 5\%$	3.845E-08	8.407E-08	5.022E-09	2.702E-08
$\bar{U}_{\text{hub}} = 20 \text{ m/s}, I_u = 10\%$	3.012E-07	4.366E-07	5.282E-08	9.982E-08
$\bar{U}_{\text{hub}} = 20 \text{ m/s}, I_u = 20\%$	2.327E-06	2.214E-06	2.501E-07	6.093E-07

quantities, which makes a qualitative comparison a bit difficult. In this regard, for the sake of visualization, Figure 6.27 depicts these same results graphically in the form of box plots and shaded areas. The latter are indicated based on the fatigue-damage maxima and minima from the control sample.

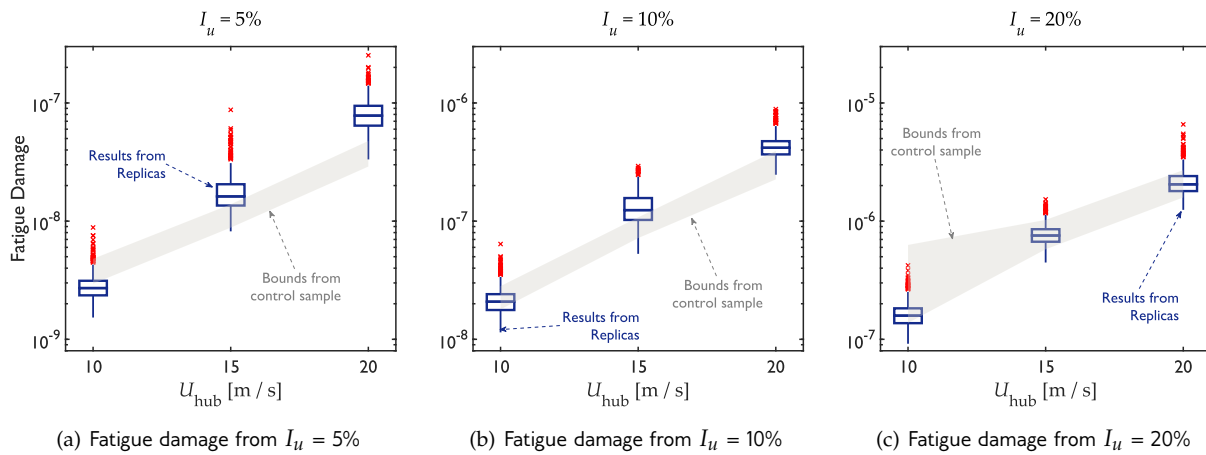


**Figure 6.27:** Fatigue damage summary from originals and replicas of stress histories at the tower base

Note that the vertical axes in Figure 6.27 are displayed on a logarithmic scale. This was done for the sake of a better appreciation of the similitudes and differences among the results. The criterion depicted in Figure 6.27 is more strict than a quantitative comparison of the values as presented in Table 6.2 inasmuch as the box plots from the figure also indicate the elements that fall too far from the first and third quartiles of the samples. Notwithstanding these cases, the overall tendency of fatigue damage appears to be fairly captured from the replicated stress signals with the approach discussed herein. Moreover, it is important to observe that the dispersion of the results from the control sample is covered by those from the replicated signals. Regarding the latter, observe that these results generally lead to conservative fatigue damage estimates. This fact was anticipated by looking at the rain-flow histograms (Figure 6.24) and approximated joint PDF of stress cycles (Figure 6.25), and its occurrence was justified in the loss of information at high frequencies implied in the replication process. Regardless of these shortcomings, the simulated results demonstrate that the simplified method for fatigue damage estimation is attractive for its practical application in the early stages of design or reliability evaluation, inasmuch as it tends to produce results that are rather conservative, howbeit, with ranges of variability acceptable for preliminary analyses.

## 6.6 Conclusions

In this chapter, a simplified approach has been described, intended for the provision of massive samples of structural response data for prompt and preliminary reliability analyses. The methodology relies fundamentally on the adequate spectral characterization of loads and responses on a wind turbine support structure, as well as on the determination of their statistical characteristics. This approach proved to be computationally economical, however, with some minuses. Notwithstanding, the results in the majority of the analyzed cases showed to be of usefulness for practical purposes, inasmuch as either the greater part of results was proved to be similar at conventional levels of significance, or these displayed to be rather conservative within acceptable ranges of imprecision for preliminary results.

The application of the methodology discussed herein has been centered on the analysis of response maxima from the support structure, as well as from its fatigue analysis. Nevertheless, the approach can be used for diverse problems and structural elements, to the degree that the required information

is the spectral density of the process under analysis and its statistical moments. Finally, the following comments from this chapter are outlined:

- In the cases covered in this chapter, it has been assumed that the analyzed processes are stationary. However, in reality, non-stationary features can be encountered describing the processes of interest, given the variable nature of the operation loads of a wind turbine. In that regard, the approach discussed herein can be easily extrapolated to these non-stationary cases, or even from diverse phenomena, if adequate criteria are applied. That is, non-stationary processes are commonly represented analytically either by the addition of a time-varying mean and a fluctuating component or by the product of a time-varying variance and a fluctuating non-dimensional component. For example, some applications of these criteria have been published in the literature for environmental phenomena.<sup>42,43</sup> In this regard, it is often the case that the fluctuating part is the one simulated stochastically, usually by any of the approaches mentioned in this chapter.<sup>35,40</sup> Insofar as these parts of the process show concordance in their amplitude among the original case and its replica, it could be expected the process to be fairly represented. This can be pursued by means of the approaches discussed in this chapter. Unfortunately, the exploration of non-stationary cases falls out of the temporal frame of the present study.
- The spectral amplitude distortion observed from the replicated processes by means of the non-parametric transformation criterion presented in this chapter is rather minimal. However, an iterative algorithm can be implemented where the simulated signal is scaled until an acceptable difference is observed between the spectral density of the simulated process and its original. Iterative criteria for such cases have been proposed in the literature.<sup>44</sup>
- Among the discussed advantages of the reduced-order structural analysis detailed in this chapter, it is worth underlining that it avails of the lack of correlation among the loads in- or around- a particular axis and their orthogonal counterparts. That is, inasmuch as there is no correlation between the resulting forces on the wind turbine rotor in the  $x$ -direction and those in the  $y$ -direction, two independent stochastic simulations can be performed to represent these loads, without the need of defining a cross-spectrum matrix for the processes. Furthermore, this advantage is also supported by the fact that the forces in the  $x$ -direction and the moments around the  $x$ -axis displayed nearly-perfect correlation, and this is analogous to the forces along- and around- the  $y$ -axis.
- Notwithstanding the advantages commented in the previous lines, the reduced-order structural model was found to be highly dependent on the coupled terms and the values of aeroelastic damping. This is appreciated in the spectral densities of structural response estimated from the simplified model, where absent features of the spectral density of response are indeed observed in the full-model results, such features are proper from coupled degrees of freedom discarded in the simplified analysis. Nevertheless, if a more sophisticated method for the identification of the aeroelastic damping is employed, a better estimation of the structural response is expected from the reduced-order model. This assertion is justified in the similitudes observed in the tendencies of the maxima of the structural displacements.
- The formulation on which the reduced-order model was deduced is based on the responses at the top of the tower, furthermore under the assumption that the first bending mode of this element dominates the structural response. Based on these premises, in this chapter, it is mentioned that structural responses at intermediate heights (i.e., at locations between the tower base and the nacelle) can be approximated assuming that the structure behaves as an Euler-Bernoulli cantilevered beam. Although this hypothesis is shown to provide adequate results for the tower-top responses, it remains to be validated for structural responses at intermediate heights. However, regardless of the adequateness of such a hypothesis, load or response signals can be obtained from an elaborate structural model, and similar approaches to the ones covered in Subsection 6.5.3 can thus be applied to such signals, in case that information from intermediate points is needed for analysis.

- The fatigue damage evaluation performed from the simulated signals provided results rather conservative. This fact is preferable when evaluating a method for preliminary analyses. Notwithstanding, the overprediction of fatigue damage from the simplified approach has been attributed to the loss of information at high frequencies in the spectral density of stresses.

## References

1. Isyumov, N. Alan G. Davenport's mark on wind engineering. *Journal of Wind Engineering and Industrial Aerodynamics* **104–106**, 12–24 (2012). doi: 10.1016/j.jweia.2012.02.007.
2. Davenport, A. G. Past, present and future of wind engineering. *Journal of Wind Engineering and Industrial Aerodynamics* **90**, 1371–1380 (2002). doi: 10.1016/S0167-6105(02)00383-5.
3. Toft, H. S., Svenningsen, L., Sørensen, J. D., Moser, W. & Thøgersen, M. L. Uncertainty in wind climate parameters and their influence on wind turbine fatigue loads. *Renewable Energy* **90**, 352–361 (2016). doi: 10.1016/j.renene.2016.01.010.
4. Dimitrov, N., Kelly, M. C., Vignaroli, A. & Berg, J. From wind to loads: wind turbine site-specific load estimation with surrogate models trained on high-fidelity load databases. *Wind Energy Science* **3**, 767–790 (2018). doi: 10.5194/wes-3-767-2018.
5. Bitner-Gregersen, E. M., Ewans, K. C. & Johnson, M. C. Some uncertainties associated with wind and wave description and their importance for engineering applications. *Ocean Engineering* **86**, 11–25 (2014). doi: 10.1016/j.oceaneng.2014.05.002.
6. Frandsen, S. *Turbulence and turbulence-generated structural loading in wind turbine clusters* English. PhD thesis (Technical University of Denmark, 2007). ISBN: 87-550-3458-6. Risø-R-1188(EN).
7. Slot, R. M., Sørensen, J. D., Sudret, B., Svenningsen, L. & Thøgersen, M. L. Surrogate model uncertainty in wind turbine reliability assessment. *Renewable Energy* **151**, 1150–1162 (2020). doi: 10.1016/j.renene.2019.11.101.
8. Chen, B. *et al.* Online DWT algorithm for identification of aerodynamic damping in wind turbines. *Mechanical Systems and Signal Processing* **152**, 107437 (2021). doi: 10.1016/j.ymsp.2020.107437.
9. Ozbek, M. & Rixen, D. J. Operational modal analysis of a 2.5 MW wind turbine using optical measurement techniques and strain gauges. *Wind Energy* **16**, 367–381 (2012). doi: 10.1002/we.1493.
10. Ozbek, M., Meng, F. & Rixen, D. J. Challenges in testing and monitoring the in-operation vibration characteristics of wind turbines. *Mechanical Systems and Signal Processing* **41**, 649–666 (2013). doi: 10.1016/j.ymsp.2013.07.023.
11. Damgaard, M., Ibsen, L. B., Andersen, L. V. & Andersen, J. K. F. Cross-wind modal properties of offshore wind turbines identified by full scale testing. *Journal of Wind Engineering and Industrial Aerodynamics* **116**, 94–108 (2013). doi: 10.1016/j.jweia.2013.03.003.
12. Koukoura, C., Natarajan, A. & Vesth, A. Identification of support structure damping of a full scale offshore wind turbine in normal operation. *Renewable Energy* **81**, 882–895 (2015). doi: 10.1016/j.renene.2015.03.079.
13. Valamanesh, V. & Myers, A. T. Aerodynamic damping and seismic response of horizontal axis wind turbine towers. *Journal of Structural Engineering* **140**, 04014090 (2014). doi: 10.1061/(ASCE)ST.1943-541X.0001018.
14. Chen, C., Duffour, P. & Fromme, P. Modelling wind turbine tower-rotor interaction through an aerodynamic damping matrix. *Journal of Sound and Vibration* **489**, 115667 (2020). doi: 10.1016/j.jsv.2020.115667.
15. Chen, B., Zhang, Z., Hua, X., Basu, B. & Nielsen, S. R. K. Identification of aerodynamic damping in wind turbines using time-frequency analysis. *Mechanical Systems and Signal Processing* **91**, 198–214 (2017). doi: 10.1016/j.ymsp.2017.01.010.



16. Ortegon, K., Nies, L. F. & Sutherland, J. W. Preparing for end of service life of wind turbines. *Journal of Cleaner Production* **39**, 191–199 (2013). doi: 10.1016/j.jclepro.2012.08.022.
17. Li, S. & Caracoglia, L. Surrogate Model Monte Carlo simulation for stochastic flutter analysis of wind turbine blades. *Journal of Wind Engineering and Industrial Aerodynamics* **188**, 43–60 (2019). doi: 10.1016/j.jweia.2019.02.004.
18. Morató, A., Sriramula, S. & Krishnan, N. Kriging models for aero-elastic simulations and reliability analysis of offshore wind turbine support structures. *Ships and Offshore Structures* **14**, 545–558 (2019). doi: 10.1080/17445302.2018.1522738.
19. Li, X. & Zhang, W. Long-term fatigue damage assessment for a floating offshore wind turbine under realistic environmental conditions. *Renewable Energy* **159**, 570–584 (2020). doi: 10.1016/j.renene.2020.06.043.
20. Wilkie, D. & Galasso, C. Gaussian process regression for fatigue reliability analysis of offshore wind turbines. *Structural Safety* **88**, 102020 (2021). doi: 10.1016/j.strusafe.2020.102020.
21. Rubert, T., McMillan, D. & Niewczas, P. A decision support tool to assist with lifetime extension of wind turbines. *Renewable Energy* **120**, 423–433 (2018). doi: 10.1016/j.renene.2017.12.064.
22. Beganovic, N. & Söffker, D. Structural health management utilization for lifetime prognosis and advanced control strategy deployment of wind turbines: An overview and outlook concerning actual methods, tools, and obtained results. *Renewable and Sustainable Energy Reviews* **64**, 68–83 (2016). doi: 10.1016/j.rser.2016.05.083.
23. Loraux, C. & Brühwiler, E. *The use of long term monitoring data for the extension of the service duration of existing wind turbine support structures* in *Journal of Physics: Conference Series* **753** (2016), 072023. doi: 10.1088/1742-6596/753/7/072023.
24. Rubert, T. *et al.* Wind turbine lifetime extension decision-making based on structural health monitoring. *Renewable Energy* **143**, 611–621 (2019). doi: 10.1016/j.renene.2019.05.034.
25. IEC. *Wind turbines – Part 1: Design requirements* 3rd ed. International Electrotechnical Commission (Geneva, Switzerland, 2005).
26. ASTM. *Standard practices for cycle counting in fatigue analysis* tech. rep. E1049-85(2011) (American Society for Testing and Materials, 2011).
27. Nielsen, M. *et al.* *Wind Simulation for Extreme and Fatigue Loads* English. Denmark. Forskningscenter Risoe. *Risoe-R* **1437(EN)**. ISBN: 87-550-3281-8 (2003).
28. Grigoriu, M. Crossings of non-Gaussian translation processes. *Journal of Engineering Mechanics* **110**, 610–620 (1984). doi: 10.1061/(ASCE)0733-9399(1984)110:4(610).
29. Winterstein, S. R. Non-normal responses and fatigue damage. *Journal of Engineering Mechanics* **111**, 1291–1295 (1985). doi: 10.1061/(ASCE)0733-9399(1985)111:10(1291).
30. Winterstein, S. R. Nonlinear vibration models for extremes and fatigue. *Journal of Engineering Mechanics* **114**, 1772–1790 (1988). doi: 10.1061/(ASCE)0733-9399(1988)114:10(1772).
31. Winterstein, S. R. & Kashef, T. Moment-based load and response models with wind engineering applications. *J. Sol. Energy Eng.* **122**, 122–128 (2000). doi: 10.1115/1.1288028.
32. Ding, J. & Xinzhong, C. Moment-based translation model for hardening non-Gaussian response processes. *Journal of Engineering Mechanics* **142**, 06015006 (2016). doi: 10.1061/(ASCE)EM.1943-7889.0000986.
33. Jonkman, J. M. & Buhl Jr., M. L. *FAST User's Guide* National Renewable Energy Laboratory (Golden, Colorado, 2005). NREL/EL-500-29798.
34. Jonkman, J., Butterfield, S., Musial, W. & Scott, G. *Definition of a 5-MW Reference Wind Turbine for Offshore System Development* tech. rep. NREL/TP-500-38060 (National Renewable Energy Laboratory, Golden, USA, Feb. 2009).

35. Shinozuka, M. & Deodatis, G. Simulation of Stochastic Processes by Spectral Representation. *Applied Mechanics Reviews* **44**, 191–204 (1991). doi: 10.1115/1.3119501.
36. Rao, S. S. *Mechanical Vibrations* 5th (Pearson, 2012).
37. Chopra, A. K. *Dynamics of Structures: Theory and Applications of Earthquake Engineering* 4th ed. (ed Hall, W. J.) (Prentice Hall, 2011).
38. Crandall, S. H. & Mark, W. D. *Random Vibration in Mechanical Systems* (Academic Press, 1963).
39. Kooijman, H. J. T., Lindenburg, C., Winkelaar, D. & van der Hooft, E. L. *DOWEC 6 MW Pre-Design: Aero-elastic modeling of the DOWEC 6 MW pre-design in PHATAS* tech. rep. (Energy Research Center of the Netherlands, 2003).
40. Samaras, E., Shinozuka, M. & Tsurui, A. ARMA representation of random processes. *Journal of Engineering Mechanics* **111**, 449–461 (1985). doi: 10.1061/(ASCE)0733-9399(1985)111:3(449).
41. Xiong, J. & Shenoi, R. A load history generation approach for full-scale accelerated fatigue tests. *Engineering Fracture Mechanics* **75**, 3226–3243 (2008). doi: 10.1016/j.engfracmech.2007.12.004.
42. Hong, H. P. Modeling of nonstationary winds and its applications. *Journal of Engineering Mechanics* **142**, 04016004 (2016). doi: 10.1061/(ASCE)EM.1943-7889.0001047.
43. Huang, P., Xie, W. & Gu, M. A comparative study of the wind characteristics of three typhoons based on stationary and nonstationary models. *Natural Hazards* **101**, 785–815 (2020). doi: 10.1007/s11069-020-03894-0.
44. Yamazaki, F. & Shinozuka, M. Digital generation of non-Gaussian stochastic fields. *Journal of Engineering Mechanics* **114**, 1183–1197 (1988). doi: 10.1061/(ASCE)0733-9399(1988)114:7(1183).

## Chapter 7

### Concluding remarks

As long as humankind populates the earth, the role of wind phenomena in the atmosphere will remain a primary subject of interest. From heat and momentum exchange of small scales near the surface of the earth to large circulation systems in the atmosphere, the wind is fundamental for the development of the energy cycle on the planet. The movement of wind currents originates from the solar radiation intercepted in the atmosphere, where complex thermodynamic and mechanical processes occur. Today, an extensive debate revolves around the effects of greenhouse gases on atmospheric phenomena, which has motivated the search for alternative sources of energy that avail of renewable resources for the sake of lowering the emissions of CO<sub>2</sub> towards the atmosphere. Wind energy has become one of the principal actors in pursuing this goal, and it is one of the main contributors to the energy schemes adopted by many nations. This fact has aroused the growth of theoretical and technical advancements for optimal wind resource harnessing. Notwithstanding the technological development that wind energy has experienced due to its current role in energy production, its reliable deployment still represents a significant effort for scientific and engineering disciplines.

As wind turbines increase in size to achieve more energy extraction from the wind flowing in the atmosphere, the analysis and fabrication of the elements composing these structures require more detail. This tendency toward enlarged elements demands their study in facilities that are non-ubiquitous, as well as a higher cost of manufacturing and testing. In that regard, finite element analysis of structural elements has become a reliable approach for mechanical analyses. Notwithstanding, recent studies centered on the context of wind power plants also rely upon numerical analysis to study the ambient conditions within wind farms. These are motivated by the interest in the adequate modeling of links between large, medium, and small-scale atmospheric wind flow from numerical and analytic approaches, as well as the interaction with the dynamic response of wind turbine components. All of these studies have been enabled by the growth of computational capabilities. The boundary layer flow field under extreme wind events, such as tropical cyclones, also has availed of such capabilities. However, many of the applications and analyses above-mentioned are still computationally expensive. Hence, the implementation of computationally economical solutions for wind turbine analysis is peremptory for wind energy development. This dissertation has dealt with some identified gaps on these subjects concerning structural engineering, fundamentally from a numerical standpoint — insofar as this is the more conventional manner to approach many wind-turbine-related issues.

This chapter summarizes the conclusions from the topics discussed in the dissertation. It also includes commentaries about the drawbacks observed from each of the methods and approaches explored in the thesis, as well as possible themes for future research. In concordance with the formatting adopted for the present document, the commentaries of each chapter are presented in individual sections.

## 7.1 Structural response of wind turbine support structures under tropical cyclones

Tropical cyclones are the phenomena that represent the largest yearly economic losses for many countries. They become even more relevant under the expectation of stronger future cyclones. Research related to their origins and development is overall conclusive in tendencies towards intensification of these phenomena in the upcoming years. Despite this fact, the provisions from applicable codes appear insufficient. For example, although the impact of tropical cyclones is of concern for many places in the world, international wind turbine standards are unintended for their actions. Recent research has centered on studying the wind-induced response of wind turbine structures under hurricanes and typhoons. Despite these valuable researches, disregard for the super-gradient wind that characterizes tropical cyclones is preponderant, and the studies that account for it are focused solely on offshore wind turbines. Concerning onshore wind energy, insofar as inland wind turbines still have great potential for wind energy development, adequate studies on their response to cyclone-induced loads are relevant. Moreover, although some literature and studies related to the mean wind-speed profile from tropical cyclones suggest that super-gradient-wind effects are irrelevant for low elevations, its differences concerning synoptic wind are consequential at typical wind-turbine heights, as seen in Chapter 3 from semi-empirical models that define the tropical-cyclone profile.

To contribute to filling the abovementioned gaps, the study performed in Chapter 3 analyzes the aeroelastic structural response of a wind turbine under cyclone-induced loads. These loads are presumably associated with tropical cyclones insofar as they come from models that describe the behavior of the different parameters that characterize the storm. Some of the deductions needed to apply the parameter models are part of the contributions from this work. Through these parameter models, the wind velocity profile concordant to tropical-cyclone observations was computed, assuming two hypothetical locations in Mexico, correspondent to sites with high wind potential. The hazard context of these sites suggests that the wind speed intensities for a 200-year return period (as indicated in current Mexican standards) correspond to hurricanes of Categories I and III. This assumption served the definition of parameters necessary for the evaluation of the wind-field models and the simulation of turbulent wind speed signals. Probability distribution proposals for such parameters have been introduced in this work also. The spectral representation method served the simulation of wind-speed signals, which accounted for stationary-flow assumptions. Regarding these simulations, modified turbulence spectra as proposed from numerical studies of the tropical-cyclone flow field were used, instead of the conventional expressions suggested in common wind engineering standards. The numerical analyses that originated these spectra are presumed to be concordant with observations from actual tropical cyclones.

The three-dimensional turbulent wind velocity simulations were used to perform time-history analyses on a finite-element model of a reference wind turbine. The numerical model of the structure considered the effects of aeroelasticity under quasi-steady assumptions. A methodology to account for the aeroelastic effects on numerical models is part of the contributions of this work. Among the relevant findings from the results is that the fluid-structure interaction for the considered flow incidence appears inconsequential in terms of the spectral amplitudes of the structural response. However, the differences observed between analyses that consider the aeroelastic effects and those which disregarded them were statistically significant. These differences implied underestimation of the structural response in the along-wind direction, and overestimation in the across-wind response, from the analyses that disregarded aeroelastic effects. Another observation from the analysis results is that, for the assumed flow conditions, the peak factor proposed in conventional wind-engineering standards is adequate for uni-directional estimation of the maximum response, whereas it underestimates the maximum combined response. That is, owing to the noticeable dynamic symmetry of the structure in the defined two main axes, the maximum combined response exceeds the values predicted by conventional formulae, whereas the maximum structural response in the along-wind direction is estimated conservatively well from the well-known expressions. A simple equation for the peak factor of the combined response is included in this work.

Possible future refinement of the analyses performed in Chapter 3 includes the following observations: (i) Validation of independence assumptions of the storm parameters employed for the flow-field simulations is still required. That is, although the probability-distribution parameters of those that describe the storm were based on data from published literature, they were premised as mutually independent. This assumption can be validated or discarded from databases of measured tropical-cyclone data. (ii) The analyses were performed considering only a single direction of flow incidence. This was done assuming that the yawing system of the turbine remained in operation during the storm. However, a literature review of studies concerning cyclone-affected turbines indicates that such a hypothesis represents an idealized scenario insofar as malfunctions in the operating systems of the turbine are common during hurricane occurrence. Further research would need to consider a plausible misalignment between the rotor axis and the prevailing wind direction. (iii) The turbulent wind-speed signals were assumed as stationary processes. Recent literature has studied the non-stationary nature of tropical-cyclone winds. Hence, the effects of non-stationary cyclone-induced loads on wind turbine structures remain a task for future studies. (iv) The structural responses were computed from the assumption of linear-elastic behavior of the structural elements. However, the approach employed in Chapter 3 can be applied considering the material non-linearities of the structural elements in the model. This implies adequate modeling of the non-linear behavior and failure mechanism of the elements of the structure.

## 7.2 Fragility evaluation of representative wind turbines under cyclone hazard

Mexico is a country with a vast catalog of natural hazards, which include tropical cyclones. Hurricanes make landfall in the country every year from the Atlantic as well as from the Pacific Oceans. Notwithstanding, it is also a country with high wind potential. However, after nearly three decades since the first built wind farm in Mexico, there is still a long way to advance toward the availability of the inland wind resource. Nowadays, the totality of the electricity produced from wind resources in the country comes from land-based wind turbines. Considering that most of the wind turbines installed in Mexico are structures of medium size, they are vulnerable to wind-induced loads (as well as earthquakes — if their fundamental period of vibration is ‘short’). However, wind hazard is of more serious concern due to the evident wind sensibility of these structures. Existing wind turbine projects (as well as future ones) must be provided with hazard information for their viability evaluation. Hence, the assessment of structural vulnerability from the turbines currently installed in Mexican soil is preemptory, and thus, a premier step for this purpose is the definition of the probability of damage on each particular structure.

Three hypothetical wind turbines premised as representatives of those installed — or to be installed — in Mexico were defined in Chapter 4 for their analysis under cyclone-induced aerodynamic loads. The dimension proposals for the turbines were guided by the statistics of currently installed turbines in Mexico, and the primary elements that govern the structural behavior of the turbine were dimensioned aided by reference models derived from statistics of actual wind turbines. Although a formal design protocol was omitted for the definition of the three turbine structures, their structural properties agree with tendencies displayed from reference wind turbines found in the literature. The evaluation of the structural reliability of the three structures accounted for three performance levels. Each of these levels is associated with different damage states of the structure. Furthermore, similarly to the procedures adopted in Chapter 3, time-history analyses of the three turbines were performed howbeit for different wind speed intensity levels rather than a single one.

The values of maximum structural response associated with each wind intensity, according to their respective damage states, were fitted to different probability distributions. From the probability distributions evaluated to represent the structural response maxima, the Generalized Extreme Value distribution exhibited the closest resemblance, while the Lognormal distribution also displayed a fair

representation of the structural response maxima. Fragility functions were fitted to these estimated values of damage probability for the three structures and the three damage states. The parameters that define these fragility functions from the two forenamed probability distributions are reported in Chapter 4. Considerable differences are noticeable in the fragility estimated from the Generalized Extreme Value and Lognormal distributions for the highest turbines, aside from the resemblant fits displayed by both distributions to the response data. Overall, the Lognormal distribution led to the lower values of fragility estimates for the three structures and their three evaluated damage states.

It was demonstrated inferentially that the analyzed models adequately represent the structural characteristics of actual turbines, regardless of the fact that the definition of the structures came from no detailed design. Concerning the analyses performed on the three turbines, these disregarded the aeroelastic effects due to the fluid-structure interaction for the sake of computing-time economy. They differ from the criterion adopted for the analyses described in Chapter 3, which accounted for the fluid-structure interaction effects. On the other hand, a similitude between the analysis criteria adopted in Chapters 3 and 4 is the angle of flow incidence on the structures, which is assumed non-varying and aligned with the rotor axis of the turbines. Notwithstanding these shortcomings, more exquisite analyses of these turbines were disregarded due to the numerous hypotheses considered in their definition.

### 7.3 Reliability enhancement of wind turbine support structures by passive damping devices

In this dissertation, it was emphasized that the support structures of modern wind turbines are flexible elements dominated by their first mode of vibration. This mode corresponds to the bending of the tower, resembling a cantilevered beam, and its participation with respect to others may even differ by orders of magnitude. This behavior is suitable for tuned mass dampers (TMDs) implementation on the support structure for response control. The employment of TMDs on wind turbines is no novelty. Several studies in the literature centered on evaluating the structural response of wind turbine components fitted with TMDs, preponderantly from numerical analyses. As a matter of fact, commonplace codes for wind turbine analysis already count with modules for including passive, semi-active, and active TMDs in the structure. Virtually all the recent research that has covered the topic of TMD implementation in wind turbines has centered on wind-speed intensities within operation ranges. Withal, only a minute fraction of forenamed studies have approached the response-enhancement evaluation from a probabilistic standpoint. Of these few studies, none have researched cyclone-induced actions on wind turbine structures. Hence, contributions to fill this gap have been discussed in Chapter 5.

The finite element models elaborated to analyze the three wind turbines described in Chapter 4 were used to study their structural response when fitted with TMDs. In this regard, a single TMD located at the nacelle of each wind turbine was assumed. An early approximation of the optimal TMD parameters was performed from harmonic analyses on each of the three structures. This criterion was reported by no other reference in the literature surveyed for this study. Results from these analyses served to identify the parametric combinations that displayed the lowest values of structural response amplitudes, measured at the top of the towers of the three turbines. Subsequently, time-history structural analyses were performed on the turbines fitted with TMDs, considering the identified combinations of parameters that produce the lowest response. The load signals computed for the studies in Chapter 4 were also applied to the structures with TMDs.

The maxima of the responses used to measure the damage states defined for the fragility analyses, as in Chapter 4, were obtained from the time-history analyses. Regression models established to represent the median of these maxima were defined. These models include coefficients related to wind intensity and the TMD parameters. No other reference in the literature surveyed for this study reported similar criteria. The relevance of the regression models stands in the definition of the mean and standard deviation of the limit-state function related to each damage state. After their estab-

lishment, fragility comparisons were performed between the estimated values corresponding to the undamped structures and those considering the inclusion of a TMD. Results from these comparisons denote that the failure probability is reduced by nearly 80% for some ranges of wind intensity (for the conditions assumed in the analyses). These ranges varied depending on the damage state under evaluation and the studied wind turbine structure. In this regard, the maximum reduction achieved by installing TMDs on the wind turbines appears to locate at lower wind intensities for the less rigid structures. The fragility results of the three turbines served a subsequent prompt evaluation of risk reduction achieved by installing the passive-damping devices. The hazard curve employed for such an evaluation corresponds to the state of Oaxaca (Mexico) and is concurring to published studies. The structural risk evaluation indicates that installing TMDs — with the assumed characteristics and in wind turbines such as those studied herein — reduces the annual failure rate on average 2.5 times compared to the rate for cases without TMDs.

The analyses performed in Chapter 5 derived from the aerodynamic loads and models employed in other chapters. Subsequently, they also share some of their limitations. Considering a single wind-incidence angle in the structural analyses is one of such limitations. Apart from these drawbacks, some criteria from the study can improve with further research. For example, as in most numerical models of actual structures, a rigid support is a mere idealization to simplify the analysis and identify structural particularities. In this regard, some of the studies surveyed in Chapter 5 are emphatic about the uncertain nature of the dynamic characteristics of structures. Such uncertain behavior has its origin in foundation flexibility as well as in the variability of the material properties. Such phenomena imply that the TMD can suffer mistuning, which entails that the control of the structural response can diminish or even induce greater loads on the structure. Elaboration on these implications can also be performed from the bases that Chapter 5 defines. Aside from that, the methodology and results described in Chapter 5 are applicable to further research topics. For example, the optimization of the response-enhancing systems can avail of those results. That is, the maximum reduction of fragility can be sought to occur at load intensities concordant to a predefined return period. However, further and more elaborate considerations have to be defined for such studies.

## 7.4 Simplified structural analyses for reliability evaluation

Loads on operating wind turbines are of great interest for structural engineering because these govern the fatigue damage on the structure. Notwithstanding, due to the random nature of wind and the variable operation conditions of wind turbines, these loads are uncertain to a great degree. A way to approach this problem is to rely on massive databases where as-many-as-possible loading combinations of the turbine are analyzed. However, the conformation of these databases is highly demanding computationally. For this reason, state-of-the-art approaches are heading towards using non-parametric surrogate models. These are possible only with the aid of computational power. However, despite the practicality of commonplace codes for wind turbine analyses, the conformation of the databases for surrogate models still demands high computational expenses. Chapter 6 explored alternatives to contribute to the reduction of computational costs for the elaboration of surrogate models and related analyses.

In Chapter 6, a simplified method to cater to databases of structural responses in a computationally economical manner has been explored. The methodology relies fundamentally upon the transformation of stochastic processes. This transformation is of great relevance since the load characteristics on the wind turbine structure diverge considerably from Gaussianity, a fact evinced in the distortion of their probability distribution at its tails. Two popular methods to perform such a transformation are summarized. The methods are based on the statistical moments of an original sample. Also, a non-parametric transformation criterion is presented, which avails of the large sample sizes that constitute aerodynamic load signals and their empirical cumulative distribution function. No other reference in the extensive literature survey conducted for the studies described in Chapter 6 presents such a non-parametric criterion. In the same chapter, a reduced-order structural model is deduced

for estimating the response from the wind-turbine support structure, and an algorithm for the simulation of stress signals for fatigue-damage evaluation is described. Such an algorithm is another contribution from the present dissertation. All these concepts are tested for validation in a numerical example performed from the reference wind turbine described and analyzed in Chapter 3.

For this example, nine different environmental conditions were analyzed, which resulted from the combination of three wind-speed and three turbulence intensities. Since these combinations correspond to several states of wind turbine operation, they successfully describe the behavior of the wind turbine under analysis. Seed and control samples were defined from results computed from a noted code for wind turbine analysis. Such clusters determined the statistical and spectral characteristics of the aerodynamic loads on the structure. From the statistical moments and spectral densities, equivalent load signals were simulated and applied to the reduced-order model. Thus structural responses from such a model were computed. Results indicate that the structural-response tendencies displayed by the simplified model resemble the ones from the complete one. Such a resemblance is noticeable in the amplitudes of the response PSDFs and the response-amplitude maxima. Regardless of such similarities, the accuracy of the results from the reduced-order structural model exhibited to be coupling-dependent. That is to say, the coupling magnitude between the considered degrees of freedom needs to be determined with great precision. In the studies from Chapter 6, a misestimation of coupling is attributed to the shortcomings of the method selected for aeroelastic damping identification. However, more resemblance between the results from both models is expected if a more sophisticated damping-identification technique is used.

Concerning the simulation of signals for fatigue damage analyses, they can replicate with satisfactory quality the spectral characteristics of the originals. Several similitudes between the rain-flow histograms derived from both groups of signals are also evident. However, the replicas tend to overestimate the fatigue damage. In this work, such an overestimation is attributed to high-frequency information losses from the replicated signal. These losses are also related to the stochastic-simulation method employed in the study. Regardless of these issues, the stress overestimation implies conservative fatigue damage evaluations from signals replicated with the proposed criteria. Conservative fatigue estimates are preferable insofar as the method is intended for preliminary and prompt analyses, as commented in Chapter 6. Regarding the scattering of the results from the simplified fatigue damage estimation, these displayed more spread dispersion. However, the simplified results followed the same tendencies shown by conventional analyses.

As commented in Chapter 6, results from the covered cases are intended for idealized scenarios of wind turbine operation. Actual operation conditions, however, might imply different characteristics than the ones analyzed. For example, non-stationary aerodynamic loads on the rotor due to pitch-angle variation or wind direction misalignment. Notwithstanding, the discussed methods can adjust to account for other stochastic characteristics, such as non-stationariness. Moreover, the non-parametrically transformed processes displayed a minimal distortion of the spectral amplitudes at some frequency ranges. However, this was observed only in the spectra that exhibited higher energy contributions at low frequencies. A possible cause of this effect can be the loss of information at high frequencies in the simulated signals. Algorithms that are of application to overcome this situation can be found in the literature forenamed in Chapter 6. Concerning the reduced-order structural model, one of its drawbacks is the necessity of precise identification of coupled terms, specifically aeroelastic damping terms. As commented previously, better results are expected if more sophisticated methods for damping identification are used. Lastly, the methodology defined for the simulation of fatigue-equivalent stress signals is unexclusive for wind turbine support structures. That is, it is also applicable to a wide variety of problems in engineering since it relies on spectral and statistical characteristics of an original stress signal.



## Appendix A

# Commentaries on Chapter 3 with possible applications to standards and practice

Conventional wind turbine standards cover a variety of plausible load combinations during the normal operation of the turbine. Regarding extreme wind intensities, such as those correspondent to tropical cyclones, in said standards for onshore structures, it is explicitly stated that they are unintended for tropical cyclone conditions. For such cases, the turbine must be designed as a special classification, under different considerations to those provided for standard turbines. Later standards, intended for offshore turbines, provide a slightly more ample definition of the wind environment during tropical cyclones. These criteria rely fundamentally upon the modeling of the wind field during the tropical cyclone from noted models for the surface pressure during the storm. However, no further specifications are provided.

In the specific context of Mexico, the Manual of Civil Works of the Federal Electricity Commission (CFE, acronym in Spanish) defines that wind turbines installed in Mexico must be designed to withstand wind intensities correspondent to a 200-year return period. This reference states that the cases covered are unintended for operation conditions, but rather for extreme wind speeds. The wind speeds provided by CFE are correspondent to wind statistics from onshore sites. Notwithstanding, for some regions in Mexico, these values correspond to wind intensities of the order of those measured in tropical cyclones.

### A.1 Commentaries about the mean-speed profile

Virtually all the wind engineering references that regard high wind speeds indicate the use of either the logarithmic or the power-law mean-speed profiles. As commented in Chapter 2, this description is adequate for many cases of interest for structural engineering concerning synoptic wind. However, the analyses carried out in Chapter 3, which have been derived from semi-empirical models as well as from the numerical solution of the cyclonic flow field, account for the occurrence of higher wind speeds due to the presence of super-gradient winds. These are observed at high elevations and it indicates that, despite the similarities among the values of mean wind speed observed at near-10-m heights, the difference between the two profiles becomes considerably significant at greater altitudes.

The results from Chapter 3 indicate that the support structure of a typical land-based wind turbine, such as the one analyzed in the aforementioned chapter, can sustain Category-I hurricane winds with a conservative reliability criterion, such as the one suggested by the CFE. Notwithstanding, greater hurricane categories might demand more robust designs, which underlines the need for a criterion for the definition of the wind intensities acting on the structure. In this dissertation, an approach to perform structural analyses at diverse intensities has been presented.

Simulation of the flow field concordant to tropical cyclones is of practical implementation as performed in the study of Chapter 3. This approach relies on the Monte Carlo simulation of storm parameters and their evaluation from notable models reported in the literature. For that purpose, the following algorithm can be followed:

- (i) Simulate values of the central pressure deficit ( $\Delta p_s$ ) of the storm for the Saffir-Simpson category concordant to the return period and wind speed of interest. See Table 3.1.
- (ii) With the values obtained in the previous step, simulate (or evaluate) the radius of maximum winds ( $r_{vm}$ ) from a developed model, or a model reported in the literature. In the presented studies, the one from Equation 3.12 was employed.
- (iii) Simulate (or evaluate) the Holland's  $b$  parameter from a selected model. In the studies developed herein, Equation 3.11 was used.
- (iv) With the values obtained from Steps (ii) and (iii), evaluate the surface pressure derivatives (Equations 3.9 and 3.10).
- (v) Estimate the gradient wind and its derivative (Equations 3.6 and 3.7).
- (vi) For the latitude of the site of interest ( $\phi$ ), estimate the Coriolis Parameter  $f_c$  (defined as  $2\omega \sin \phi$ ).
- (vii) Estimate the inertial instability ( $I$ ) and the modified Rossby number ( $Ro_s$ ) according to Equations 3.4 and 3.5.
- (viii) Estimate the mean-speed profile (in Chapter 3, the model reported in the literature as summarized in Equations 3.1 to 3.3 was employed).
- (ix) Perform the stochastic flow-field simulation accounting for the obtained wind profile and a selected turbulence model. In this dissertation, the spectral densities as summarized in Subsection 3.2.2 were employed.

The previous list summarizes the steps followed to perform the flow-field simulations as employed in this dissertation. However, concerning the evaluation of structural reliability, the different standards accounted for in this work pose different criteria. For example, the criteria defined in the documents by the International Electrotechnical Commission (IEC), a return period of 50 years is defined for the extreme turbulence model, whereas the Mexican CFE states one of 200 years. The evaluation carried out in Chapter 3 accounts for the specifications of the latter, however, the approach can be implemented as easily for a different criterion.

## A.2 Commentaries about the peak factor

Slender structures with dynamic symmetry in their two major axes might display the greatest amplitude displacement in neither of the directions of these axes. The greater structural-response amplitude is governed by the Euclidean norm of the response components in the along- and across-wind directions. In conventional wind engineering problems, the assumption of the structural responses in these directions to be Gaussian-distributed might be valid. If such responses are treated as independent, the probability distribution of the resulting response would tend to be represented by a Rayleigh distribution. Nevertheless, due to the interaction of the different components of wind turbulence in a three-dimensional flow, as well as to the aerodynamic particularities of a structure, the components of structural response in the along- and across-wind directions display a certain degree of correlation. The presence of this correlation complicates the analytic deduction of a peak factor to be applied to structures with symmetric behavior.

As discussed in Chapter 3, the structural responses in the two major axes for the analyzed case are rather non-Gaussian. However, conventional expressions for the estimation of the peak factor ( $k_p$ ) proved to be adequate (and conservative to a certain degree) for their individual analysis. In the forenamed chapter, an intuitive approximation for the peak factor from the resulting response was suggested. However, a more elaborate analysis is required to provide a more sustained expression.

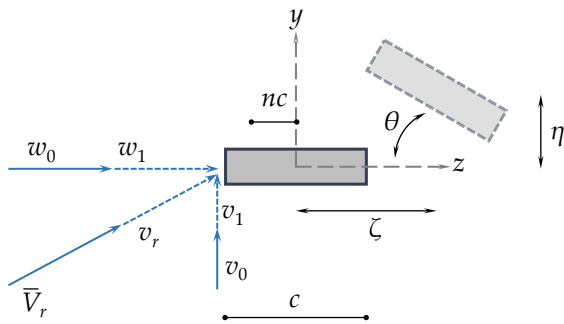
## Appendix B

# Quasi-steady aeroelastic terms

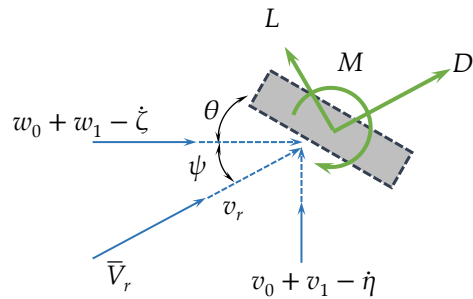
This appendix describes the assumptions for the quasi-steady derivation of the fluid damping and fluid rigidity matrices, as applied in some of the case studies explained in this dissertation. Moreover, the implementation of these deductions in the FEA software APDL is also summarized.

### B.1 Fluid damping and rigidity matrices

Consider a flow-excited bar-like structural element with a cross-section that can be modeled as a 3-DOF system as the one displayed in Figure B.1(a). The flow-induced forces on the element produce structural responses which can alter the pressure distribution on its section and, consequently, the resultant forces. In Figure B.1(a) the quasi-static components of velocity in the  $y$ - and  $z$ -directions are denoted as  $v_0$  and  $w_0$ , respectively. The quasi-static resultant velocity is denoted as  $\bar{V}_r$ , whereas its time-varying component is denoted as  $v_r$ . The time-varying components of wind velocity in the  $y$ - and  $z$ -directions are  $v_1$  and  $w_1$ , respectively. The aerodynamic center of the cross-section of the element is assumed to be located at a distance  $nc$  from the origin of the axes, where  $c$  represents the chord length (in the case of airfoils), or an equivalent characteristic length (in the case of other shapes). The structural displacements in the  $y$ - and  $z$ -directions are denoted as  $\eta$  and  $\zeta$ , respectively; whereas the structural rotation around the longitudinal axis of the element is represented as  $\theta$ .



(a) Fluid-induced response of a structural element



(b) Decomposition of fluid-induced forces on a structural element

**Figure B.1:** Fluid-induced forces on a structural element and responses

The structural response of the element can be of significance to the relative flow speed acting on it, as presented in Figure B.1(b). It can be seen in the figure that  $\dot{\eta}$  and  $\dot{\zeta}$  can imply lower or higher values of the resultant flow speed on the element. The incidence angle of the relative flow velocity on the element is denoted as  $\psi$ , whereas the flow forces are  $L$ ,  $D$ , and  $M$ , which are the flow-induced lift, drag, and moment, respectively. Moreover, from Figure B.1(b) two observations become pertinent:

(i) the angle of attack  $\alpha$  on the element is obtained from  $\theta + \psi$ , and (ii) it can be assumed that the quasi-static component of  $\psi$  (i.e.,  $\psi_0$ ) equals the quasi-static component of  $\alpha$ . The angle of attack  $\alpha$  can thus be expressed as:

$$\alpha = \arctan \left( \frac{v_0 + v_1 - \dot{\eta} - nc\dot{\theta}}{w_0 + w_1 - \dot{\zeta}} \right) + \theta \quad (\text{B.1})$$

The relative velocity  $V_r$  can be computed from the trigonometric relationship between the flow and response components from:

$$V_r = \sqrt{(v_0 + v_1 - \dot{\eta})^2 + (w_0 + w_1 - \dot{\zeta})^2} = \bar{V}_r + v_r \quad (\text{B.2})$$

Assuming that the products between time-varying components are considerably small, their contribution can be neglected and the relative velocity can be approximated as:

$$V_r^2 \approx v_0^2 + w_0^2 + 2(v_0v_1 + w_0w_1 - v_0\dot{\eta} - w_0\dot{\zeta}) \quad (\text{B.3})$$

Under the adopted criterion for the product of time-varying components, the mean resultant velocity can be expressed as  $\bar{V}_r^2 = v_0^2 + w_0^2$ , and the time-varying resultant velocity component can be estimated as:

$$v_r \approx \frac{v_0v_1 + w_0w_1 - v_0\dot{\eta} - w_0\dot{\zeta}}{\bar{V}_r} \quad (\text{B.4})$$

Based on these assumptions, the angle of attack can be linearly approximated from a first-order Taylor series around 0, leading to  $\alpha \approx \alpha_0 + \alpha_1$ , where an approximation to its time-varying component results as:

$$\alpha_1 \approx \frac{w_0v_1 - v_0w_1 + v_0\dot{\zeta} - w_0\dot{\eta} - ncw_0\dot{\theta}}{\bar{V}_r^2} + \theta \quad (\text{B.5})$$

### B.1.1 Equation of motion

The equation of motion of the 3-DOF system displayed in Figure B.1 can be written as:

$$\mathbf{M}_s \ddot{\mathbf{d}} + \mathbf{C}_s \dot{\mathbf{d}} + \mathbf{K}_s \mathbf{d} = \mathbf{f}_f \quad (\text{B.6})$$

where  $\mathbf{M}_s$ ,  $\mathbf{C}_s$ , and  $\mathbf{K}_s$  are the mass, damping, and stiffness matrices of the structural element, respectively. In Equation B.6,  $\mathbf{d}$  is a vector that contains the displacements in the  $y$ - and  $z$ -directions, as well as the rotation around the longitudinal axis of the element, and the dots denote time differentiation. On the right side of the equation appears  $\mathbf{f}_f$ , which is a vector containing the flow-induced forces.

As commented in this appendix, the flow-induced forces are dependent on the structural response. Moreover, they have been assumed to be decomposed into a quasi-static and a time-varying part. Thus, Equation B.6 can be rewritten as:

$$\mathbf{M}_s \ddot{\mathbf{d}} + \mathbf{C}_s \dot{\mathbf{d}} + \mathbf{K}_s \mathbf{d} = \bar{\mathbf{f}}_a + \mathbf{f}_a - \mathbf{M}_a \ddot{\mathbf{d}} - \mathbf{C}_a \dot{\mathbf{d}} - \mathbf{K}_a \mathbf{d} \quad (\text{B.7})$$

where sub-index  $a$  denotes the flow-induced quantities.  $\mathbf{M}_a$ ,  $\mathbf{C}_a$ , and  $\mathbf{K}_a$  are the fluid added mass, fluid damping, and fluid rigidity, respectively. These matrices can be moved to the left side of Equation B.6. It must be observed that the terms involving the forces of inertia from the fluid flowing have been disregarded in the graphic deductions presented so far, thus, the added mass can be omitted

in the remaining formulae. In Equation B.7, the vector  $\mathbf{f}_f$  has been separated into  $\mathbf{f}_f = \bar{\mathbf{f}}_a + \mathbf{f}_a + \mathbf{f}_s$ , where  $\bar{\mathbf{f}}_a$  and  $\mathbf{f}_a$  denote the quasi-static and time-varying fluid-flow forces, respectively, and the third term concerns the forces associated with the structural response  $\mathbf{d}$  and its derivatives.

The flow-induced forces  $L$ ,  $D$ , and  $M$ , as displayed in Figure B.1(b), can also be decomposed into a quasi-static and a time-varying component by a linearization analogous to the one described previously in this appendix for  $\alpha$ . That is, setting the lift force per unit length ( $L = 0.5\rho V_r^2 C_L(\alpha)c$ ) as an example, they can be expressed as:

$$L \approx L(\mathbf{0}) + v_1 \frac{\partial L(\mathbf{0})}{\partial v_1} + w_1 \frac{\partial L(\mathbf{0})}{\partial w_1} + \theta \frac{\partial L(\mathbf{0})}{\partial \theta} + \dot{\eta} \frac{\partial L(\mathbf{0})}{\partial \dot{\eta}} + \dot{\zeta} \frac{\partial L(\mathbf{0})}{\partial \dot{\zeta}} + \dot{\theta} \frac{\partial L(\mathbf{0})}{\partial \dot{\theta}} \quad (\text{B.8})$$

where  $\mathbf{0}$  is a vector with the values that define the point of linearization (i.e., around 0, in this case). According to the definition of the flow forces, and the assumptions deduced previously in this appendix, the partial derivatives in Equation B.8 can be defined. In the case of the lift force per unit length, these are expressed as:

$$\frac{\partial L(\mathbf{0})}{\partial v_1} = \rho c v_0 C_L(\alpha_0) + \frac{1}{2} \rho c w_0 \left. \frac{dC_L}{d\alpha} \right|_{\alpha_0} \quad (\text{B.9a})$$

$$\frac{\partial L(\mathbf{0})}{\partial w_1} = \rho c w_0 C_L(\alpha_0) - \frac{1}{2} \rho c v_0 \left. \frac{dC_L}{d\alpha} \right|_{\alpha_0} \quad (\text{B.9b})$$

$$\frac{\partial L(\mathbf{0})}{\partial \theta} = \frac{1}{2} \rho c \bar{V}_r^2 \left. \frac{dC_L}{d\alpha} \right|_{\alpha_0} \quad (\text{B.9c})$$

$$\frac{\partial L(\mathbf{0})}{\partial \dot{\eta}} = -\rho c v_0 C_L(\alpha_0) - \frac{1}{2} \rho c w_0 \left. \frac{dC_L}{d\alpha} \right|_{\alpha_0} \quad (\text{B.9d})$$

$$\frac{\partial L(\mathbf{0})}{\partial \dot{\zeta}} = -\rho c w_0 C_L(\alpha_0) + \frac{1}{2} \rho c v_0 \left. \frac{dC_L}{d\alpha} \right|_{\alpha_0} \quad (\text{B.9e})$$

$$\frac{\partial L(\mathbf{0})}{\partial \dot{\theta}} = -\frac{n\rho c^2 w_0}{2} \left. \frac{dC_L}{d\alpha} \right|_{\alpha_0} \quad (\text{B.9f})$$

This is analogous to the flow-induced drag and moment per unit length. Further, it must be noted that the terms associated with the structural responses in Equations B.8 and B.9 define the fluid damping and fluid rigidity in Equation B.7. Therefore, the fluid-flow forces per unit length, concerning only the terms where the structural responses are uninvolved, result in:

$$D \approx \frac{\rho c}{2} \bar{V}_r^2 C_D + C_D \rho c [v_0 v_1 + w_0 w_1] + \frac{\rho c}{2} \frac{dC_D}{d\alpha} [w_0 v_1 - v_0 w_1] \quad (\text{B.10})$$

$$L \approx \frac{\rho c}{2} \bar{V}_r^2 C_L + C_L \rho c [v_0 v_1 + w_0 w_1] + \frac{\rho c}{2} \frac{dC_L}{d\alpha} [w_0 v_1 - v_0 w_1] \quad (\text{B.11})$$

$$M \approx \frac{\rho c^2}{2} \bar{V}_r^2 C_M + C_M \rho c^2 [v_0 v_1 + w_0 w_1] + \frac{\rho c^2}{2} \frac{dC_M}{d\alpha} [w_0 v_1 - v_0 w_1] \quad (\text{B.12})$$

Thus, the first and second terms of  $\mathbf{f}_f$  can be expressed as:

$$\bar{\mathbf{f}}_a + \mathbf{f}_a = \begin{Bmatrix} F_y \\ F_z \\ F_\theta \end{Bmatrix} = \begin{bmatrix} \cos(\alpha_0) & \sin(\alpha_0) & 0 \\ -\sin(\alpha_0) & \cos(\alpha_0) & 0 \\ 0 & 0 & 1 \end{bmatrix} \begin{Bmatrix} L \\ D \\ M \end{Bmatrix} \quad (\text{B.13})$$

where  $L$ ,  $D$ , and  $M$  are computed from Equations B.10 to B.12. Whereas the fluid damping and fluid rigidity result in:

$$\mathbf{K}_a = \frac{\rho c \bar{V}_r^2}{2} \begin{bmatrix} \cos(\alpha_0) & \sin(\alpha_0) & 0 \\ -\sin(\alpha_0) & \cos(\alpha_0) & 0 \\ 0 & 0 & 1 \end{bmatrix} \begin{bmatrix} 0 & 0 & -\frac{dC_L}{d\alpha} \\ 0 & 0 & -\frac{dC_D}{d\alpha} \\ 0 & 0 & -c\frac{dC_M}{d\alpha} \end{bmatrix} \quad (\text{B.14})$$

$$\mathbf{C}_a = \rho c \begin{bmatrix} \cos(\alpha_0) & \sin(\alpha_0) & 0 \\ -\sin(\alpha_0) & \cos(\alpha_0) & 0 \\ 0 & 0 & 1 \end{bmatrix} \begin{bmatrix} C_L v_0 + \frac{w_0}{2} \frac{dC_L}{d\alpha} & C_L w_0 - \frac{v_0}{2} \frac{dC_L}{d\alpha} & \frac{ncw_0}{2} \frac{dC_L}{d\alpha} \\ C_D v_0 + \frac{w_0}{2} \frac{dC_D}{d\alpha} & C_D w_0 - \frac{v_0}{2} \frac{dC_D}{d\alpha} & \frac{ncw_0}{2} \frac{dC_D}{d\alpha} \\ cC_M v_0 + c\frac{w_0}{2} \frac{dC_M}{d\alpha} & cC_M w_0 - c\frac{v_0}{2} \frac{dC_M}{d\alpha} & \frac{nc^2 w_0}{2} \frac{dC_M}{d\alpha} \end{bmatrix} \quad (\text{B.15})$$

## B.2 Implementation in FEA

The deductions presented above can be implemented in ANSYS employing the element MATRIX27. MATRIX27 is an arbitrary element that can be used to modify the elastic stiffness, damping, or mass properties of a FEM. The element accounts for six degrees of freedom in each of its two nodes, thus making it a  $12 \times 12$  matrix, being composed of up to 144 different elements.

In the case of additional fluid damping and fluid rigidity, such as in the deductions presented above, each of the MATRIX27 elements used is connected to the structural model in one of its nodes. Thus, an additional complementary node has to be created in the FEM for each node affected by the added damping or rigidity matrices.

For the present case, the fluid damping matrix (for example) of the 3-DOF system under analysis can be implemented with a single MATRIX27 element, which can be presented as:

$$\mathbf{C}_{M27} = \begin{bmatrix} \mathbf{C}_{ii} & \mathbf{C}_{ij} \\ \mathbf{C}_{ji} & \mathbf{C}_{jj} \end{bmatrix} \quad (\text{B.16})$$

where  $\mathbf{C}_{ij}$ ,  $\mathbf{C}_{ji}$ , and  $\mathbf{C}_{jj}$  can be assumed as zeros for the case under study, assuming that the MATRIX27 is connected to the structure at the  $i$ -node. The elements of  $\mathbf{C}_{ii}$  are defined according to Equation B.15, leaving the upper-left part of  $\mathbf{C}_{M27}$  as:

$$\mathbf{C}_{ii} = \begin{bmatrix} c_{22}^{(a)} & c_{21}^{(a)} & 0 & 0 & 0 & c_{23}^{(a)} \\ c_{12}^{(a)} & c_{11}^{(a)} & 0 & 0 & 0 & c_{13}^{(a)} \\ 0 & 0 & 0 & 0 & 0 & 0 \\ 0 & 0 & 0 & 0 & 0 & 0 \\ 0 & 0 & 0 & 0 & 0 & 0 \\ c_{32}^{(a)} & c_{31}^{(a)} & 0 & 0 & 0 & c_{33}^{(a)} \end{bmatrix} \quad (\text{B.17})$$

The quantities  $c_{ij}^{(a)}$  indicate the elements composing  $\mathbf{C}_a$ , where  $i, j = 1, 2, 3$ . Note that the elements within  $\mathbf{C}_{M27}$  are defined under a different coordinate system than the element displayed in Figure B.1. In this case, the  $x$ -axis in the FEM is considered to be parallel to the  $z$ -axis of Figure B.1, and the right-hand rule is followed.

A brief example is presented to illustrate the implementation of  $\mathbf{C}_a$  utilizing MATRIX27. An analogous approach is used for the definition of  $\mathbf{K}_a$ . The 3-DOF system illustrated in Figure B.1 is assumed

to be a NACA type-64 airfoil. Its structural dynamic properties are assumed to be represented by a mass of 100 kg, a natural frequency of 5 rad/s for its three DOFs, and structural damping of 1% of the critical value. The values of fluid damping and fluid rigidity can be defined in an APDL code by using the following commands when the elements of the model are being defined. Exemplifying with  $C_a$ , these commands are:

```
! Definition of matrix elements
ET,5,MATRIX27,1,2,5 ! Defines an Unsymmetrical Damping matrix
R,5                ! Creates a table with real constants

! Modification of matrix elements
! ----- Upper-Left
RMODIF,5,1, c22*rho*c
RMODIF,5,2, c21*rho*c
RMODIF,5,6, c23*rho*c
RMODIF,5,13,c12*rho*c
RMODIF,5,14,c11*rho*c
RMODIF,5,18,c13*rho*c
RMODIF,5,61,c32*rho*c
RMODIF,5,62,c31*rho*c
RMODIF,5,66,c33*rho*c
```

A time-history analysis of a harmonic flow with a frequency of 5 rad/s is performed on the model. Figure B.2 displays a comparison between the results obtained from the analyses in APDL, and the ones computed from the solution of Equation B.7 through numerical integration in MATLAB.

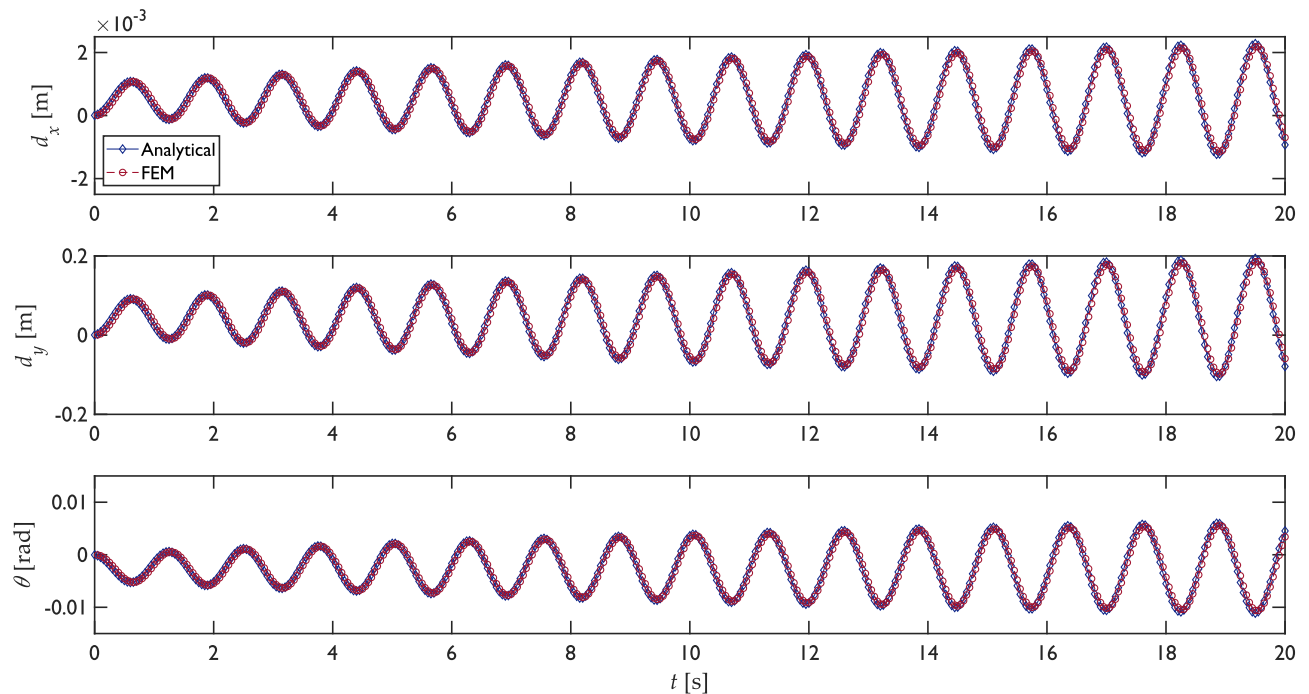


Figure B.2: Structural response of a 3-DOF system

[This page intentionally left blank]



## Appendix C

### Derived publications

Some of the research produced during the development of this dissertation has been published in archived journals. Also, results from analyses performed for this research have been sought to be communicated as well in congresses, seminars, and scientific-outreach publications. The list of publications and presentations related to the subjects covered in this dissertation are listed in this Appendix. Moreover, the academic curriculum vitae of the author is included afterward, where other collaborations by him appear.

#### Publications in refereed journals

- **Martín del Campo, J. O.** and Pozos-Estrada A. “Multi-hazard fragility analysis for a wind turbine support structure: An application to the Southwest of Mexico.” *Engineering Structures*. 2020; 209: 109929. DOI: 10.1016/j.engstruct.2019.109929.
- Jaimes, M. A., García-Soto, A., **Martín del Campo, J. O.** and Pozos-Estrada, A. “Probabilistic risk assessment on wind turbine towers subjected to cyclone-induced wind loads.” *Wind Energy*. 2020; 23: 528–546. DOI: 10.1002/we.2436.
- **Martín del Campo, J. O.**, Pozos-Estrada, A. and Pozos-Estrada, O. “Development of fragility curves of land-based wind turbines with tuned mass dampers under cyclone and seismic loading.” *Wind Energy*. 2021; 24: 737–753. DOI: 10.1002/we.2600.
- **Martín del Campo, J. O.** and Pozos-Estrada, A. “A simplified method for structural and fatigue analyses of wind turbine support structures.” *Journal of Wind Engineering & Industrial Aerodynamics*. 2022; 224: 104983. DOI: 10.1016/j.jweia.2022.104983.

#### In conference proceedings

- **Martín del Campo, J. O.** and Pozos-Estrada, A. “Estudio para la predicción de la carga lateral asociada al pandeo local de la torre de un aerogenerador.” in *Proceedings of the XXI National Congress of Structural Engineering*; November, 2018; Campeche, Mexico. (In Spanish)
- **Martín del Campo, J. O.** and Pozos-Estrada, A. “Análisis de fragilidad de turbinas eólicas ante viento turbulento debido a huracanes.” in *Proceedings of the XXII National Congress of Earthquake Engineering*; November, 2019; Moterrey, Mexico. (In Spanish)

## Invited presentations

- **Martín del Campo, J. O.** *Funciones de fragilidad de turbinas eólicas ante eventos extremos*. Presented at: Seminar of the Structural Engineering Department at the Institute of Engineering of UNAM; March, 2021; On-line. (In Spanish)

## Publications for scientific outreach

- **Martín del Campo, J. O.** and Pozos-Estrada, A. “Evaluación multipeligro de la confiabilidad de estructuras de soporte de turbinas eólicas ante eventos extremos.” *Gaceta del Instituto de Ingeniería de la UNAM*. 2021; 1 (147): 17–19. (In Spanish)
- Pozos-Estrada, A. and **Martín del Campo, J. O.** “Una energía bien sustentable, la eólica.” *Pa-Ciencia Pa’Todos*. 2021; 5 (10): 7–10. (In Spanish)

# J. Osvaldo **Martín del Campo**

PHD IN STRUCTURAL ENGINEERING · INSTITUTO DE INGENIERÍA UNAM

Universidad Nacional Autónoma de México, 3000 Universidad Av., Coyoacan, Mexico City, 04510

✉ JMartindelCampoP@iingen.unam.mx

## Education

---

### National Autonomous University of Mexico (UNAM)

PHD IN CIVIL ENGINEERING (STRUCTURAL)

- Advisor: Dr. Adrián Pozos-Estrada

Mexico City, Mexico

2018 – 2022

### National Autonomous University of Mexico (UNAM)

MENG IN CIVIL ENGINEERING (STRUCTURAL)

- Advisor: Dr. Adrián Pozos-Estrada
- Graduated with honors

Mexico City, Mexico

2015 – 2017

### Western Institute of Technology and Higher Education (ITESO)

BENG IN CIVIL ENGINEERING

Guadalajara, Mexico

2005 – 2010

## Professional Experience

---

2010 – 2015 **Structural Engineer**, FZB Diestra (Guadalajara, Mexico)

## Publications

---

### IN REFEREED JOURNALS

López-Castañeda, A. S., Reinoso, E., and **Martín del Campo, J. O.** Influence of site-specific strong-motion duration on structural performance. *Bull Earth Eng.* 2022. DOI: 10.1007/s10518-022-01499-5 (Accepted for publication)

**Martín del Campo, J. O.**, Pozos-Estrada, A. A simplified method for structural and fatigue analyses of wind turbine support structures. *J Wind Eng Ind Aerod.* 2022; 224: 104983. DOI: 10.1016/j.jweia.2022.104983.

**Martín del Campo, J. O.**, Pozos-Estrada, A. and Pozos-Estrada, O. Development of fragility curves of land-based wind turbines with tuned mass dampers under cyclone and seismic loading. *Wind Energy.* 2021; 24: 737-753. DOI: 10.1002/we.2600.

Jaimes, M. A., García-Soto, A., **Martín del Campo, J. O.** and Pozos-Estrada, A. Probabilistic risk assessment on wind turbine towers subjected to cyclone-induced wind loads. *Wind Energy.* 2020; 23: 528-546. DOI: 10.1002/we.2436.

**Martín del Campo, J. O.**, Pozos-Estrada, A. Multi-hazard fragility analysis for a wind turbine support structure: An application to the Southwest of Mexico. *Eng Struct.* 2020; 209: 109929. DOI: 10.1016/j.engstruct.2019.109929.

### UNDER REVIEW / IN PREPARATION

Pozos-Estrada, A., **Martín del Campo, J. O.**, and Pozos-Estrada, O. Fragility curves of a slender structure fitted with tuned mass dampers subjected to turbulent wind and seismic loading. *Can J Civil Eng.* 2022.

### TECHNICAL REPORTS

Pozos-Estrada, A., **Martín del Campo, J. O.**, López-Ibarra, A., Rivera-Torres, M. Propuesta de modificación y actualización del Capítulo de Efectos Dinámicos de las NTC-Viento. Elaborated by the Institute of Engineering of UNAM for the Institute of Construction Safety of Mexico City. ISCDF/CEC-04/2021-14. August, 2021.

## SCIENTIFIC-OUTREACH PUBLICATIONS

Pozos-Estrada, A. and **Martín del Campo, J. O.** Una energía bien sustentable, la eólica. *PaCiencia Pa'Todos*. 2021; 5 (10): 7–10. (In Spanish)

**Martín del Campo, J. O.** and Pozos-Estrada, A. Evaluación multipeligro de la confiabilidad de estructuras de soporte de turbinas eólicas ante eventos extremos. *Gaceta del Instituto de Ingeniería de la UNAM*. 2021; 1 (147): 17–19. (In Spanish)

## Presentations

---

### INVITED TALKS

Spring 2021. *Funciones de fragilidad de turbinas eólicas ante eventos extremos*. Invited talk: Seminar of the Structural Engineering Department at the Institute of Engineering of UNAM, On-line seminar. (In Spanish)

### CONTRIBUTED PRESENTATIONS

**Martín del Campo, J. O.**, and Pozos-Estrada, A. Análisis de fragilidad de turbinas eólicas ante viento turbulento debido a huracanes. Presented at: XXII National Congress of Earthquake Engineering; November, 2019; Moterrey, Mexico. (In Spanish)

Pozos-Estrada, A., and **Martín del Campo, J. O.** Estudio de la respuesta sísmica de un puente carretero esviado: el caso del puente La Ventosa ante el sismo del 7 de septiembre de 2017. Presented at: XXII National Congress of Earthquake Engineering; November, 2019; Moterrey, Mexico. (In Spanish)

**Martín del Campo, J. O.**, and Pozos-Estrada, A. Estudio para la predicción de la carga lateral asociada al pandeo local de la torre de un aerogenerador. Presented at: XXI National Congress of Structural Engineering; November, 2018; Campeche, Mexico. (In Spanish)

**Martín del Campo, J. O.**, and Pozos-Estrada, A. Multi-hazard structural analysis for the development of fragility curves for wind turbine structures. Presented at: VI Structural Engineering World Congress; November, 2017; Cancun, Mexico.

**Martín del Campo, J. O.**, and Pozos-Estrada, A. Análisis multipeligro para la obtención de curvas de fragilidad de aerogeneradores. Presented at: XXI National Congress of Earthquake Engineering; September, 2017; Guadalajara, Mexico. (In Spanish)

Zamorano-Bernal, F. A., and **Martín del Campo, J. O.** Dos diferentes aplicaciones del aislamiento sísmico pendular. Presented at: XIX National Congress of Earthquake Engineering; November, 2013; Boca del Río, Mexico. (In Spanish)

## Teaching Experience

---

\* *Engineering Graduate Program*

Spring 2022	<b>Wind Engineering</b> , Teaching Assistant	UNAM*
Spring 2021	<b>Wind Engineering</b> , Teaching Assistant	UNAM*
Spring 2020	<b>Wind Engineering</b> , Teaching Assistant	UNAM*
Fall 2019	<b>Mathematics for Structural Engineering</b> , Teaching Assistant	UNAM*
Spring 2019	<b>Wind Engineering</b> , Teaching Assistant	UNAM*
Fall 2018	<b>Mathematics for Structural Engineering</b> , Teaching Assistant	UNAM*
Spring 2018	<b>Wind Engineering</b> , Teaching Assistant	UNAM*